

BIORTHOGONAL CHEMISTRY TO CREATE TARGETED DIAGNOSTIC AGENTS

THE USE OF BIOORTHOGONAL CHEMISTRY TO CREATE ^{99m}Tc AND MICELLE-
BASED DIAGNOSTIC AGENTS

By

Zainab Ahmad, B. Sc.

A Thesis

Submitted to the School of Graduate Studies

In Partial Fulfillment of the Requirements

For the Degree

Doctor of Philosophy

McMaster University

© Copyright by Zainab Ahmad, 2020

Ph.D. Thesis- Z. Ahmad; McMaster University- Chemistry and Chemical Biology

DOCTOR OF PHILOSOPHY (2020)

McMaster University

Chemical Biology

Hamilton, Ontario

TITLE: THE USE OF BIOORTHOGONAL CHEMISTRY TO CREATE ^{99m}Tc AND
MICELLE-BASED DIAGNOSTIC AGENTS

AUTHOR: Zainab Ahmad, B. Sc. (McMaster University)

SUPERVISOR: Professor John Fitzmaurice Valliant

Number of Pages: XXV, 207

Abstract

Technetium-99m (^{99m}Tc) radiopharmaceuticals are widely used in nuclear medicine to diagnose a variety of diseases, including cancer. While, ^{99m}Tc is a seemingly ideal radioisotope for imaging, there is an incompatibility between the isotope's half-life (6 h) and the biological half-life of antibodies (multiple days), which are useful and prevalent targeting vectors. This misalignment in physical half-life and pharmacokinetics creates a barrier to the development of molecularly targeted ^{99m}Tc -based radiopharmaceuticals. To address this, bioorthogonal chemistry between tetrazine and *trans*-cyclooctene (TCO) derivatives labelled with ^{99m}Tc and a variety of different targeting molecules was explored to assess the feasibility of using pre-targeting versus conventional direct labeling strategies.

Initially, a new family of tridentate chelate ^{99m}Tc -tetrazine ligands of varying polarity were synthesized and characterized. The ^{99m}Tc -tetrazine ligands were evaluated *in vivo* for bone targeting through a pre-targeting strategy with a (TCO)-functionalized bisphosphonate: TCO-BP. The hydrophobic ^{99m}Tc -tetrazine derivative demonstrated targeted shoulder and knee uptake of 4.62 ± 1.36 and 9.12 ± 1.88 % ID/g, respectively, in biodistribution studies at 6 h post injection. At the same time point, accumulation of the hydrophilic ^{99m}Tc -tetrazine derivative in the shoulder (2.10 ± 0.38 % ID/g) and knee (3.15 ± 0.33 % ID/g) joints, albeit to a lesser degree, is further evidence of successful targeting of ^{99m}Tc -tetrazine ligands to a TCO-tagged site *in vivo*.

Next, the ^{99m}Tc -tetrazine ligands were evaluated *in vivo* in tumour xenografts through a pre-targeting strategy with a TCO-modified antibody targeting the A33 antigen in colon carcinomas. Biodistribution studies were performed using SPECT-CT imaging

and tissue counting following necropsy. Unfortunately, low tumour uptake ($\sim 1\%$ ID/g) was observed for both the hydrophobic and hydrophilic ^{99m}Tc -tetrazine derivatives tested. The current hypothesis is that significant uptake in metabolizing organs, notably the liver and intestines, and short blood circulation time of the tetrazine ligands limited the coupling between the two components.

To explore the impact of drug formulation on the distribution and accessibility of radiolabelled tetrazines, Pluronic F127 polymeric micelles were used where encapsulation was designed to modify the pharmacokinetics of the hydrophobic ^{99m}Tc -tetrazine. The micelles significantly increased the blood circulation time of the ^{99m}Tc -tetrazine while also significantly reducing liver uptake. Unfortunately, this did not translate into increased bone uptake of the encapsulated ^{99m}Tc -tetrazine when evaluated with the TCO-BP targeting vector through a pre-targeting strategy. This is likely because the tetrazine is not preferentially released at the sites with the high TCO-BP concentration.

The micelles used in the initial study were non-targeted. To capitalize on the chemistry developed during the preparation of the ^{99m}Tc -tetrazines, the Pluronic F127 polymers previously used for encapsulation were modified with terminal TCO groups, creating a simple way of modifying the surface of micelles with targeting vectors. A F127-TCO polymer was synthesized in high yield and the corresponding micelles were visualized by DLS and TEM to be 20-25 nm in size. A bisphosphonate-derived tetrazine (TzBP) was prepared and radiolabelled with ^{99m}Tc and combined with the TCO-modified micelles to create a new class of targeted micelles. *In vitro*, active and pre-targeting studies showed the F127-TCO micelles preferentially bound to the hydroxyapatite salt in the presence of TzBP

compared to controls. *In vivo*, F127-TCO micelles accumulated at bone at a 7-fold higher concentration when modified with [^{99m}Tc]TcTzBP compared to that seen when labelled with a non-targeted tetrazine. This approach ultimately represents a platform for the creation of targeted micelle encapsulated drugs.

Acknowledgments

First, I would like to thank my supervisor Dr. John Valliant for taking me on as an eager undergraduate student many years ago and helping me grow into the scientist I am today. I am incredibly grateful for the numerous opportunities I experienced as a result of being in his research group. I would also like to thank my committee members Dr. Michael Brook and Dr. Giuseppe Melacini for their support throughout my graduate career. An additional thanks to Dr. Sam Sadeghi for his guidance.

I would like to acknowledge the support from all the past and present members of the Valliant research group I got to know and learn from. A big thank you to Nancy, Amber, Afaf, Aimen and Shannon for all their help and support. I could not have made it through graduate school without all my wonderful confidants: Holly, Sam, Natalie, Rowan, Steph and Zoya. Also, I want to thank all my amazing friends outside of the lab for always pretending to understand and care about my work.

A very special thank you to my parents for always being my inspiration and getting me to where I am today.

Lastly, thank you to my partner Mark for always believing in me.

Dedication

I would like to dedicate this dissertation to my grandmothers, my Dadi and Nanna, for providing unconditional love and support.

Publications

Peer reviewed journal articles.

Preparation and Evaluation of ^{99m}Tc -labelled Tridentate Chelates for Pre-targeting Using Bioorthogonal Chemistry.

Holly A. Bilton,* **Zainab Ahmad***, Nancy Janzen, Shannon Czorny, John F. Valliant.

Journal of Visualized Experiments 2017; 120: e55188. DOI: 10.3791/55188.

*Co-authors

A Bone-seeking trans-cyclooctene for Pre-targeting and Bioorthogonal Chemistry: A Proof of Concept Study Using ^{99m}Tc - and ^{177}Lu -labelled Tetrazines.

Abdolreza Yazdani, Holly Bilton, Alyssa Vito, Afaf R. Genady, Stephanie M. Rathmann,

Zainab Ahmad, Nancy Janzen, Shannon Czorny, Brian M. Zeglis, Lynn C. Francesconi,

John F. Valliant. Journal of Medicinal Chemistry 2016; 59(20): 9381-89.

Manuscript prepared for publication

TCO-Functionalized Pluronic F127 Micelles as a Platform for Targeted Delivery.

Zainab Ahmad, Afaf Genady, Rowan Swann, Samantha Slikboer, Amber Faraday,

Nancy Janzen, John F. Valliant.

Published Meeting Abstracts

Encapsulation of Radiolabelled Tetrazines in Pluronic F127 Nanoparticles for Pre-targeted SPECT Imaging and Radiotherapy using Bioorthogonal Chemistry.

Zainab Ahmad, Nancy Janzen, Shannon Czorny, John F. Valliant. *J. Label. Compd. Radiopharm.* 2017; 60: S103.

Preparation and *in vivo* testing of $^{99m}\text{Tc}(\text{I})$ -tetrazines for pre-targeted imaging.

Holly A. Bilton, **Zainab Ahmad**, Nancy Janzen, Shannon Czorny, Dalya Abdel- Atti, Kimberly Edwards, Lynn C. Francesconi, Brian M. Zeglis, Jason S. Lewis, John F. Valliant. *J. Label. Compd. Radiopharm.* 2017; 60: S92.

Synthesis, Characterization and Imaging of a $^{99m}\text{Tc}(\text{I})$ -Tetrazine Tridentate Ligand Complex for Bioorthogonal Chemistry.

Zainab Ahmad, Megan Blacker, Aimen Zlitni, Holly Bilton, John Valliant. *J. Label. Compd. Radiopharm.* 2015; 58: S138.

Textbook Chapter Publication

The Radiopharmaceutical Chemistry of Technetium-99m.

Stephanie M. Rathmann, **Zainab Ahmad**, Samantha Slikboer, Holly A. Bilton, Denis P. Snider, John F. Valliant. In *Radiopharmaceutical Chemistry*; Lewis, J. S., Windhorst, A. D., Zeglis, B. M., Eds.; SpringerLink, 2019; pp 311–333.

Table of Contents

<i>Abstract</i>	<i>iv</i>
<i>Acknowledgments</i>	<i>vii</i>
<i>Dedication</i>	<i>vii</i>
<i>Publications</i>	<i>viii</i>
<i>List of Figures</i>	<i>xiii</i>
<i>List of Supporting Figures</i>	<i>xvii</i>
<i>List of Tables</i>	<i>xix</i>
<i>List of Abbreviations</i>	<i>xx</i>
Chapter 1: Introduction	26
1.1. Molecular Imaging	26
1.2. Nuclear Imaging	26
1.2.1. Single Photon Emission Computed Tomography (SPECT).....	27
1.2.2. Technetium-99m.....	29
1.3. Bioorthogonal Chemistry and Pre-targeting Strategies	33
1.4. Nanoparticles	36
1.4.1. Challenges in nanopharmaceutical development.....	38
1.5. Thesis overview	40
1.6. References	41
Chapter 2: Preparation and evaluation of ^{99m}Tc-radiolabelled tridentate chelates for pre-targeting using bioorthogonal chemistry	50
2.1. Introduction	50
2.2. Protocol	52
2.2.1. Radiolabeling of Tz-tridentate ligands with ^{99m} Tc.....	52
2.2.2. Pre-targeted Bio-distribution Studies.....	55
2.3. Results and Discussion	58
2.4. Conclusion and Future Work	65
2.5. Acknowledgments	65
2.6. References	66
Chapter 3: Evaluation of ^{99m}Tc-labelled tetrazines using trans-cyclooctene functionalized antibodies and pre-targeting	70
3.1. Introduction	70
3.2. Materials and Methods	75
3.2.1. General materials, methods, and instrumentation.....	75
3.2.2. Stability of compound 5 in PBS.....	76

3.2.3.	Stability of Compound 10 in formulations.....	76
3.2.4.	Preparation of TCO-huA33 mAb. ¹³	76
3.2.5.	Coupling compound 5 and huA33-TCO.	77
3.2.6.	<i>In vivo</i> evaluation of compound 1.	77
3.2.7.	<i>In vivo</i> evaluation of compound 5.	78
3.2.8.	Pre-targeted <i>in vivo</i> evaluation of compound 1.	78
3.2.9.	Pre-targeted <i>in vivo</i> evaluation of compound 5 (high specific activity).	78
3.2.10.	Pre-targeted <i>in vivo</i> evaluation of compound 5 (low specific activity).	79
3.3.	Results and Discussion	80
3.3.1.	Stability in phosphate buffered saline (PBS).	80
3.3.2.	Stability of compound 10.	81
3.3.3.	Preparation of TCO-huA33 antibody.	82
3.3.4.	Testing the reactivity of compound 5 towards the huA33-TCO mAb.	83
3.3.5.	<i>In vivo</i> evaluation of compound 1.	84
3.3.6.	<i>In vivo</i> evaluation of compound 5.	85
3.3.7.	Pre-targeted <i>in vivo</i> evaluation of compound 1.	86
3.3.8.	Pre-targeted <i>in vivo</i> evaluation of compound 5 (high specific activity).	88
3.3.9.	Pre-targeted <i>in vivo</i> evaluation of compound 5 (low specific activity).	90
3.3.10.	Comparison of pre-targeting with TCO-BP and huA33-TCO mAb.....	92
3.4.	Conclusion and Future Work.....	93
3.5.	References.....	94
Chapter 4: Pluronic F127 micelles for modifying the pharmacokinetics of ^{99m}Tc labelled tetrazines.....		98
4.1	Introduction	98
4.2	Materials and Methods	108
4.2.1	General materials, methods, and instrumentation	108
4.2.2	Encapsulation of cargo in Pluronic F127 micelles (mF127(cargo)).....	109
4.2.3	Synthesis of TCO-bisphosphonate (TCO-BP) (20).....	110
4.2.4	Biodistribution study of mF127(1).....	110
4.2.5	Pre-targeted <i>in vivo</i> biodistribution study of mF127(1)	111
4.3	Results and Discussion	111
4.3.1	Preparation and Characterization of Loaded Pluronic F127 micelles	112
4.3.2	Biodistribution study of mF127(1) in healthy mice	114
4.3.3	Pre-targeted biodistribution study of mF127(1) with 20	116
4.4	Conclusion and Future Work.....	118
4.5	References.....	119
4.6	Supplemental Information.....	125
Chapter 5: TCO-Functionalized Pluronic F127 Micelles as a Platform for Targeted Drug Delivery.....		126
1.	Abstract.....	126
2.	Introduction.....	127
3.	Materials and Methods.....	130
3.1.	General methods, materials and instrumentation	130
3.2.	Animal Studies	132

3.3.	Chemical Synthesis.....	133
3.4.	Quantification of reactive TCO groups on F127-TCO.....	136
3.5.	Characterization of F127-TCO Micelles (mF127-TCO).....	137
3.6.	Calcium Salt (Hydroxyapatite, HA) Binding Assay	138
3.7.	In vivo Studies	139
4.	Results and Discussion.....	141
4.1.	Synthesis of Pluronic F127-TCO Polymers	141
4.2.	Characterization of Pluronic F127-TCO Polymers	144
4.3.	Characterization of mF127-TCO(IR780)	146
4.4.	Development of a Tetrazine-Derived Targeting Vector.....	147
4.5.	Hydroxyapatite Binding	150
4.6.	<i>In vivo</i> Studies	152
5.	Conclusions and Future Work.....	160
6.	References	160
	<i>Chapter 6: Summary and Future Work.....</i>	<i>170</i>
6.1.	Summary	170
6.2.	Future Work	172
6.2.1.	Optimizing ^{99m} Tc-tetrazine ligand	172
6.2.2.	Targeting solid tumours.....	173
6.2.3.	Modifying pharmacokinetics of micelles	175
6.2.4.	Triggered release with ultrasound	176
6.3.	References.....	177
	<i>APPENDIX I.....</i>	<i>180</i>
	Supporting Information for Chapter 2.....	180
	<i>APPENDIX II</i>	<i>199</i>
	Supporting Information for Chapter 5.....	199

List of Figures

Figure 1.1. Simplified schematic of (A) SPECT imaging and a (B) single gamma camera.	26
Figure 1.2. Schematic diagram of a $^{99}\text{Mo}/^{99\text{m}}\text{Tc}$ generator.	28
Figure 1.3. Ligands used to prepare Tc-targeted radiopharmaceuticals: (A) MIP 1404, ligand for $^{99\text{m}}\text{Tc}$]Tc-Trofolostat and (B) HYNIC-TOC, ligand for $^{99\text{m}}\text{Tc}$]Tc-HYNIC-TOC.	31
Figure 1.4. Bioorthogonal reactions pairs: A) azide and functionalized phosphine (Staudinger ligation), B) azide and strained cyclooctene (SPAAC), C) tetrazine and <i>trans</i> -cyclooctene (IEDDA reaction).	32
Figure 1.5. The pre-targeting approach using the bioorthogonal [4+2] inverse electron demand Diels-Alder (IEDDA) cycloaddition reaction between a TCO-derived antibody and a radiolabelled tetrazine.	33
Figure 1.6. Successive biological barriers encountered by nanoparticles when administered intravenously. ⁴⁶	37
Figure 2.1. The bioorthogonal IEDDA reaction between tetrazine and <i>trans</i> -cyclooctene.	50
Figure 2.2. Compounds 1-5 were produced using different linkers (Y) and chelators (X) as shown (bottom). All compounds were radiolabelled with $^{99\text{m}}\text{Tc}(\text{CO})_3(\text{H}_2\text{O})_3^+$ using the same reaction conditions (top), with the exception of 1 , which did not require step (ii).	57
Figure 2.3. Stability test results using compound 4 . γ -HPLC traces of 4 incubated in PBS at 37 °C for 1, 4 and 6 h.	58
Figure 2.4. Bio-distribution results for $^{99\text{m}}\text{Tc}$ -labelled tetrazine derivatives 1-5 (bars indicated). Data shown were obtained from selected tissues and fluids taken 6 h post injection of the radiolabelled derivatives, and activity was normalized to tissue or fluid weight, as mean percent injected dose per gram of tissue or fluid (% ID/g) \pm SEM. Bone targets are indicated by *. NOTE: All remaining tissues not shown had mean % ID/g that was less than 1%.	59
Figure 2.5. Bio-distribution results for control study using $^{99\text{m}}\text{Tc}$ -labelled tetrazine (2) without prior injection of TCO-BP. Data shown were obtained from selected tissues and fluids taken from 3 mice at 0.5, 1, 4, and 6 h post injection of 2 . Activity was normalized to tissue or fluid weight, as mean percent injected dose per gram of tissue or fluid (% ID/g) \pm SEM.	60
Figure 3.1. PET images for mice bearing A431 (a) and BT-474 (b) xenografts in right shoulders pre-targeted with (a) TCO-cetuximab and (b)TCO-trastuzumab respectively, followed by ^{18}F]F-TAF 72 h later. Coronal (I), sagittal (II) and transverse (III) images obtained at 4 hours post injection of tetrazine. Yellow arrows identify tumour (T), liver (L) and intestines (In). Reprinted with permission from Keinänen, O. <i>et al.</i> EJNMMI Res. 2017, 7 (95), 1–16. Copyright Springer Nature. 70	
Figure 3.2. A) PET/CT images for mice bearing SW1222 xenografts pre-targeted with huA33-TCO mAb followed by ^{64}Cu -labelled tetrazine. B) Biodistribution data for	

mice bearing SW1222 xenografts pre-targeted with huA33-TCO mAb followed by ⁶⁴ Cu-labelled tetrazine. Reprinted (adapted) with permission from Zeglis, B.M. <i>et al.</i> J. Nucl. Med. 2013, 54 (8), 1389-1396. Copyright 2013 SNMMI.	71
Figure 3.3. HPLC chromatograms (γ -detection) of compound 5 , incubated in PBS at 37 °C, at t= 1 (top), 4 (middle) and 6 (bottom) hours.	78
Figure 3.4. Absorbance (UV-Vis) data from studies to assess the stability of compound 10 in different formulations monitored over 400-600 nm. Compound 10 was formulated at 1 mg/mL in both PBS and PBS + 0.5% BSA + 0.01 % Tween80 and absorbance data collected at 0, 0.5, 1, 2, 4 and 6 hours.	80
Figure 3.5. Radio TLC analyses of compound 5 (left) and the reaction mixture 10 min following the combination of compound 5 and huA33-TCO mAb (right).	82
Figure 3.6. SPECT/CT images of mice (n=4) administered compound 1 (~50 MBq) obtained at 4 and 6 hours. Mouse 2 is shown as an example. Significant accumulation in the hepatobiliary system, notably the liver and intestines, was observed with little difference in distribution between the 4 and 6-hour imaging time points.	83
Figure 3.7. SPECT/CT images of mice (n=2) administered compound 5 (16-18 MBq) obtained at 1, 4 and 6 h post-injection. Mouse 1 is shown as an example. Clearance of the compound was initially via the renal system while the later time points shows some residual activity in the intestines and feces.	84
Figure 3.8. SPECT/CT images of mice (n=4) administered compound 1 (46-51 MBq), 24 hours after administration of huA33-TCO mAb, obtained at 4 and 6 hours post-tetrazine injection. Mouse 2 is shown as an example. Uptake in the gall bladder, liver, and large and small intestines was seen while no signal was observed in the tumour (denoted by white arrow). SW1222-tumour located by the right shoulder.	85
Figure 3.9. Biodistribution study data associated with the imaging study shown in Figure 3.8. Data is reported as the percent injected dose per gram (% ID/g).	86
Figure 3.10. SPECT/CT images of mice (n=4) administered compound 5 (19-22 MBq), 24 hours after administration of huA33-TCO mAb, obtained at 1, 4 and 6 hours post-tetrazine injection. Mouse 1 is shown as an example. Clearance through the renal system and minimal uptake in the tumour (white arrow) was seen. SW1222-tumours were located on the right shoulder.	87
Figure 3.11. Biodistribution study data associated with the imaging study in Figure 3.9. Data is reported as percent injected dose per gram (% ID/g).	88
Figure 3.12. SPECT/CT images of mice (n=4) administered a mixture of compounds 5 (19-21 MBq) and 10 (0.75 nM), 24 hours after administration of huA33-TCO mAb, obtained at 1, 4 and 6 hours post-tetrazine injection. Mouse 2 is shown as an example. Similar to above, clearance through the renal system and minimal tumour uptake (white arrow) was observed. The addition of compound 10 did not appear to alter the biodistribution when observed by imaging. SW1222 tumours were located on the right shoulder.	89
Figure 3.13. Biodistribution study data associated with the imaging study in Figure 3.12. Data is reported as percent injected dose per gram (% ID/g).	90

- Figure 4.1.** Kaplan-Meier plot depicting overall survival rate of patients undergoing phase II trial of SP1049C. Median survival was 10 months while 24 % of patients survived past 1 year. Reprinted with permission from Springer Nature: Valle *et al. Invest. New Drugs* 2011, 29 (5), 1029–1037. Copyright 2010.99
- Figure 4.2.** Photoacoustic study data conducted using Balb/C mice bearing 4T1 xenografts which were administered aza-BDTP F127 micelles and aza-BDTP/PTX F127 micelles intravenously. A) PA images of tumours at various time points. B) Quantified PA signal obtained from *ex vivo* imaging of key organs at 24 h compared to intravenous administration of saline as the control. Reprinted with permission from John Wiley and Sons: Zhang *et al. Small* 2018, 14 (44), 1802991. Copyright 2018. 101
- Figure 4.3.** A) Excretion of nanonaps over 24 h in feces (black) and urine (red). B) Histology images of the intestine of a mouse administered the saline control (left) and a mouse administered the ONc nanonaps (right) 24 h post administration, right. Reprinted with permission from Springer Nature: Zhang *et al. Nat. Nanotechnol.* 2014, 9 (8), 631–638. 102
- Figure 4.4.** PET imaging (A) and biodistribution data (B) of ⁶⁴Cu-ONc nanonaps administered orally to Balb/C mice. Reprinted with permission from Springer Nature: Zhang *et al. Nat. Nanotechnol.* 2014, 9 (8), 631–638. 103
- Figure 4.5.** PET imaging (A) and biodistribution data (B) of ⁶⁴Cu-ONc nanonaps administered intravenously to Balb/C mice bearing 4T1 breast cancer xenografts in right shoulders (white arrows). Biodistribution was conducted at 24 h post injection. Reprinted by permission from The Royal Society of Chemistry: Zhang *et al. Nanoscale.* (2017) 9, 3391-3398. 104
- Figure 4.6.** Balb/C-nu mice received ¹¹¹In-PS-bPEO (22 MBq) micelles intravenously. A) SPECT/CT images obtained at 30 min, 4 h, and 24 h post injection. B) Results of biodistribution study at 24 h post injection. Values are reported as % injected dose/g (% ID/g). 105
- Figure 4.7.** Dynamic light scattering data for mF127(1) (top) and mF127(6) (bottom) at 25 °C. Micelle size from DLS was 27.5 ± 0.8 nm (PDI: 0.25) and 31.2 ± 0.6 nm (PDI: 0.28) from TEM. 111
- Figure 4.8.** Transmission electron microscopy image of F127(6). The micelles were ~18 nm in size. 112
- Figure 4.9.** Biodistribution data of **1** alone and mF127(1) reported as % ID/g. Animals were sacrificed at 1 and 6 h p.i. of the radiolabelled compound. A) Biodistribution data for compound **1** in healthy CD1 mice (n=3). B) Biodistribution data for mF127(1) in healthy CD1 mice (n=3). 114
- Figure 4.10.** Biodistribution data for compound **1** (A) and mF127(1) (B) when pre-targeted with compound **20** (TCO-BP) reported as % ID/g. Compound **1** and mF127(1) were injected 1 hour after the TCO-BP injection in healthy CD1 mice (n=3) and animals were sacrificed at 6 hours p.i. 115
- Fig 1.** A) Schematic representation of TCO-functionalized F127 micelles (mF127-TCO) for targeted delivery of payload using tetrazine-based targeting vectors. B) [4+2]

- inverse electron demand Diels-Alder (IEDDA) cycloaddition reaction between a tetrazine and TCO. 142
- Fig 2.** TCO-modification of Pluronic F127 polymers. 142
- Fig 3.** ^1H NMR of F127 derivatives with key peaks identified. A) ^1H NMR of F127-CDI (600 MHz, CDCl_3). B) ^1H NMR of F127- NH_2 (600 MHz, CDCl_3). C) ^1H NMR of F127-TCO (600 MHz, CDCl_3), black squares correspond to carbamate protons, other peaks from ^1H NMR were at ppm= 1.13 (t, 3 H \times 65, CH_3 group of PPO (**h**)), 1.69 (m, 2H, CH_2 of TCO ring (**e**)), 1.90 – 1.98 (m, 4 H, CH_2 of TCO ring (**k**, **d**)), 2.31-2.38 (m, 4H, CH_2 of TCO ring (**c**, **f**)), 2.46 (m, 2 H, CH_2 of ethylene linker (**m**)), 2.70 (m, 2H, CH_2 of ethylene linker (**l**)), 3.40 (m, 2 H \times 65, CH_2 of PPO(**j**)), 3.54 (m, 1 H \times 65, CH of PPO(**i**)), 3.64 (m, 2 H \times 200, CH_2 of PEO(**n**)), 4.32 (m, 1 H, CH of TCO ring (**g**))...... 143
- Fig 4.** Example of titration curve showing UV absorption at 540 nm following the addition of F127-TCO polymer to increasing amounts of compound **1**. Conducted in triplicate. The red arrow delineates the equivalence point..... 146
- Fig 5.** A) The hydrophobic NIR dye IR780 iodide that was encapsulated in mF127-TCO. B) Size distribution of mF127-TCO(IR780) (25 ± 10 nm) obtained by DLS and reported by % volume. C) Transmission electron microscopy image of Pluronic F127-TCO micelles (~ 20 nm). 147
- Fig 6.** A) Synthesis of a tetrazine-derived targeting vector: TzBP. B) Radiolabelling of TzBP to form $^{99\text{m}}\text{Tc}$]TcTzBP. The structure $^{99\text{m}}\text{Tc}$ -BPs has not been concretely identified but X-ray crystallography of $^{99\text{m}}\text{Tc}$ -BPs suggests two BP groups coordinate to a single $^{99\text{m}}\text{Tc}$ atom.[47]. 149
- Fig 7.** A) Percent binding of TzBP-mF127-TCO(IR780) and mF127-TCO(IR780) alone to hydroxyapatite (HA). % binding was calculated by using a no salt control. Significant difference was seen in binding to HA with TzBP-mF127-TCO(IR780) vs. mF127-TCO(IR780) micelles suggesting specific binding occurs due to the presence of the tetrazine modified BP. $p = 0.05$ ($n=3$). B) Percent binding of TzBP-mF127-TCO(IR780) and mF127-TCO(IR780) pre-targeted to HA after 1, 6, and 24 h. The percent binding was calculated by using a no salt control. $p = 0.05$ ($n=3$). ... 151
- Fig 8.** Compound $^{99\text{m}}\text{Tc}$]TcTzPy was prepared according to a literature method [33] and used to radiolabel mF127-TCO(IR780) for biodistribution studies. 153
- Fig 9.** Biodistribution results for $^{99\text{m}}\text{Tc}$]TcTzPy-mF127-TCO. Data shown was obtained from selected tissues and fluids taken from mice at 1, 6, and 24 h post injection of ($^{99\text{m}}\text{Tc}$]TcTzPy-mF127-TCO. Activity was normalized to tissue or fluid weight, as the mean percent injected dose per gram of tissue or fluid (% ID/g) \pm SEM. Full biodistribution results can be found in the supporting information (Fig S6). 154
- Fig 10.** A) Biodistribution results for $^{99\text{m}}\text{Tc}$]TcTzBP-mF127-TCO(IR780) in healthy Balb/C mice. Data shown was obtained from selected tissues and fluids taken from mice at 1, 4, and 24 h post injection of $^{99\text{m}}\text{Tc}$]TcTzBP-mF127-TCO(IR780). Activity was normalized to tissue or fluid weight, as mean percent injected dose per gram of tissue or fluid (% ID/g) \pm SEM. Full biodistribution results can be found in the supporting information (Fig S7). B) B-Mode ultrasound images with superimposed photoacoustic images of knee and shoulder joints obtained *ex vivo* at

t= 1, 4, and 24 h post injection of [^{99m} Tc]TcTzBP-mF127-TCO(IR780). Green is signal corresponding to IR780.	155
Fig 11. Comparison of [^{99m} Tc]TcTzPy-mF127-TCO and [^{99m} Tc]TcTzBP-mF127-TCO(IR780) uptake in bone (leg + knee) and blood concentrations at 1 and 24 h post injection. An increase of 6.6 and 6.8-fold increase in bone uptake was observed with [^{99m} Tc]TcTzBP-mF127-TCO(IR780) versus [^{99m} Tc]TcTzPy-mF127-TCO which does not contain a BP at 1 and 24 h, respectively (p < 0.01).....	157
Fig 12. A) Biodistribution data obtained for pre-targeting study of mF127-TCO(IR780) with [^{99m} Tc]TcTzBP in healthy Balb/c mice at 1, 4, and 24 h, reported as % ID/g. Activity was normalized to tissue or fluid weight, as mean percent injected dose per gram of tissue or fluid (% ID/g) ± SEM. Full biodistribution results can be found in the supporting information (Fig S8). B) B-Mode ultrasound images with superimposed photoacoustic images of knee and shoulder joints, lungs and spleen obtained <i>ex vivo</i> at t= 1, 4, and 24 h post injection of mF127-TCO(IR780). The green colour is the signal corresponding to IR780.	158
Figure 6.1. Functionalization of BSA with tetrazines.....	173

List of Supporting Figures

Figure S4.1. Structure of compound 20 (TCO-BP) used in pre-targeting experiment. ...	115
Figure S4.2. ¹ H NMR (600 MHz, D ₂ O) of TCO-BP (20).	115
Figure S2.1. Synthesis of 1 from 13 . a) NaBH(OAc) ₃ , DCE, 6-aminocaproic acid, rt, 12 h. b) NHS, EDC, ACN, rt, 12 h. c) (4-(1,2,4,5-tetrazin-3-yl) phenyl) methanamine hydrochloride, Et ₃ N, ACN, rt, 1 h.	180
Figure S2.2. ¹ H NMR (600 MHz, CDCl ₃) of 12	181
Figure S2.3. ¹³ C NMR (150 MHz, CDCl ₃) of 12	182
Figure S2.4. ¹ H NMR (600 MHz, CDCl ₃) of 13	183
Figure S2.5. ¹³ C NMR (150 MHz, CDCl ₃) of 13	183
Figure S2.6. ¹ H NMR (600 MHz, CDCl ₃) of 14	184
Figure S2.7. ¹³ C NMR (150 MHz, CDCl ₃) of 14	185
Figure S2.8. Synthesis of 1 and 6 from 14 . a) [M(CO) ₃ (H ₂ O) ₃] ⁺ , MW, 20 min, 60 °C, pH 3.5, MeOH, saline. M= ^{99m} Tc (1) and Re (6).	185
Figure S2.9. HPLC chromatograms (UV and γ) of 6 (top) co-injected with 1 (bottom).	186
Figure S2.10. Synthesis of compound 5 from 15 . a) Bromoacetyl bromide, Et ₃ N, DCM, rt, 2 h. b) Imidazole 2-carboxaldehyde, potassium iodide, DIPEA, DMF, 80 °C, 12 h. c) NH ₂ -PEG ₁₀ -CH ₂ CH ₂ COOH, NaBH(OAc) ₃ , DCE, rt, 12 h. d) (4-(1,2,4,5-tetrazin-3-yl) phenyl) methanamine hydrochloride, PyBOP, DIPEA, DMF, rt, 12 h.	187
Figure S2.11. ¹ H NMR (600 MHz, CDCl ₃) of 16	188
Figure S2.12. ¹³ C NMR (150 MHz, CDCl ₃) of 16	189
Figure S2.13. ¹ H NMR (600 MHz, CDCl ₃) of 17	190

Figure S2.14. ^{13}C NMR (150 MHz, CDCl_3) of 17	191
Figure S2.15. ^1H NMR (600 MHz, CDCl_3) of 18	192
Figure S2.16. ^{13}C NMR (150 MHz, CDCl_3) of 18	193
Figure S2.17. ^1H NMR (600 MHz, CDCl_3) of 19	195
Figure S2.18. ^{13}C NMR (150 MHz, CDCl_3) of 19	196
Figure S2.19. Synthesis of compounds 5 and 10 from 19 . a) $[\text{M}(\text{CO})_3(\text{H}_2\text{O})_3]^+$, MW, 20 min, 60 °C, pH 3.5, MeOH, saline $\text{M}=\text{}^{99\text{m}}\text{Tc}$ (5) and Re (10). b) DCM, TFA, MW, 60 °C, 10 min (5), 11 min (10).....	197
Figure S2.20. HPLC chromatograms (UV and γ) of 10 (top) co-injected with 5 (bottom).	198
Fig S 1. COSY NMR of F127-TCO polymers (3).....	192
Fig S 2. ^1H NMR of TzNHS (4)	193
Fig S 3. ^1H NMR of TzBP (5).	194
Fig S 4. iTLC of $[\text{}^{99\text{m}}\text{Tc}]\text{TcTzBP}$ (6) and $^{99\text{m}}\text{TcTzBP} + \text{F127-TCO}$ polymers run using water and acetone as eluents: 12 % $^{99\text{m}}\text{TcO}_2$ ($R_f = 0.069$), 88 % $^{99\text{m}}\text{TcTzBP} + ^{99\text{m}}\text{TcO}_4^-$ ($R_f = 0.53$), and 2 % $^{99\text{m}}\text{TcO}_4^-$ ($R_f = 0.56$), 98 % $^{99\text{m}}\text{TcTzBP} + ^{99\text{m}}\text{TcO}_2$ ($R_f = 0.054$).	195
Fig S 5. Radiolabeling scheme of $[\text{}^{99\text{m}}\text{Tc}]\text{TcTzPy}$ (7).	195
Fig S 6. Biodistribution results for $[\text{}^{99\text{m}}\text{Tc}]\text{TcTzPy-mF127-TCO}$, full tissue list. Data shown was obtained from selected tissues and fluids taken from mice at 1, 6, and 24 h post injection of $[\text{}^{99\text{m}}\text{Tc}]\text{TcTzPy-mF127-TCO}$. Activity was normalized to tissue or fluid weight, as mean percent injected dose per gram of tissue or fluid (% ID/g) \pm SEM.	196
Fig S 7. Biodistribution results for $[\text{}^{99\text{m}}\text{Tc}]\text{TcTzBP-mF127-TCO}(\text{IR780})$ micelles in healthy Balb/C mice. Data shown was obtained from selected tissues and fluids taken from mice at 1, 4, and 24 h post injection of $[\text{}^{99\text{m}}\text{Tc}]\text{TcTzBP-mF127-TCO}(\text{IR780})$. Activity was normalized to tissue or fluid weight, as mean percent injected dose per gram of tissue or fluid (% ID/g) \pm SEM.	197
Fig S 8. Biodistribution data obtained for $[\text{}^{99\text{m}}\text{Tc}]\text{TcTzBP}$ when pre-targeting for subsequent administration of mF127-TCO(IR780) in healthy Balb/C mice at 1, 4, and 24 h, reported as % ID/g. Activity was normalized to tissue or fluid weight, as mean percent injected dose per gram of tissue or fluid (% ID/g) \pm SEM.	198
Fig S 9. Biodistribution data obtained for $[\text{}^{99\text{m}}\text{Tc}]\text{TcTzBP}$ in healthy Balb/C mice at 1, 4, and 6 h, reported as % ID/g. Activity was normalized to tissue or fluid weight, as mean percent injected dose per gram of tissue or fluid (% ID/g) \pm SEM.	199
Fig S 10. Absorbance measurements of IR-780 dye (green), F17-TCO(IR780) micelles (red), and blank F127-TCO micelles (blue) scanned over 550-1000 nm. The absorbance maxima for IR780 around 780 nm remains unchanged when the dye is encapsulated within the micelles. The micelles do not exhibit any absorbance signal at that wavelength.	200

List of Tables

Table 1.1. Key characteristics of clinical nuclear imaging modalities. ⁹⁻¹²	28
Table 1.2. Select nuclear and decay properties of commonly used SPECT radioisotopes. ⁶ EC= electron capture, IT = internal transition.	29
Table 1.3. Examples of nanoparticle formulations currently approved for clinical use or in clinical trials for oncology. ⁴⁴ This list is not exhaustive. <i>Nab</i> = <i>NP albumin-bound</i> , <i>NSCLC</i> = <i>non-small cell lung cancer</i>	36
Table 2.4 Bone tissue: blood ratios determined from bio-distribution studies.	62

List of Abbreviations

A

Abs	Absorbance
ACN	Acetonitrile
AREB	Animal research ethics board
a.u.	Arbitrary unit

B

BP	Bisphosphonate
BSA	Bovine serum albumin

C

δ	Chemical shift
CAF	McMaster central animal facility
CCAC	Canadian council on animal care
CDCl ₃	Deuterated chloroform
CDI	Carbonyldiimidazole
CMC	Critical micelle concentration
CPM	Counts per minute
CT	Computed tomography

D

D ₂ O	Deuterated water
DCM	Dichloromethane

DI	Deionized water
DIPEA	Diisopropylethylamine
DLS	Dynamic light scattering
DMF	Dimethylformamide
DMSO	Dimethyl sulfoxide
DOTA	1,4,7,10-Tetraazacyclododecane-1,4,7,10-tetraacetic acid
DOX	Doxorubicin
DSC	N,N'-Disuccinimidyl carbonate
E	
EC	Electron capture
EDC	1-Ethyl-3-(3-dimethylaminopropyl)carbodiimide
EGFR	Epidermal growth factor receptor
EPR	Enhanced permeability and retention
ESI-MS	Electrospray ionization mass spectrometry
EtOH	Ethanol
EtOAc	Ethyl acetate
F	
FA	Formic acid
G	
GI	Gastrointestinal
γ	Gamma
H	

h	Hour(s)
HA	Hydroxyapatite
HCl	Hydrochloric acid
HER2	Human epidermal growth factor receptor 2
HPLC	High performance liquid chromatography
HRMS	High resolution mass spectrometry
HYNIC	Hydrazinonicotinic acid
I	
% ID/g	Percent injected dose per gram
i.v.	Intravenous
ICG	Indocyanine green
IEDDA	Inverse electron demand Diels Alder
IR	Infrared
IT	Internal transition
iTLC	Instant thin layer chromatography
K	
k_2	Second order rate constant
kDa	Kilodalton
keV	Kiloelectronvolt
M	
mAb	Monoclonal antibody
MALDI-MS	Matrix-assisted laser desorption/ionization mass spectrometry

MBq	Megabecquerel
mCi	Millicurie
MDR	Multidrug resistance
MeOD	Deuterated methanol
MeOH	Methanol
MeV	Megaelectronvolt
MI	Molecular imaging
min	Minute(s)
MPS	Mononuclear phagocyte system
MWCO	Molecular weight cut off
N	
NET	Neuroendocrine tumour
NHS	N-hydroxysuccinimide
NIR	Near infrared
NMR	Nuclear magnetic resonance
NP	Nanoparticle(s)
O	
OD	Optical density
OS	Overall survival
P	
P-gp	P-glycoprotein
p.i.	Post injection

PA	Photoacoustic
PBS	Phosphate buffered saline
PCa	Prostate cancer
PDI	Polydispersity index
PEG	Polyethylene glycol
PEO	Polyethylene oxide
PET	Positron emission tomography
PK	Pharmacokinetic
PMT	Photomultiplier tube
ppm	Parts per million
PPO	Polypropylene oxide
PSMA	Prostate specific membrane antigen
PTT	Photothermal therapy
PTX	Paclitaxel
R	
RES	Reticuloendothelial system
rpm	Revolutions per minute
R_t	Retention time
S	
SEM	Standard error of mean
SPAAC	Strain promoted azide alkyne cycloaddition
SPECT	Single photon emission computer tomography

T

$t_{1/2}$	Half-life
TCO	Trans-cyclooctene
TCO-BP	Trans-cyclooctene-bisphosphonate
TEA	Triethylamine
TEM	Transmission electron microscopy
TFA	Trifluoroacetic acid
TLC	Thin layer chromatography
TME	Tumour microenvironment
Tz	Tetrazine
TzBP	Tetrazine-bisphosphonate

U

US	Ultrasound
UV	Ultraviolet

Chapter 1: Introduction

1.1. Molecular Imaging

Molecular imaging (MI) is a non-invasive technique for monitoring biochemical processes, pathways, and targets within the body.¹ MI is increasingly playing a crucial role in cancer diagnosis and treatment as well as for monitoring disease progression.¹⁻³ In oncology, advancements in treatments have been limited by the tumour heterogeneity observed within and between patients leading to an increasing number of clinicians seeking the benefits of personalized medicine.^{4,5} With MI's ability to identify tumour-specific biomarkers, it can play a significant role in developing targeted therapeutics. This should translate to better outcomes, less invasive procedures, shorter hospital stays, fewer complications and greater patient satisfaction.

1.2. Nuclear Imaging

Nuclear imaging, a branch of MI, involves the application of radioisotopes for diagnostic imaging.^{6,7} Radioisotopes decay with a characteristic half-life ($t_{1/2}$) through particle emission (alpha, beta, positron) or release of electromagnetic radiation (x-rays and gamma rays), at varying energies. The differing energies and decay modes determine which isotopes are better suited for diagnostic imaging or therapy or a combination of both. For imaging, nuclear modalities have been transformative as they are far more sensitive than anatomical imaging modalities such as computed tomography (CT) or X-ray imaging. The improved sensitivity is due in part to the small quantities of radioisotope that are required

and because the radiopharmaceutical injected specifically localizes to the site of interest providing high signal-to-noise ratios. High contrast images can be obtained with radiopharmaceutical doses as low as 6 MBq and as high as 1110 MBq, which translates to only nanomolar quantities of the administered pharmaceutical. This low mass enables the radiopharmaceutical to function as a tracer for biological processes without perturbing the biological system; a concept known as the tracer principle.

Positron emission tomography (PET) and single photon emission computed tomography (SPECT) are the two prominent nuclear imaging modalities used for diagnostic purposes. These modalities can be combined with density-based CT scanning to obtain images that provide anatomical as well as biochemical data, where the latter is derived from the administered radiopharmaceutical.^{6,8}

1.2.1. Single Photon Emission Computed Tomography (SPECT)

SPECT involves the use of a rotating gamma camera to obtain diagnostic images by detecting gamma rays (i.e. photons) of the appropriate energy that are emitted from radiopharmaceuticals administered to patients (Figure 1.1).⁶ Gamma cameras, which have been in use since the late 1950s are comprised of a collimator along with a sodium iodide (NaI) scintillation crystal coupled to photomultiplier tubes (PMT). The collimator serves to filter out radiation which does not strike the detector at an angle that is perpendicular to the gamma camera. SPECT scanners have two or more gamma cameras which rotate around the patient to obtain multiple planar images which are compiled into 3D images of the patient.

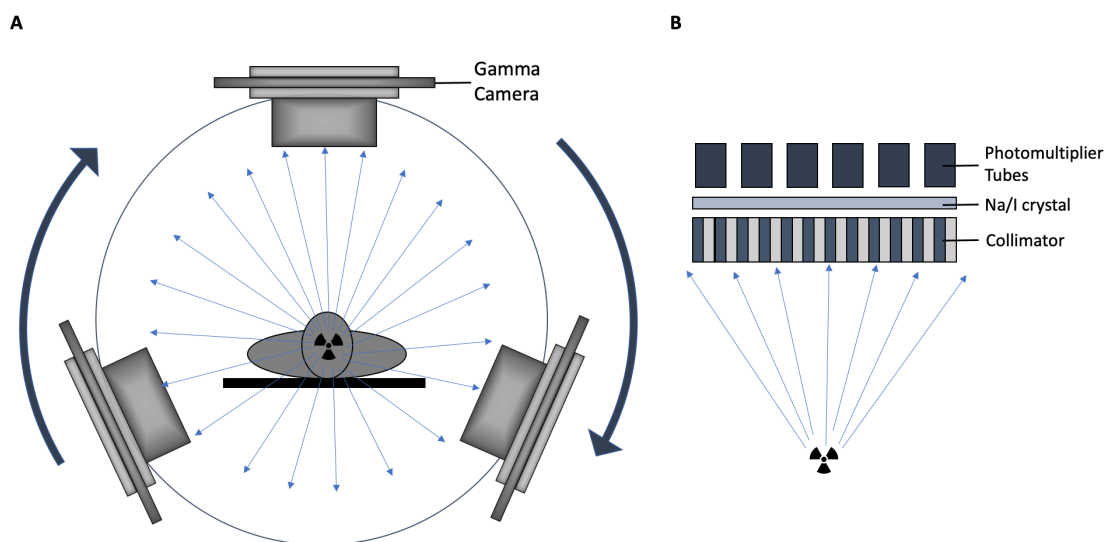


Figure 1.1. Simplified schematic of (A) SPECT imaging and a (B) single gamma camera.

Table 1.1. Key characteristics of clinical nuclear imaging modalities.⁹⁻¹²

<i>Imaging Modality</i>	<i>Spatial Resolution</i>	<i>Sensitivity (M)</i>	<i>Cost</i>
<i>PET</i>	4 to 6 mm	10^{-11} to 10^{-12}	\$ 2.5 to 4 million
<i>SPECT</i>	8 to 12 mm	10^{-10} to 10^{-11}	\$ 0.6 to 1 million

Clinical PET offers superior spatial resolution and sensitivity compared to clinical SPECT imaging, producing images with better contrast (Table 1.2).^{6,9-12} However, PET scanners are traditionally more expensive than gamma cameras and therefore less readily accessible. Also, SPECT isotopes generally have longer half-lives than common PET isotopes like ^{18}F ($t_{1/2} = 110$ min) and ^{11}C ($t_{1/2} = 20$ min) providing greater flexibility for synthesis, quality control, and distribution. Commonly used radioisotopes for SPECT include iodine-123 ($t_{1/2} = 13.2$ h), indium-111 ($t_{1/2} = 2.80$ d), gallium-67 ($t_{1/2} = 3.30$ d), thallium-

201 ($t_{1/2}$ = 3.04 d), and technetium-99m ($t_{1/2}$ = 6.01 h), where the latter is the most widely used diagnostic isotope (Table 1.1).¹³⁻²⁰

Table 1.2. Select nuclear and decay properties of commonly used SPECT radioisotopes.⁶ EC= electron capture, IT = internal transition.

<i>Isotope</i>	<i>$t_{1/2}$</i>	<i>Decay type</i>	<i>Decay Energy (MeV)</i>
<i>Gallium-67 (^{67}Ga)</i>	3.30 d	EC	1.00
<i>Indium-111 (^{111}In)</i>	2.80 d	EC	0.245
<i>Iodine-123 (^{123}I)</i>	13.2 h	EC	0.158
<i>Technetium-99m ($^{99\text{m}}\text{Tc}$)</i>	6.01 h	IT	0.140
<i>Thallium-201 (^{201}Tl)</i>	3.04 d	IT	0.167

1.2.2. Technetium-99m

Technetium-99m ($^{99\text{m}}\text{Tc}$) is used in approximately 40 million procedures worldwide; predominantly for cardiac perfusion imaging, bone imaging, renal imaging as well as cerebral, thyroid, and GI imaging.⁶ It is conveniently obtained from a molybdenum-99 (^{99}Mo)/ $^{99\text{m}}\text{Tc}$ generator which plays a role in its frequent use.^{6,21} The bench-top generator contains ^{99}Mo ($t_{1/2}$ = 66 h), a byproduct of uranium-235 fission, adsorbed onto an alumina (Al_2O_3) column as molybdate ($^{99}\text{Mo}[\text{MoO}_4^{2-}]$) and shielded with a lead casing. Upon decay of ^{99}Mo , $^{99\text{m}}\text{Tc}$ is produced as pertechnetate ($^{99\text{m}}\text{Tc}[\text{TcO}_4^-]$) which can be selectively eluted from the alumina column using sterile saline into an evacuated collection vial in high purity (Figure 1.2). The generator can be eluted up to a few times a day to provide 50 - 80 patient doses per day for approximately a week before needing replacement.²¹

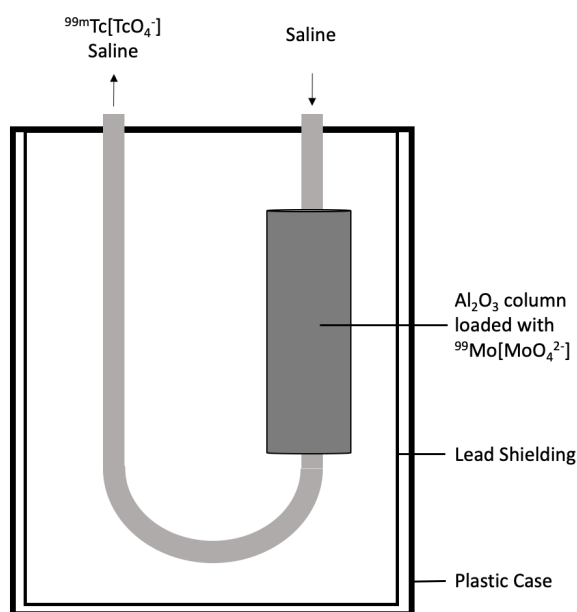


Figure 1.2. Schematic diagram of a $^{99}\text{Mo}/^{99m}\text{Tc}$ generator.

In addition to being readily accessible from a generator, ^{99m}Tc is widely used due to its nearly ideal decay characteristics ($t_{1/2} = 6$ h, γ -decay, 140 keV).^{6,22-24} The γ -energy is optimal for detection by gamma cameras while the half-life is suitable for most imaging applications. While ^{99m}Tc is useful for patient imaging, it lacks a non-radioactive isotope that can be used for developing new radiopharmaceuticals, optimizing new radiolabeling procedures and structural characterization of new compounds where large quantities of material are required.^{6,24} For such purposes, Re, another group 7 metal, is used as an analogue of ^{99m}Tc because they have similar chemical properties as a result of the lanthanide contraction.⁸ Tc coordination chemistry spans eight oxidation states (-1 to +7) and therefore ^{99m}Tc complexes can vary greatly in structure based on the number of ligands bound.

$[^{99m}\text{Tc}]\text{TcO}_4^-$, a $^{99m}\text{Tc}(\text{VII})$ ion, can be used for the detection of thyroid cancer or incorporated into other molecules using a suitable ligand and reducing agent (e.g. SnCl_2 , $\text{K}_2[\text{BH}_3\text{CO}_2]$).^{6,24} ^{99m}Tc -radiopharmaceuticals can be classified as Tc-essential compounds, which are agents based on coordination of ligand(s) to the metal, or Tc-targeted compounds, which are agents consisting of a targeting molecule and a Tc-chelate.^{6,8,25,26} For example, Cardiolite™ ($[^{99m}\text{Tc}]\text{Tc}$ -Sestamibi) is a Tc-essential compound where the Tc(I) cationic complex of isonitrile ligands is used for cardiac perfusion imaging. Here the radiopharmaceutical accumulates in cardiac tissue by entering cardiomyocytes as a result of their negative membrane potential.⁶ Similarly, $[^{99m}\text{Tc}]\text{Tc}$ -MAG₃ (^{99m}Tc -mercaptoacetyltriglycine) or Technescan MAG₃™ for renal imaging and $[^{99m}\text{Tc}]\text{Tc}$ -Exametazime, or Ceretec™ for cerebral perfusion imaging are also examples of Tc-essential complexes albeit of Tc(V).

In contrast to Tc-essential radiopharmaceuticals, Tc-targeted compounds are not nearly as prevalent in the clinic. One of the early successes was $[^{99m}\text{Tc}]\text{Tc}$ -TRODAT which targets the dopamine transporters to image the dopaminergic system for diagnosis of Parkinson's disease.^{27,28} More recently, $[^{99m}\text{Tc}]\text{Tc}$ -Trofolostat is a Tc-targeted, $^{99m}\text{Tc}(\text{I})$ complex consisting of a tridentate ^{99m}Tc chelate and a small molecule for targeting the prostate specific membrane antigen (PSMA) (Figure 1.3A).^{6,29} It has recently completed phase II clinical trials for SPECT/CT imaging of prostate cancer (PCa), detecting 94 % of lesions compared to the 86 % identified by MRI. Behera *et al.* reported a ^{99m}Tc -radiolabelled somatostatin-targeting agent $[^{99m}\text{Tc}]\text{Tc}$ -HYNIC-TOC for imaging neuroendocrine tumours (NETs) which overexpress somatostatin receptors (Figure 1.3B).⁶

The agent was more sensitive than Octreoscan™ ($[^{111}\text{In}]\text{In-DTPA-octreotide}$), which is used in somatostatin receptor scintigraphy for detection of NETs, but suffered from high non-target pancreatic uptake suggesting the need for further work. This outcome highlights the potential utility and interest in Tc-targeted agents but also the challenges in creating viable radiopharmaceuticals for routine clinical use.

The focus of most of the development of Tc-targeted agents focused on small molecule and peptide-based targeting vectors. The challenge here is that the large Tc-chelate complex often has a detrimental impact on the desired biodistribution. Monoclonal antibodies (mAbs), which have been used successfully to prepare targeted radiopharmaceuticals with other isotopes could be a potential solution. However, antibodies, which have high affinity and specificity for biomarkers have slow *in vivo* kinetics where localization and clearance can take several days to weeks. This pharmacokinetic profile is not compatible with the short half-life of $^{99\text{m}}\text{Tc}$ ($t_{1/2} = 6 \text{ h}$). To use both antibodies and $^{99\text{m}}\text{Tc}$ to create Tc-targeted radiopharmaceuticals, an alternative strategy must be employed to overcome the limitation.

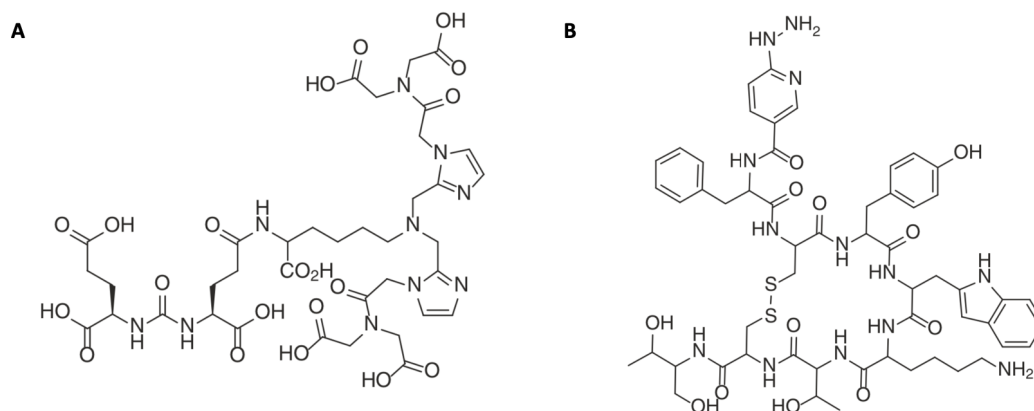


Figure 1.3. Ligands used to prepare Tc-targeted radiopharmaceuticals: (A) MIP 1404, ligand for [^{99m}Tc]Tc-Trofolastat and (B) HYNIC-TOC, ligand for [^{99m}Tc]Tc-HYNIC-TOC.

1.3. Bioorthogonal Chemistry and Pre-targeting Strategies

Bioorthogonal chemistry was developed to study biochemical processes *in vivo* that had previously been difficult to target through the use of abiotic reactive groups.^{30,31} For a reaction to be considered bioorthogonal and be useful for the development of diagnostics and therapeutics, it must not interfere with biological processes, be capable of occurring under physiological conditions, and not be toxic.³¹ The Staudinger ligation first reported in 2003 by Bertozzi *et al.* helped launch the field of bioorthogonal chemistry. Based on the Staudinger reaction discovered in 1919, the ligation reaction occurs between an azide and a functionalized phosphine which can occur *in vivo* (Figure 1.4A). While promising, the reaction was limited by its slow reaction kinetics ($k_2 = 2 \times 10^{-3} \text{ M}^{-1}\text{s}^{-1}$).^{31,32} In efforts to improve kinetics, Bertozzi and colleagues adapted a Huisgen copper-catalyzed azide-alkyne [3+2] cycloaddition to develop a copper-free variation: the strain-promoted alkyne-azide cycloaddition (SPAAC) ($k_2 = 4.2 \times 10^{-3}$ to $0.31 \text{ M}^{-1}\text{s}^{-1}$) (Figure 1.4B).³⁰⁻³² Building

on this approach in 2008, Fox and coworkers reported an inverse electron demand Diels-Alder (IEDDA) reaction between a tetrazine and a *trans*-cyclooctene (TCO), which showed significantly faster reaction kinetics ($k_2=6 \times 10^3$ to $2.7 \times 10^5 \text{ M}^{-1}\text{s}^{-1}$) (Figure 1.4C).

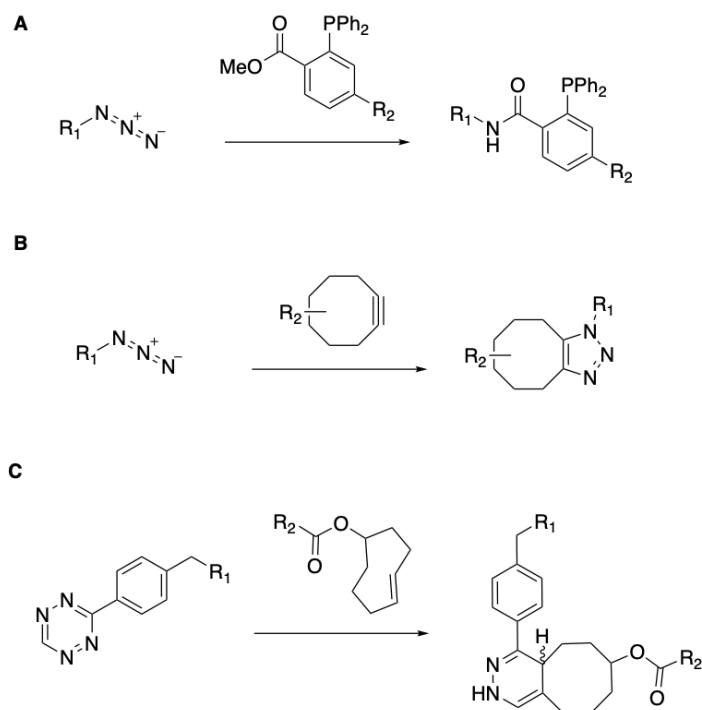


Figure 1.4. Bioorthogonal reactions pairs: A) azide and functionalized phosphine (Staudinger ligation), B) azide and strained cyclooctene (SPAAC), C) tetrazine and *trans*-cyclooctene (IEDDA reaction).

In 2009, Weissleder and colleagues used the tetrazine-TCO reaction to develop a pre-targeting strategy for *in vitro* imaging of lung cancer cells using a TCO-functionalized mAb in conjunction with a fluorophore-labelled tetrazine.³³ Subsequently in 2010, Rossin *et al.* employed IEDDA chemistry for *in vivo* imaging for the first time.^{30,32} Their team used a pre-targeting two-step approach (Figure 1.5).³² First, a TCO-functionalized antibody

was administered and allowed to accumulate at its target. After allowing sufficient time to maximize target accumulation and clearance from non-target tissue, a radiolabelled tetrazine was injected. The TCO and tetrazine then coupled *in vivo* where the SPECT/CT data showed tumour uptake three hours post injection of tetrazine with high contrast. The tetrazine-TCO reaction pair has yet to be used in the clinic but is a promising avenue for research and is being exploited by numerous researchers for the development of targeted radiopharmaceuticals.^{15,32,34-40}

One of the advantages of the pre-targeting and biorthogonal chemistry approach to developing radiopharmaceuticals, is that it offers a way to overcome the incompatibility between the half-life of ^{99m}Tc and the PK profile of antibodies. There is however a lack of viable ^{99m}Tc -labelled tetrazines despite the widespread use of ^{99m}Tc . This topic is explored further in Chapter 3 as a way to use short-lived radioisotopes such as ^{99m}Tc with antibodies. Based on arising data, the same chemistry was exploited to develop targeted nanoparticles, specifically TCO-modified micelles (Chapter 5).

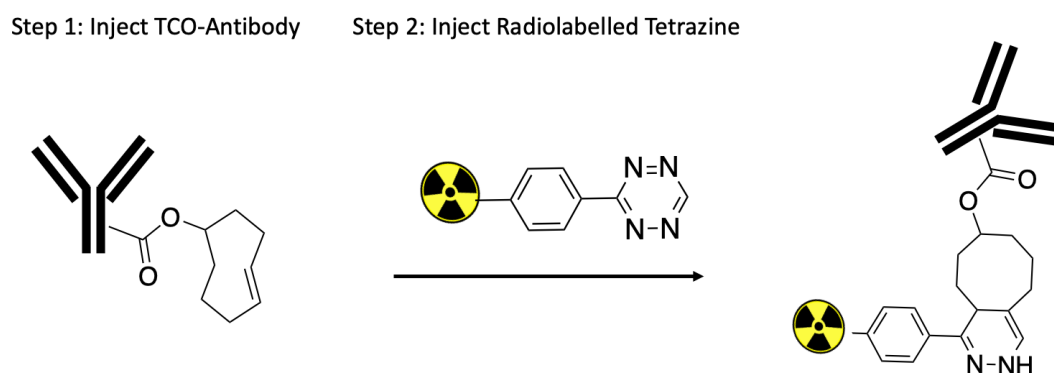


Figure 1.5. The pre-targeting approach using the bioorthogonal [4+2] inverse electron demand Diels-Alder (IEDDA) cycloaddition reaction between a TCO-derived antibody and a radiolabelled tetrazine.

1.4. Nanoparticles

According to a report published by Grand View Research Inc. on “Nanomedicine Market Analysis”, the nanomedicine market is expected to be valued at \$350 billion USD by 2025. Although nanomedicine encompasses everything from quantum dots to lab on a chip technology, a continually expanding market relates to nanoparticles (NPs) for diagnostic and therapeutic applications. The category covers inorganic NPs such Au NPs as well as organic NPs notably liposomes, dendrimers, phospholipid and polymeric micelles amongst others.

For oncology, NPs are increasing in importance in drug development due to their ability to improve efficacy, reduce toxicity, modify the pharmacokinetic profile of cargo, trigger release of cargo, engage in passive or active targeting, and offer the ability to prepare theranostic formulations.^{41–43} Select examples of NP formulations which are currently in clinic or clinical trials are highlighted below (Table 1.3).⁴¹ Based on the most recent analysis, there are currently 15 clinically approved NPs, where over 50 % are liposome-based, and 75 NPs undergoing clinical trials for treating various cancer types.

Table 1.3. Examples of nanoparticle formulations currently approved for clinical use or in clinical trials for oncology.⁴⁴ This list is not exhaustive. *Nab*=NP albumin-bound, *NSCLC*= non-small cell lung cancer.

<i>Generic name and/or Proprietary name</i>	<i>Nanotechnology Platform</i>	<i>Active Ingredient</i>	<i>Cancer Type</i>	<i>Status (Outcome)</i>
<i>Doxil</i>	Pegylated liposome	Doxorubicin	HIV-related Kaposi sarcoma, ovarian cancer, and multiple myeloma	FDA approved

<i>DaunoXome</i>	Liposome	Daunorubicin	HIV-related Kaposi sarcoma	FDA approved
<i>Myocet</i>	Liposome	Doxorubicin	Metastatic breast cancer	FDA approved
<i>Abraxane</i>	Albumin NP (Nab)	Paclitaxel	Breast, lung and pancreatic cancer	FDA approved
<i>Genexol-PM</i>	Polymeric Micelle	Paclitaxel	Breast Cancer	FDA approved
<i>Vyxeos</i>	Liposome	Daunorubicin & Cytarabine	Leukemia	FDA approved
<i>Apealea</i>	Polymeric Micelles	Paclitaxel	Ovarian, peritoneal, and fallopian tube cancer	FDA approved
<i>Lipoplatin</i>	Liposome	Cisplatin	NSCLC	Phase III (positive)
<i>EndoTAG-1</i>	Liposome	Paclitaxel	Breast cancer, pancreatic adenocarcinoma	Phase III (ongoing)
<i>NK-105</i>	Polymeric micelle	Paclitaxel	Metastatic or recurrent breast cancer	Phase III (negative)
<i>BIND-014</i>	Polymeric NP	Docetaxel	Prostate cancer and NSCLC	Phase II (positive)
<i>SGT-53</i>	Liposome	p53 plasmid	Pancreatic cancer and glioblastoma	Phase II (ongoing)
<i>CRLX-101</i>	Polymeric NP	Camptothecin	NSCLC, metastatic renal cell carcinoma and recurrent ovarian, tubal or peritoneal cancer	Phase II (negative)
<i>ABI-009</i>	Albumin NP	Rapamycin	Recurrent and advanced bladder, breast, prostate, cervical, ovarian, and renal cell cancers	Phase I (positive/ongoing)
<i>MM-302</i>	HER2-targeting liposome	Doxorubicin	HER2-positive breast cancer	Phase I (positive)
<i>EphA2-siRNA-DOPC</i>	Liposome	EphA2 siRNA	Advanced cancers	Phase I (ongoing)

Liposomal formulation of doxorubicin (Doxil®) for ovarian cancer, multiple myeloma and HIV-related Kaposi sarcoma, and protein-bound paclitaxel (Abraxane®) for breast, lung and pancreatic cancer are two prominent examples of established NP

formulations with reduced toxicity and improved tumour uptake, respectively, compared to the free drug.⁴⁵ With a majority of the formulations in Table 1.3 being administered systemically, solid tumours are ideal targets for drug-loaded NPs due to their ability to extravasate into the leaky vasculature of the tumours and be retained due to the poor lymphatic drainage of the tumours, known as the enhanced permeability and retention (EPR) effect. However, the nature of the interactions between NPs and biological barriers *in vivo* are yet to be fully understood deterring translation from preclinical studies to clinic settings.⁴⁶⁻⁴⁸

1.4.1. Challenges in nanopharmaceutical development

While NP formulations of chemotherapy drugs have proven to improve pharmacokinetic and biodistribution profiles, Vyxeos (Jazz Pharmaceuticals, FDA approved in 2017) is the only liposomal formulation that has shown an improvement in overall survival (OS) in comparison to its free drugs (daunorubicin and cytarabine).⁴¹ Nanopharmaceutical development has been hindered by the biological barriers encountered by NPs *in vivo* (Figure 1.6).⁴⁶

Immediately after administration, NPs are subjected to opsonization and sequestration by the mononuclear phagocyte system (MPS), a system of phagocytic cells, mostly macrophages residing in the spleen, liver, and lymph nodes (Figure 1.6A).⁴⁶⁻⁴⁸ Opsonization occurs through adsorption of plasma proteins such as serum albumin and immunoglobulins on to the surface of the foreign NP. The subsequently formed “protein corona” recognizes and binds to phagocytic markers resulting in NP sequestration to the liver and spleen, resulting in an increase in off-target uptake. The formation of the protein

corona can be especially unfavourable for NPs bearing surface targeting ligands often rendering them useless. Strategies such as PEGylation and the attachment of CD47 ‘self’ peptides have shown to be somewhat effective in decreasing off-target uptake in preclinical studies.⁴⁶

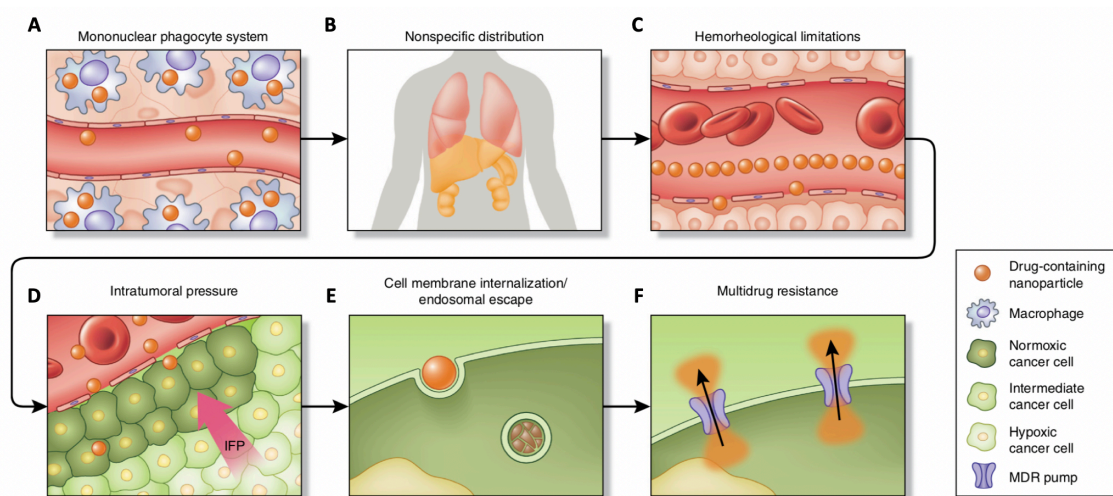


Figure 1.6. Successive biological barriers encountered by nanoparticles when administered intravenously.⁴⁶

In addition to MPS sequestration which contributes to non-specific uptake (Figure 1.6B), NPs encounter hemorheological limitations (Figure 1.6C).⁴⁶ Smaller, spherical NPs (< 5 nm) flow parallel to the vessel walls in the cell-free layer, whereas larger, non-spherical (especially discoidal) particles can tumble through the vessels, bouncing from cells to blood vessel walls resulting in greater endothelial-NP interactions which promotes penetration through the weak endothelial junctions in the tumour vasculature.⁴⁶ Successively, the NP accumulation in tumours is also limited by the high intratumoural pressure occurring due to a dense extracellular matrix and impaired lymphatic drainage as a result of the rapid angiogenesis in the tumour (Figure 1.6D).⁴⁶ Although NP accumulation due to the EPR

effect is reliant on the leaky vasculature, high interstitial fluid pressures can greatly hinder this accumulation. Recognizing these features and to show their importance, Diop-Frimpong *et al.* successfully increased tumour accumulation of doxorubicin liposomes by administering an angiotensin II receptor antagonist which reduced collagen concentration in the tumour.⁴⁹

Upon successful avoidance of the above-mentioned hurdles, NPs bearing targeting ligands can bind to their corresponding receptors to release their cargo at the site of interest to achieve the intended diagnostic or therapeutic effect.⁴⁶ However, if internalized, NPs and their cargo often struggle to survive the endosomal compartmentalization (low pH environment and enzymes) which causes degradation of the particle and the cargo (Figure 1.6E). Even after reaching the tumour microenvironment, NP efficacy can be limited by multidrug resistance (MDR): the efflux of drugs including chemotherapeutics, from the cell as a developed defense mechanism (Figure 1.6F). Expulsion of the drug from the cell causes increased toxicity as neighbouring healthy cells are exposed to toxins and eventually requires an increase in patient doses which can lead to adverse reactions and mortality. However, Kabanov *et al.* recently showed formulation of chemotherapeutics with Pluronic® block copolymers can circumvent MDR through multiple mechanisms.^{50,51} As a result, several Pluronic®-based micellar formulations are now undergoing preclinical studies.⁵²⁻⁵⁶

1.5. Thesis overview

A longstanding problem in nuclear imaging is to develop ^{99m}Tc based molecular imaging probes. There are very few small molecules that when linked to a Tc complex can

drive localization to specific tissues. Antibodies, with their high affinity for specific biomarkers and ability to be derivatized even with large substituents while retaining the ability to bind to their *in vivo* targets, offer a potential solution. Unfortunately, as previously highlighted, there is a mismatch between the half-life of the antibody and the half-life of the ^{99m}Tc precluding the use of traditional radiopharmaceutical chemistry.

The goal of this thesis was to study the potential use of bioorthogonal chemistry to address this problem. Employing a pre-targeting strategy for the bioorthogonal reaction between tetrazine and TCO is a possible way to overcome limitations of directly radiolabelled antibodies. The initial approach required developing tridentate chelate ligands containing a tetrazine that could be radiolabelled with $^{99m}\text{Tc(I)}$. Once prepared, a family of ^{99m}Tc -tetrazines were evaluated *in vivo* with a TCO-derived small molecule as a proof of concept (Chapter 2) and later with TCO-functionalized monoclonal antibodies (Chapter 3). Based on the results, a new class of Pluronic F127 micelles were created with the aim of improving the pharmacokinetic profile of the synthesized ^{99m}Tc -tetrazines through encapsulation (Chapter 4). Concurrently, Pluronic F127 polymers functionalized with TCO moieties were prepared and characterized along with a tetrazine targeting vector creating a platform for targeted delivery of encapsulated agents using the IEDDA reaction that was being studied for work with ^{99m}Tc (Chapter 5).

1.6. References

- (1) Wu, A. M. Engineered Antibodies for Molecular Imaging of Cancer. *Methods* **2014**, *65* (1), 139–147.
- (2) Weissleder, R.; Schwaiger, M. C.; Gambhir, S. S.; Hricak, H. Imaging Approaches

- to Optimize Molecular Therapies. *Sci. Transl. Med.* **2016**, *8* (355ps16), 1–7.
- (3) Janib, S. M.; Moses, A. S.; MacKay, J. A. Imaging and Drug Delivery Using Theranostic Nanoparticles. *Adv. Drug Deliv. Rev.* **2010**, *62* (11), 1052–1063.
- (4) Schork, N. J. Personalized Medicine: Time for One-Person Trials. *Nature* **2015**, *520* (7549), 609–611.
- (5) Weinstein, M.; Skinner, J. Limits to Personalized Cancer Medicine. *N. Engl. J. Med.* **2011**, *362* (5), 567–571.
- (6) *Radiopharmaceutical Chemistry*; Lewis, J. S., Windhorst, A. D., Zeglis, B. M., Eds.; Springer International Publishing: Cham, 2019.
- (7) Atkins, H. L. Radiopharmaceuticals. *Phys. Rep.* **1975**, *21* (6), 315–367.
- (8) Bartholomä, M.; Valliant, J.; Maresca, K. P.; Babich, J.; Zubieta, J. Single Amino Acid Chelates (SAAC): A Strategy for the Design of Technetium and Rhenium Radiopharmaceuticals. *Chem. Commun. (Camb)*. **2009**, *7345* (5), 493–512.
- (9) Rahmim, A.; Zaidi, H. Pet versus Spect: Strengths, Limitations and Challenges. *Nucl. Med. Commun.* **2008**, *29* (3), 193–207.
- (10) Martinuk, S. D. *The Use of Positron Emission Tomography (PET) for Cancer Care Across Canada*; 2011.
- (11) Pimlott, S. L.; Sutherland, A. Molecular Tracers for the PET and SPECT Imaging of Disease. *Chem. Soc. Rev.* **2011**, *40* (1), 149–162.
- (12) Khalil, M. M.; Tremoleda, J. L.; Bayomy, T. B.; Gsell, W. Molecular SPECT Imaging: An Overview. *Int. J. Mol. Imaging* **2011**, *2011*, 1–15.
- (13) Muehllehner, G.; Karp, J. S. Positron Emission Tomography. *Phys. Med. Biol.*

2006, *51*, R117–R137.

- (14) Uematsu, T.; Yuen, S.; Yukisawa, S.; Aramaki, T.; Morimoto, N.; Endo, M.; Furukawa, H.; Uchida, Y.; Watanabe, J. Comparison of FDG PET and SPECT for Detection of Bone Metastases in Breast Cancer. *AJR. Am. J. Roentgenol.* **2005**, *184* (4), 1266–1273.
- (15) Zeglis, B. M.; Sevak, K. K.; Reiner, T.; Mohindra, P.; Carlin, S. D.; Zanzonico, P.; Weissleder, R.; Lewis, J. S. A Pre-targeted PET Imaging Strategy Based on Bioorthogonal Diels-Alder Click Chemistry. *J. Nucl. Med.* **2013**, *54* (8), 1389–1396.
- (16) Seabold, J. E.; Palestro, C. J.; Brown, M. L.; Datz, F. L.; Forstrom, L. a; Greenspan, B. S.; McAfee, J. G.; Schauwecker, D. S.; Royal, H. D. Procedure Guideline for Gallium Scintigraphy in Inflammation. Society of Nuclear Medicine. *J. Nucl. Med.* **2004**, *38* (6), 994–997.
- (17) Viola-Villegas, N. T.; Carlin, S. D.; Ackerstaff, E.; Sevak, K. K.; Divilov, V.; Serganova, I.; Kruchevsky, N.; Anderson, M.; Blasberg, R. G.; Andreev, O. a; et al. Understanding the Pharmacological Properties of a Metabolic PET Tracer in Prostate Cancer. *Proc. Natl. Acad. Sci. U. S. A.* **2014**, *111* (20), 7254–7259.
- (18) Rossin, R.; Verkerk, P. R.; van den Bosch, S. M.; Volders, R. C. M.; Verel, I.; Lub, J.; Robillard, M. S. In Vivo Chemistry for Pre-targeted Tumor Imaging in Live Mice. *Angew. Chem. Int. Ed.* **2010**, *49* (19), 3375–3378.
- (19) Hillier, S. M.; Kern, A. M.; Maresca, K. P.; Marquis, J. C.; Eckelman, W. C.; Joyal, J. L.; Babich, J. W. 123I-MIP-1072, a Small-Molecule Inhibitor of Prostate-

- Specific Membrane Antigen, Is Effective at Monitoring Tumor Response to Taxane Therapy. *J. Nucl. Med.* **2011**, *52* (7), 1087–1093.
- (20) Jurgens, S.; Herrmann, W. A.; Kuhn, F. E. Rhenium and Technetium Based Radiopharmaceuticals: Development and Recent Advances. *J. Organomet. Chem.* **2014**, *751*, 83–89.
- (21) National Research Council. *Medical Isotope Production Without Highly Enriched Uranium*; National Academies Press: Washington, D.C., 2009.
- (22) Gleave, J. a; Valliant, J. F.; Doering, L. C. ^{99m}Tc-Based Imaging of Transplanted Neural Stem Cells and Progenitor Cells. *J. Nucl. Med. Technol.* **2011**, *39* (2), 114–120.
- (23) Armstrong, A. F.; Lemon, J. a; Czorny, S. K.; Singh, G.; Valliant, J. F. Evaluation of Single Amino Acid Chelate Derivatives and Regioselective Radiolabelling of a Cyclic Peptide for the Urokinase Plasminogen Activator Receptor. *Nucl. Med. Biol.* **2009**, *36* (8), 907–917.
- (24) Zolle, I. *Technetium-99m Pharmaceuticals: Preparation and Quality Control in Nuclear Medicine*; Zolle, I., Ed.; Springer Berlin Heidelberg, 2007.
- (25) Coogan, M. P.; Doyle, R. P.; Valliant, J. F.; Babich, J. W.; Zubieta, J. Single Amino Acid Chelate Complexes of the M(CO)₃ (+) Core for Correlating Fluorescence and Radioimaging Studies (M = (^{99m}) Tc or Re). *J. Label. Compd. Radiopharm.* **2014**, *57* (4), 255–261.
- (26) Maresca, K. P.; Hillier, S. M.; Femia, F. J.; Zimmerman, C. N.; Levadala, M. K.; Banerjee, S. R.; Hicks, J.; Sundararajan, C.; Valliant, J.; Zubieta, J.; et al.

- Comprehensive Radiolabeling, Stability, and Tissue Distribution Studies of Technetium-99m Single Amino Acid Chelates (SAAC). *Bioconjug. Chem.* **2009**, *20* (8), 1625–1633.
- (27) Sasannezhad, P.; Juibary, A. G.; Sadri, K.; Sadeghi, R.; Sabour, M.; Kakhki, V. R. D.; Alizadeh, H. ^{99m}Tc-TRODAT-1 SPECT Imaging in Early and Late Onset Parkinson's Disease. *Asia Ocean. J. Nucl. Med. Biol.* **2017**, *5* (2), 114–119.
- (28) Kung, M. P.; Stevenson, D. A.; Plössl, K.; Meegalla, S. K.; Beckwith, A.; Essman, W. D.; Mu, M.; Lucki, I.; Kung, H. F. [^{99m}Tc]TRODAT-1: A Novel Technetium-99m Complex as a Dopamine Transporter Imaging Agent. *Eur. J. Nucl. Med.* **1997**, *24* (4), 372–380.
- (29) Schmidkonz, C.; Hollweg, C.; Beck, M.; Reinfelder, J.; Goetz, T. I.; Sanders, J. C.; Schmidt, D.; Prante, O.; Bäuerle, T.; Cavallaro, A.; et al. ^{99m}Tc-MIP-1404-SPECT/CT for the Detection of PSMA-Positive Lesions in 225 Patients with Biochemical Recurrence of Prostate Cancer. *Prostate* **2018**, *78* (1), 54–63.
- (30) Borrmann, A.; van Hest, J. C. M. Bioorthogonal Chemistry in Living Organisms. *Chem. Sci.* **2014**, *5*, 2123.
- (31) Sletten, E. M.; Bertozzi, C. R. From Mechanism to Mouse: A Tale of Two Bioorthogonal Reactions. *Acc. Chem. Res.* **2011**, *44* (9), 666–676.
- (32) Rossin, R.; Robillard, M. S. Pre-targeted Imaging Using Bioorthogonal Chemistry in Mice. *Curr. Opin. Chem. Biol.* **2014**, *21*, 161–169.
- (33) Devaraj, N. K.; Upadhyay, R.; Haun, J. B.; Hilderbrand, S. A.; Weissleder, R. Fast and Sensitive Pre-targeted Labeling of Cancer Cells via Tetrazine/Trans-

- Cyclooctene Cycloaddition. *Angew. Chemie Int. Ed.* **2009**, *48* (38), 7013–7016.
- (34) van Duijnhoven, S. M. J.; Rossin, R.; van den Bosch, S. M.; Wheatcroft, M. P.; Hudson, P. J.; Robillard, M. S. Diabody Pre-targeting with Click Chemistry In Vivo. *J. Nucl. Med.* **2015**, *56* (9), 1422–1428.
- (35) Yazdani, A.; Bilton, H.; Vito, A.; Genady, A. R.; Rathmann, S. M.; Ahmad, Z.; Janzen, N.; Czorny, S.; Zeglis, B. M.; Francesconi, L. C.; et al. A Bone-Seeking Trans -Cyclooctene for Pre-targeting and Bioorthogonal Chemistry: A Proof of Concept Study Using ^{99m}Tc- and ¹⁷⁷Lu-Labeled Tetrazines. *J. Med. Chem.* **2016**, *59* (20), 9381–9389.
- (36) Albu, S. A.; Al-Karmi, S. A.; Vito, A.; Dzandzi, J. P. K.; Zlitni, A.; Beckford-Vera, D.; Blacker, M.; Janzen, N.; Patel, R. M.; Capretta, A.; et al. ¹²⁵I-Tetrazines and Inverse-Electron-Demand Diels-Alder Chemistry: A Convenient Radioiodination Strategy for Biomolecule Labeling, Screening, and Biodistribution Studies. *Bioconjug. Chem.* **2016**, *27* (1), 207–216.
- (37) Bilton, H. A.; Ahmad, Z.; Janzen, N.; Czorny, S.; Valliant, J. F. Preparation and Evaluation of ^{99m}Tc-Labeled Tridentate Chelates for Pre-Targeting Using Bioorthogonal Chemistry. *J. Vis. Exp.* **2017**, No. 120, e55188.
- (38) Zeglis, B. M.; Brand, C.; Abdel-Atti, D.; Carnazza, K. E.; Cook, B. E.; Carlin, S.; Reiner, T.; Lewis, J. S. Optimization of a Pre-targeted Strategy for the PET Imaging of Colorectal Carcinoma via the Modulation of Radioligand Pharmacokinetics. *Mol. Pharm.* **2015**, *12* (10), 3575–3587.
- (39) Lämpchen, T.; Rossin, R.; van Mourik, T. R.; Gruntz, G.; Hoeben, F. J. M.;

- Versteegen, R. M.; Janssen, H. M.; Lub, J.; Robillard, M. S. DOTA-Tetrazine Probes with Modified Linkers for Tumor Pre-targeting. *Nucl. Med. Biol.* **2017**, *55*, 19–26.
- (40) Reiner, T.; Zeglis, B. M. The Inverse Electron Demand Diels-Alder Click Reaction in Radiochemistry. *J. Label. Compd. Radiopharm.* **2014**, *57* (4), 285–290.
- (41) Shi, J.; Kantoff, P. W.; Wooster, R.; Farokhzad, O. C. Cancer Nanomedicine: Progress, Challenges and Opportunities. *Nat. Rev. Cancer* **2017**, *17* (1), 20–37.
- (42) Chen, F.; Ehlerding, E. B.; Cai, W. Theranostic Nanoparticles. *J. Nucl. Med.* **2014**, *55* (12), 1919–1922.
- (43) Oerlemans, C.; Bult, W.; Bos, M.; Storm, G.; Nijsen, J. F. W.; Hennink, W. E. Polymeric Micelles in Anticancer Therapy: Targeting, Imaging and Triggered Release. *Pharm. Res.* **2010**, *27* (12), 2569–2589.
- (44) He, H.; Liu, L.; Morin, E. E.; Liu, M.; Schwendeman, A. Survey of Clinical Translation of Cancer Nanomedicines - Lessons Learned from Successes and Failures. *Acc. Chem. Res.* **2019**, *52* (9), 2673–2683.
- (45) Ventola, C. L. Progress in Nanomedicine: Approved and Investigational Nanodrugs. *Pharm. Ther.* **2017**, *42* (12), 742–755.
- (46) Blanco, E.; Shen, H.; Ferrari, M. Principles of Nanoparticle Design for Overcoming Biological Barriers to Drug Delivery. *Nat. Biotechnol.* **2015**, *33* (9), 941–951.
- (47) Nel, A. E.; Mädler, L.; Velegol, D.; Xia, T.; Hoek, E. M. V.; Somasundaran, P.; Klaessig, F.; Castranova, V.; Thompson, M. Understanding Biophysicochemical

- Interactions at the Nano-Bio Interface. *Nat. Mater.* **2009**, *8* (7), 543–557.
- (48) Salvati, A.; Pitek, A. S.; Monopoli, M. P.; Prapainop, K.; Bombelli, F. B.; Hristov, D. R.; Kelly, P. M.; Åberg, C.; Mahon, E.; Dawson, K. A. Transferrin-Functionalized Nanoparticles Lose Their Targeting Capabilities When a Biomolecule Corona Adsorbs on the Surface. *Nat. Nanotechnol.* **2013**, *8* (2), 137–143.
- (49) Diop-frimpong, A. B.; Chauhan, V. P.; Krane, S.; Boucher, Y.; Jain, R. K.; Diop-frimpongabc, B.; Chauhanac, V. P.; Kraned, S.; Boucher, Y.; Jain, R. K. High-Resolution Dose—Response Screening Using Droplet-Based Microfluidics. *Proc. Natl. Acad. Sci. U. S. A.* **2012**, *109* (2), 378–383.
- (50) Kabanov, A. V.; Batrakova, E. V.; Alakhov, V. Y. Pluronic[®] Block Copolymers as Novel Polymer Therapeutics for Drug and Gene Delivery. *J. Control. Release* **2002**, *82*, 189–212.
- (51) Alakhova, D. Y.; Zhao, Y.; Li, S.; Kabanov, A. V. Effect of Doxorubicin/Pluronic SP1049C on Tumorigenicity, Aggressiveness, DNA Methylation and Stem Cell Markers in Murine Leukemia. *PLoS One* **2013**, *8* (8).
- (52) Song, H.; He, R.; Wang, K.; Ruan, J.; Bao, C.; Li, N.; Ji, J.; Cui, D. Anti-HIF-1?? Antibody-Conjugated Pluronic Triblock Copolymers Encapsulated with Paclitaxel for Tumor Targeting Therapy. *Biomaterials* **2010**, *31* (8), 2302–2312.
- (53) Tao, Y.; Han, J.; Wang, X.; Dou, H. Nano-Formulation of Paclitaxel by Vitamin E Succinate Functionalized Pluronic Micelles for Enhanced Encapsulation, Stability and Cytotoxicity. *Colloid Surface B* **2013**, *102*, 604–610.

- (54) Liu, Z.; Liu, D.; Wang, L.; Zhang, J.; Zhang, N. Docetaxel-Loaded Pluronic P123 Polymeric Micelles: In Vitro and in Vivo Evaluation. *Int. J. Mol. Sci.* **2011**, *12* (3), 1684–1696.
- (55) Zhang, Y.; Feng, L.; Wang, J.; Tao, D.; Liang, C.; Cheng, L.; Hao, E.; Liu, Z. Surfactant-Stripped Micelles of Near Infrared Dye and Paclitaxel for Photoacoustic Imaging Guided Photothermal-Chemotherapy. *Small* **2018**, *14* (44), 1802991.
- (56) Wang, Y.; Yu, L.; Han, L.; Sha, X.; Fang, X. Difunctional Pluronic Copolymer Micelles for Paclitaxel Delivery: Synergistic Effect of Folate-Mediated Targeting and Pluronic-Mediated Overcoming Multidrug Resistance in Tumor Cell Lines. *Int. J. Pharm.* **2007**, *337* (1–2), 63–73.

Chapter 2: Preparation and evaluation of ^{99m}Tc -radiolabelled tridentate chelates for pre-targeting using bioorthogonal chemistry

Note that the following format is from the paper: H.A. Bilton,* Z. Ahmad,* N. Janzen, S. Czorny, J.F. Valliant. *J. Vis. Exp.* 2017, *120*, e55188. DOI: 10.3791/55188.

* Co-first authors.

With respect to this publication, I was responsible for the synthesis, characterization, and labeling optimization of compounds **1** and **5**, and Holly Bilton for compounds **2-4**. Holly and I were responsible for the preparation and execution of biodistribution studies, where Nancy Janzen and Shannon Czorny completed the administration and necropsy work. Professor John Valliant was the PI.

2.1. Introduction

^{99m}Tc remains the dominant radioisotope used in diagnostic nuclear medicine, with over 50 million imaging procedures conducted per year worldwide.¹⁻⁴ The majority of ^{99m}Tc agents used clinically are perfusion type radiopharmaceuticals. There are a limited number of actively targeted compounds in which ^{99m}Tc is directed to bind a specific biomarker through ligation to a targeting construct. The creation of targeted ^{99m}Tc radiopharmaceuticals is often hindered by the influence of ^{99m}Tc -ligand complexes on the ability of the targeting molecule to bind the biomarker of interest, or the isotopes half-life is not long enough for use with higher molecular weight biomolecules such as antibodies.

The latter typically requires several days before images are acquired in order for the biomolecule to clear from non-target tissues. Pre-targeting offers an alternative approach to overcome these challenges.

Pre-targeting combined with bioorthogonal chemistry has been shown to be an effective way to develop new molecular imaging probes for both fluorescence and radio-imaging.⁵⁻⁹ The inverse electron demand Diels-alder (IEDDA) reaction between 1,2,4,5-tetrazine (Tz) and *trans*-cyclooctene (TCO) derivatives, as shown in Figure 1, has been shown to be particularly effective.⁶ The IEDDA reaction with these components can exhibit fast kinetics in PBS ($k_2 \approx 6000 \text{ M}^{-1} \text{ s}^{-1}$) and high selectivity, making it ideal for *in vivo* pre-targeting applications.^{10, 11}

The most common approach used involves administering a TCO-derived targeting vector and following a sufficient delay period, a radiolabelled tetrazine is administered. Radiolabelled tetrazines based on ^{11}C , ^{18}F , ^{64}Cu , ^{89}Zr , and ^{111}In have been reported.¹²⁻¹⁶ In contrast, there are only two reports of a $^{99\text{m}}\text{Tc}$ -labelled Tz, which was prepared using a HYNIC type ligand requiring the use of co-ligands to prevent protein binding and degradation *in vivo*.^{17, 18} As an alternative, we report here the synthesis of $^{99\text{m}}\text{Tc}(\text{I})$ labelled tetrazines using a family of ligands which form stable tridentate complexes with a $[\text{}^{99\text{m}}\text{Tc}(\text{CO})_3]^+$ core.

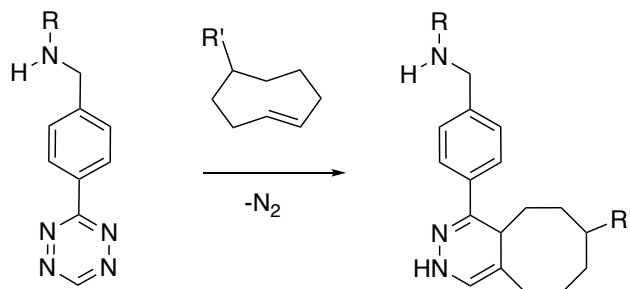


Figure 2.1. The bioorthogonal IEDDA reaction between tetrazine and *trans-cyclooctene*.

The family of ligands prepared contain tridentate chelates that vary in polarity and the nature of the linker group between the metal binding region and the Tz (Figure 2). The goal was to identify a ^{99m}Tc -Tetrazine construct that could effectively localize and react with TCO-labelled sites *in vivo* and rapidly clear when not bound, in order to yield high target-to-non-target ratios. To test the ligands, a TCO-derivative of a bisphosphonate (TCO-BP) was used.¹⁹ We have shown previously that TCO-BP localizes to areas of active bone metabolism and can react with radiolabelled tetrazines *in vivo*.²⁰ It is a convenient reagent to test new tetrazines, because it can be prepared in a single step and experiments can be performed in normal mice where localization occurs primarily in the joints (knees and shoulders).

2.2. Protocol

Animal studies were approved by the Animal Research Ethics Board at McMaster University in accordance with Canadian Council on Animal Care (CCAC) guidelines.

2.2.1. Radiolabeling of Tz-tridentate ligands with ^{99m}Tc

CAUTION: The following procedures require the use of radioactive compounds. Work should only be done in a licensed laboratory with adherence to safety and disposal regulations. Microwave reactions should be performed in a microwave specifically designed for chemical synthesis. (Note that the following stepwise procedure is the format used in the Journal where this work was published).

2.2.1.1. Synthesis of $[^{99m}\text{Tc}(\text{CO})_3(\text{H}_2\text{O})_3]^+$ ^{21, 22}

2.2.1.1.1. In a microwave vial, combine 8 mg $\text{K}_2[\text{BH}_3\text{CO}_2]$, 15 mg Na_2CO_3 , 20 mg $\text{Na}_2\text{B}_4\text{O}_7 \cdot 10\text{H}_2\text{O}$, and 25 mg $\text{KOCO}[\text{CH}(\text{OH})_2\text{COONa} \cdot 4\text{H}_2\text{O}]$. Purge the vial for 10 min with argon gas.

2.2.1.1.2. Add 4 mL of $^{99m}\text{TcO}_4^-$ (~ 1100 MBq, ~ 30 mCi) in 0.9% saline to the vial.

2.2.1.1.3. Heat the reaction in a microwave for 3.5 min at 110 °C after 10 s of stirring to ensure thorough mixing of reagents.

2.2.1.1.4. Adjust the pH of the solution to 3.5-4 using ~ 400 μL of 1 M HCl. Verify using pH paper.

2.2.1.2. Radiolabeling of Tetrazine ligands 1-5

2.2.1.2.1. Dissolve 2 mg of each ligand (compounds **1-5**) in 250 μL MeOH.²³

2.2.1.2.2. Add 250 μL of $[^{99m}\text{Tc}(\text{CO})_3(\text{H}_2\text{O})_3]^+$ (~ 74 MBq, ~ 2 mCi) to each solution.

2.2.1.2.3. Heat the reaction mixture using a microwave for 20 min at 60 °C.

NOTE: This step was identical for all 5 tetrazines.

2.2.1.2.4. For compounds **2-5** evaporate the solvent and re-dissolve the resulting products in 1 mL of 1:1 v/v DCM:TFA.

2.2.1.2.5. Heat the dissolved reaction products (**2-5**) at 60 °C in a microwave for 6 min (**2-4**) or 10 min (**5**).

2.2.1.2.6. After cooling to room temperature, evaporate the solvent using an evaporator (36 °C, 8 mbar, 3 min, 6000 rpm) and dissolve the dried

compound in 1:1 ACN:H₂O or 1:1 MeOH:H₂O, prior to HPLC purification.

- 2.2.1.2.7. Purify the ^{99m}Tc-labelled compounds (**1-5**), including separating the labelled product from unlabelled tetrazine ligand, using HPLC (C₁₈ reversed-phase). Typically, use an elution gradient of 30:70 ACN:H₂O (both with 0.1% TFA) to 40:60 ACN:H₂O over 20 min (18 min) and a C₁₈ analytical 4.6 x 100 mm column. Use both UV (254 nm) and gamma detection.
- 2.2.1.2.8. Take a small sample of each labelled product and compare its HPLC retention time to that of a co-injected, non-radioactive, Re-labelled standard (0.125 mg in 20% methanol-H₂O). The Re-labelled standard is identified in the UV HPLC trace, and will elute at the same time as the ^{99m}Tc-labelled compound in the γ -HPLC trace. This co-injection shows peaks at comparable retention times, confirming the identity of the ^{99m}Tc-labelled compound.
- 2.2.1.2.9. Evaporate the solvent from HPLC fractions using an evaporator (36 °C, 8 mbar, 3 min, 6000 rpm).
- 2.2.1.2.10. Formulate the purified compound at a concentration of 7.4 kBq/ μ L in PBS, containing 0.5% BSA and 0.01% Tween-80.
- 2.2.1.2.11. To ensure the labelled compounds are stable, perform an *in vitro* stability study. Incubate the formulated compound at 37 °C for 1, 4

and 6 hours, injecting a small amount (3.7 MBq) of the mixture on the HPLC at each time point to assess stability.

2.2.2. Pre-targeted Bio-distribution Studies

2.2.2.1. Preparation of animals

2.2.2.1.1. Using 7-9 weeks old, female Balb/c mice (n=3), administer TCO-BP formulated in saline (20 mg/kg) (5 µg/µL), via tail-vein injection.

2.2.2.1.2. Place mouse in physical restraint device, and identify the veins located on the lateral surfaces of the tail and wipe with an alcohol swab. At approximately 2 cm from the end of the tail, insert a 30-gauge needle at a shallow angle, parallel to the vein. Slowly depress the plunger to inject, remove needle and apply clean gauze sponge at injection site with slight pressure until bleeding stops.

2.2.2.1.3. At 1 h post injection of TCO-BP, administer ~0.74 MBq (20 µCi) of ^{99m}Tc-tetrazine formulated in 100 µL of 0.5% BSA, 0.01% Tween-80 in PBS, via tail-vein injection.

2.2.2.2. Bio-distribution studies

2.2.2.2.1. At the desired time point (t = 6 h), anaesthetize the mice using 3% isoflurane and 2% oxygen gas mixture. Demonstrate a toe pinch withdrawal on the anesthetized mouse to ensure they are under surgical plane of anesthesia.

2.2.2.2.2. Collect blood (1 mL) via cardiac puncture using a syringe pre-treated with heparin. Place mouse on its back with nose in the nose cone for

continued anesthesia and locate the xiphoid process on the animal. Insert a 25-gauge needle, slightly to the left of the animal's midline under the xiphoid process, at a 20-degree angle. Fully insert the needle, and slowly pull back on the plunger to see blood in the needle hub if the heart was punctured. Slightly readjust the needle while holding the plunger if necessary, to puncture the heart. Slowly draw blood into the syringe.

- 2.2.2.2.3. Euthanize the animal by cervical dislocation, while under anesthesia.
- 2.2.2.2.4. Place each animal in a plastic bag and use a dose calibrator (^{99m}Tc setting) to measure the whole-body activity level.
- 2.2.2.2.5. Collect the following tissues and fluids in pre-weighed counting tubes: blood, bone (knee and shoulder), gall bladder, kidneys, liver, stomach (with contents), small intestines (with contents), large intestines and caecum (with contents), thyroid and trachea, urinary bladder with urine, and tail.
- 2.2.2.2.6. Rinse appropriate tissues (excluding blood, gall bladder, and urinary bladder) in PBS to remove blood and blot dry before placing the tissues in appropriate counting tubes.
- 2.2.2.2.7. Place animal carcass in a plastic bag and measure residual whole-body activity using a dose calibrator.
- 2.2.2.2.8. Weigh each tube containing a tissue sample. Subtract initial weight of the tube to obtain mass of the tissue.

2.2.2.2.9. Use a dose calibrator (^{99m}Tc setting) to measure the amount of activity in a test sample (100 μL) at the time of injection for each mouse. NOTE: This test sample is equal to the injection volume, thus giving the activity count at the time of injection.

2.2.2.2.10. At the time of tissue measurement, aliquot 5 μL of the test sample used previously. Use a multi-detector gamma counter (^{99m}Tc setting) and count to obtain the count per minute (CPM) for the 5 μL test sample.

2.2.2.2.11. Use the two values obtained in 2.2.2.2.9 and 2.2.2.2.10 to calculate the activity and CPM relationship using equation 1 to obtain a conversion factor ($\text{CPM } \mu\text{Ci}^{-1}$).

$$\frac{\text{Standard CPM} * \left(\frac{\text{dose cal volume}}{\text{gamma counter volume}} \right)}{\mu\text{Ci in Standard at time of injection}} \quad (1)$$

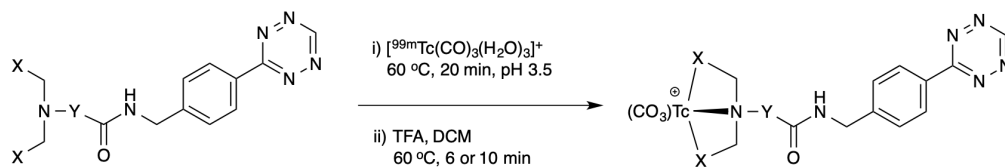
2.2.2.2.12. Use the gamma counter to measure the amount of radioactivity in each tissue or fluid sample.

2.2.2.2.13. Use equation 1 to calculate the amount of activity in each tissue or fluid at the time of measurement relative to the total injected dose. This value is then normalized by organ weight and reported as percent injected dose per gram (i.e. % ID/g) of tissue.

2.2.2.2.14. Follow steps 2.2.2.1.2 to 2.2.2.2.13 to conduct a negative control experiment using the ^{99m}Tc -labelled tetrazine ligands in the absence of TCO-BP. Sacrifice mice ($n=3$) at 0.5, 1, 4 and 6 h post injection and obtain tissue or fluid as described above.

2.3. Results and Discussion

The ligands were synthesized using different linkers and chelators via a simple reductive amination strategy (Figure 2), followed by coupling of the product to a commercially available tetrazine.^{24, 25} Radiolabeling was performed using the same method for all compounds and was highly reproducible. The process was optimized by varying the pH, amount of ligand, reaction time and temperature whereupon the ^{99m}Tc-radiolabelled compounds **1-5** were obtained in moderate to high radiochemical yield: 83% (**1**), 45% (**2**), 31% (**3**), 42% (**4**), and 54% (**5**). Following HPLC purification from unreacted ligand and evaporation using an evaporator, the compounds were formulated in PBS containing 0.5% BSA and 0.01% Tween80 prior to injection. The specific activity of the purified ^{99m}Tc-labelled tetrazine was ~1.48 MBq/μg. Studies were conducted to assess the stability of the ^{99m}Tc-labelled tetrazine ligands prior to *in vivo* studies. The stability was monitored by HPLC at 1, 4 and 6 h with no visible degradation over 6 h ($R_t = 14$ min), as seen in Figure 3 for compound **4** as an example.



		Compound				
		1	2	3	4	5
X						
Y						

Figure 2.2. Compounds **1-5** were produced using different linkers (Y) and chelators (X) as shown (bottom). All compounds were radiolabelled with $[^{99m}\text{Tc}(\text{CO})_3(\text{H}_2\text{O})_3]^+$ using the same reaction conditions (top), with the exception of **1**, which did not require step (ii).

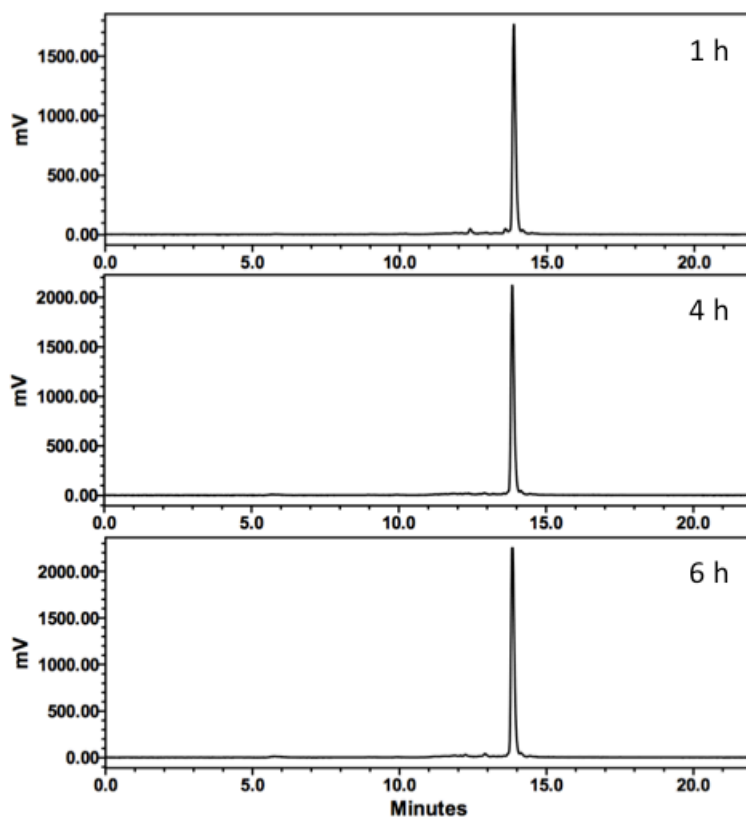


Figure 2.3. Stability test results using compound 4. γ -HPLC traces of 4 incubated in PBS at 37 °C for 1, 4 and 6 h.

For *in vivo* testing, healthy Balb/c mice were used. Briefly, for each compound, groups of mice (n=3) were injected with TCO-BP (100 μ L, 20 mg/kg), which was followed by administration of the ^{99m}Tc -labelled compounds 1 h later. At 6 h post-injection of the ^{99m}Tc complexes, the animals were sacrificed and the activity concentrations in various tissues and fluids determined. The resulting data is reported as percent injected dose per gram tissue (% ID/g) and is shown in Figure 4. Representative ratios of bone (knee or shoulder) to blood for each of the five ^{99m}Tc -labelled Tz compounds are shown on Table 2.1. These data indicate clearly that compound 3 provided optimal targeting combined with clearance from blood, and that there was substantial variation among the ^{99m}Tc -labelled

compounds in regard to off-target tissue localization. A negative control study using CD1 mice (n=3) was conducted, where mice were injected with ^{99m}Tc -tetrazine ligands in the absence of TCO-BP. Mice were sacrificed at 0.5, 1, 4 and 6 h and % ID/g was determined for all tissues and fluids. For all compounds tested, where data for compound **2** is presented in Figure 5, no significant uptake was seen in bone or other tissues (heart, lungs, spleen, skeletal muscle) not shown in Figure 4.

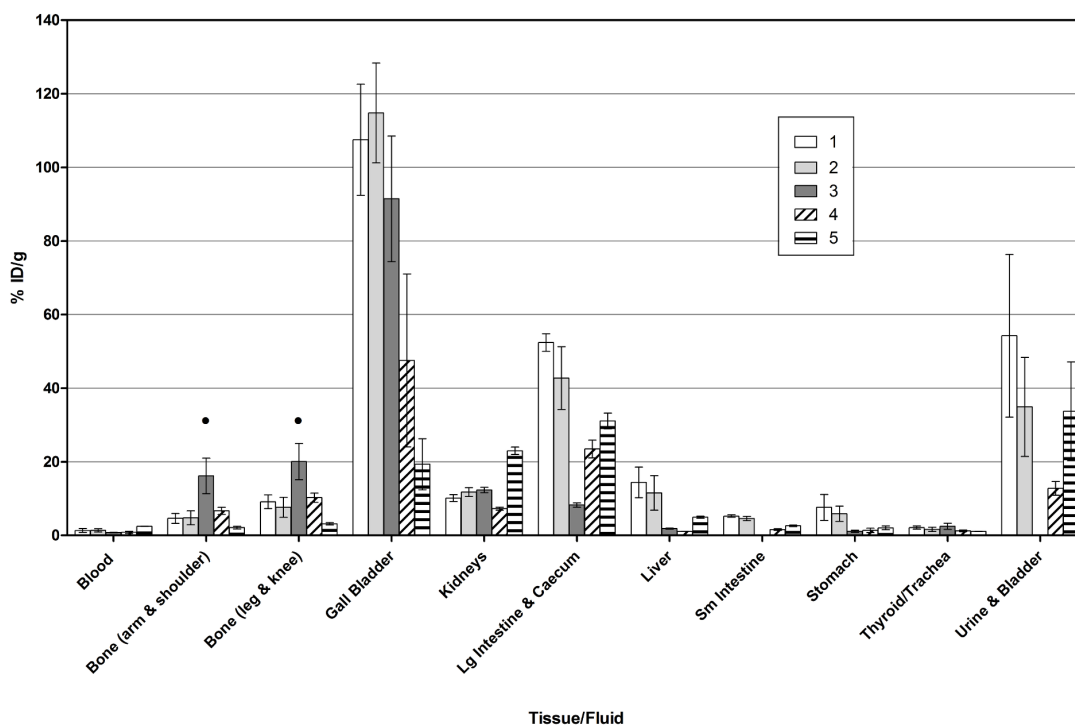


Figure 2.4. Bio-distribution results for ^{99m}Tc -labelled tetrazine derivatives **1-5** (bars indicated). Data shown were obtained from selected tissues and fluids taken 6 h post injection of the radiolabelled derivatives, and activity was normalized to tissue or fluid weight, as mean percent injected dose per gram of tissue or fluid (% ID/g) \pm SEM. Bone targets are indicated by *. NOTE: All remaining tissues not shown had mean % ID/g that was less than 1%.

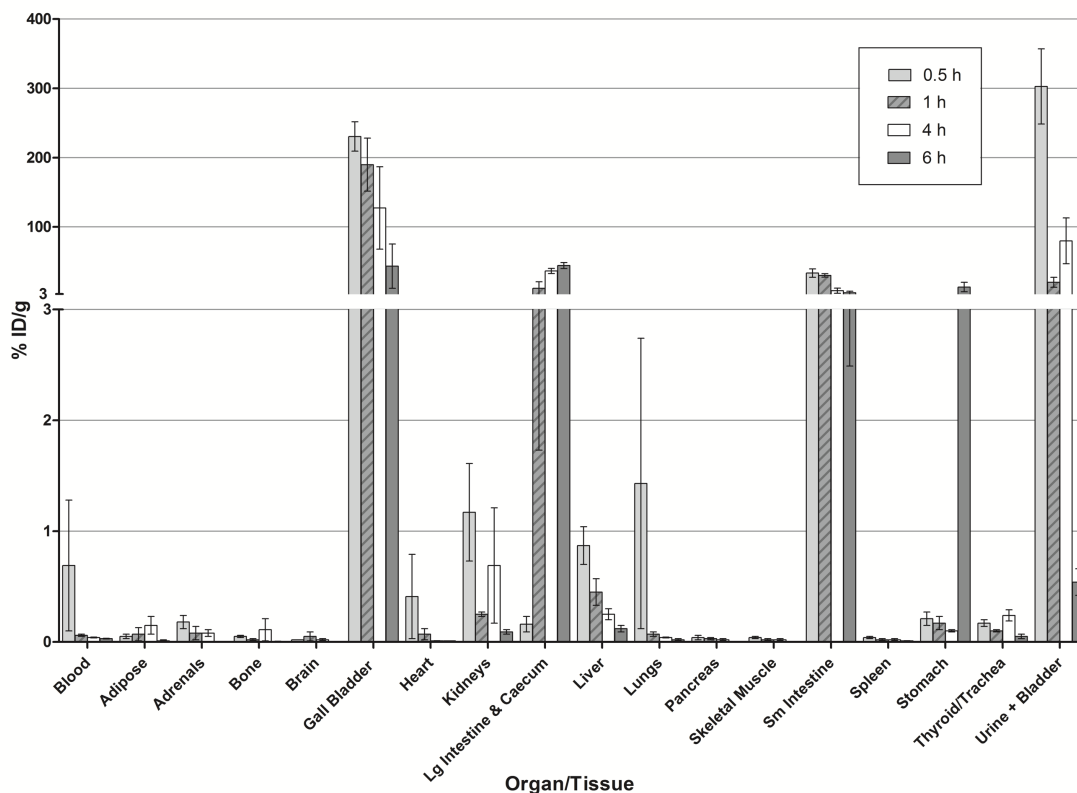


Figure 2.5. Bio-distribution results for control study using ^{99m}Tc -labelled tetrazine (**2**) without prior injection of TCO-BP. Data shown were obtained from selected tissues and fluids taken from 3 mice at 0.5, 1, 4, and 6 h post injection of **2**. Activity was normalized to tissue or fluid weight, as mean percent injected dose per gram of tissue or fluid (% ID/g) \pm SEM.

Table 2.4 Bone tissue: blood ratios determined from bio-distribution studies.

Tissue (%ID/g) ^a	Compound Number				
	1	2	3	4	5
Blood	1.33 \pm 0.52	1.37 \pm 0.44	0.77 \pm 0.07	0.85 \pm 0.30	2.46 \pm 0.05
Bone (arm & shoulder)	4.62 \pm 1.36	4.77 \pm 1.88	16.16 \pm 4.84	6.66 \pm 0.96	2.10 \pm 0.38
Bone (leg & knee)	9.12 \pm 1.88	7.64 \pm 2.72	20.07 \pm 4.91	10.24 \pm 1.28	3.15 \pm 0.33
Ratio					
Shoulder : Blood	3.47 \pm 1.70	3.48 \pm 1.77	20.99 \pm 6.57	7.84 \pm 2.99	0.85 \pm 0.16
Knee : Blood	6.86 \pm 3.03	5.58 \pm 2.67	26.10 \pm 6.80	12.05 \pm 4.51	1.28 \pm 0.14

A collection of tetrazine-linked tridentate chelates of varying polarities was prepared, and the utility of their ^{99m}Tc complexes in the IEDDA reaction with a TCO

derivative *in vivo* was assessed. An effective and reproducible ^{99m}Tc labelling method was developed for five tetrazine-chelates, where the ligand concentration was 10^{-3} M. The labeling step was followed by deprotection of *t*-butyl groups (for compounds **2-5**). The high concentration of ligand was used to improve the radiochemical yield and reduce reaction times which minimized degradation of the tetrazine²³. The product was isolated and separated from unlabelled ligand and any radiochemical impurities by HPLC, resulting in radiochemical yields ranging from 31-83%, with all having > 99% radiochemical purity and a high specific activity of ~ 1.48 MBq/ μg . All compounds were shown to be stable in PBS containing 0.5% BSA and 0.01% Tween80 for up to 6 h (Figure 3).

Bisphosphonate compounds, like TCO-BP, localize to regions of active bone metabolism or injury, which include knee and shoulder joints in mice. TCO-BP therefore provides a simple means to assess the effectiveness of new radiolabelled tetrazines to deliver isotopes *in vivo*. Evaluation of the bio-distribution of all five ^{99m}Tc -tetrazines showed uptake in knee and shoulder joints 6 h post injection, demonstrating successful pre-targeting to bone *in vivo* (Figure 4). Previous studies confirmed that radiolabelled TCO-BP accumulates at the bone,²⁰ whereas the ^{99m}Tc -tetrazine construct (**2**) given alone does not (Figure 5). This allows one to conclude that bone uptake was due to the IEDDA reaction.

The more lipophilic constructs **1** and **2** had similar distribution data including high uptake in the knee (9.1 ± 1.9 (**1**) and 7.6 ± 2.7 (**2**) % ID/g, respectively) and the shoulder (4.6 ± 1.4 (**1**) and 4.8 ± 1.9 (**2**) % ID/g, respectively). High radioactivity concentrations were also seen in the gall bladder, liver and intestines, which is consistent with the distribution of the lipophilic ^{99m}Tc -tetrazine compound **2** in the absence of TCO-BP (Figure

5). Other non-target tissues and organs such as the skeletal muscle and spleen did not show any significant uptake (<1%) when bio-distribution studies were performed on the ^{99m}Tc -tetrazines in the absence of the TCO-BP (Figure 5), so these organs were not taken for the pre-targeting experiments. Additionally, bio-distribution experiments with the ^{99m}Tc -tetrazines alone revealed good clearance from non-target tissues at 6 h post injection. Consequently, this time point, which is within one half-life of the isotope, was selected as the time point for comparing the different radiolabelled tetrazine ligands.

The more polar ^{99m}Tc -tetrazine compound **3** bearing a PEG₅ linker showed very high knee and shoulder uptake (16.2 ± 4.8 and 20.7 ± 4.9 % ID/g, respectively). There was also lower activity observed in the liver and intestines. The corresponding PEG₁₀ derivative also showed binding to the bone and reduced uptake in the liver compared to compounds **1** and **2**. The most polar derivative **5**, showed lower bone binding than all other constructs which is likely due to its rapid clearance.

The high bone uptake and bone: blood ratios (Table 1) particularly for compounds **3** and **4** demonstrate that pre-targeting and the IEDDA reaction can be used to localize ^{99m}Tc -labelled compounds *in vivo*. The methods reported here can be used to evaluate any radiolabelled tetrazine including next generation of Tc(I)-tetrazine ligands. It should be noted that for the class of ligands that were used in this study, the structures can be readily varied by changing the nature of the donor groups and linkers between the metal complex and the tetrazine, without significantly altering the ligand synthesis method.²¹ Once a lead molecule is identified, an instant kit method, which will likely include solid phase purification methods, can be developed to support clinical translation.

The Tc(I) complexes reported here create the opportunity to prepare new ^{99m}Tc radiopharmaceuticals using a wide array of different TCO-derived targeting molecules including antibodies. Antibodies, despite their excellent targeting properties prior to the creation of technetium labelled tetrazines, would not typically be used with ^{99m}Tc because of their slow clearance (days), which is much longer than the half-life of the isotope (~ 6 h). An additional application of the chemistry reported here is that the same class of ligands can be prepared with the beta emitting radionuclides ^{186}Re and ^{188}Re . The isostructural Re(I) analogues of the Tc(I) agents when combined with the tumour seeking properties of TCO-BP can be used to treat bone metastases.

2.4. Conclusion and Future Work

In conclusion, five novel ^{99m}Tc -labelled tetrazine ligands were synthesized, radiolabelled, characterized, and evaluated *in vivo* for pre-targeted imaging. Additionally, successful pre-targeting was observed with TCO-BP with high bone uptake. The next step requires utilizing the pre-targeting strategy with a TCO-antibody conjugate to evaluate the tumour targeting ability of the synthesized ^{99m}Tc -tetrazines.

2.5. Acknowledgments

This work supported by research grant funding from the Natural Sciences and Engineering Research Council (NSERC) of Canada, the Ontario Institute for Cancer Research (OICR, #P.SI.015.8), and the Canadian Cancer Society (CCS, #703857). The authors acknowledge the contributions of Dr. Denis Snider who provided assistance in preparing the manuscript.

2.6. References

1. Boschi, A., Uccelli, L., Martini, P. A picture of modern Tc-99m radiopharmaceuticals: Production, chemistry, and applications in molecular imaging. *Applied Sciences (Switzerland)*. **9** (12), 1–16, doi: 10.3390/app9122526 (2019).
2. Jurisson, S.S., Lydon, J.D. Potential Technetium Small Molecule Radiopharmaceuticals. *Chemical Reviews*. **99** (9), 2205–2218, doi: 10.1021/cr980435t (1999).
3. Kluba, C.A., Mindt, T.L. Click-to-chelate: Development of technetium and rhenium-tricarbonyl labeled radiopharmaceuticals. *Molecules*. **18** (3), 3206–3226, doi: 10.3390/molecules18033206 (2013).
4. Amato, I. Nuclear Medicines Conundrum. *Chem. Eng. News*. **87** (36), 58–70 (2009).
5. Hnatowich, D.J., Virzi, F., Ruszkowski, M. Investigations of avidin and biotin for imaging applications. *Journal of nuclear medicine : official publication, Society of Nuclear Medicine*. **28** (8), 1294–302 (1987).
6. Blackman, M.L., Royzen, M., Fox, J.M. Tetrazine Ligation: Fast Bioconjugation Based on Inverse-Electron-Demand Diels-Alder Reactivity. *Journal of American Chemical Society*. **130**, 13518–13519 (2008).
7. Devaraj, N.K., Weissleder, R., Hilderbrand, S. a Tetrazine-Based Cycloadditions: Application to Pre-targeted Live Cell Imaging. *Bioconjugate chemistry Imaging*. **19** (12), 2297–2299, doi: 10.1021/bc8004446.Tetrazine-Based (2008).

8. Rossin, R. *et al.* In Vivo Chemistry for Pre-targeted Tumor Imaging in Live Mice. *Angewandte Chemie International Edition*. **49** (19), 3238–3238, doi: 10.1002/anie.201001645 (2010).
9. Zeglis, B.M. *et al.* Optimization of a Pre-targeted Strategy for the PET Imaging of Colorectal Carcinoma via the Modulation of Radioligand Pharmacokinetics. *Molecular pharmaceuticals*. **12** (10), 3575–3587, doi: 10.1021/acs.molpharmaceut.5b00294 (2015).
10. Rossin, R. *et al.* Highly reactive trans-cyclooctene tags with improved stability for Diels-Alder chemistry in living systems. *Bioconjugate chemistry*. **24** (7), 1210–7, doi: 10.1021/bc400153y (2013).
11. Rossin, R., Robillard, M.S. Pre-targeted imaging using bioorthogonal chemistry in mice. *Current opinion in chemical biology*. **21**, 161–9, doi: 10.1016/j.cbpa.2014.07.023 (2014).
12. Denk, C. *et al.* Development of a (18) F-Labeled Tetrazine with Favorable Pharmacokinetics for Bioorthogonal PET Imaging. *Angewandte Chemie*. 1–6, doi: 10.1002/anie.201404277 (2014).
13. Herth, M.M., Andersen, V.L., Lehel, S., Madsen, J., Knudsen, G.M., Kristensen, J.L. Development of a (11)C-labeled tetrazine for rapid tetrazine-trans-cyclooctene ligation. *Chemical communications (Cambridge, England)*. **49** (36), 3805–7, doi: 10.1039/c3cc41027g (2013).

14. Li, Z. *et al.* Tetrazine-trans-cyclooctene ligation for the rapid construction of ¹⁸F labeled probes. *Chemical communications (Cambridge, England)*. **46** (42), 8043–5, doi: 10.1039/c0cc03078c (2010).
15. Nichols, B., Qin, Z., Yang, J., Vera, D.R., Devaraj, N.K. ⁶⁸Ga chelating bioorthogonal tetrazine polymers for the multistep labeling of cancer biomarkers. *Chemical communications (Cambridge, England)*. **50**, 5215–7, doi: 10.1039/c3cc49530b (2014).
16. Zeglis, B.M. *et al.* A Pre-Targeted PET Imaging Strategy Based on Bioorthogonal Diels-Alder Click Chemistry- Supplemental data. *Journal of Nuclear Medicine*. **54** (8) (2013).
17. Garcia, M.F. *et al.* ^{99m}Tc-bioorthogonal click chemistry reagent for in vivo pre-targeted imaging. *Bioorganic and Medicinal Chemistry*. **24** (6), 1209–1215, doi: 10.1016/j.bmc.2016.01.046 (2016).
18. García, M.F. *et al.* Synthesis of hydrophilic HYNIC-[1,2,4,5]tetrazine conjugates and their use in antibody pre-targeting with ^{99m}Tc. *Organic and Biomolecular Chemistry*. **16** (29), 5275–5285, doi: 10.1039/c8ob01255e (2018).
19. Russell, R.G.G. Bisphosphonates: The first 40 years. *Bone*. **49** (1), 2–19, doi: 10.1016/j.bone.2011.04.022 (2011).
20. Yazdani, A. *et al.* A Bone-Seeking trans-Cyclooctene for Pre-targeting and Bioorthogonal Chemistry: A Proof of Concept Study Using ^{99m}Tc- and ¹⁷⁷Lu-Labeled Tetrazines. *Journal of Medicinal Chemistry*. **59** (20), 9381–9389, doi: 10.1021/acs.jmedchem.6b00938 (2016).

21. Alberto, R., Schibli, R., Egli, A., Schubiger, A.P., Abram, U., Kaden, T.A. A novel organometallic aqua complex of technetium for the labeling of biomolecules: Synthesis of $[^{99m}\text{Tc}(\text{OH}_2)_3(\text{CO})_3]^+$ from $[^{99m}\text{TcO}_4]^-$ in aqueous solution and its reaction with a bifunctional ligand [8]. *Journal of the American Chemical Society*. **120** (31), 7987–7988, doi: 10.1021/ja980745t (1998).
22. Alberto, R., Ortner, K., Wheatley, N., Schibli, R., Schubiger, A.P. Synthesis and properties of boranocarbonate: A convenient in situ CO source for the aqueous preparation of $[^{99m}\text{Tc}(\text{OH}_2)_3(\text{CO})_3]^+$. *Journal of the American Chemical Society*. **123** (13), 3135–3136, doi: 10.1021/ja003932b (2001).
23. Lu, G. *et al.* Synthesis and SAR of $^{99m}\text{Tc}/\text{Re}$ -labeled small molecule prostate specific membrane antigen inhibitors with novel polar chelates. *Bioorganic & medicinal chemistry letters*. **23** (5), 1557–63, doi: 10.1016/j.bmcl.2012.09.014 (2013).
24. Maresca, K.P. *et al.* Small molecule inhibitors of PSMA incorporating technetium- 99m for imaging prostate cancer: Effects of chelate design on pharmacokinetics. *Inorganica Chimica Acta*. **389**, 168–175, doi: 10.1016/j.ica.2012.03.002 (2012).
25. Bartholomä, M.D. *et al.* Synthesis, cytotoxicity, and insight into the mode of action of $\text{Re}(\text{CO})_3$ thymidine complexes. *ChemMedChem*. **5** (9), 1513–1529, doi: 10.1002/cmdc.201000196 (2010).

Chapter 3: Evaluation of ^{99m}Tc -labelled tetrazines using *trans*-cyclooctene functionalized antibodies and pre-targeting

3.1. Introduction

Antibody-based therapies are emerging as treatment options for a variety of diseases such as multiple sclerosis, rheumatoid arthritis, age-related macular degeneration and cancer.¹ For the latter, the ability of antibodies to selectively target tumour-specific antigens, activate the immune system and disrupt the tumour microenvironment (TME), which can lead to selective cell death, has transformed medicine.²⁻⁴ While the development of murine monoclonal antibodies was an early breakthrough, it was the advances in technology that allowed for murine antibodies to be modified into chimeric, humanized, and fully human antibodies which pushed antibody-based therapeutics into the mainstream of modern medicine.^{2,5,6}

Not surprisingly, the number of radiolabelled antibodies used for disease diagnosis and treatment has in parallel been increasing particularly for oncology.³ For example, zirconium-89 (^{89}Zr) ($t_{1/2} = 78.4$ h) labelled trastuzumab is currently undergoing clinical investigation for PET imaging in patients with human epidermal growth factor 2 (HER2) positive esophagogastric cancer.^{7,8} Additionally, in 2020 Ulaner *et al.* reported that ^{89}Zr -labelled daratumumab, an FDA approved CD38 targeting monoclonal antibody (mAb), detected multiple myeloma metastases which had been overlooked by [^{18}F]F-FDG PET/CT

imaging.⁹ However, due to the slow clearance and long circulation time of antibodies, radiolabelled antibodies require the use of longer-lived isotopes that can result in higher than desired radiation doses to patients.^{10,11}

One approach that is being employed to allow for the use of isotopes with shorter half-lives, involves pre-targeting and bioorthogonal chemistry. Notable ligation strategies include reactive pairs such as azides with functionalized phosphines and tetrazines with *trans*-cyclooctene (TCO) derivatives.⁶ The latter, which has predominantly employed TCO-tagged mAb in conjunction with tetrazines radiolabelled with short-lived isotopes, has been shown to be effective in delineating, characterizing, and treating tumours with a variety of radioisotopes as well as different antibodies. For example, Keinänen *et al.* reported successful visualization of tumours using TCO-cetuximab and TCO-trastuzumab with a ¹⁸F-labelled ($t_{1/2}$ = 110 min) tetrazine ([¹⁸F]¹⁸F-TAF).¹² Cetuximab binds to the epidermal growth factor receptor (EGFR) overexpressed in many different cancers while trastuzumab targets the HER2 receptor. Using a pre-targeting strategy, mice bearing A431 epidermoid carcinoma or BT-474 ductal carcinoma xenografts received TCO-cetuximab or TCO-trastuzumab, respectively, at 24, 48 or 72 h prior to administration of carrier-added [¹⁸F]¹⁸F-TAF. Tumours were clearly visible through PET imaging which was conducted at 4 h (Figure 3.1). The highest tumour-to-blood (T/B) ratio for TCO-cetuximab was observed when there was a 72-h gap between administration of the antibody and the tracer (lag time) with a maximum tumour uptake of 3.7 ± 0.1 % ID/g (at 4 h post-tetrazine administration). TCO-trastuzumab T/B ratios were similar at all lag times; the maximum tumour uptake achieved was 1.5 ± 0.1 % ID/g with the 24 h lag time.

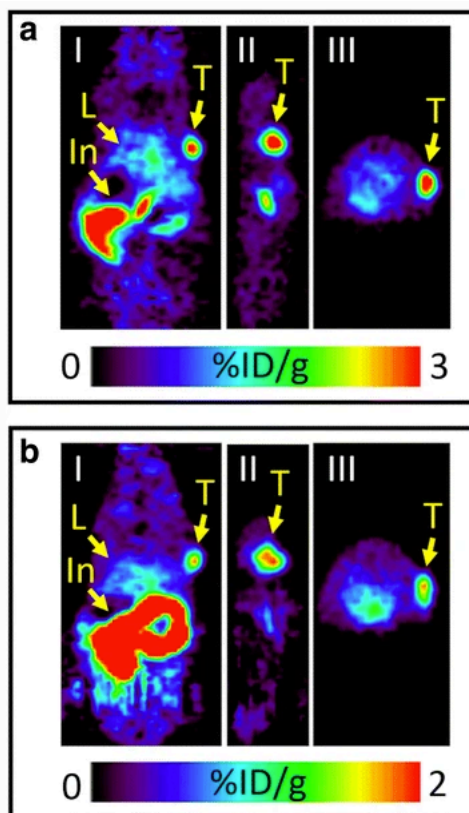


Figure 3.1. PET images for mice bearing A431 (a) and BT-474 (b) xenografts in right shoulders pre-targeted with (a) TCO-cetuximab and (b) TCO-trastuzumab respectively, followed by [^{18}F] ^{18}F -TAF 72 h later. Coronal (I), sagittal (II) and transverse (III) images obtained at 4 hours post injection of tetrazine. Yellow arrows identify tumour (T), liver (L) and intestines (In). Reprinted with permission from Keinänen, O. *et al.* EJNMMI Res. 2017, 7 (95), 1–16. Copyright Springer Nature.

Zeglis *et al.* determined the maximum accumulation of a TCO-derived humanized A33 mAb (huA33-TCO) which binds to the A33 antigen overexpressed on 95% of colorectal cancers.¹³ For these studies they employed a PET isotope, copper-64 (^{64}Cu) ($t_{1/2}$ = 12.7 h) for radiolabelling a NOTA chelate-tetrazine ligand to be used with the huA33-TCO mAb through a pre-targeting approach. Mice bearing SW1222 colon cancer xenografts were administered huA33-TCO, which was followed by ^{64}Cu -labelled tetrazine 24 hours later. PET images obtained at 2, 6, 12 and 18 h showed rapid accumulation of the

radiotracer in the tumour by the 2 h time point, clear delineation of the tumour by 12 h, and retention of the tetrazine up to the 18 h imaging time point which is indicative of successful ligation at the tumour site (Figure 3.2A). Biodistribution studies using the huA33-TCO antibody and ^{64}Cu -labelled tetrazine, following the aforementioned pre-targeting protocol, demonstrated rapid tumour accumulation of the tetrazine with 4.1 ± 0.3 % ID/g at 1 h which was sustained up to 24 h (4.0 ± 0.9 % ID/g) (Figure 3.2B). Uptake in all other organs, excluding feces which is the route of clearance, were quite low (generally less than 1 % ID/g).

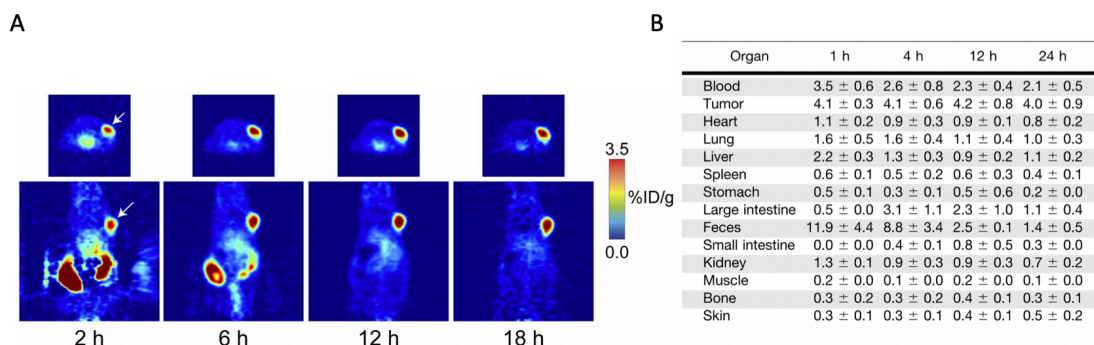


Figure 3.2. A) PET/CT images for mice bearing SW1222 xenografts pre-targeted with huA33-TCO mAb followed by ^{64}Cu -labelled tetrazine. B) Biodistribution data for mice bearing SW1222 xenografts pre-targeted with huA33-TCO mAb followed by ^{64}Cu -labelled tetrazine. Reprinted (adapted) with permission from Zeglis, B.M. *et al.* J. Nucl. Med. 2013, 54 (8), 1389-1396. Copyright 2013 SNMMI.

In addition to the ^{18}F and ^{64}Cu -labelled tetrazine derivatives, Edem *et al.* recently developed a ^{68}Ga -labelled ($t_{1/2} = 67.7$ min) tetrazine to be used with CC49-TCO mAb which targets the tumour-associated glycoprotein 72 (TAG-72) overexpressed by various cancer types.¹⁴ Utilizing the pre-targeting strategy, mice bearing LS174T colon cancer xenografts were administered the ^{68}Ga -tetrazine 24 hours post-injection of the CC49-TCO mAb. PET

imaging and biodistribution data obtained at 2 h post injection of tetrazine resulted in tumour uptake of 5.8 ± 0.3 % ID/g, with a T/B ratio of 1.1.¹⁵ In 2014, the Aboagye group developed a tetrazine-DOTA construct to be labelled with ^{68}Ga which was then tested with a TCO-modified IgG1 mAb which targets EGFR.¹⁶ PET imaging in mice with A431 xenografts exhibited tumour uptake of 3.48 % ID/mL, however high uptake in the liver and other non-target tissues was also observed. Although the uptake is similar to that of the ^{64}Cu -labelled tetrazine, the high off target uptake of the ^{68}Ga -labelled tetrazine resulted in poorer tumour delineation. While not antibody based, in 2016, Denk *et al.* reported the first instance of pre-targeted PET imaging with a ^{11}C -labelled ($t_{1/2} = 20.4$ min) tetrazine when paired with TCO-functionalized silica nanoparticles for lung imaging.¹⁷ Observing a moderate target uptake of $\sim 3\%$ ID/g (1 h post tetrazine administration) with such a short lived isotope exemplifies the rapid kinetics of the TCO-tetrazine reaction.

In 2015, A. Vito from our research group presented the first $^{99\text{m}}\text{Tc}$ -labelled ($t_{1/2} = 6.0$ h) tetrazine at the International Symposium on Radiopharmaceutical Sciences.¹⁸ Shortly thereafter, the Quinn group at the University of Missouri published a manuscript regarding a $^{99\text{m}}\text{Tc}$ -labelled HYNIC tetrazine to be used with the CC49-TCO mAb.¹⁹ Pre-targeted biodistribution studies conducted using mice bearing LS174T xenografts demonstrated modest tumour uptake (1.4 ± 0.4 % ID/g) at 2 hours post injection. The majority of the radioactivity was localized in the hepatobiliary system suggesting the need for further optimization of the ligands used.

While the literature has demonstrated successful *in vivo* coupling of TCO-modified antibodies and radiolabelled tetrazines, an effective $^{99\text{m}}\text{Tc}$ -tetrazine has yet to be identified.

As noted previously, ^{99m}Tc has a number of advantages over other key medical radioisotopes due to its low cost in addition to convenient half-life and decay energy (140 keV). Given the success achieved in Chapter 2 using TCO-BP, work was initiated through a collaboration with the Zeglis group to assess the utility of ^{99m}Tc -tetrazines with TCO-modified antibodies notably the previously described huA33-TCO mAb.

3.2. Materials and Methods

3.2.1. General materials, methods, and instrumentation.

Unless otherwise stated, all reagents were used as obtained from the supplier without further purification. The solvents used were purchased from Caledon and Sigma Aldrich. Potassium sodium tartrate ($\text{K/NaC}_4\text{H}_4\text{O}_6 \cdot 4\text{H}_2\text{O}$) and sodium borate ($\text{Na}_2\text{B}_4\text{O}_7 \cdot 10\text{H}_2\text{O}$) were acquired from Achemia Canada Inc., while sodium carbonate (Na_2CO_3) was acquired from EM science. Microwave reactions were done on a Biotage Initiator 60 microwave reactor.

High performance liquid chromatography (HPLC) was performed for purification using a Varian ProStar model 230 instrument, fitted with a Varian ProStar model 330 PDA detector monitoring at 254 nm with a model 230 delivery system using analytical Waters X-bridge C-18 column ($100 \text{ mm} \times 4.6 \text{ mm} \times 5 \mu\text{m}$) operating at 1 mL/min. Solvents were evaporated using a rotary evaporator under reduced pressure or via the Biotage V10 solvent evaporation system. Solvent A: $\text{H}_2\text{O} + 0.1 \%$ TFA, solvent B: $\text{ACN} + 0.1 \%$ TFA.

All *in vivo* experiments were conducted according to the Memorial Sloan-Kettering Institutional Animal Care and Use Committee or the Animal Research Ethics Board at McMaster University in accordance with Canadian Council on Animal Care (CCAC) guidelines. Humanized A33 antibody was provided by the Zeglis group at Hunter College, City University of New York. Eight-week old athymic nude female mice (n=4, Charles River Laboratories, Kingston, NY) received SW1222 tumours (human colorectal cancer cell line) on the right shoulder via subcutaneous injections of 5.0×10^6 cells in a 200 μL cell suspension at approximately nine weeks of age. SPECT/CT images were obtained on an X-SPECT (Gamma Medica, Northridge, CA.)

3.2.2. Stability of compound 5 in PBS.

Compound **5** was incubated in 100% PBS at 37 °C and analyzed at 1, 4 and 6 hours using analytical HPLC (5-39 % solvent B over 12 min, 39-100% solvent B over 12-20 min): $R_t = 14.9$ min.

3.2.3. Stability of Compound 10 in formulations.

Compound **10** was formulated (1 mg/mL) in PBS, and PBS + 0.5% BSA + 0.01 % Tween80 (w/v) and analyzed by UV/VIS spectroscopy (400-600 nm) at 0, 0.5, 1, 2, 4, and 6 hours post synthesis.

3.2.4. Preparation of TCO-huA33 mAb.¹³

The hu-A33 antibody (2 mg) was dissolved in 210 μL of PBS and the pH of the solution was adjusted to 9.0 using 0.1 M Na_2CO_3 (30 μL). To this was added (E)-cyclooct-

4-enyl-2,5-dioxypyrrolidin-1-yl carbonate (TCO-NHS, 50 μg) in DMSO (2 μL) and the solution was shaken at room temperature for one hour. The TCO-modified antibody was purified using an Amicon- Ultra centrifugal unit with a 50 kDa cut off and washed with additional PBS (25 mL). The solution was centrifuged for 5 minutes at 3000 rpm and concentrated down to 1 mL from the centrifugation. A final concentration of 1.7 mg/mL TCO-Ab was achieved as determined by spectrophotometry analysis (280 nm).

3.2.5. Coupling compound 5 and huA33-TCO.

To verify the coupling of **5** and the TCO-modified antibody, 11 μL of huA33-TCO (1.7 mg/mL) was incubated with 10 μL of **5** (3.7 MBq) for 10 min before spotting 1.0 μL on TLC plate. After drying, the plate was immersed in an eluent consisting of 1:1 v/v H_2O + 0.1 % TFA and ACN + 0.1 % TFA. Compound **5** was also spotted alone and run using the same solvent conditions. Both plates were read using a radioTLC scanner.

3.2.6. *In vivo* evaluation of compound 1.

Mice bearing subcutaneous SW1222 xenografts (100-150 mm^3 , 18-21 days post inoculation) were administered compound **1** (~50 MBq) in 200 μL PBS + 0.5% BSA + 0.01% Tween80 via tail-vein injection. Approximately 5 minutes before imaging, mice were anesthetised by inhalation of 2% isoflurane (Baxter healthcare): oxygen gas mixture and placed on the scanner bed; anaesthesia was maintained during the experiment using the 2% isoflurane-oxygen gas mixture. SPECT/CT images were obtained at 4 and 6-hours post injection.

3.2.7. *In vivo* evaluation of compound 5.

Mice (n=2) were administered with compound **5** (16-18 MBq) in 200 μ L PBS + 0.5% BSA + 0.01% Tween80 via tail-vein injection. Mice were anesthetized using a 2% isoflurane: oxygen mixture and full body SPECT/CT images were obtained at 1, 4, and 6-hours post injection.

3.2.8. Pre-targeted *in vivo* evaluation of compound 1.

Mice bearing subcutaneous SW1222 xenografts (100-150 mm³, 18-21 days post inoculation) were administered huA33-TCO (100 μ g in 200 μ L of 0.9% sterile saline) via tail-vein injection. After 24 hours, mice were administered compound **1** (46-51 MBq) in 200 μ L PBS + 0.5% BSA + 0.01% Tween80 via tail-vein injection. Approximately 5 minutes before imaging, mice were anesthetised by inhalation of 2% isoflurane (Baxter healthcare): oxygen gas mixture and placed on the scanner bed; anaesthesia was maintained during the experiment using 2% isoflurane: oxygen gas mixture. SPECT/CT images were obtained at 4- and 6-hours post injection.

3.2.9. Pre-targeted *in vivo* evaluation of compound 5 (high specific activity).

Mice bearing subcutaneous SW1222 xenografts (100-150 mm³, 18-21 days post inoculation) were administered huA33-TCO (100 μ g in 200 μ L of 0.9% sterile saline) via tail-vein injection. After 24 hours, mice were administered compound **5** (19-22 MBq) in 200 μ L PBS + 0.5% BSA+ 0.01% Tween80. Approximately 5 minutes before imaging, mice were anesthetised by inhalation of 2% isoflurane (Baxter healthcare): oxygen gas

mixture and placed on the scanner bed; anaesthesia was maintained during the experiment using 2% isoflurane: oxygen gas mixture. SPECT images were obtained at 1, 4, and 6-hours post injection. Bio-distribution studies were conducted 6-hours post injection of compound **5**. The mice were euthanized by CO₂(g) asphyxiation and tissues (including tumour) and organs were removed. The tissues and organs were weighed and counted in a gamma counter. Gamma counts were repeated 12 hours post organ-excision and the counts converted to activity using a calibration curve of known standards.

3.2.10. Pre-targeted *in vivo* evaluation of compound 5 (low specific activity).

Mice bearing subcutaneous SW1222 xenografts (100-150 mm³, 18-21 days post inoculation) were administered huA33-TCO (100 µg in 200 µL of 0.9% sterile saline) via tail-vein injection. After 24 hours, mice were administered a coformulation of compound **5** (19-21 MBq) and compound **10** (0.75 nM) in 200 µL PBS + 0.5% BSA + 0.01% Tween80. Approximately 5 minutes before imaging, mice were anesthetised by inhalation of 2% isoflurane (Baxter healthcare): oxygen gas mixture and placed on the scanner bed; anaesthesia was maintained during the experiment using 2% isoflurane: oxygen gas mixture. SPECT images were obtained at 1, 4, and 6-hours post injection. Bio-distribution studies were conducted 6-hours post injection of compounds **5** + **10**. Mice were euthanized by CO₂ (g) asphyxiation and tissues (including tumour) and organs were removed. The tissues and organs were weighed and counted in a gamma counter. Gamma counts were repeated 12 hours post organ-excision and the counts converted to activity using a calibration curve of known standards.

3.3. Results and Discussion

3.3.1. Stability in phosphate buffered saline (PBS).

Although the $^{99\text{m}}\text{Tc}(\text{I})$ -tridentate chelate complexes are known to be stable *in vitro* and *in vivo*, the stability of compound **5** needed to be confirmed prior to conducting *in vivo* studies. To this end, recently purified compound **5** in PBS was incubated at 37 °C. HPLC analysis was conducted at 1, 4 and 6 hours where compound **5** did not appear to degrade under the conditions tested (Figure 3.3).

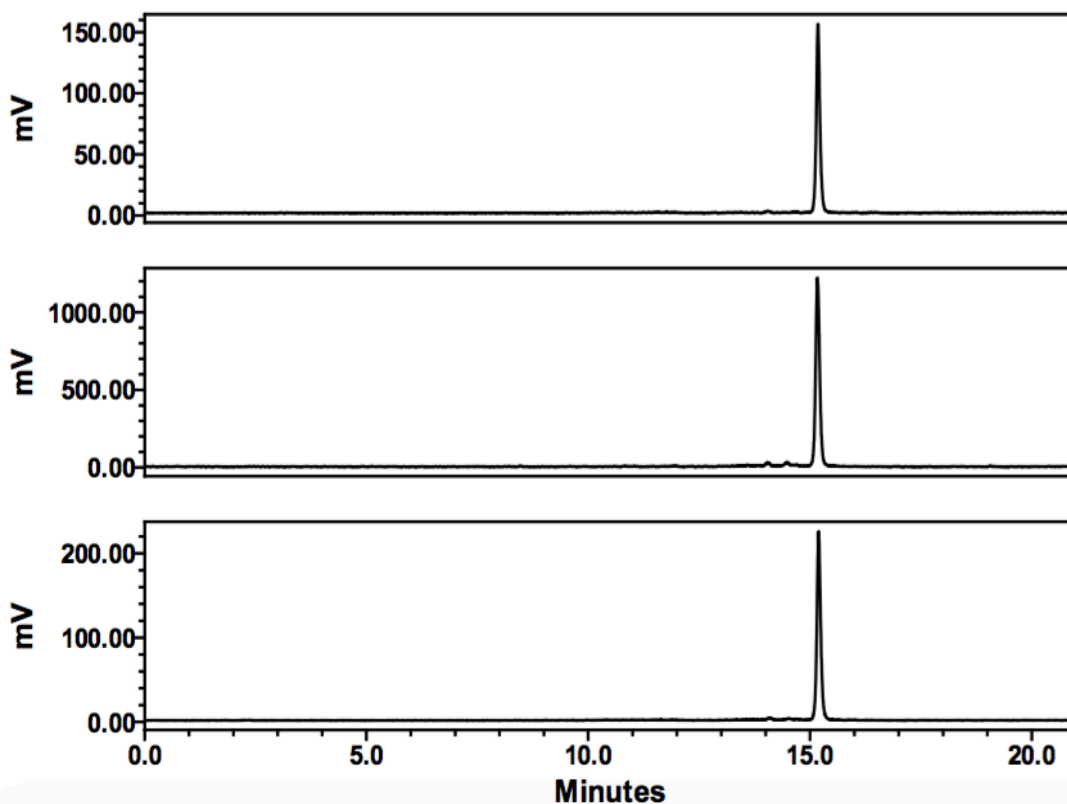


Figure 3.3. HPLC chromatograms (γ -detection) of compound **5**, incubated in PBS at 37 °C, at t= 1 (top), 4 (middle) and 6 (bottom) hours.

3.3.2. Stability of compound 10.

The stability of compound **10**, the Re analogue of **5**, in PBS alone and PBS with different additives was evaluated using UV/Vis spectroscopy (400-600 nm). The additives, bovine serum albumin (BSA) and Tween80, a non-ionic surfactant, were used to ensure compounds **5** and **10** were prepared in the same formulation as compounds **1** and **6**. Stability was assessed out to 6 hours at room temperature (Figure 3.4) to align with the longest imaging and biodistribution time point. Little to no degradation of compound **10** was seen in any of the formulations or at any point in the study.

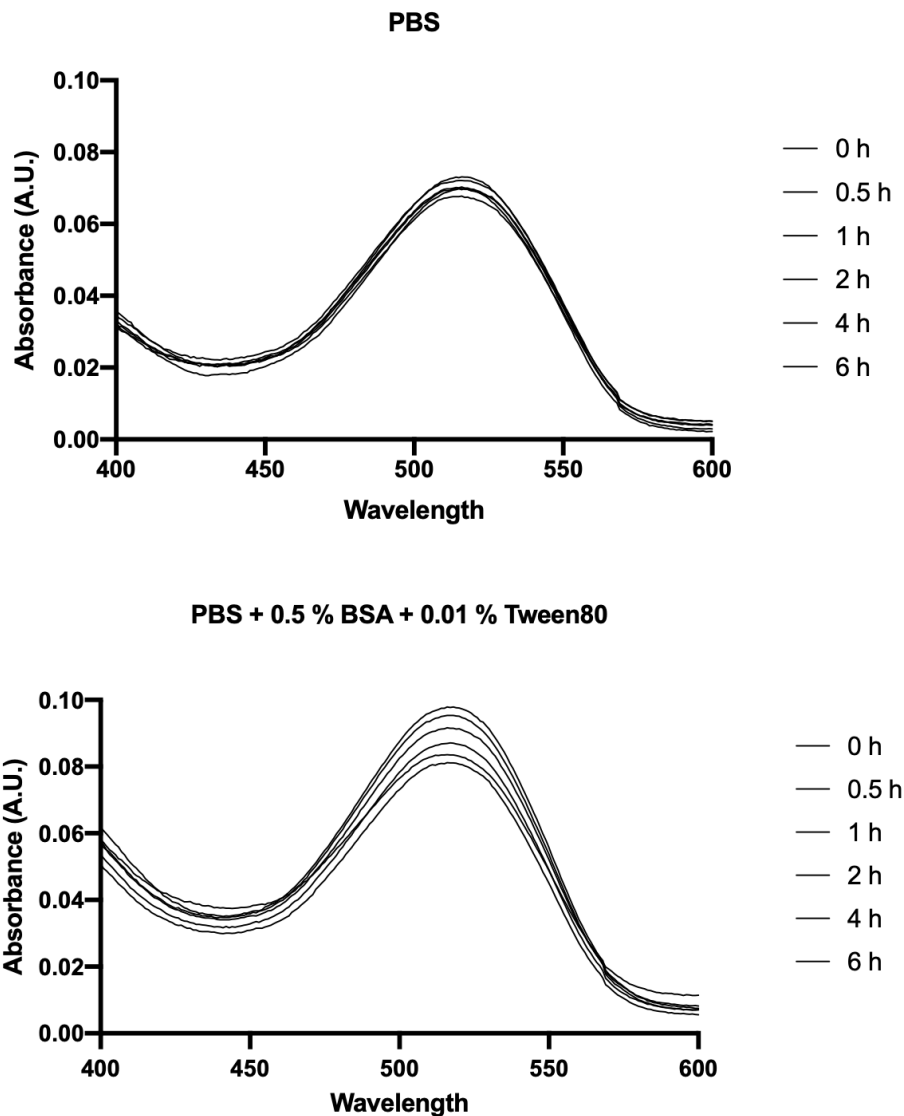


Figure 3.4. Absorbance (UV-Vis) data from studies to assess the stability of compound **10** in different formulations monitored over 400-600 nm. Compound **10** was formulated at 1 mg/mL in both PBS and PBS + 0.5% BSA + 0.01 % Tween80 and absorbance data collected at 0, 0.5, 1, 2, 4 and 6 hours.

3.3.3. Preparation of TCO-huA33 antibody.

The huA33 antibody experiments were conducted through a collaboration with the Zeglis, Francesconis and Lewis groups at Hunter College and Memorial Sloan Kettering Cancer Centre (MSKCC) in New York, USA. The huA33 antibody binds to the A33

antigen which is a transmembrane glycoprotein overexpressed in > 95% of colorectal cancers.¹⁰ As noted in the introduction, the humanized A33 antibody functionalized with TCO has been used by various groups for *in vivo* pre-targeting experiments yielding high tumour uptake as the antibody exhibits minimal internalization when bound to cells, making it a suitable targeting vector for pre-targeting experiments.^{13,20,21} Adding TCO to the huA33 antibody was executed using a literature procedure.¹³ The huA33 antibody was combined with TCO-NHS in solution of PBS at a pH of 9.0 followed by incubation for 30 minutes at room temperature with gentle shaking. The TCO-huA33 was then purified by centrifugal filtration (MWCO= 50 kDa) and obtained at a concentration of 1.7 mg/mL as determined by spectrophotometry.

3.3.4. Testing the reactivity of compound 5 towards the huA33-TCO mAb.

To assess the coupling of compound **5** with a TCO functionalized antibody, the tetrazine was incubated with the purified huA33-TCO mAb for 10 minutes at room temperature with gentle shaking. The inverse electron demands Diels-Alder (IEDDA) reaction was verified by radio-iTLC analysis by comparing the retention times of huA33-TCO-**5** and **5** alone using 1:1 v/v H₂O and ACN with 0.1 % TFA as the eluent. As shown in Figure 3.5, compound **5** travelled ~30 mm off the baseline while the conjugate was retained on the baseline (marked in red). This change in R_f is expected due to the polarity of the antibody which causes any conjugated product to remain on the baseline.

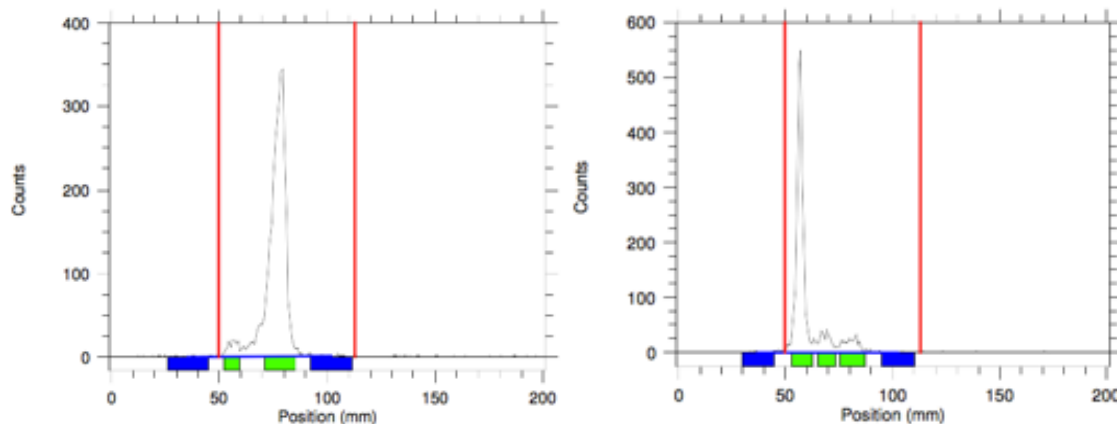


Figure 3.5. Radio TLC analyses of compound **5** (left) and the reaction mixture 10 min following the combination of compound **5** and huA33-TCO mAb (right).

3.3.5. *In vivo* evaluation of compound **1**.

Prior to conducting *in vivo* studies with the huA33-TCO mAb, the intrinsic biodistribution of compound **1** in athymic nude mice was determined. Mice bearing SW122 tumours in their right shoulders were administered compound **1** via tail-vein injection and SPECT/CT images obtained 4 and 6-hours post injection (Figure 3.6). Based on the images, there was negligible tumour localization where uptake of compound **1** was seen in the liver, small and large intestines. The compound appears to be clearing through the hepatobiliary system which was not surprising given its lipophilic nature (LogP= 0.4).

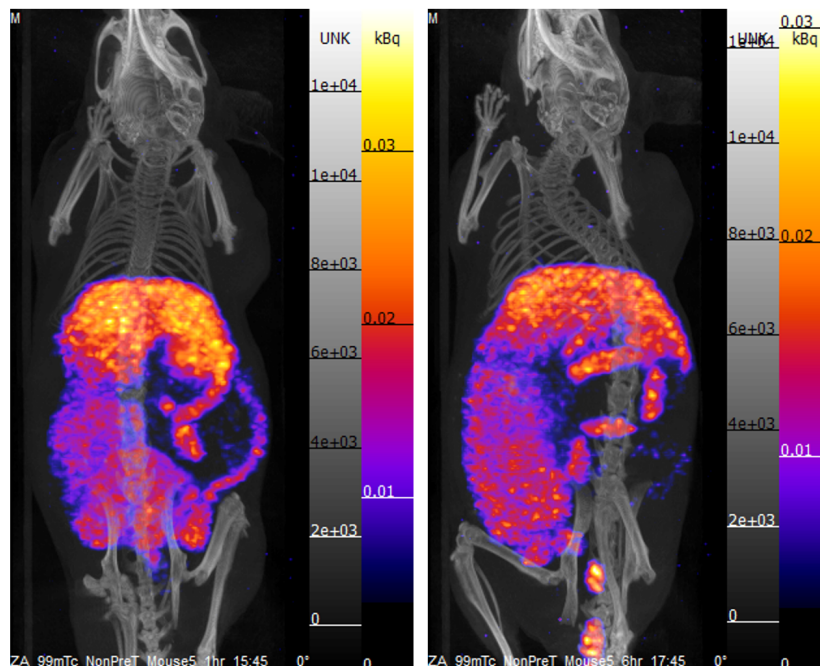


Figure 3.6. SPECT/CT images of mice (n=4) administered compound **1** (~50 MBq) obtained at 4 and 6 hours. Mouse 2 is shown as an example. Significant accumulation in the hepatobiliary system, notably the liver and intestines, was observed with little difference in distribution between the 4 and 6-hour imaging time points.

3.3.6. *In vivo* evaluation of compound **5**.

Similar to the studies with compound **1**, the inherent biodistribution of compound **5** was also evaluated. Mice received doses via tail-vein injection and SPECT/CT images were obtained at 1, 4 and 6-hours post injection (Figure 3.7). The substitution of the bispyridyl chelate with the diacid groups along with the addition of the PEG-10 linker was designed to increase the hydrophilicity of the compound. As a result of these modifications, compound **5** cleared rapidly through the renal system as seen by the high bladder uptake at the 1 h time point. Residual compound was cleared through the gastrointestinal (GI) system where activity was evident in the intestines and feces at 4 and 6-hours post-injection.

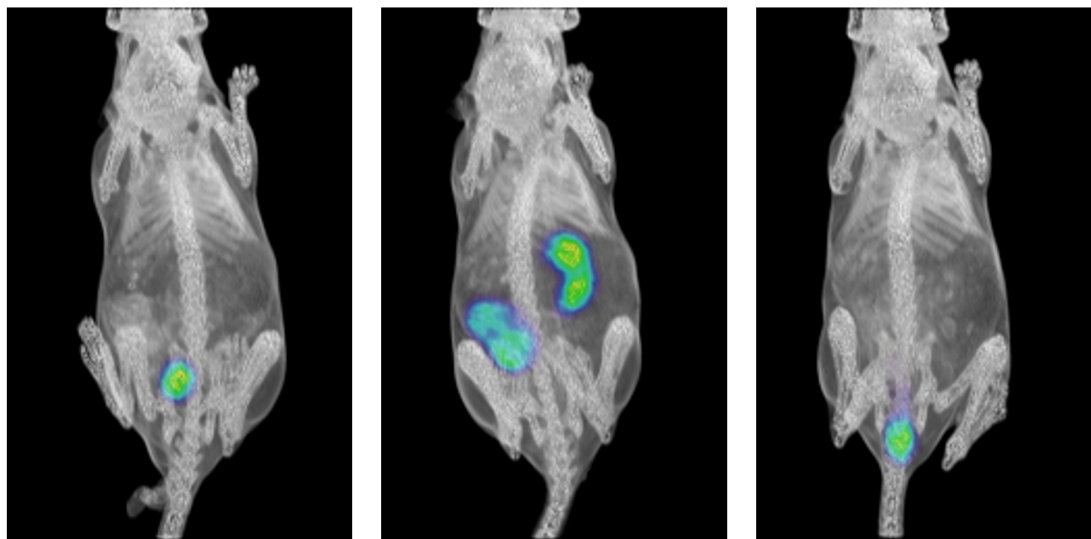


Figure 3.7. SPECT/CT images of mice (n=2) administered compound **5** (16-18 MBq) obtained at 1, 4 and 6 h post-injection. Mouse 1 is shown as an example. Clearance of the compound was initially via the renal system while the later time points shows some residual activity in the intestines and feces.

3.3.7. Pre-targeted *in vivo* evaluation of compound **1**.

Pre-targeting studies using huA33-TCO mAb were conducted with nude mice bearing SW1222 tumours (100-150 mm³, 18-21 days post inoculation) in their right shoulders. The antibody derivative (100 µg) was administered 24 hours prior to injection of compound **1** SPECT/CT images were obtained at 4 and 6-hours post injection of **1** (Figure 3.8). After the last imaging time point, mice were sacrificed and tissues/organs were excised, weighed, and the radioactivity counted using a gamma counter. The biodistribution data is plotted in Figure 3.9 below as percent inject dose per gram (% ID/g) for each tissue/organ.

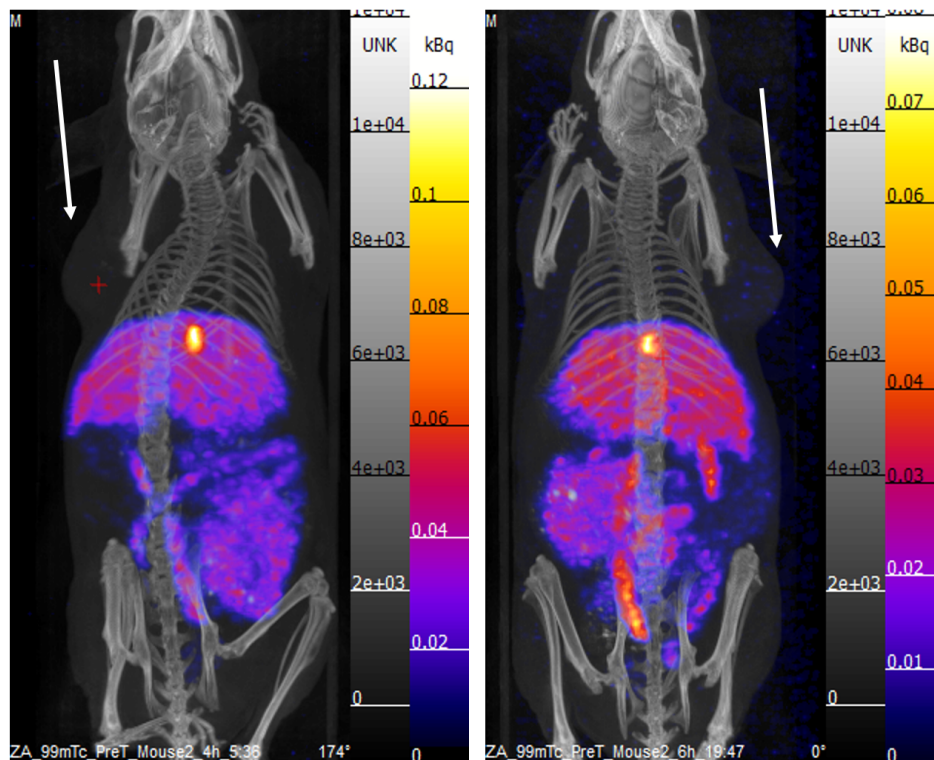


Figure 3.8. SPECT/CT images of mice (n=4) administered compound **1** (46-51 MBq), 24 hours after administration of huA33-TCO mAb, obtained at 4 and 6 hours post-tetrazine injection. Mouse 2 is shown as an example. Uptake in the gall bladder, liver, and large and small intestines was seen while no signal was observed in the tumour (denoted by white arrow). SW1222-tumour located by the right shoulder.

The SPECT/CT images and biodistribution data showed predominant uptake in the gall bladder (66.5 ± 12.5 % ID/g), liver (33.8 ± 3.9 % ID/g), and large intestine (17.3 ± 6.7 % ID/g) at 6 h post-injection which is consistent with hepatobiliary clearance. Similar gall bladder, and GI uptake was observed in the SPECT/CT images at 4 h. Low tumour uptake was seen (1.1 ± 0.1 % ID/g) with a tumour: blood ratio of 3.0, although no tumour uptake was visible in the images due to the high background uptake in the GI tract.

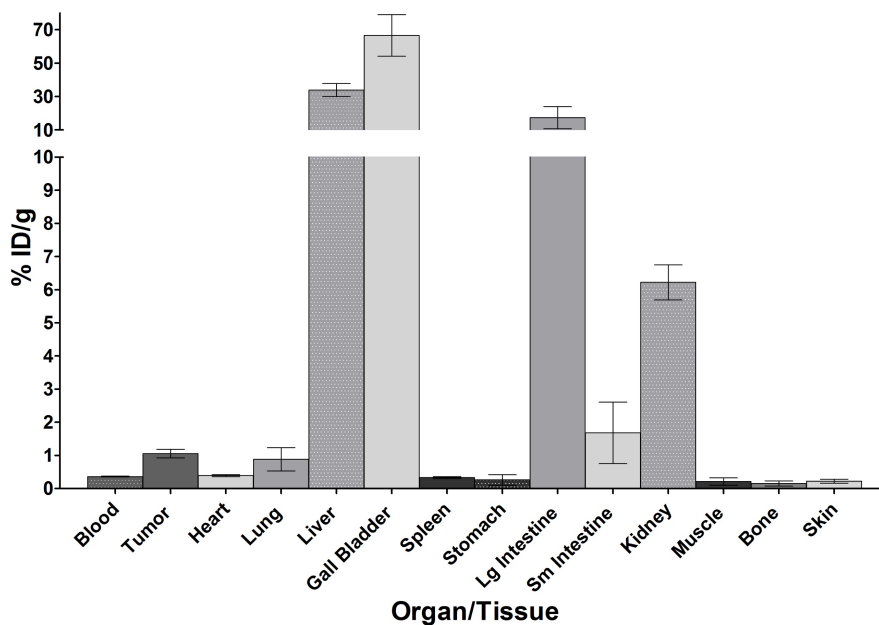


Figure 3.9. Biodistribution study data associated with the imaging study shown in Figure 3.8. Data is reported as the percent injected dose per gram (% ID/g).

3.3.8. Pre-targeted *in vivo* evaluation of compound 5 (high specific activity).

Next, the most hydrophilic of the developed ^{99m}Tc -tetrazines, compound 5 was evaluated in combination with huA33-TCO mAb. Similar to the procedure used to test compound 1, mice bearing SW1222 tumours were administered with huA33-TCO mAb 24 hours prior to injection of compound 5. Mice were imaged at 1, 4 and 6-hours post injection followed by removal and counting of the tissues and fluids after the last set of images were taken (Figure 3.10). Biodistribution data is again plotted as % ID/g per tissue/organ/fluid and shown in Figure 3.11.

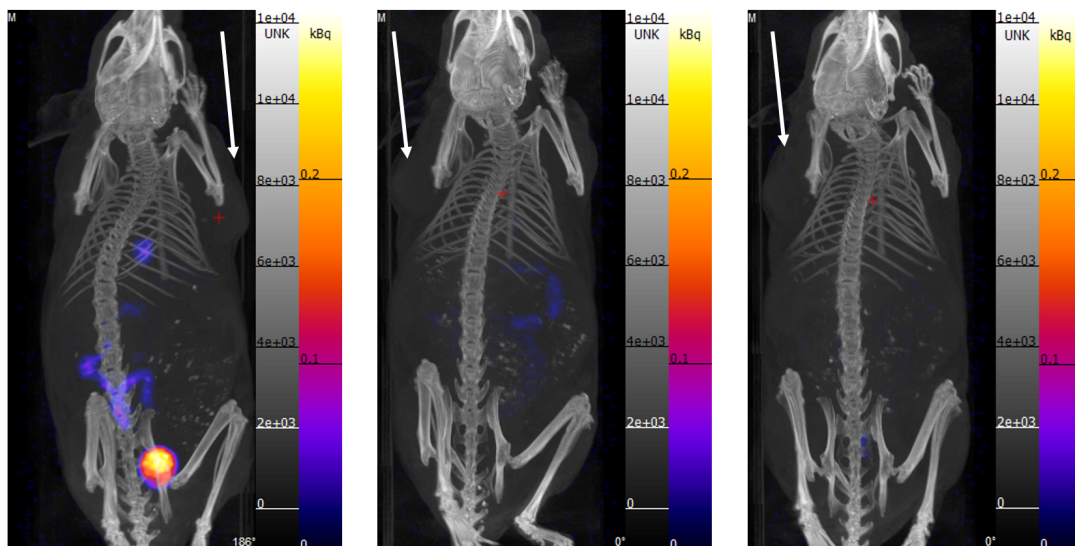


Figure 3.10. SPECT/CT images of mice (n=4) administered compound **5** (19-22 MBq), 24 hours after administration of huA33-TCO mAb, obtained at 1, 4 and 6 hours post-tetrazine injection. Mouse 1 is shown as an example. Clearance through the renal system and minimal uptake in the tumour (white arrow) was seen. SW1222-tumours were located on the right shoulder.

Biodistribution data yielded a tumour to blood ratio of 0.53 as a result of the low tumour uptake (0.9 ± 0.2 % ID/g). Unfortunately, compound **5** rapidly cleared through the renal system as seen by activity in the bladder that was evident in the SPECT/CT image at 1 hour. At the 6-hour time point, minimal retention of the compound was seen with < 2 % ID/g found in all other tissues and organs. The low tumour uptake is likely due to insufficient interaction between the huA33-TCO mAb at the tumour site and compound **5** which appears to clear rapidly.

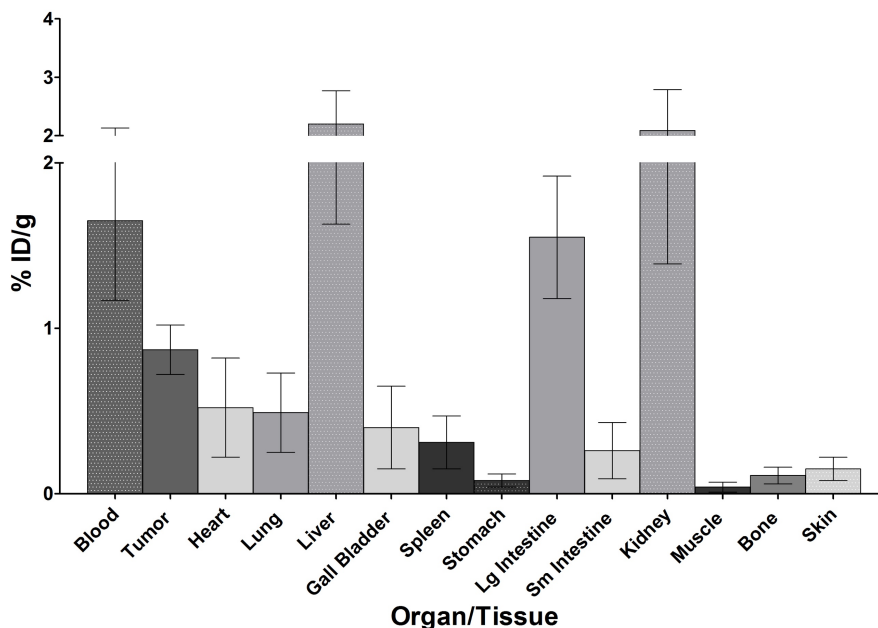


Figure 3.11. Biodistribution study data associated with the imaging study in Figure 3.9. Data is reported as percent injected dose per gram (% ID/g).

3.3.9. Pre-targeted *in vivo* evaluation of compound **5** (low specific activity).

Literature reports show that administration of a radiolabelled compound at a lower effective specific activity by co-formulation with excess ligand can yield increased tumour uptake.²² In the case of pre-targeting, the increased uptake is likely due to the higher tetrazine concentration. To test this here, the *in vivo* study with compound **5** was repeated where the specific activity was reduced by adding **10** prior to injection. The total tetrazine concentration was 0.75 nM which is 724 times higher than that used when compound **5** alone was administered. Mice were imaged at 1, 4, and 6-hours post injection followed by a biodistribution after the 6-hour imaging time point (Figure 3.12). Biodistribution data is again plotted as % ID/g per tissue/organ and shown in Figure 3.13.

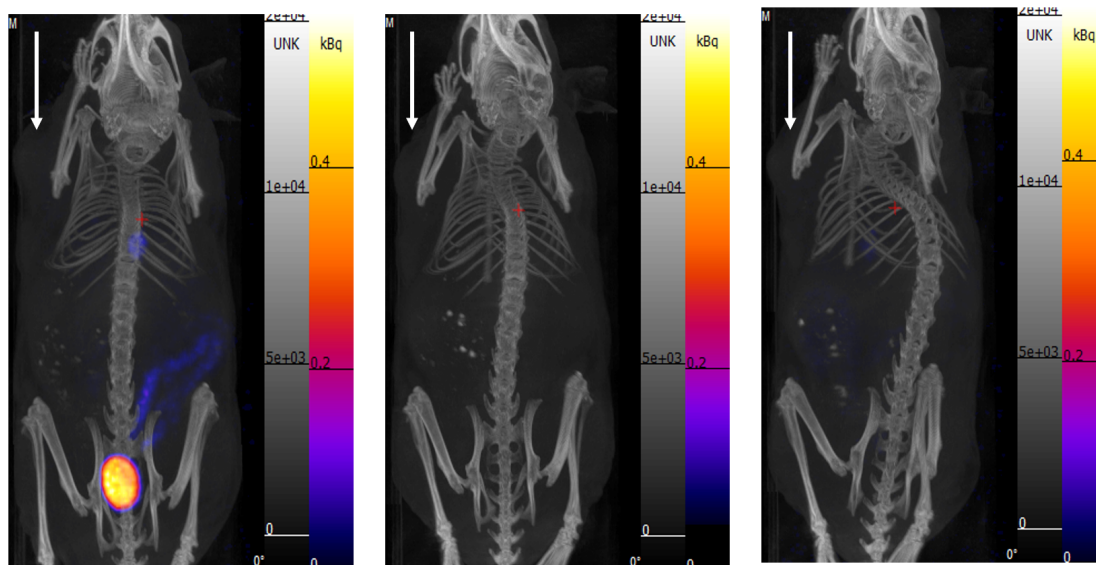


Figure 3.12. SPECT/CT images of mice (n=4) administered a mixture of compounds **5** (19-21 MBq) and **10** (0.75 nM), 24 hours after administration of huA33-TCO mAb, obtained at 1, 4 and 6 hours post-tetrazine injection. Mouse 2 is shown as an example. Similar to above, clearance through the renal system and minimal tumour uptake (white arrow) was observed. The addition of compound **10** did not appear to alter the biodistribution when observed by imaging. SW1222 tumours were located on the right shoulder.

Based on the biodistribution data, tumour uptake was marginally higher (1.1 ± 0.01 % ID/g) with a tumour to blood ratio of 0.6. Similar to the previous experiment, the formulation of compound **5** + **10** still appears to clear rapidly through the renal system. The highest amounts of radioactivity measured were found in the liver (3.0 ± 0.2 % ID/g), large intestine (4.7 ± 1.2 % ID/g) and kidneys (3.6 ± 0.3 % ID/g) at 6 h.

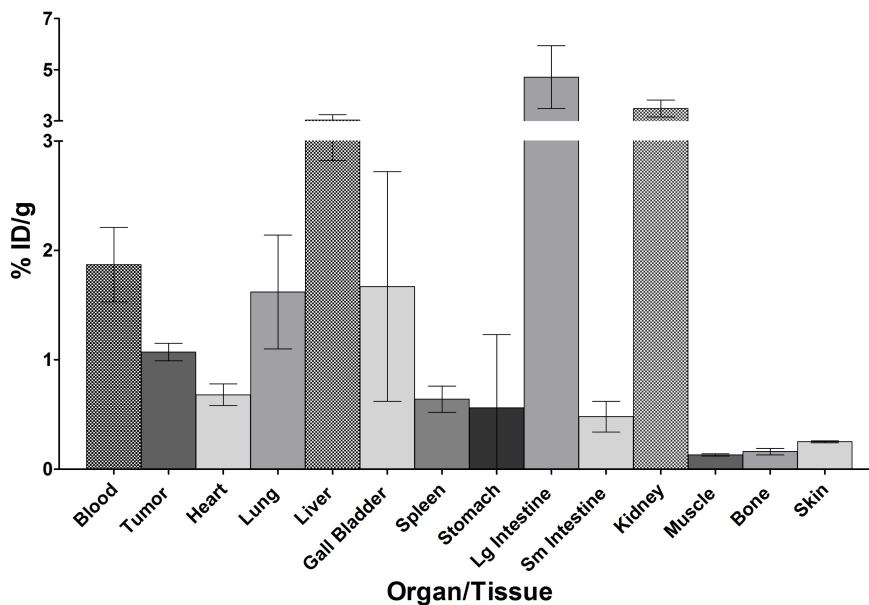


Figure 3.13. Biodistribution study data associated with the imaging study in Figure 3.12. Data is reported as percent injected dose per gram (% ID/g).

3.3.10. Comparison of pre-targeting with TCO-BP and huA33-TCO mAb

Previous *in vivo* pre-targeting studies with TCO-BP exhibited reasonably good uptake for compound **1** in the knee and shoulder joints (9.12 ± 1.88 and 4.62 ± 1.36 % ID/g, respectively). In comparison, for the same study, compound **5** demonstrated lower uptake in the knee and shoulder joints (3.15 ± 0.33 and 2.10 ± 0.38 % ID/g, respectively) at 1-hour post injection. Despite the fact that the ^{99m}Tc -tetrazines could be targeted using a small molecule TCO-derivative, the results with the huA33-TCO mAb were disappointing. The issue is likely not due to the TCO-mAb as the Zeglis group has proven its utility with a ^{64}Cu -labelled tetrazine which showed 4.1 ± 0.3 % ID/g in the SW1222 tumours.¹³

The low tumour uptake is likely due to the poor pharmacokinetics of the ^{99m}Tc -tetrazine compounds. The hydrophobic nature of compound **1** resulted in sustained liver

and GI uptake up to 6 hours while compound **5** cleared too rapidly through the renal system, with the majority being cleared from the subject within the first hour, to allow for the coupling reaction to occur. Although the tridentate chelate of compound **5** is analogous to that of MIP-1404 (a prostate specific membrane antigen (PSMA)-derived compound) which is undergoing promising clinical trials,²³ the presence of a PEG10 linker in our compound resulted in rapid clearance. The success with TCO-BP versus the TCO-mAb is likely associated with the lower amount of the huA33-TCO mAb (0.66 nmol) used compared to the small molecule TCO-BP (75 μ mol). This impacts the overall reaction rate and efficiency of coupling where with TCO-BP the concentration of the coupling partner is seemingly sufficient to overcome the limited bioavailability of the ^{99m}Tc-tetrazines. The lower concentration of the antibody resulted in insufficient coupling following first pass circulation whereupon the compound is cleared via the hepatobiliary system for compound **1** or the renal system for compound **5**.

3.4. Conclusion and Future Work

While compounds **1** and **5** demonstrated target (bone) uptake when pre-targeting was done using a small molecule TCO-BP derivative (Chapter 2), less than ideal results were observed with a TCO-modified antibody. The hypothesis is that compound **1** proved to be too hydrophobic while compound **5** proved to be too hydrophilic leading to inadequate concentration in the blood for efficient coupling to the mAb. Additionally, while literature reports have shown that decreasing specific activity can increase target uptake, a similar result was not observed here. One approach to improving the ligands was to prepare ^{99m}Tc-

tetrazine ligands with polarities between the two extremes of compounds **1** and **5** which was an avenue of research explored by another member of the group.²⁴ A second alternative, involved the use of micelles to help improve the pharmacokinetics of ^{99m}Tc-tetrazines: an approach which is described in chapter 4.

3.5. References

1. Li, J. & Zhu, Z. Research and development of next generation of antibody-based therapeutics. *Acta Pharmacol. Sin.* **31**, 1198–1207 (2010).
2. Adams, G. P. & Weiner, L. M. Monoclonal antibody therapy of cancer. *Nat. Biotechnol.* **23**, 1147–1157 (2005).
3. Weiner, L. M., Surana, R. & Wang, S. Monoclonal antibodies: versatile platforms for cancer immunotherapy. *Nat. Rev. Immunol.* **10**, 317–327 (2010).
4. Finn, O. J. Immuno-oncology: Understanding the function and dysfunction of the immune system in cancer. *Ann. Oncol.* **23**, 8–11 (2012).
5. Imai, K. & Takaoka, A. Comparing antibody and small-molecule therapies for cancer. *Nat. Rev. Cancer* **6**, 714–27 (2006).
6. Fleuren, E. D. G. *et al.* Theranostic applications of antibodies in oncology. *Mol. Oncol.* **8**, 799–812 (2014).
7. Tsai, W. T. K. & Wu, A. M. Aligning physics and physiology: Engineering antibodies for radionuclide delivery. *J. Label. Comp. Radiopharm.* **61**, 693–714 (2018).
8. Ulaner, G. A. *et al.* Detection of HER2-positive metastases in patients with HER2-

- negative primary breast cancer using ^{89}Zr -trastuzumab PET/CT. *J. Nucl. Med.* **57**, 1523–1528 (2016).
9. Ulaner, G. A. *et al.* CD38-targeted Immuno-PET of Multiple Myeloma: From Xenograft Models to First-in-Human Imaging. *Radiology* 192621 (2020).
doi:10.1148/radiol.2020192621
 10. Zeglis, B. M. *et al.* Optimization of a Pre-targeted Strategy for the PET Imaging of Colorectal Carcinoma via the Modulation of Radioligand Pharmacokinetics. *Mol. Pharm.* **12**, 3575–3587 (2015).
 11. Rossin, R. & Robillard, M. S. Pre-targeted imaging using bioorthogonal chemistry in mice. *Curr. Opin. Chem. Biol.* **21**, 161–9 (2014).
 12. Keinänen, O. *et al.* Pre-targeting of internalizing trastuzumab and cetuximab with a ^{18}F -tetrazine tracer in xenograft models. *EJNMMI Res.* **7**, 1–16 (2017).
 13. Zeglis, B. M. *et al.* A pre-targeted PET imaging strategy based on bioorthogonal Diels-Alder click chemistry. *J. Nucl. Med.* **54**, 1389–96 (2013).
 14. Nichols, B., Qin, Z., Yang, J., Vera, D. R. & Devaraj, N. K. ^{68}Ga chelating bioorthogonal tetrazine polymers for the multistep labeling of cancer biomarkers. *Chem. Commun.* **50**, 5215–5217 (2014).
 15. Edem, P. E. *et al.* Evaluation of a ^{68}Ga -labeled DOTA-tetrazine as a PET alternative to ^{111}In -SPECT pre-targeted imaging. *Molecules* **25**, 1–14 (2020).
 16. Evans, H. L. *et al.* A bioorthogonal ^{68}Ga -labelling strategy for rapid in vivo imaging. *Chem. Commun.* **50**, 9557–9560 (2014).
 17. Denk, C. *et al.* Design, Synthesis, and Evaluation of a Low-Molecular-Weight 11

- C-Labeled Tetrazine for Pre-targeted PET Imaging Applying Bioorthogonal in Vivo Click Chemistry. *Bioconjug. Chem.* **27**, 1707–1712 (2016).
18. Vito, A., Alarabi, H., Kent, J. & Valliant, J. F. Preparation and evaluation of a single tetrazine-based synthon for labeling biomolecules with both ^{99m}Tc and ^{18}F . *J. Label. Comp. Radiopharm.* **58**, 018 (2015).
 19. García, M. F. *et al.* ^{99m}Tc -bioorthogonal click chemistry reagent for in vivo pre-targeted imaging. *Bioorg. Med. Chem.* **24**, 1209–1215 (2016).
 20. Zeglis, B. M. & Lewis, J. S. The Bioconjugation and Radiosynthesis of ^{89}Zr -DFO-labeled Antibodies. *J. Vis. Exp.* 1–8 (2015). doi:10.3791/52521
 21. O'Donoghue, J. A. *et al.* ^{124}I -huA33 Antibody Uptake is Driven by A33 Antigen Concentration in Tissues from Colorectal Cancer Patients Imaged by Immuno-PET. *J. Nucl. Med.* **52**, 1878–1885 (2011).
 22. Rossin, R., Läppchen, T., van den Bosch, S. M., Laforest, R. & Robillard, M. S. Diels–Alder Reaction for Tumor Pre-targeting: In Vivo Chemistry Can Boost Tumor Radiation Dose Compared with Directly Labeled Antibody. *J. Nucl. Med.* **54**, 1989–1995 (2013).
 23. Schmidkonz, C. *et al.* ^{99m}Tc -MIP-1404-SPECT/CT for the detection of PSMA-positive lesions in 225 patients with biochemical recurrence of prostate cancer. *Prostate* **78**, 54–63 (2018).
 24. Bilton, H. The Synthesis and Evaluation New Radiopharmaceuticals and Multimodal Imaging Probes: The Synthesis, Evaluation and Mechanistic Study of New ^{99m}Tc (I)-Tetrazines for the Development of New Radiopharmaceuticals and

Multimodal Imaging Probes. (McMaster University, 2019).

Chapter 4: Pluronic F127 micelles for modifying the pharmacokinetics of ^{99m}Tc labelled tetrazines

4.1 Introduction

The current drug approval process takes approximately 15 years and has a success rate of < 0.02 %.¹ A recent approach to overcoming this traditionally lengthy drug development approval process has been to repurpose and improve older clinically validated drugs through the application of nanotechnology. For this reason, nanoparticle drug carriers have been employed to improve pharmacokinetic (PK) properties for enhancing therapeutic efficacy and reducing adverse effects of established pharmaceuticals.^{2,3} The last half decade has seen an increase in clinical translation of micelle-based drug delivery systems specifically, where the focus had previously largely been on liposomes and polymeric nanoparticles.^{4,5} Micelles, like other nanoparticles, are ideal delivery platforms due to their small size (1-100 nm) which enables them to passively accumulate in tumour tissue. Therefore, the ability to passively target existing pharmaceuticals while also improving their PK profile makes micelle-based delivery platforms an attractive avenue of research.

In aqueous solutions, amphiphilic copolymers self-assemble into micelles with a hydrophobic core and hydrophilic corona. Micelles form above a specific polymer concentration known as the critical micelle concentration (CMC). The CMC determines the stability of the micelle *in vivo* and the release kinetics of the payload from the micellar core. The core can be used to encapsulate hydrophobic compounds to improve their PK,

namely increased bioavailability, enhanced circulation time, reduced gastrointestinal (GI) uptake and toxicity.⁶⁻⁸ With the ability to encapsulate hydrophobic molecules and tunable drug-release properties, micelles are versatile platforms that can be utilized in conjunction with different diagnostic modalities as well as delivery vehicles for therapeutics. In the context of the work being done with radiolabelled tetrazines, micelle-encapsulated diagnostics developed to date include contrast agents for MR imaging, radiolabelled molecules for PET/SPECT imaging, and NIR dyes for photoacoustic imaging.⁹

Pluronic (poly(oxyethylene) (PEO)-poly(oxypropylene) (PPO) block copolymers) are one of the most widely used polymers for creating drug-encapsulated micelles due to their biocompatibility. A variety of Pluronic copolymers exist such as F127, L35, L61, F68, P85, L101, and P105 which differ based on their ethyleneoxide (EO) to propyleneoxide (PO) ratio which impacts their physical properties including physical state at room temperature (e.g. solid, liquid, or paste).¹⁰ As a nanoparticle, Pluronic micelles have the ability to passively accumulate in tumour tissue as a result of the enhanced permeability and retention (EPR) effect. The EPR effect is seen especially in solid tumours which exhibit leaky vasculature because rapid angiogenesis during tumour growth leads to fenestrations between endothelial cells.³ This allows the micelles to enter the interstitial tumour tissue where Pluronic polymers are also known to inhibit the P-glycoprotein (P-gp) drug efflux transport system that is involved in the multidrug resistance (MDR) exhibited by many cancer cells.¹¹

Tumour targeting properties coupled with their commercial availability and biocompatibility have led to multiple investigations of Pluronic micelles encapsulating

chemotherapeutics including paclitaxel and doxorubicin.¹²⁻²² As a commonly used first-line chemotherapeutic agent doxorubicin alone has been able to provide an overall survival period of 7.7-12.7 months and response rates ranging from 16 % to 27 % in patients with soft tissue cancer.²³ However, the treatment frequently leads to cancer cells developing MDR and thus requires increasing doses of doxorubicin to achieve the same results. These increased doses can eventually result in unfortunate complications for patients such as myelosuppression and cardiomyopathy.

To address this, a mixed micellar formulation of Pluronic F127 (2 % w/v, 20 mg/mL) and L61 (0.25 % w/v, 2.5 mg/mL) containing doxorubicin (2 mg/mL), SP1049C, was developed and successfully completed phase I and II clinical trials for patients suffering from advanced adenocarcinoma of the upper gastrointestinal (GI) tract.¹⁸ Due to the Pluronic polymers ability to target P-gp, this particular formulation works by disrupting the P-gp function in cellular membranes of doxorubicin-resistant cells to enable doxorubicin permeation into these cells. Phase I results displayed a favorable pharmacokinetic profile for SP1049C compared to doxorubicin as a result of slower clearance of the micelles, and a maximum tolerated dose of 70 mg/m² doxorubicin as an intravenous infusion every 3 weeks was determined.²⁴ In the subsequent phase II clinical trial, the antitumour efficacy of SP1049C was evaluated.¹⁸ Twenty one patients received a dose of 75 mg/m² (doxorubicin [mg]) via intravenous injection over 30 min, followed by 10 mL of saline flushing. This was repeated every 3 weeks, up to six cycles. The majority (86.4 %) of patients received at least two rounds of treatment while 38.1 % were able to receive six rounds. No deaths occurred as a result of toxicity and all side effects were

reported as manageable and reversible. The early clinical data demonstrated the micellar formulation of doxorubicin had superior antitumour activity compared to the free drug. An objective response rate of 47 % was observed for patients after at least one round of treatment. Additionally, a median overall survival period of 10.0 months was determined with 24 % of patients surviving past 1 year (Figure 4.1). Despite the survival period being similar to that of doxorubicin alone, the reduced side effects and the increased response rate highlight the benefits of SP1049C compared to free doxorubicin. The data was sufficiently promising to advance SP1049C to phase III clinical trials, which are ongoing, and shows the potential utility that can be derived from micelles as drug carriers.²⁵

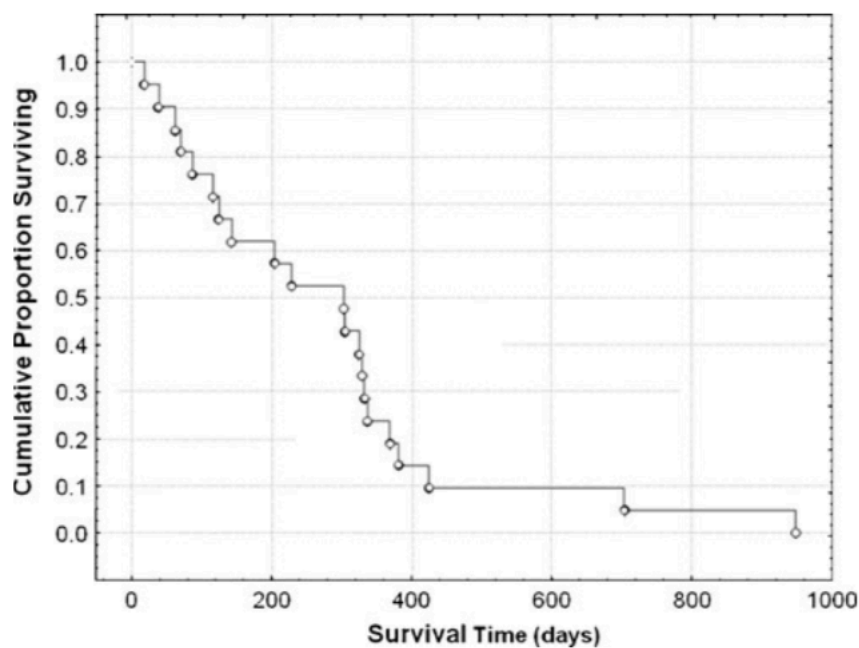


Figure 4.1. Kaplan-Meier plot depicting overall survival rate of patients undergoing phase II trial of SP1049C. Median survival was 10 months while 24 % of patients survived past 1 year. Reprinted with permission from Springer Nature: Valle *et al. Invest. New Drugs* 2011, 29 (5), 1029–1037. Copyright 2010.

In 2018, Zhang *et al.* developed Pluronic F127 micelles encapsulating paclitaxel (PTX), which is a hydrophobic chemotherapy agent, the NIR dye BODIPY, and β -thiophene-fused BF₂-azadipyrrromethene (aza-BDTP), to create a multi-purpose agent for photothermal therapy (PTT) and chemotherapy.²⁶ The prepared micelles were 21 nm in size and exhibited stability in water and PBS for up to 3 weeks. The fluorescence quenching of the dye due to aggregation in the micellar core resulted in enhanced photothermal conversion capacity of over 30 % for aza-BDTP/PTX F127 micelles and aza-BDTP F127 micelles compared to 17 % for aza-BDTP in solution at the same concentration, suggesting micellar formulations to be more effective PTT agents. Additionally, both aza-BDTP and aza-BDTP/PTX F127 micelles proved to have greater photothermal stability when incubated with 4T1 breast cancer cells compared to the clinically approved dye, indocyanine green (ICG), when exposed to multiple cycles of irradiation from a 785 nm laser.

Zhang *et al.* then conducted *in vivo* photoacoustic (PA) imaging using aza-BDTP/PTX F127 and aza-BDTP F127 micelles.²⁶ PA imaging uses non-ionizing laser pulses on tissues which causes thermal expansion. This expansion generates acoustic waves which can then be detected using an ultrasound transducer to produce higher resolution images compared to optical imaging.²⁷ Balb/C mice bearing 4T1 breast cancer tumours were administered either aza-BDTP or aza-BDTP/PTX F127 micelles intravenously with both exhibiting tumour accumulation over 4 h post injection and sustained retention at 8 and 24 h post injection (Figure 4.2A).²⁶ Conclusions on the biodistribution were made from the 24 h PA images by quantifying PA signal in key organs: liver, spleen, kidney, heart,

and tumour (Figure 4.2B). While there was some tumour uptake, both the aza-BDTP and aza-BDTP/PTX F127 micelles also showed higher liver and splenic uptake, compared to the saline control dose, likely due to sequestration of the micelles by the mononuclear phagocyte system (MPS). A comparison to the non-micellar formulations of aza-BDTP or aza-BDTP/PTX was not reported.

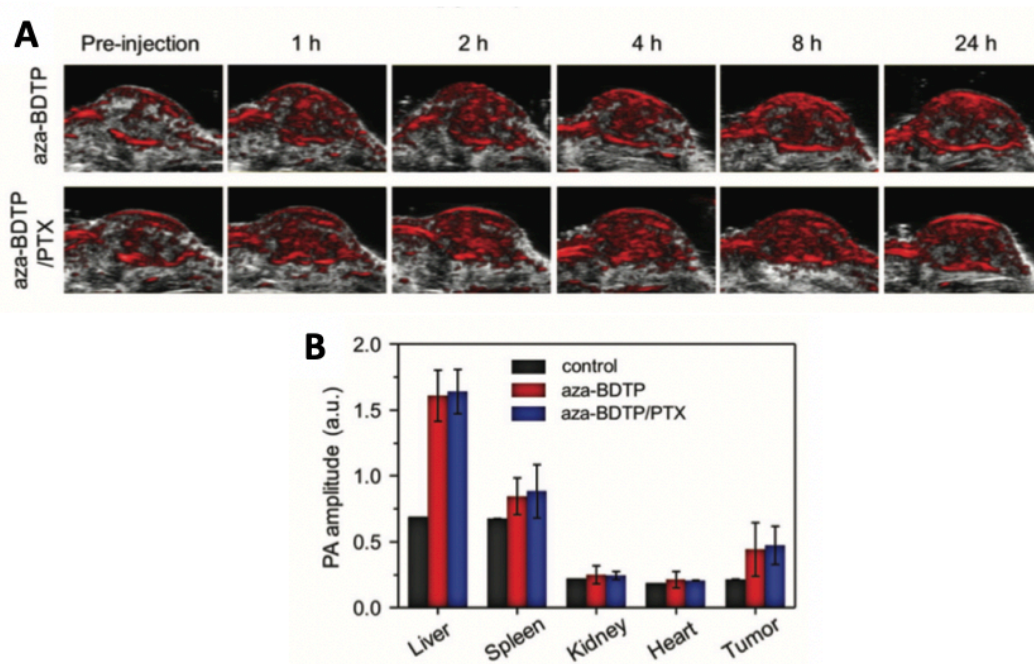


Figure 4.2. Photoacoustic study data conducted using Balb/C mice bearing 4T1 xenografts which were administered aza-BDTP F127 micelles and aza-BDTP/PTX F127 micelles intravenously. A) PA images of tumours at various time points. B) Quantified PA signal obtained from *ex vivo* imaging of key organs at 24 h compared to intravenous administration of saline as the control. Reprinted with permission from John Wiley and Sons: Zhang *et al. Small* **2018**, *14* (44), 1802991. Copyright 2018.

In 2014, Lovell *et al.* prepared Pluronic F127 micelles for GI imaging by encapsulating various hydrophobic naphthalocyanine dyes which exhibit strong PA properties.²⁸ The prepared micelles were 20 nm in size as determined by DLS and TEM. Balb/C mice were administered 100 ODs of dye-containing micelles (ONc nanonaps) via

oral gavage and kept in metabolic cages for the duration of the study to collect their feces and urine. Absorbance measurements revealed the ONc nanonaps excreted exclusively through feces (>80 % by 8 h post administration) (Figure 4.3A) and histology after imaging showed no noticeable inflammatory response in intestinal tissue (Figure 4.3B). With these results, the ONc nanonaps show potential utility as GI imaging agents to identify bowel obstructions.

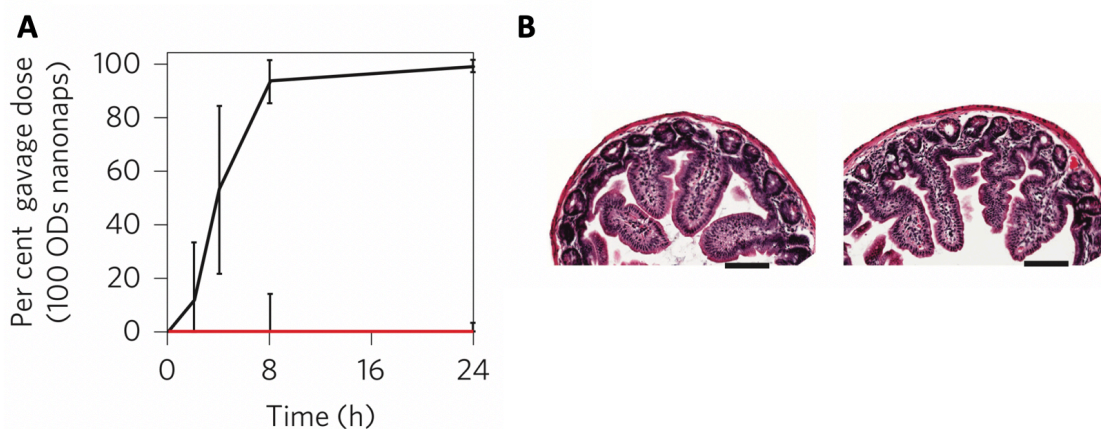


Figure 4.3. A) Excretion of nanonaps over 24 h in feces (black) and urine (red). B) Histology images of the intestine of a mouse administered the saline control (left) and a mouse administered the ONc nanonaps (right) 24 h post administration, right. Reprinted with permission from Springer Nature: Zhang et al. *Nat. Nanotechnol.* 2014, 9 (8), 631–638.

Although PA imaging is promising, it is not a quantitative imaging technique therefore the nanonap encapsulated dyes were labelled with copper-64 (^{64}Cu) so PET imaging could be used.²⁸ To prepare the radioactive micelles, naphthalocyanine dyes were encapsulated within the micelles prior to the addition of ^{64}Cu which was able to infiltrate the micellar core and bind to the chelate achieving a radiochemical yield > 65% after 30 min. Balb/C mice were again administered 100 ODs ^{64}Cu -ONc nanonaps orally. PET images showed uptake in the stomach and upper intestine at 0.5 h and clearance through

the GI system at 3 h (Figure 4.4A). Biodistribution data obtained at 24 h post administration showed fecal clearance in 24 h for ^{64}Cu -ONc nanonaps and $< 1.5\%$ ID/g was measured in all other organs (Figure 4.4B).

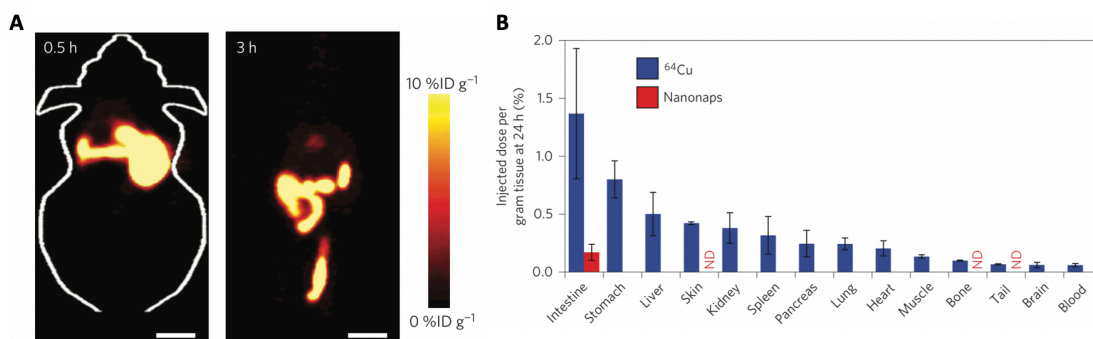


Figure 4.4. PET imaging (A) and biodistribution data (B) of ^{64}Cu -ONc nanonaps administered orally to Balb/C mice. Reprinted with permission from Springer Nature: Zhang *et al. Nat. Nanotechnol.* 2014, 9 (8), 631–638.

In 2017, Lovell *et al.* modified the route of administration to intravenous and looked at tumour uptake of ^{64}Cu -ONc nanonaps. Balb/C mice with 4T1 xenografts in their right shoulders received ^{64}Cu -ONc nanonaps and were subject to PET imaging at 0.5, 3.5, 16 and 22 h followed by a biodistribution at 24 h post injection (Figure 4.5). Whole body images showed uptake of ^{64}Cu -ONc nanonaps in tumours via the EPR effect as early as 3.5 h and quantitative image analysis determined uptake of 7.5% ID/g in the tumour at 22 h. ^{64}Cu -ONc nanopap accumulation in the liver seen by the PET images was confirmed with a biodistribution and measured to be 15% ID/g, higher than all other tissues including the tumour. This is likely due to sequestration of a portion of the intravenously administered micelles by the MPS.

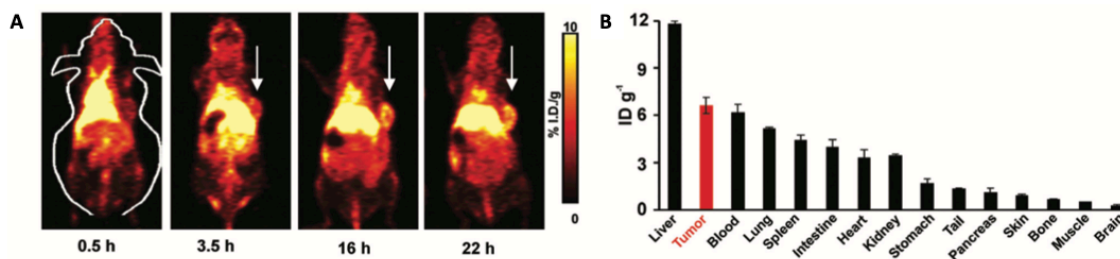


Figure 4.5. PET imaging (A) and biodistribution data (B) of ^{64}Cu -ONc nanonaps administered intravenously to Balb/C mice bearing 4T1 breast cancer xenografts in right shoulders (white arrows). Biodistribution was conducted at 24 h post injection. Reprinted by permission from The Royal Society of Chemistry: Zhang *et al.* *Nanoscale*. (2017) 9, 3391-3398.

In terms of other radiopharmaceuticals encapsulated in micelles, Laan *et al.* used polystyrene-*b*-poly(ethylene oxide) di-block copolymers to encapsulate a hydrophobic ligand radiolabelled with indium-111.²⁹ The ^{111}In -PS-*b*-PEO micelles produced micelles that were 97 ± 13 nm in size, the majority of which were spherical with some rod-like micelles also present. *In vivo* SPECT/CT imaging was conducted at 30 min, 4 hours and 24 hours post injection of ^{111}In -PS-*b*-PEO micelles into Balb/C-*nu* mice. Uptake of the micelles in the spleen was observed as early as 30 min post injection and increased over the 24-hour period. By 24 hours, based on the images, micelles appear to be cleared from circulation and the activity is localized in the spleen and liver. Biodistribution data obtained at 24 hours post-injection corroborated imaging data showing high splenic (176 ± 97 % ID/g) and moderate liver (30 ± 6 % ID/g) uptake along with significant blood concentration (21 ± 8 % ID/g) (Figure 4.6).

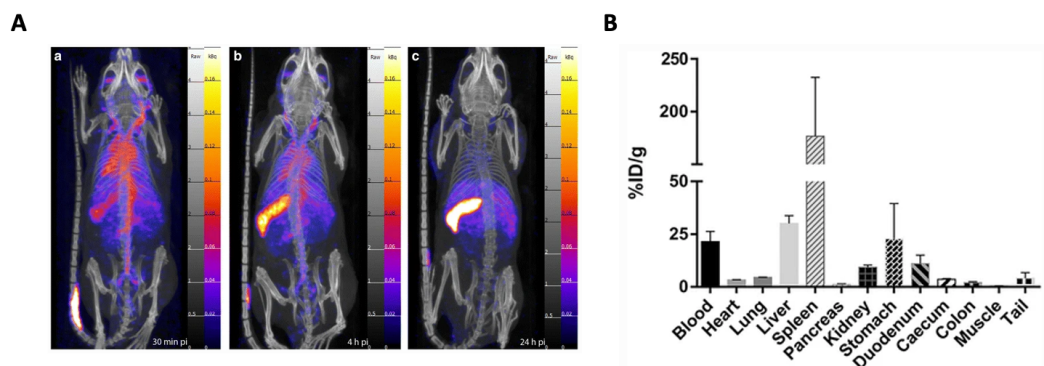


Figure 4.6. Balb/C-nu mice received ^{111}In -PS-bPEO (22 MBq) micelles intravenously. A) SPECT/CT images obtained at 30 min, 4 h, and 24 h post injection. B) Results of biodistribution study at 24 h post injection. Values are reported as % injected dose/g (% ID/g).

Given that micelles have been shown to improve the PK profile of a number of diagnostic and therapeutic agents, and that it is feasible to create micelles that can encapsulate radiolabelled compounds, work was initiated to assess their utility for the ligands reported in chapters 2 and 3. For the most hydrophobic $^{99\text{m}}\text{Tc}$ -tetrazine ligand, which contained a bispyridyl chelate, imaging and biodistribution data had showed the compound was concentrating quickly in the gastrointestinal system precluding coupling to TCO-modified antibodies. Pluronic F127 (EO₁₀₀-PO₆₅-EO₁₀₀) (MW=12.6 kDa) which has a CMC of 2.8×10^{-6} M at 37 °C, one of the lowest values of all Pluronic polymers, was used to encapsulate the $^{99\text{m}}\text{Tc}$ -tetrazine.³⁰ The ultimate goal was to determine if the micelles could reduce off-target uptake and enhance *in vivo* coupling to TCO derived molecules. To this end, the initial focus was to develop a method for encapsulating $^{99\text{m}}\text{Tc}$ -labelled tetrazines in Pluronic F127 micelles. Additionally, targeted analogues through

functionalization of the micelle periphery were developed which is described in Chapter 5.¹⁶

4.2 Materials and Methods

4.2.1 General materials, methods, and instrumentation

Unless otherwise stated, all reagents were used as obtained from the supplier without further purification. *Trans*-cyclooctene-NHS (TCO-NHS) was purchased from Conju-Probe, LLC and alendronic acid from AK scientific. The solvents used were purchased from Caledon and Sigma Aldrich. The anhydrous solvents were dried using the Pure Solv drying apparatus (Innovative Technology). Deuterated solvents for NMR samples were bought from Cambridge Isotope Laboratories. A generator supplied by Lantheus Medical Imaging was used to obtain ^{99m}Tc-Pertechnetate [^{99m}TcO₄]⁻ in saline from a ⁹⁹Mo/^{99m}Tc generator. Potassium sodium tartrate (K/NaC₄H₄O₆•4H₂O) and sodium borate (Na₂B₄O₇•10H₂O) were acquired from Achemia Canada Inc., while sodium carbonate (Na₂CO₃) was acquired from EM science. Microwave reactions were done on a Biotage Initiator 60 microwave reactor.

Nuclear magnetic resonance spectra (¹H) were documented on a Bruker AV600 spectrometer at ambient temperature. Dynamic light scattering data was obtained on a Malvern Zetasizer Nano ZS (ZEN3600). Transmission electron microscopy images were obtained by Dr. Carmen Andrei at the Canadian Centre for Electron Microscopy at McMaster University.

Unless specified, purification of compounds was done using Silica Gel 60 (particle size 0.04-0.063 mm) acquired from EMD chemicals. High performance liquid chromatography (HPLC) was performed for purification on a Water 1525 HPLC system connected to a 2998 photodiode array detector monitoring at 220 nm with a polar-RP semipreparative column (250 × 10 mm, 5 µm) with a 4 mL/min flow rate. The solvents used for compound purification for HPLC were A: H₂O + 0.005% triethylamine (TEA), B: acetonitrile (ACN) + 0.005% TEA, C: H₂O + 0.1 % trifluoroacetic acid (TFA), D: ACN + 0.1 % TFA. Solvents were evaporated using a rotary evaporator under reduced pressure or via the Biotage V10 solvent evaporation system. Compounds were lyophilized using VirTis Benchtop lyophilizer fitted with an Edwards RV5 pump.

Animal studies were approved by the Animal Research Ethics Board at McMaster University in accordance with Canadian Council on Animal Care (CCAC) guidelines.

4.2.2 Encapsulation of cargo in Pluronic F127 micelles (mF127(cargo))

A 10 % w/v solution of Pluronic F127 polymers in dH₂O or saline or PBS (5 mL) was prepared. The compound (dye or tetrazine) to be encapsulated (1 mg) was dissolved in DCM (1 mL) and stirred until the organic solvent evaporated. Unincorporated F127 was removed via CMC switching, where the solution was cooled on ice (30 min) and subjected to centrifugal filtration (MWCO 100 kDa, 4000 rpm × 25 min × 3) at 4 °C until < 1 mL of solution was retained. Fresh dH₂O or saline or PBS was added for each wash. The concentrated solution (~200 µL) was retrieved using a P200 pipette, reconstituted in 2 mL of aqueous solvent and filtered through a 0.25 µm syringe filter prior to analysis. Dynamic

light scattering data was measured using the BrookHaven Nano90Plus particle size analyzer.

4.2.3 Synthesis of TCO-bisphosphonate (TCO-BP) (20)

Compound **20** was synthesized according to a literature procedure and provided by Dr. Afaf Genady.³¹ Briefly, TCO-NHS (35 mg, 0.13 mmol) and alendronic acid (49 mg, 0.18 mmol) were combined in a dry 5 mL vial. Water (1 mL) was added followed by a solution of TEA (6 eq) and DMSO (1 mL). The reaction was left to stir for 24 h at room temperature in the dark. The solution was diluted with water (20 mL) and purified by semi-preparative HPLC using a polar-RP column and the following elution gradient: 2-6.5 min, 24 % B; 6.5-7 min, 100 % B; 7-9 min, 100 % B. Fractions were concentrated and dissolved in water for lyophilization yielding a white powder (17 mg, 32 %). ¹H NMR (600 MHz, D₂O): δ (ppm) 5.70 (m, 1 H), 5.62 (m, 1 H), 4.29 (b, 1 H), 3.21 (q, $J = 7.3$ Hz, 6 H), 3.13 (t, $J = 6.6$ Hz, 2 H), 2.34 (m, 3 H), 1.96 (m, 6 H), 1.78 (m, 2 H), 1.66 (m, 3 H), 1.29 (t, $J = 7.4$ Hz, 9 H).

4.2.4 Biodistribution study of mF127(1)

Compound **1** was synthesized and radiolabelled according to a literature procedure.³² Briefly, ^{99m}TcO₄⁻ (100 MBq) in 4 mL of saline was reduced to [^{99m}Tc(CO)₃(OH)₂]₃⁺ through a microwave reaction (3 minutes at 100 °C with 10 s of pre-stirring) using K₂[BH₃CO₂]. The pH of the solution was adjusted to 3.5 with 1M HCl and 250 μ L of [^{99m}Tc(CO)₃(OH)₂]₃⁺ (82.88 MBq) was added to **14** (2 mg, 0.004 mmol) dissolved in 250 μ L MeOH. The reaction mixture was heated in a microwave for 20

minutes at 60 °C and purified by HPLC. $R_t=11.2$ min (R.C.Y.: 80%). Compound **1** (20 MBq) was subsequently encapsulated within mF127 using the procedure described above. After CMC switching, mF127(**1**) (8.7 MBq) was obtained. Healthy CD1 mice (Charles River Laboratories, Kingston, NY) (n= 6) were administered mF127(**1**) (0.51- 0.59 MBq) in saline via tail vein injection. At t= 1 and 6 h post injection, animals were anesthetized with 3% isoflurane and euthanized by cervical dislocation and blood, bone, adipose, adrenals, brain, gall bladder, heart, kidneys, large intestine, liver, lungs, pancreas, skeletal muscle, small intestine, spleen, stomach, thyroid/trachea, and urine and bladder were collected. The tissues and fluids were weighed and counted in a gamma detector. All data were decay corrected and reported as % ID/g.

4.2.5 Pre-targeted *in vivo* biodistribution study of mF127(1**)**

mF127(**1**) (21 MBq) were prepared as described above. Healthy CD1 mice (Charles River Laboratories, Kingston, NY) (n= 3) were administered (20 mg/kg) a 5 mg/mL solution of compound **20** in saline via tail vein injection 1 h prior to the administration of mF127(**1**) (0.48- 0.59 MBq) in saline via tail vein injection. At 6 h p.i. animals were anesthetized with 3% isoflurane and euthanized by cervical dislocation and blood, bone (knee and shoulder), adipose, adrenals, brain, gall bladder, heart, kidneys, large intestine, liver, lungs, pancreas, skeletal muscle, small intestine, spleen, stomach, thyroid/trachea, and urine and bladder were collected. The tissues and fluids were weighed and counted in a gamma detector. The measurements were decay corrected and data reported as % ID/g.

4.3 Results and Discussion

4.3.1 Preparation and Characterization of Loaded Pluronic F127 micelles

In an attempt to modify its biodistribution, we encapsulated the hydrophobic ^{99m}Tc -tetrazine **1**, which previously showed the highest gastrointestinal uptake, within Pluronic F127 micelles adapting the protocol published by Zhang *et al.*³³ In brief, the procedure involved adding a solution of **1** in DCM to a stirring solution of 10% w/v Pluronic F127 polymers in dH₂O. The mixture was stirred for 2 hours at room temperature to allow the dichloromethane to evaporate as the compound transitioned from the organic phase into the hydrophobic micelle pocket. Subsequently, the micelles were cooled on ice for 30 min before being subject to centrifugal filtration (MWCO= 100 kDa, 4000 rpm \times 25 min \times 3) where fresh dH₂O was added for each cycle. The concentrated, purified mF127(**1**) were reconstituted in dH₂O and filtered through a syringe filter before analyzing their size distribution using dynamic light scattering (DLS). Prior to DLS measurement, mF127(**1**) were allowed to decay for 2 days as samples could not be analyzed by DLS while radioactive. For comparison, the Re-standard of compound **1**, compound **6**, was similarly encapsulated to prepare mF127(**6**). DLS measurements for mF127(**6**) were conducted up to 48 h to align with the decay time for mF127(**1**). The size of mF127(**1**) and mF127(**6**) was 27.5 ± 0.8 nm (PDI: 0.25) and 31.2 ± 0.6 nm (PDI: 0.28) at 25 °C, respectively (Figure 4.7). The size distribution mF127(**6**) was consistent over the 48-h period and aligned well with the distribution of mF127(**1**). Literature values for comparable cargo loaded Pluronic F127 micelle size have been reported as ranging between 20 and 30 nm.^{16,28,34}

The size of mF127(**6**) was also assessed using transmission electron microscopy (TEM) (Figure 4.8) and determined to be \sim 18 nm. Since compound **6** is the non-radioactive

congener for compound **1**, the size distribution for mF127(**1**) is expected to be similar. The size discrepancy between the DLS and TEM methods is expected (5-10 nm) due to the difference in solvation states of the samples.³⁵ For DLS measurements, the micelles are fully hydrated in solution whereas for TEM analysis, the micelles are dried on copper grids.

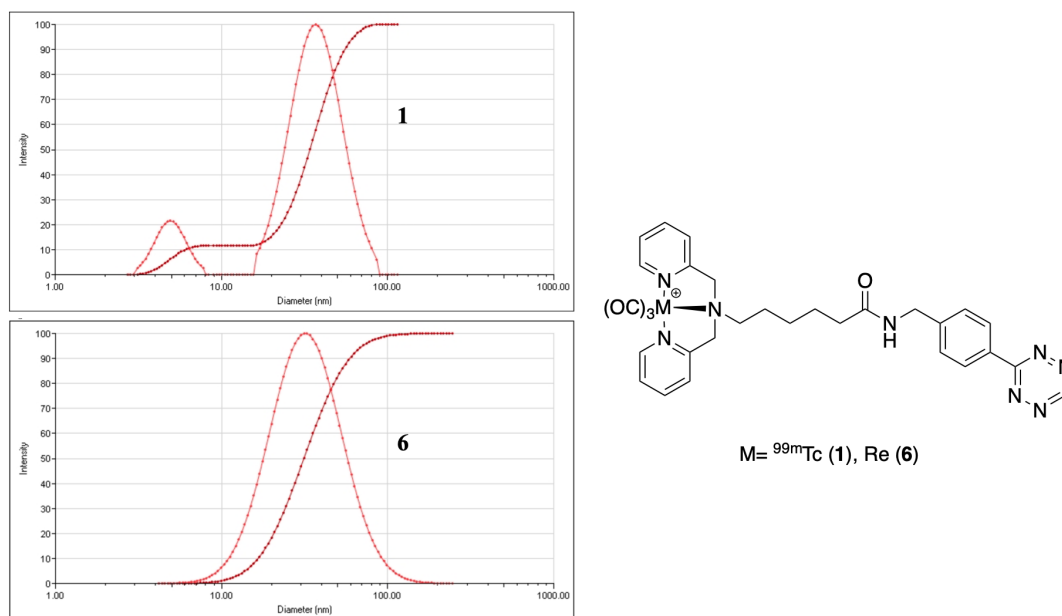


Figure 4.7. Dynamic light scattering data for mF127(**1**) (top) and mF127(**6**) (bottom) at 25 °C. Micelle size from DLS was 27.5 ± 0.8 nm (PDI: 0.25) and 31.2 ± 0.6 nm (PDI: 0.28) from TEM.

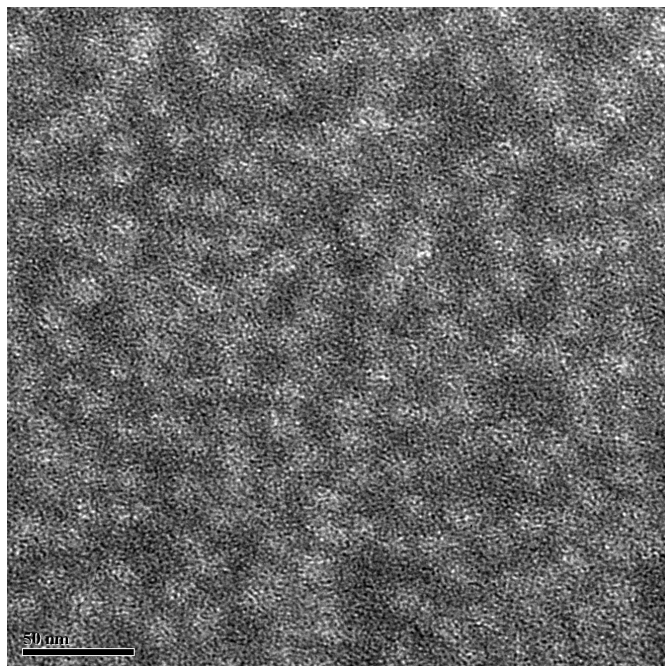


Figure 4.8. Transmission electron microscopy image of F127(6). The micelles were ~ 18 nm in size.

4.3.2 Biodistribution study of mF127(1) in healthy mice

Having successfully encapsulated compound **1** within the Pluronic F127 micelles, a preliminary biodistribution study was performed. Healthy CD1 mice ($n=6$) were administered compound **1** encapsulated in Pluronic F127 micelles (mF127(**1**)). The animals were sacrificed at 1 and 6 h post injection ($n=3$), and tissues and fluids were collected and counted (Figure 4.9). As expected, there was a higher concentration in the blood at both the 1 and 6 h time points for mF127(**1**) versus that for compound **1** alone. At the 1 h time point blood concentration for mF127(**1**) was 1.22 ± 0.01 % ID/g compared 0.32 ± 0.04 % ID/g for **1** alone. mF127(**1**) remained in circulation longer than **1** as well, as evident by a blood concentration of 0.55 ± 0.01 % ID/g compared to 0.01 ± 0.00 % ID/g at 6 h post injection. It is also noteworthy that there was a decrease in liver uptake as a result of encapsulating

compound **1** within micelles (10.14 ± 1.00 % ID/g compared to 35.00 ± 3.59 % ID/g for **1** alone) at 6 h. To determine whether the distribution of **1** alone and mF127(**1**) were significantly different from one another, multiple t-tests (individual t-test for each organ/tissue) were conducted (GraphPad Prism Version 8.4.2). Of all organs and tissues, only changes in blood concentrations at 1 and 6 h ($p < 0.0005$) and liver uptake at 6 h ($p < 0.005$) were considered statistically significant and are likely a direct result of the encapsulation. Differences in biodistribution measured for the adrenal glands, adipose, bone, brain, heart, gall bladder, kidneys, large intestine, lungs, pancreas, skeletal muscle, small intestine, spleen, stomach and the thyroid/trachea were not considered significant ($p < 0.005$) at either time point.

With the data showing that the encapsulation of compound **1** in the micelles decreased uptake in the liver and increased blood residence time, the micelles could potentially increase the ability of the ^{99m}Tc -labelled tetrazines to react with TCO-derived biomolecules *in vivo*. By evading first pass clearance and increasing blood concentrations, the rate and probability of the tetrazine-TCO reactions *in vivo* could potentially be improved. This would however require the tetrazine to be released from the micelle at the site of interest at a high enough concentration for ligation.

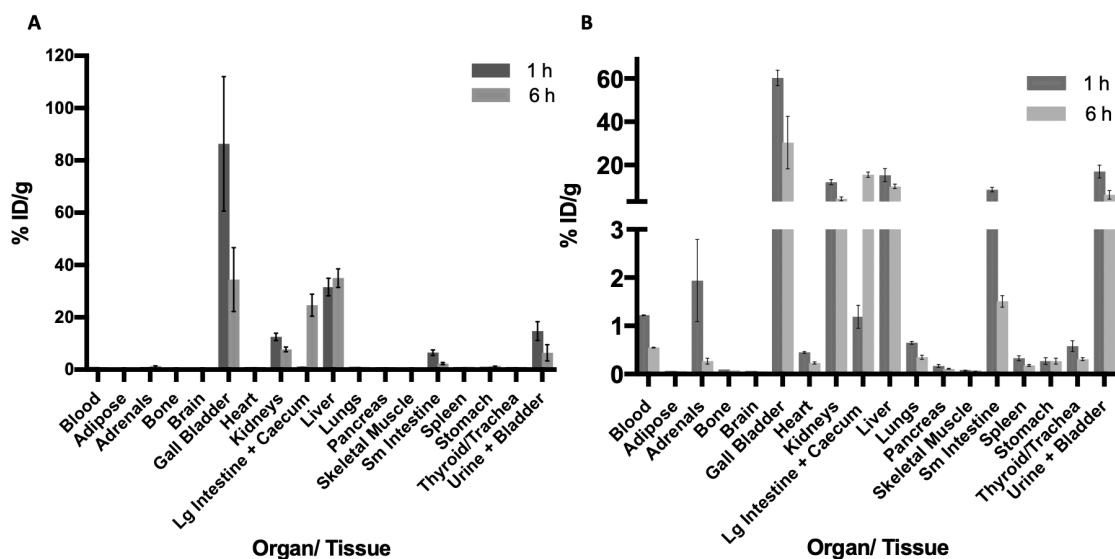


Figure 4.9. Biodistribution data of **1** alone and mF127(**1**) reported as % ID/g. Animals were sacrificed at 1 and 6 h p.i. of the radiolabelled compound. A) Biodistribution data for compound **1** in healthy CD1 mice (n=3). B) Biodistribution data for mF127(**1**) in healthy CD1 mice (n=3).

4.3.3 Pre-targeted biodistribution study of mF127(**1**) with **20**

Following the positive results from the biodistribution study of mF127(**1**), a pre-targeted study was conducted using a TCO-targeting vector: TCO-BP (Figure S4.1). Healthy CD1 mice (n=3) were administered the *trans*-cyclooctene modified bisphosphonate (TCO-BP, **20**) (100 μ L, 5 μ g/ μ L) used in chapter 2, followed by an injection of mF127(**1**) (0.54 MBq) 1 hour later. Animals were sacrificed and a biodistribution study was conducted at 6 h p.i. of mF127(**1**) (Figure 4.10). No earlier time point was chosen based on the data shown in Figure 4.9B, as the mF127(**1**) had not yet cleared from non-target tissue at 1 h.

The hypothesis was that the encapsulation of compound **1** and the associated reduced liver uptake and increased circulation would result in greater uptake at the bone compared to compound **1** alone. However, the biodistribution data showed a decrease in

uptake at the shoulder (4.62 ± 1.36 % ID/g vs. 0.46 ± 0.07 % ID/g) and knee joint (9.12 ± 1.88 to 0.71 ± 0.05 % ID/g) for mF127(**1**) versus compound **1** alone, respectively. To determine whether the distribution of **1** alone and mF127(**1**) when pre-targeted with bisphosphonate were significantly different from one another, multiple t-tests were conducted using GraphPad Prism (Version 8.4.2). The decreased bone uptake at the knee and shoulder joints was considered statistically significant ($p < 0.05$) and attributed to the encapsulation. Changes in blood concentration, gall bladder, heart, kidneys, large intestine, lungs and pancreas uptake were also considered significant ($p < 0.05$).

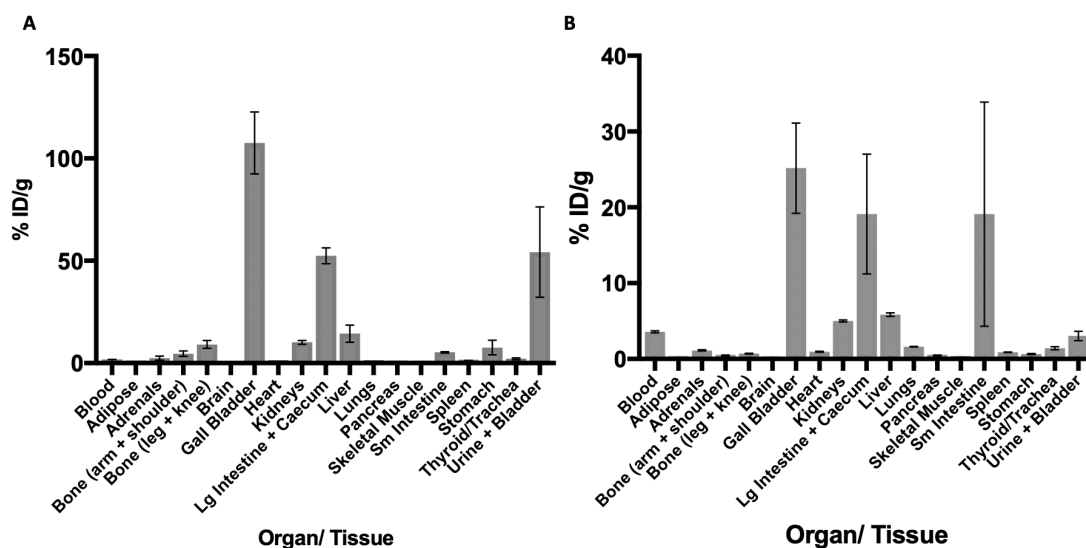


Figure 4.10. Biodistribution data for compound **1** (A) and mF127(**1**) (B) when pre-targeted with compound **20** (TCO-BP) reported as % ID/g. Compound **1** and mF127(**1**) were injected 1 hour after the TCO-BP injection in healthy CD1 mice ($n=3$) and animals were sacrificed at 6 hours p.i.

The results suggest that the mF127(**1**) were able to increase the blood concentrations over time and decrease liver uptake for compound **1**. Unfortunately this did

not translate into increased uptake at the bone with the use of TCO-BP targeting vector. This lack of target uptake may be a result of our choice of the target. Pluronic micelles are best suited for well vascularized targets such as tumours as opposed to bone which is less permeable.^{6,15,16,36} Furthermore, the long circulation time of micelle carriers also aids in accumulation in tumour tissue suggesting the use of a tumour model to evaluate passive targeting of the micelles may be beneficial.²⁰ Bisphosphonates like compound **20** bind to hydroxyapatite found on the bone surface as opposed to within a tumour.^{37,38} As the micelles likely do not passively accumulate at key areas of high calcium turnover, the release of compound **1** from the micelles is not occurring at sites which have the highest concentration of **20** but rather is spread out over a larger area likely decreasing the efficiency of coupling. This problem could potentially be overcome by evaluating uptake in tumour models, which is pending investigation, or preparing micelles functionalized with a targeting vector (explored in Chapter 5) to direct the micelles to a specific site for subsequent release of the payload. The latter was felt to have a higher potential impact and general utility and was therefore selected as the point of emphasis.

4.4 Conclusion and Future Work

A method for encapsulating a ^{99m}Tc-tetrazine (**1**) in Pluronic F127 micelles was developed to produce mF127(**1**). The prepared micelles were 28 nm in size as determined by DLS which is consistent with the data for cargo loaded Pluronic micelles used for drug delivery. The mF127(**1**) were successful in increasing the blood half-life of the ^{99m}Tc-tetrazine ligand as demonstrated by a significant increase in blood concentrations at both 1

and 6 hours accompanied with decreased liver uptake at 6 h. However, when used in conjunction with the TCO-BP targeting vector and a pre-targeting strategy, the increase in circulation time did not translate to increased bone uptake.

4.5 References

1. Takebe, T., Imai, R. & Ono, S. The Current Status of Drug Discovery and Development as Originated in United States Academia: The Influence of Industrial and Academic Collaboration on Drug Discovery and Development. *Clin. Transl. Sci.* **11**, 597–606 (2018).
2. McNeil, S. E. Nanoparticle therapeutics: A personal perspective. *Wiley Interdiscip. Rev. Nanomedicine Nanobiotechnology* **1**, 264–271 (2009).
3. Blanco, E., Shen, H. & Ferrari, M. Principles of nanoparticle design for overcoming biological barriers to drug delivery. *Nat. Biotechnol.* **33**, 941–951 (2015).
4. Datta, P. & Ray, S. Nanoparticulate formulations of radiopharmaceuticals: Strategy to improve targeting and biodistribution properties. *J. Label. Comp. Radiopharm.* **63**, 333–355 (2020).
5. Bobo, D., Robinson, K. J., Islam, J., Thurecht, K. J. & Corrie, S. R. Nanoparticle-Based Medicines: A Review of FDA-Approved Materials and Clinical Trials to Date. *Pharm. Res.* **33**, 2373–2387 (2016).
6. Sezgin, Z., Yüksel, N. & Baykara, T. Preparation and characterization of polymeric micelles for solubilization of poorly soluble anticancer drugs. *Eur. J. Pharm. Biopharm.* **64**, 261–268 (2006).

7. Bohorquez, M., Koch, C., Trygstad, T. & Pandit, N. A Study of the Temperature-Dependent Micellization of Pluronic F127. *J. Colloid Interface Sci.* **216**, 34–40 (1999).
8. Zhang, W. J. *et al.* Synthesis and Characterization of Thermally Responsive Pluronic F127-Chitosan Nanocapsules for Controlled Release and Intracellular Delivery of Small Molecules. *ACS Nano* **4**, 6747–6759 (2010).
9. Oerlemans, C. *et al.* Polymeric micelles in anticancer therapy: Targeting, imaging and triggered release. *Pharm. Res.* **27**, 2569–2589 (2010).
10. Kabanov, A. V, Batrakova, E. V & Alakhov, V. Y. Pluronic[®] block copolymers as novel polymer therapeutics for drug and gene delivery. *J. Control. Release* **82**, 189–212 (2002).
11. Wang, H. *et al.* Pluronic F127-based micelles for tumor-targeted bufalin delivery. *Int. J. Pharm.* **559**, 289–298 (2019).
12. Shah, N., Chaudhari, K., Dantuluri, P., Murthy, R. S. R. & Das, S. Paclitaxel-loaded PLGA nanoparticles surface modified with transferrin and Pluronic((R))P85, an in vitro cell line and in vivo biodistribution studies on rat model. *J. Drug Target.* **17**, 533–42 (2009).
13. Tao, Y., Han, J., Wang, X. & Dou, H. Nano-formulation of paclitaxel by vitamin E succinate functionalized pluronic micelles for enhanced encapsulation, stability and cytotoxicity. *Colloid Surface B* **102**, 604–610 (2013).
14. Song, H. *et al.* Anti-HIF-1 antibody-conjugated pluronic triblock copolymers encapsulated with Paclitaxel for tumor targeting therapy. *Biomaterials* **31**, 2302–

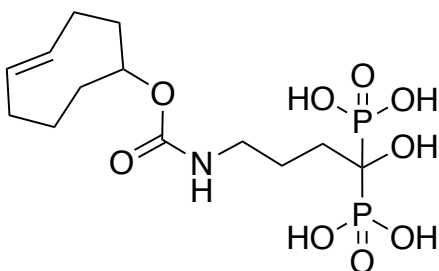
- 2312 (2010).
15. Wang, Y., Yu, L., Han, L., Sha, X. & Fang, X. Difunctional Pluronic copolymer micelles for paclitaxel delivery: Synergistic effect of folate-mediated targeting and Pluronic-mediated overcoming multidrug resistance in tumor cell lines. *Int. J. Pharm.* **337**, 63–73 (2007).
 16. Zhang, W. *et al.* Multifunctional Pluronic P123/F127 mixed polymeric micelles loaded with paclitaxel for the treatment of multidrug resistant tumors. *Biomaterials* **32**, 2894–2906 (2011).
 17. Liu, Z., Liu, D., Wang, L., Zhang, J. & Zhang, N. Docetaxel-Loaded pluronic P123 polymeric micelles: In vitro and in vivo evaluation. *Int. J. Mol. Sci.* **12**, 1684–1696 (2011).
 18. Valle, J. W. *et al.* A phase 2 study of SP1049C, doxorubicin in P-glycoprotein-targeting pluronics, in patients with advanced adenocarcinoma of the esophagus and gastroesophageal junction. *Invest. New Drugs* **29**, 1029–1037 (2011).
 19. Cao, A. *et al.* Multifunctionalized Micelles Facilitate Intracellular Doxorubicin Delivery for Reversing Multidrug Resistance of Breast Cancer. *Mol. Pharm.* **16**, 2502–2510 (2019).
 20. Marin, A. *et al.* Drug delivery in pluronic micelles: Effect of high-frequency ultrasound on drug release from micelles and intracellular uptake. *J. Control. Release* **84**, 39–47 (2002).
 21. Munshi, N., Rapoport, N. & Pitt, W. G. Ultrasonic activated drug delivery from Pluronic P-105 micelles. *Cancer Lett.* **118**, 13–19 (1997).

22. Rapoport, N. Stabilization and activation of Pluronic micelles for tumor-targeted drug delivery. *Colloid Surface B* **16**, 93–111 (1999).
23. Sleijfer, S., Seynaeve, C. & Verweij, J. Using Single-Agent Therapy in Adult Patients with Advanced Soft Tissue Sarcoma Can Still Be Considered Standard Care. *Oncologist* **10**, 833–841 (2005).
24. Danson, S. *et al.* Phase I dose escalation and pharmacokinetic study of pluronic polymer-bound doxorubicin (SP1049C) in patients with advanced cancer. *Br. J. Cancer* **90**, 2085–2091 (2004).
25. Zhao, Y. *et al.* Eradication of cancer stem cells in triple negative breast cancer using doxorubicin/pluronic polymeric micelles. *Nanomed-Nanotechnol* **24**, 102124 (2020).
26. Zhang, Y. *et al.* Surfactant-Stripped Micelles of Near Infrared Dye and Paclitaxel for Photoacoustic Imaging Guided Photothermal-Chemotherapy. *Small* **14**, 1802991 (2018).
27. Valluru, K. S. & Willmann, J. K. Clinical photoacoustic imaging of cancer. *J. Ultrason.* **35**, 267–280 (2016).
28. Zhang, Y. Y. *et al.* Non-invasive multimodal functional imaging of the intestine with frozen micellar naphthalocyanines. *Nat. Nanotechnol.* **9**, 631–638 (2014).
29. Laan, A. C. *et al.* Radiolabeling polymeric micelles for in vivo evaluation: a novel, fast, and facile method. *EJNMMI Res.* **6**, 12 (2016).
30. Almeida, H., Amaral, M. H., Lobão, P. & Lobo, J. M. S. Pluronic® F-127 and Pluronic Lecithin Organogel (PLO): main features and their applications in topical

- and transdermal administration of drugs. *J. Pharm. Pharm. Sci.* **15**, 592–605 (2012).
31. Yazdani, A. *et al.* A Bone-Seeking trans -Cyclooctene for Pre-targeting and Bioorthogonal Chemistry: A Proof of Concept Study Using ^{99m}Tc- and ¹⁷⁷Lu-Labeled Tetrazines. *J. Med. Chem.* **59**, 9381–9389 (2016).
 32. Bilton, H. A., Ahmad, Z., Janzen, N., Czorny, S. & Valliant, J. F. Preparation and Evaluation of ^{99m}Tc-labeled Tridentate Chelates for Pre-targeting Using Bioorthogonal Chemistry. e55188 (2017). doi:doi:10.3791/55188
 33. Zhang, Y. *et al.* Therapeutic surfactant-stripped frozen micelles. *Nat Commun* **7**, 11649 (2016).
 34. Managa, M., Pitchou Ngoy, B., Mafukidze, D. & Nyokong, T. Incorporation of metal free and Ga 5,10,15,20-tetrakis(4-bromophenyl) porphyrin into Pluronic F127-folic acid micelles. *J. Lumin.* **194**, 739–746 (2018).
 35. Lam, Y.-M., Grigorieff, N. & Goldbeck-Wood, G. Direct visualisation of micelles of Pluronic block copolymers in aqueous solution by cryo-TEM. *Phys. Chem. Chem. Phys.* **1**, 3331–3334 (1999).
 36. Akash, M. S. H. & Rehman, K. Recent progress in biomedical applications of pluronic (PF127): Pharmaceutical perspectives. *J. Control. Release* **209**, 120–138 (2015).
 37. Kattimani, V. S., Kondaka, S. & Lingamaneni, K. P. Hydroxyapatite—Past, Present, and Future in Bone Regeneration. *Bone Tissue Regen. Insights* **7**, BTRI.S36138 (2016).
 38. Bandyopadhyay-Ghosh, S. Bone as a collagen-hydroxyapatite composite and its

repair. *Trends Biomater. Artif. Organs* **22**, 112–120 (2008).

4.6 Supplemental Information



20

Figure S4.1. Structure of compound **20** (TCO-BP) used in pre-targeting experiment.

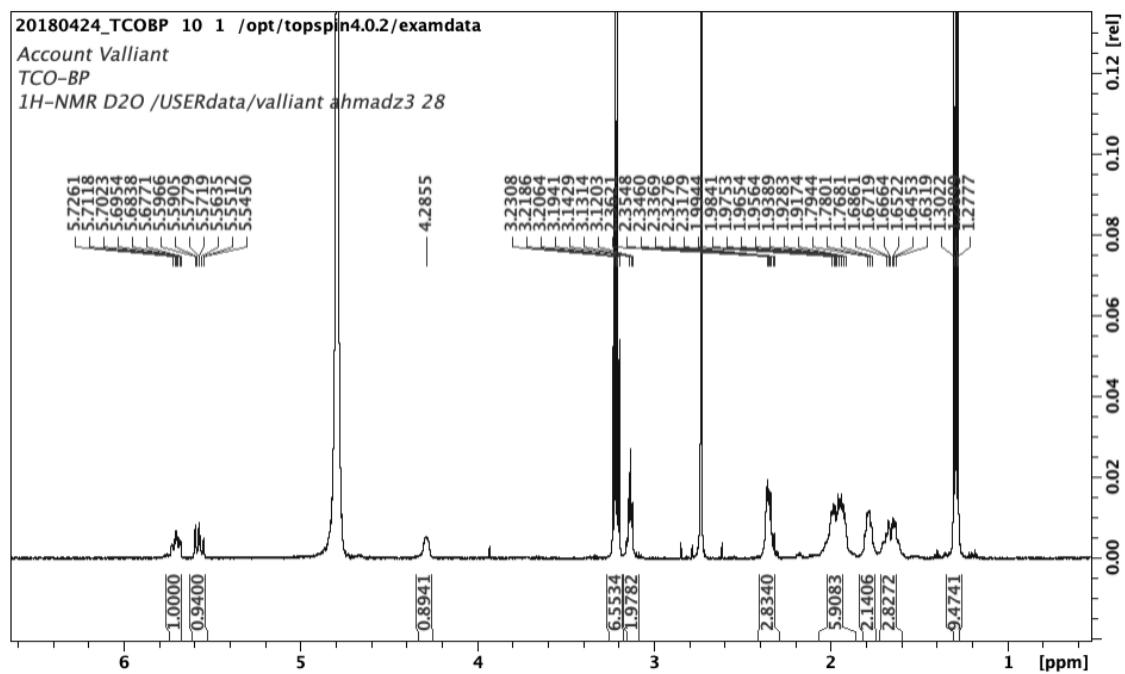


Figure S4.2. ^1H NMR (600 MHz, D_2O) of TCO-BP (**20**).

Chapter 5: TCO-Functionalized Pluronic F127 Micelles as a Platform for Targeted Drug Delivery

Zainab Ahmad¹, Afaf Genady¹, Rowan Swann¹, Samantha Slikboer¹, Amber Faraday¹, Nancy Janzen¹, John F. Valliant¹.

¹*Department of Chemistry and Chemical Biology, McMaster University, 1280 Main Street West, Hamilton, Ontario, L8S 4M1, Canada.*

Note that the following chapter is formatted as a manuscript for publication in the Journal of Controlled Release.

In terms of contributions, Dr. Afaf Genady was responsible for the development of the tetrazine derived bisphosphonate (TzBP), while Rowan Swann, Samantha Slikoboer, Amber Faraday, and Nancy Janzen were responsible for the planning and execution of the *in vivo* photoacoustic imaging experiments. All other work was performed by the author.

1. Abstract

Targeted micelles are being explored as tools for drug delivery notably to increase bioavailability and reduce unwanted side effects. Generally prepared through modification of the polymer backbone with a targeting biomolecule, this approach is cumbersome and results in single use micelles able to bind one specific target. As an alternative, more modular approach, a micelle-platform that can be readily modified with a variety of targeting biomolecules was developed. To this end, *trans*-cyclooctene (TCO)-functionalized micelles were prepared to be used in conjunction with tetrazine-derived

targeting vectors to take advantage of the rapid and irreversible inverse electron demand Diels-Alder (IEDDA) reaction. Pluronic F127-TCO polymers were synthesized in > 70 % yield and characterized by ^1H NMR spectroscopy where in aqueous media arising micelles were found to ~20-25 nm in size. To evaluate the platform, a tetrazine-derived bisphosphonate (TzBP) was developed and used as a targeting vector to promote binding to the hydroxyapatite (HA) which is a main component of bone. The F127-TCO micelles modified with TzBP exhibited a 4-fold increase in binding to HA *in vitro* compared to the no-salt control. *In vivo*, a 6.6-fold increase in bone uptake was observed when the F127-TCO micelles were tagged with [$^{99\text{m}}\text{Tc}$]TcTzBP compared to a tetrazine with no targeting vector. This data suggests that the TCO-functionalized micelles are a promising platform for targeted delivery when used with a corresponding tetrazine targeting vector.

2. Introduction

Interest in micelle-based technologies has seen a resurgence recently as delivery platforms for gene therapies (miRNA, siRNA) and immunomodulators.[1–4] Micelles can improve pharmacokinetic (PK) properties, notably improving bioavailability and solubility, leading to enhanced therapeutic efficacy and decreased toxicity.[5,6] Feng *et al.* reported a targeted mixed micellar system for delivery of antifibrotic genes (miRNA-29) in animal models which significantly reduced the progressive fibrosis in intervertebral discs, a characteristic of intervertebral disc degeneration (IDD).[7] The injectable formulation of miRNA-29 would be an appreciable alternative to surgical intervention for IDD treatment.

Intrinsic accumulation of micelles, and most nanoparticles (< 400 nm), in tumour tissues via the enhanced permeability and retention (EPR) effect is a characteristic that has

been extensively exploited for drug delivery. [8–10] The leaky vasculature of tumours as a result of rapid, uncontrolled growth leads to fenestrations between endothelial cells of the blood vessels which creates a pathway for the micelles to infiltrate the tumour tissue. Furthermore, the poor lymphatic drainage system of tumours also promotes retention of the micelles within the tissue for payload release. However, relying on the EPR effect has its limitations, notably lack of homogenous drug delivery, incomplete reduction of side effects and enhanced drug resistance.[11] Rather than simply relying on passive accumulation for cancer applications, there is a shift towards using biomarker-modified micelles for targeted delivery by adding targeting moieties for tumour-specific biomarkers to the polymeric backbone of the micelles.[12–16] Recently, Wei *et al.* successfully developed synergistic polymeric micelles for enhanced chemo-immunotherapy that delivered doxorubicin (DOX) and also targeted tumour-associated macrophages.[17] *In vivo*, these micelles significantly increased cytokine production which combined with the DNA damage caused by DOX, resulted in an 80 % survival rate in mice after 46 days of treatment. Functionalized micelles for targeted delivery are largely in the preclinical stage and have yet to make it to clinic for oncological purposes.[18–21]

Pluronic (ABA poly(oxyethylene)-poly(oxypropylene) block copolymers) are FDA-approved, bio-compatible, amphiphilic copolymers arranged as a triblock: EO_x-PO_y-EO_x (EO= oxyethylene, PO= oxypropylene).[22,23] Pluronic polymers are also unique in their ability to inhibit the P-glycoprotein (P-gp) drug efflux transport system involved in multidrug resistance (MDR). Therefore, these polymers are excellent candidates for use in developing tumour-targeting micelles. Pluronic micelles have been successfully

functionalized with different types of targeting moieties.[24] Substituents ranging from large biomolecules such as heparin and chitosan to small molecules like folate and vitamin E derivatives have been explored with mixed results. [9,16,24] The one common theme in these publications is that the addition of targeting molecules to the Pluronic polymer is nontrivial where biomolecule specific synthesis and purification procedures were required for each micelle construct.

An alternative and more modular approach is to use bioorthogonal chemistry to create targeted micelles. A particularly effective bioorthogonal reaction is the [4+2] inverse electron demand Diels-Alder (IEDDA) cycloaddition reaction between tetrazines and *trans*-cyclooctene (TCO).[25] This reaction has fast kinetics ($k_2 = 6 \times 10^3 \text{ M}^{-1}\text{s}^{-1}$, $t_{1/2} = 2.8$ min in PBS), is irreversible, highly selective, and has been used successfully *in vitro* and *in vivo*. [25,26] In 2010, Weissleder *et al.* demonstrated the versatility of this reaction by applying it to nanoparticles.[27] Using tetrazine-modified magneto-fluorescent nanoparticles (Tz-MFNPs), they reported higher nanoparticle binding to cells when the MFNPs were administered using a pre-targeting approach (TCO-antibodies followed by Tz-MFNPs) compared to direct conjugation of MFNPs to the same antibodies. Emmetiere *et al.* developed F-18 tagged TCO-liposomes ($[^{18}\text{F}]\text{F-TCO-liposomes}$) which accumulated preferentially in tetrazine-tagged ovarian tumours ($3.5 \pm 1.3 \text{ \% ID/g}$) compared to the untreated tumour ($0.46 \pm 0.04 \text{ \% ID/g}$) at 2 h post-intravenous injection.[28] However higher uptake in the liver ($12.8 \pm 2.0 \text{ \% ID/g}$) and intestines ($16.0 \pm 8.0 \text{ \% ID/g}$) was also observed. van Onzen *et al.* reported a TCO-functionalized small molecule based nanoparticle (TCO-SMNP) consisting of short, pi-conjugated oligomers.[29] The

distribution of the TCO-SMNPs was assessed using an In-111 labelled DOTA-tetrazine ($[^{111}\text{In}]\text{In-DOTA-Tz}$) which demonstrated rapid clearance from the blood and uptake in the liver and spleen. PET imaging by Goos *et al.* showed low tumour and high kidney uptake of TCO-modified nanostars when evaluated with a radio-fluorinated NODA-tetrazine ($[^{18}\text{F}]\text{F-NODA-Tz}$) through a pre-targeting strategy.[30] Kramer *et al.* prepared tetrazine-modified micelles, used in conjunction with TCO-antibodies, and showed that the second order rate constant for the tetrazine-TCO reaction was not significantly different for polymers compared to small molecules.[31] With these promising results, further research regarding the TCO-tetrazine reaction and its application with nanoparticles is of great interest to us.

To this end, a method to prepare TCO-functionalized Pluronic F127 polymers was developed to enable the facile addition of targeting vectors to micelles (Fig 1). This modular approach not only allows for tagging micelles with a wide array of targeting molecules, it can also be used to add radiolabelled or fluorophore-modified tetrazines which make it possible to assess new micelles through quantitative biodistribution and *in vivo* imaging studies.

3. Materials and Methods

3.1. General methods, materials and instrumentation

Unless otherwise stated, all reagents were used as obtained from the supplier without further purification. Solvents were purchased from Caledon and Sigma Aldrich. Deuterated solvents were purchased from Cambridge Isotope Laboratories. 99m-

Pertechnetate [$^{99m}\text{TcO}_4^-$] was obtained from the McMaster University Medical Centre Radiopharmacy in saline from a $^{99}\text{Mo}/^{99m}\text{Tc}$ generator. Potassium sodium tartrate ($\text{KNaC}_4\text{H}_4\text{O}_6 \cdot 4\text{H}_2\text{O}$) and sodium borate ($\text{Na}_2\text{B}_4\text{O}_7 \cdot 10\text{H}_2\text{O}$) were acquired from Achemia Canada Inc., while sodium carbonate (Na_2CO_3) was acquired from EM science.

Microwave reactions were performed on a Biotage Initiator 60 microwave reactor. Nuclear magnetic resonance spectra (^1H , COSY, NOESY) were documented on Bruker AV600 or AV800 spectrometers and analyzed using TopSpin NMR software. For these analyses approximately 8-10 mg of each compound was dissolved in 500-600 μL of CDCl_3 . Dynamic light scattering data was obtained on a Malvern Zetasizer Nano ZS (ZEN3600) with a 175° backscattering angle. Transmission electron microscopy images were obtained at the Canadian Centre for Electron Microscopy at McMaster University using a Philips CM 12 (LaB6 filament, 120 keV, magnification 30-660 000 \times) TEM instrument.

Unless otherwise specified, purification of compounds was performed using Silica Gel 60 (particle size 0.04-0.063 mm) from EMD chemicals. Purification of compounds was also performed using the Biotage SP1 flash purification system with Biotage flash cartridges and loading samplets. Radiolabelled compounds were purified and analyzed using HPLC on a Waters 1525 Binary (Midford, MA, USA) monitored using 2998 Photodiode Array detector at 254 nm in line with a Bioscan gamma detector with NaI (T1) scintillator and data analyzed using the Empower software package. The analytical Waters X-bridge C-18 column (100 mm \times 4.6 mm \times 5 μm) operating at 1 mL/min and semi-preparative Waters X-bridge C-18 column (100 mm \times 10 mm \times 5 μm) operating at 4 mL/min were used. The solvents used for HPLC were A: H_2O + 0.1 % trifluoroacetic acid

(TFA), B: acetonitrile + 0.1 % TFA. Elution gradient: 95- 50% B (0-12 min), 50- 95% B (12-15 min), 95- 5 % B (15-21 min), 5% B (21-22 min). Solvents were evaporated using a rotary evaporator under reduced pressure or via the Biotage V10 solvent evaporation system. Compounds were lyophilized using VirTis Benchtop lyophilizer fitted with an Edwards RV5 pump. TLC analysis was performed using iTLC-SG glass microfiber chromatography paper (Agilent Technologies, SGI0001) plates using distiller water or acetone as the eluent and visualized on a Bioscan AR2000 Imaging Scanner. For each TLC, plates were spotted with $\sim 2 \mu\text{L}$ (3.7 kBq) of sample.

3.2. Animal Studies

Animal studies were approved by the Animal Research Ethics Board (AREB) at McMaster University in accordance with Canadian Council on Animal care (CCAC) guidelines. Biodistribution studies were performed using healthy CD1 mice (Charles River Laboratories, Kingston, NY). Photoacoustic imaging was performed using Vevo LAZR-X (FUJIFILM VisualSonics Inc., Toronto, ON, Canada) imaging system equipped with a 680-970 nm laser. For *in vivo* imaging, mice were anaesthetized with 3 % isoflurane and 2 % oxygen, and set up on a platform that monitored the respiration rate and the heart rate of the mouse. The hair on the hindlimb was removed using Nair™ for Sensitive Skin while the mouse was anaesthetized. A 30-MHz, linear array ultrasound transducer with integrated fiber optic light delivery (LZ-400 and MX-400, FUJIFILM VisualSonics, Inc.) was positioned laterally overtop the hindlimb knee joint. The integrated fiber bundle delivered 15 to 20 mJ/cm^2 of light to the hindlimb of the mouse. For *ex vivo* imaging, organs were

submerged in MilliQ water in a Vevo Phantom imaging chamber (Fujifilm VisualSonics Inc., Toronto).

3.3. Chemical Synthesis

3.3.1. Preparation of carbonyldiimidazole-activated Pluronic F127 polymers

(F127-CDI, 1).[9]

F127-CDI (**1**) was synthesized according to a previously reported method.[9] Briefly, Pluronic F127 (6.4 g, 0.51 mmol) was purified by dissolving in acetone and precipitating into ice-cold hexanes. The precipitate was collected through vacuum filtration after washing with excess ice-cold hexanes. Purified F127 was subsequently dissolved in anhydrous ACN (7.5 mL) and carbonyldiimidazole (CDI) (0.82 g, 5.1 mmol) in anhydrous ACN (7.5 mL) added dropwise over 2 hours. The reaction was left to stir for an additional 4 hours at room temperature. The reaction mixture was concentrated and washed with diethyl ether (3 × 30 mL) and collected using vacuum filtration yielding a white solid (4.6 g, 71 %).

3.3.2. Preparation of amine-functionalized Pluronic F127 polymers (F127-

NH₂, 2). [32]

F127-CDI (2.0 g, 0.16 mmol) was dissolved in dry ACN (3.5 mL) and added dropwise to excess ethylene diamine (2.5 mL) at room temperature over 2 h. The reaction was stirred at room temperature overnight, followed by removal of excess ethylene diamine under reduced pressure. The residue was collected by filtration and washed with diethyl ether (3 × 30 mL) yielding F127-NH₂ (**2**) as a fine white powder (1.4 g, 70 %).

3.3.3. Preparation of TCO-functionalized Pluronic F127 polymers (F127-TCO, 3).

For this synthesis, all reagents and solvent were stored and handled under argon. F127-NH₂ (50.4 mg, 0.00391 mmol) was combined with *trans*-cyclooctene (TCO) NHS-ester (20.9 mg, 0.0794 mmol), and DIPEA (50 μ L, 0.287 mmol) in anhydrous DMF (1 mL). The reaction mixture was stirred overnight at room temperature. DMF was removed under vacuum and the sample re-dissolved in MeOH (3 mL). F127-TCO was purified using a GE Vivaspin 6, 5-6 kDa MWCO sample concentrator. The Vivaspin column was first rinsed with MeOH (4 mL) (10 min \times 4000 rpm), and the F127-TCO solution subsequently centrifuged (20 min \times 4000 rpm \times 3) with additional MeOH (5 mL) for each cycle. The concentrated sample was retrieved from the Vivaspin column and dried using rotary evaporation yielding a thin film. The film was dissolved in Nanopure water and lyophilized overnight, yielding a white solid (42.8 mg, 82 %).

3.3.4. Preparation of 2,5-Dioxopyrrolidin-1-yl-5-((4-(1,2,4,5-tetrazin-3-yl)-benzyl) amino)-5-oxopentanoate) (TzNHS, 4).

Glutaric anhydride (27.2 mg, 0.238 mmol) was added to a stirring solution of (4-(1,2,4,5-tetrazin-3-yl)phenyl)methanamine hydrochloride (50.0 mg, 0.223 mmol) and Et₃N (120 μ L, 0.681 mmol) in DCM (1 mL). The reaction mixture was stirred for 1.5 h at room temperature. N, N'-disuccinimidyl carbonate (DSC) (86.9 mg, 0.339 mmol) was added, and the reaction mixture was stirred for an additional 1.5 h at room temperature. The product was isolated using silica column chromatography using 5 % MeOH/DCM, yielding TzNHS as a pink solid (78.1 mg, 88 %). ¹H NMR (600 MHz, CDCl₃): δ (ppm) 10.24 (s, 1

H), 8.61 (d, $J= 8.3$ Hz, 2 H), 7.56 (d, $J= 8.3$ Hz, 2 H), 6.46 (b, 1 H), 4.60 (d, $J= 5.9$ Hz, 2 H), 2.83 (t, $J= 7.3$ Hz, 2 H), 2.73 (t, $J= 6.8$ Hz, 2 H), 2.43 (d, $J= 7.1$ Hz, 2 H), 2.20 (dt, $J= 6.8, 7.3$ Hz, 2 H), 1.24 (d, $J= 6.6$ Hz, 2H).

3.3.5. Preparation of (4-(5-((4-(1,2,4,5-tetrazin-3-yl)benzyl)amino)-5-oxopentanamido)-1-hydroxybutane-1,1-diyl)diphosphonic acid (TzBP, 5).

TzNHS (15.3 mg, 0.0384 mmol) was dissolved in DMSO (1 mL) and added slowly to a premixed solution of alendronic acid (14.3 mg, 0.0574 mmol) and Et₃N (30 μ L, 0.215 mmol in 0.5 mL H₂O). The reaction mixture was stirred for 2 h at room temperature. The product was isolated by semi-preparative HPLC using a Polar-RP column and the solvent removed by rotary evaporation. The product was dried under high vacuum yielding TzBP as a pink oil (18 mg, 83%) $R_t= 10.4$ min. ¹H NMR (600 MHz, MeOD): δ (ppm) 10.31 (s, 1 H), 8.56 (d, $J= 8.3$ Hz, 2 H), 7.57 (d, $J= 8.3$ Hz, 2 H), 4.50 (s, 2 H), 3.20 (m, 4 H), 2.32 (t, $J= 7.3$ Hz, 2 H), 2.25 (t, $J= 7.3$ Hz, 2 H), 1.95 (t, $J= 7.3$ Hz, 2 H), 1.90 (m, 2 H).

3.3.6. Preparation of technetium-99 m (4-(5-((4-(1,2,4,5-tetrazin-3-yl)benzyl)amino)-5-oxopentanamido)-1-hydroxybutane-1,1-diyl)diphosphonic acid ([^{99m}Tc]TcTzBP, 6).

A solution of TzBP (3 mg in 0.5 mL saline) was combined with 100 μ L of a solution of SnCl₂ (1 mg/mL in 0.5 M HCl) and 150 μ L [^{99m}Tc]TcO₄⁻ (307.1 MBq) added. The pH was adjusted to 6.0 by dropwise addition of PBS (340 μ L, 0.2 M, pH 8) and the solution adjusted to a total volume of 1.5 mL with saline, followed by mixing for 45 min at room

temperature. [^{99m}Tc]TcTzBP was obtained in 88 % radiochemical yield and 88 % purity as determined by iTLC.

**3.3.1. Preparation of (technetium-99m 6-{bis[(2- pyridyl)methyl]amino}-1-
({[p-(1,2,4,5- tetrazin-3- yl)phenyl]methyl}amino)-1- hexanone)
([^{99m}Tc]TcTzPy, 7).**

[^{99m}Tc]TcTzPy was synthesized according to a previously reported literature method.[33]. Briefly, [^{99m}Tc]TcO₄⁻ (1100 MBq in 0.9 % saline) was reduced to [^{99m}Tc]Tc(CO)₃(OH₂)₃⁺ using K₂[BH₃CO₂] salt as the CO source. [^{99m}Tc (CO)₃(OH₂)₃]⁺ (500 MBq) was then combined with the tetrazine precursor (TzPy) (0.3 mg) in MeOH (0.5 mL) and the mixture heated in the microwave for 20 minutes at 60 °C. The labelled compound was purified using HPLC using the published method and dried using a Biotage V10 solvent evaporation system. R_t =10 min, > 99 % radiochemical purity and 83 % radiochemical yield.

3.4. Quantification of reactive TCO groups on F127-TCO

In triplicate, (4-(1,2,4,5-tetrazin-3-yl)phenyl)methanamine hydrochloride (compound **1**) in dH₂O (100 μL, 0.02-0.16 mmol (0.2- 0.16 mM), 0.1 mmol increments) was combined with F127-TCO (4 × 10⁵ mmol (0.4 mM, 100 μL)) in each well and incubated for 5 min at room temperature. Following this, the absorbance signal at 540 nm (λ_{max} of **1**) was monitored using a TECAN M200 plate reader. Absorbance for dH₂O was used as a blank for background subtraction. The number of reactive TCO groups was quantified using equation 1 where 'x' refers to the moles of compound **1** used to reach the

equivalence point during titration and $8 \times 10^{-5} \text{ mmol}$ is the amount of **1** needed to reach equivalence point for a F127-TCO polymer with two TCO groups.

$$\# \text{ of reactive TCO} = \frac{x}{8 \times 10^{-5} \text{ mmol}} \quad (1)$$

3.5. Characterization of F127-TCO Micelles (mF127-TCO)

3.5.1. Encapsulation of IR 780 in mF127-TCO (mF127-TCO(IR780))

Micellar solutions (mF127-TCO) were prepared as a mixture of 10 % F127-TCO polymers and unfunctionalized F127 polymers in aqueous solution (saline, PBS or dH₂O) to total polymer concentration of 10% w/v following a literature procedure.[34,35] IR 780 iodide (1 mg) was dissolved in DCM (1 mL) and added dropwise to a stirring aqueous solution of mF127-TCO and left to stir overnight to allow the DCM to evaporate. Subsequently, the micelles were cooled on ice for 30 min followed by purification via centrifugal filtration (100 kDa MWCO, 4000 rpm \times 25 min \times 3) at 4 °C. The concentrated micelles (~250 μ L) were reconstituted in saline (3 mL) resulting in a golden-brown solution (mF127-TCO(IR780)) that was filtered through a 0.2 μ m syringe filter.

3.5.2. Dynamic Light Scattering

The size distribution of mF127-TCO(IR780) was measured via dynamic light scattering using a Malvern Zetasizer Nano ZS (ZEN3600) with a 175° scattering angle with a 633 nm laser and at 25 °C. mF127-TCO(IR780) were prepared as described above and filtered using a 0.2 μ m syringe filter prior to measurement. Measurements are reported as distribution by volume. A 50 nm Au nanoparticle (Cat# 753629, Sigma Aldrich) solution was used as a standard: measuring at 54 ± 17 nm with a PDI value of 0.078. The stability

of the mF127-TCO(IR780) was measured by DLS up to 48 h where the product was stored at 4 °C between measurements.

3.5.3. Transmission Electron Microscopy

Transmission electron microscopy (TEM) was conducted using a Philips CM12. The sample was prepared as described above. mF127-TCO(IR780) (< 10 µL) was spotted on a copper grid and stained with a 1% uranyl acetate solution for microscopy.

3.6. Calcium Salt (Hydroxyapatite, HA) Binding Assay

A stock solution of mF127-TCO(IR780) (6 mL) was prepared and split in half, and combined with either TzBP (0.5 mL, 0.01 mM in saline) or just saline (0.5 mL). Samples were incubated for 30 min at room temperature yielding TzBP-mF127-TCO(IR780) and mF127-TCO(IR780) (negative control), respectively. The protocol for measuring binding to HA was performed according to a literature method. [36] Briefly, in triplicate, 250 µL of either TzBP-mF127-TCO(IR780) or mF127-TCO(IR780) was added to 1.25 mL of 1 mg/mL solutions of hydroxyapatite (BioRad) in 50 mM Tris pH 6.9 buffer. A no HA salt control was also included using just Tris buffer. Samples were incubated with gentle shaking for 1 h at room temperature and then centrifuged (10000 rpm × 5 min). A 200 µL aliquot of the supernatant was taken and absorbance measured at 790 nm. The % binding was calculated using equation 2, where Abs_s is the absorbance of the supernatant for samples incubated with HA and the Abs_c is the absorbance of the supernatant for samples not incubated with HA (no salt control):

$$\% \text{ Binding} = \left[1 - \left(\frac{Abs_s}{Abs_c} \right) \right] * 100 \quad (2)$$

For the pre-targeting variation, 1.25 mL of 1 mg/mL solutions of hydroxyapatite (BioRad) in 50 mM Tris pH 6.9 buffer was combined with TzBP (0.5 mL, 0.01 mM in saline) or saline (0.5 mL). No-HA salt controls were prepared using 1.25 mL of 50 mM Tris pH 6.9 buffer and combined with TzBP (0.5 mL, 0.01 mM in saline) or saline (0.5 mL). Samples were incubated with gentle shaking for 1 h at room temperature and then centrifuged (10000 rpm \times 5 min). mF127-TCO(IR780) were prepared as described above and 250 μ L was added to all samples followed by incubation with gentle shaking for 1 h at room temperature and then centrifugation (10000 rpm \times 5 min). A 200 μ L aliquot of the supernatant was retrieved and absorbance measured at 790 nm. The % binding was calculated using equation 2 as described above. The incubation, centrifugation, and absorbance measurement processes were repeated after an additional 5 and 23 hours ($t= 6$ and 24 h post initial incubation).

3.7. *In vivo* Studies

3.7.1. Biodistribution of mF127-TCO labelled with [^{99m}Tc]TcTzPy

A solution of mF127-TCO was prepared as described above and combined with [^{99m}Tc]TcTzPy (14 MBq) under gentle stirring at room temperature for 30 min. Unbound [^{99m}Tc]TcTzPy was removed through centrifugal filtration (100 kDa, MWCO, 4000 rpm \times 20 min). [^{99m}Tc]TcTzPy-mF127-TCO (10.5 MBq) were recovered from the filter and diluted with saline (2.75 mL) for injections. Balb/C mice ($n=3$) were injected with [^{99m}Tc]TcTzPy-mF127-TCO (0.42-0.61 MBq) via tail-vein injection and biodistribution studies conducted at 1, 6, and 24 hours post-injection. At each time point, animals were anesthetized with 3 % isoflurane and euthanized by cervical dislocation and blood, adipose,

adrenals, blood, brain, gall bladder, heart, kidneys, large intestine, liver, lungs, pancreas, skeletal muscle, small intestine, spleen, stomach, thyroid/trachea, and urine and bladder were collected. The tissues and fluids were weighed and counted in a gamma detector. All radioactivity measurements were decay corrected and reported as % injected dose per gram (% ID/g).

3.7.2. Biodistribution of mF127-TCO(IR780) labelled with [^{99m}Tc]TcTzBP

A solution of mF127-TCO(IR780) was prepared as described above. [^{99m}Tc]TcTzBP (14.7 MBq) was prepared as described above and diluted with TzBP (6 mg/1 mL in saline) for biological work. The solution was incubated with mF127-TCO(IR780) under gentle stirring for 30 min at room temperature. Balb/C mice (n=3) were injected with [^{99m}Tc]TcTzBP-mF127-TCO(IR780) (0.37-0.59 MBq) via tail-vein injection. Biodistribution studies were conducted at 1, 4, and 24 hours post injection. At each time point, animals were anesthetized with 3% isoflurane and euthanized by cervical dislocation and blood, adipose, adrenals, bone (shoulder and knee joints), brain, gall bladder, heart, kidneys, large intestine, liver, lungs, pancreas, skeletal muscle, small intestine, spleen, stomach, thyroid/trachea, and urine and bladder were collected. The tissues and fluids were weighed and counted in a gamma detector. The measurements were decay corrected and reported as % ID/g.

3.7.3. Biodistribution of mF127-TCO(IR780) pre-targeted with [^{99m}Tc]TcTzBP

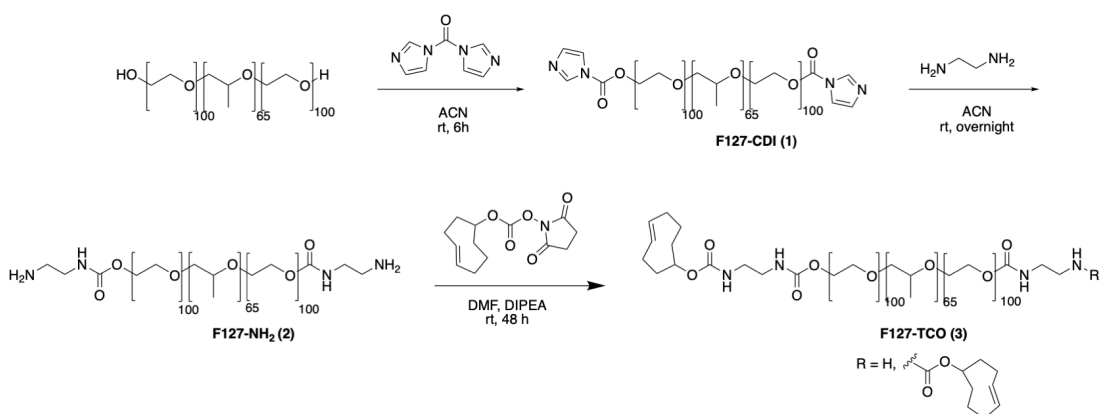
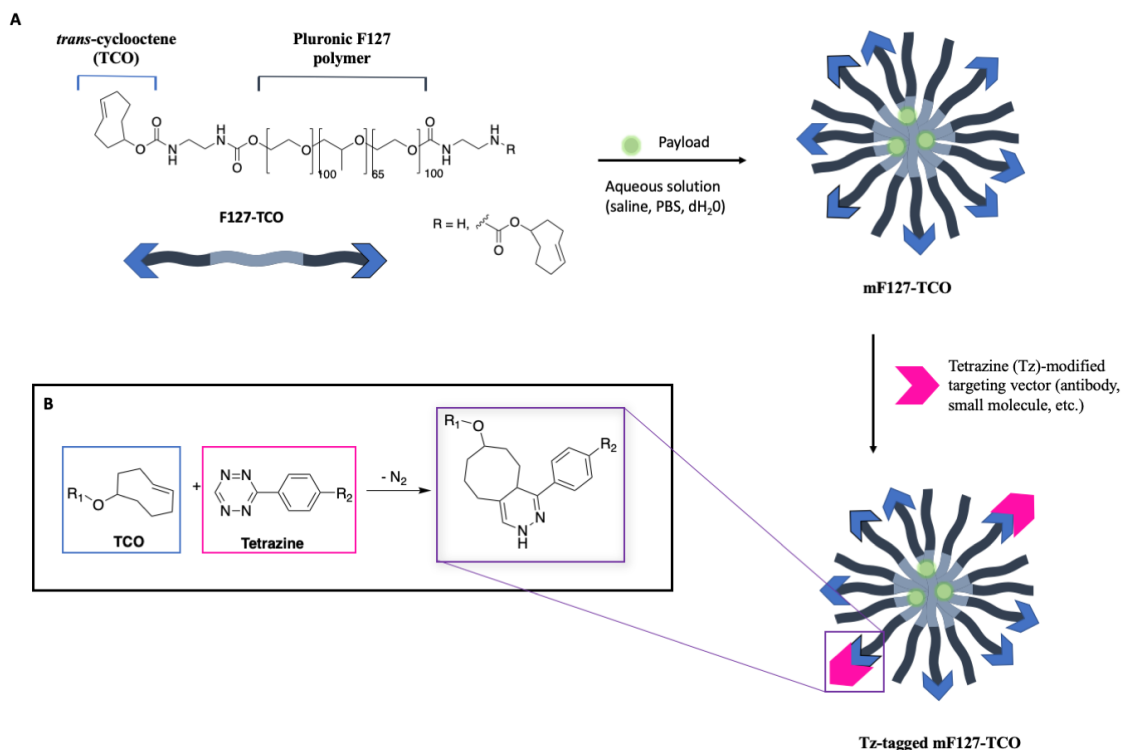
Solutions of mF127-TCO(IR780) and [^{99m}Tc]TcTzBP (15.6 MBq, diluted with TzBP (7 mg/ 1.1 mL) were prepared as described above. Mice were administered

[^{99m}Tc]TcTzBP (0.25- 0.55 MBq), followed by mF127-TCO(IR780) 1 hour later. Biodistribution studies were conducted at 1, 4, and 24 hours post injection. At each time point, animals were anesthetized with 3% isoflurane and euthanized by cervical dislocation and blood, adipose, adrenals, bone (shoulder and knee joints), brain, gall bladder, heart, kidneys, large intestine, liver, lungs, pancreas, skeletal muscle, small intestine, spleen, stomach, thyroid/trachea, and urine and bladder were collected. The tissues and fluids were weighed and counted in a gamma detector. The measurements were decay corrected and data analyzed using GraphPad Prism Version 8.4.2 (GraphPad Software, San Diego, CA, USA).

4. Results and Discussion

4.1. Synthesis of Pluronic F127-TCO Polymers

Following the method of Zhang *et al.*, Pluronic F127 polymers were treated with carbonyl diimidazole (CDI) to generate the synthetic intermediate (F127-CDI) (Fig 2). The product was isolated in a 71% yield by precipitation using ice-cold diethyl ether, collected by vacuum filtration and dried under vacuum. Subsequently, the amine-terminated polymer, F127-NH₂ was synthesized by adding excess ethylene diamine to F127-CDI which yielded the product in 70 % yield following the same purification procedure as the precursor (Fig 2). Characterization data for F127-CDI and F127-NH₂ matched that reported in the literature.[9] The F127-TCO modified polymer was obtained by combining F127-NH₂ with *trans*-cyclooctene (TCO) NHS-ester (TCO-NHS), followed by purification through multiple rounds of centrifugal filtration (5-6 kDa MWCO) to remove unreacted TCO-NHS (Fig 2).



TCO (600 MHz, CDCl₃), black squares correspond to carbamate protons, other peaks from ¹H NMR were at ppm= 1.13 (t, 3 H × 65, CH₃ group of PPO (**h**)), 1.69 (m, 2H, CH₂ of TCO ring (**e**)), 1.90 – 1.98 (m, 4 H, CH₂ of TCO ring (**k**, **d**)), 2.31-2.38 (m, 4H, CH₂ of TCO ring (**c**, **f**)), 2.46 (m, 2 H, CH₂ of ethylene linker (**m**)), 2.70 (m, 2H, CH₂ of ethylene linker (**l**)), 3.40 (m, 2 H × 65, CH₂ of PPO(**j**)), 3.54 (m, 1 H × 65, CH of PPO(**i**)), 3.64 (m, 2 H × 200, CH₂ of PEO(**n**)), 4.32 (m, 1 H, CH of TCO ring (**g**)).

4.2. Characterization of Pluronic F127-TCO Polymers

4.2.1. NMR Characterization

Detailed NMR characterization of modified Pluronic polymers is not commonly reported in the literature due to the difficulty in assigning the peaks which show minimal coupling interactions with neighboring protons or are overshadowed by the larger signal from the polymer backbone.[37] Nevertheless, it is critically important here to be able to confirm functionalization of the polymer backbone with the TCO group. ¹H NMR for F127-CDI showed characteristic aromatic peaks at 8.2 ppm (**a**), 7.5 ppm (**b**), and 7.1 ppm (**c**) associated with the imidazole group (Fig 3A). Following the treatment of F127-CDI with ethylenediamine, ¹H NMR of the product F127-NH₂ revealed the disappearance of the aromatic peaks of the imidazole groups and appearance of additional peaks associated with the ethylene groups: 2.83 (**a**) and 3.24 ppm (**b**), (Fig 3B). The ¹H NMR of Pluronic F127-TCO depicts peaks at 5.50 (**a**) and 5.54 ppm (**b**) which correspond to the olefinic ¹H of the TCO and at 2.46 (**m**) and 2.70 ppm (**l**) which correspond to the CH₂ groups of the ethylene linker (Fig 3C). Carbamate protons associated with the coupling of the TCO group gave rise to the peaks at 5.39 and 5.15 ppm, which were confirmed by 2D NMR notably a COSY spectrum (Fig S1). The presence of these carbamate protons suggests successful coupling of the amine with TCO-NHS.

4.2.2. Quantification of Reactive TCO Groups

The degree of TCO-functionalization of the Pluronic F127 polymers was determined following the isolation of F127-TCO. In triplicate, F127-TCO was titrated against increasing concentrations of (4-(1,2,4,5-tetrazin-3-yl)phenyl)methanamine hydrochloride, a commercially available tetrazine (compound 1). The amount of tetrazine in solution was monitored by measuring absorbance at 540 nm. The equivalence point is denoted by the sharp increase in absorbance corresponding to free tetrazine as a result of consumption of all the available TCO groups. As seen in the example titration in Fig 4, the equivalence point was identified at 0.11 mmol and equation 1 was used to calculate the number of reactive TCO groups per polymer. The data indicated 1.3 ± 0.2 TCO groups per polymer were available. Despite attempts at modifying the reaction parameters (molar ratios, temperature, time), it was not possible to increase the ratio further. This may be a result of a side reaction occurring between the nucleophile (F127-NH₂) and the endocyclic carbonyl of the TCO-NHS.[38,39] As a result of this nucleophilic attack, succinimidyl carbonates can undergo a Lossen rearrangement that would result in a terminal isocyanate (-NCO) group on the F127 polymer as opposed to the intended TCO group. Due to the minimal difference (< 100-200 Da) in the molecular weight of the F127-TCO product and F127-NCO by-product, they would not be separated during centrifugal filtration. Although the F127-NH₂ will still react preferentially at the exocyclic carbonyl of the TCO-NHS, this side reaction can reduce the intended degree of functionalization.

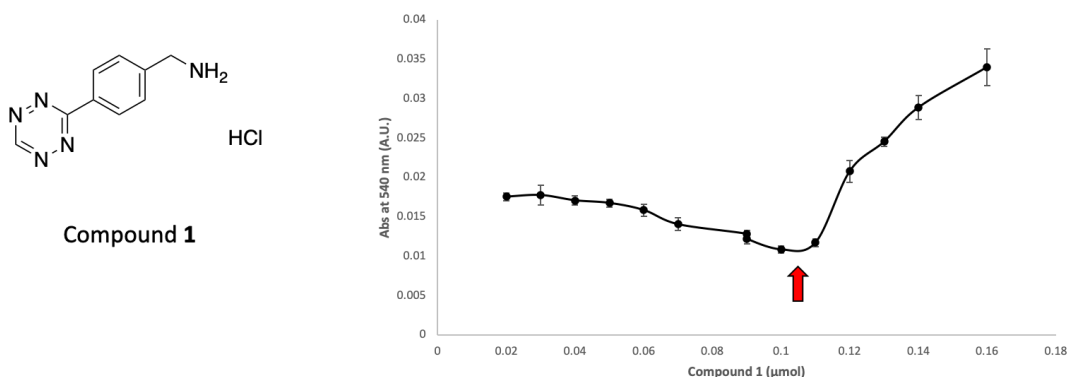


Fig 4. Example of titration curve showing UV absorption at 540 nm following the addition of F127-TCO polymer to increasing amounts of compound **1**. Conducted in triplicate. The red arrow delineates the equivalence point.

4.3. Characterization of mF127-TCO(IR780)

A near-IR dye (NIR), IR780 (Fig 5A) was encapsulated in F127-TCO micelles (mF127-TCO) using a procedure adapted from Zhang *et al.* to allow for photoacoustic imaging to be used to visualize bone uptake. [35] Briefly, IR780 was dissolved in DCM and added to a 10 % w/v stirring solution of mF127-TCO, and the mixture allowed to stir overnight to allow for the DCM to evaporate. The mixture was subsequently cooled on ice to remove unincorporated polymers by lowering the CMC, and subject to centrifugal filtration (MWCO=100 kDa) before reconstitution in 3 mL of saline. The prepared solution of IR780 in F127-TCO micelles (mF127-TCO(IR780)) was filtered through a 0.2 μm syringe filter to remove any large particulates prior to measurement. As determined by DLS, the mF127-TCO(IR780) were 25 ± 10 nm in size with a polydispersity index (PDI) value of 0.43 (Fig 5B), which is comparable to published data for Pluronic F127 micelles.[9,34] The wide distribution of micelle size is expected due to the free polymers

being in dynamic equilibrium with formed micelles.[18] Additionally, mF127-TCO(IR780) were imaged by TEM (Fig 5C) where the average size observed was approximately 20 nm which correlates with the DLS results. The variability between TEM and DLS results is expected as the samples are under different degrees of solvation during analysis, with the DLS sample being in solution while the TEM sample is dried on a copper grid.[40]

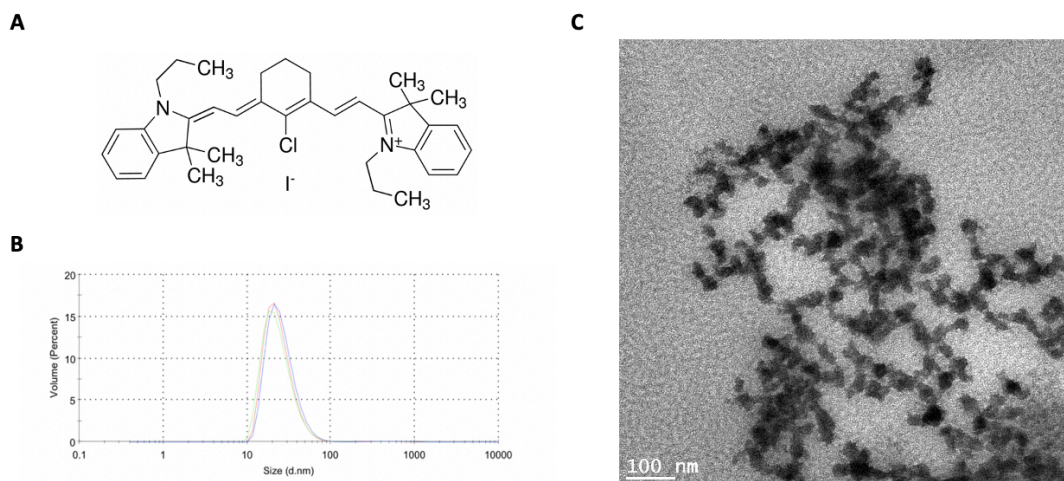


Fig 5. A) The hydrophobic NIR dye IR780 iodide that was encapsulated in mF127-TCO. B) Size distribution of mF127-TCO(IR780) (25 ± 10 nm) obtained by DLS and reported by % volume. C) Transmission electron microscopy image of Pluronic F127-TCO micelles (~ 20 nm).

4.4. Development of a Tetrazine-Derived Targeting Vector

While the majority of micelle based drug delivery systems have focused on solid tumours, strategies for targeting bone diseases is also of interest.[41–43] Bisphosphonates (BPs) (also known as diphosphonates), are a potential targeting vector, since drugs containing these groups are commonly used for the treatment of bone-related disorders.

[41–43] Disorders such as osteoporosis, multiple myeloma, Paget’s disease, and bone metastases are characterized by increased skeletal turnover.[44,45] BPs serve as potent inhibitors of bone resorption by binding to hydroxyapatite (HA), a calcium-containing compound present in bone, to promote apoptosis of osteoclasts which mediate the bone-resorption. These properties also make radiolabelled BPs well-suited for bone scintigraphy.[36] As an example, technetium-99m methyl diphosphonate ($^{99m}\text{Tc-MDP}$) is used clinically for SPECT imaging and the detection of bone metastases, osteomyelitis, as well as soft tissue tumours containing calcium deposits.[46] BP-derived micelles would offer a way to deliver therapeutic payloads to sites of bone lesions and fractures, and are a simple way to test the feasibility of using the IEDDA reaction with micelles.

4.4.1. Synthesis of Tetrazine Bisphosphonate (TzBP)

A tetrazine-derived bisphosphonate (TzBP) (Fig 6A) was synthesized to be used in conjunction with F127-TCO micelles. The ligand was prepared via a one pot reaction, where commercially available (4-(1,2,4,5-tetrazin-3-yl)phenyl)methanamine hydrochloride was combined with glutaric anhydride and the resulting carboxylic acid subsequently activated with DSC to form the activated ester (TzNHS). TzNHS was subsequently isolated by silica column chromatography in 88 % yield as a pink oil. Next, alendronic acid was added to TzNHS to afford the BP tetrazine derivative (TzBP) in 83 % yield after HPLC purification.

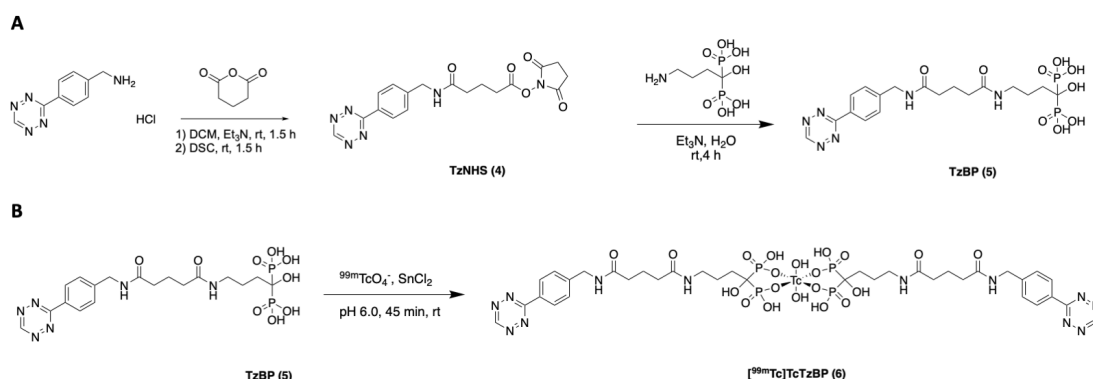


Fig 6. A) Synthesis of a tetrazine-derived targeting vector: TzBP. B) Radiolabelling of TzBP to form $[^{99m}\text{Tc}]\text{TcTzBP}$. The structure ^{99m}Tc -BPs has not been concretely identified but X-ray crystallography of ^{99}Tc -BPs suggests two BP groups coordinate to a single ^{99}Tc atom.[47]

4.4.2. Preparation of $[^{99m}\text{Tc}]\text{TcTzBP}$

To determine the ability of BP functionalized micelles to target regions of calcium turnover, a method to radiolabel TzBP was developed taking advantage that BPs can bind ^{99m}Tc . To this end, a solution of TzBP in saline (3 mg/ 0.5 mL) was combined with SnCl_2 and $[^{99m}\text{Tc}]\text{TcO}_4^-$ in saline (Fig 6B). The pH was adjusted to 6.0 using 0.2 M PBS (pH 8), and the reaction was shaken at room temperature for 45 min. The product, $[^{99m}\text{Tc}]\text{TcTzBP}$ was obtained routinely in ~85-90 % purity as determined by iTLC (Fig S4). When water is used as the eluent, the product ($[^{99m}\text{Tc}]\text{TcTzBP}$) and colloidal ^{99m}Tc ($^{99m}\text{TcO}_2$) elute off the baseline while free $[^{99m}\text{Tc}]\text{TcO}_4^-$ remains. When acetone is used, the product and $^{99m}\text{TcO}_2$ remain on the baseline while free $^{99m}\text{TcO}_4^-$ migrates with the solvent front. With these two solvents, the purity of $[^{99m}\text{Tc}]\text{TcTzBP}$ can be determined.

4.5. Hydroxyapatite Binding

A hydroxyapatite (HA) binding assay was performed to evaluate the binding of mF127-TCO(IR780) to HA *in vitro* in the presence and absence of TzBP. IR780 is a hydrophobic cyanine dye that is readily encapsulated in the mF127-TCO, enabling the use of UV spectrophotometry to determine the extent of binding. The HA binding study was adapted from a literature procedure.[36] Briefly, two solutions of mF127-TCO(IR780) were prepared and each combined either with TzBP or saline resulting in TzBP-mF127-TCO(IR780) and mF127-TCO(IR780), respectively. In triplicate, these solutions were combined with HA in tris buffer in addition to a no-salt control (tris buffer). The samples were incubated for 1 hour at room temperature, centrifuged, and the supernatant aliquoted for spectroscopic measurements. As seen in Fig 7A, there is a significant difference in binding to the HA salt for TzBP-mF127-TCO(IR780) (24 ± 3 %) versus mF127-TCO(IR780) (6 ± 1 %): a four-fold increase. These results suggest that the TCO groups on the surface of the micelle successfully reacted with TzBP, which was in turn able to promote binding to HA. In the absence of the TzBP, the micelles are unable to specifically bind to the HA and largely remain in the supernatant except for a small amount of non-specific binding.

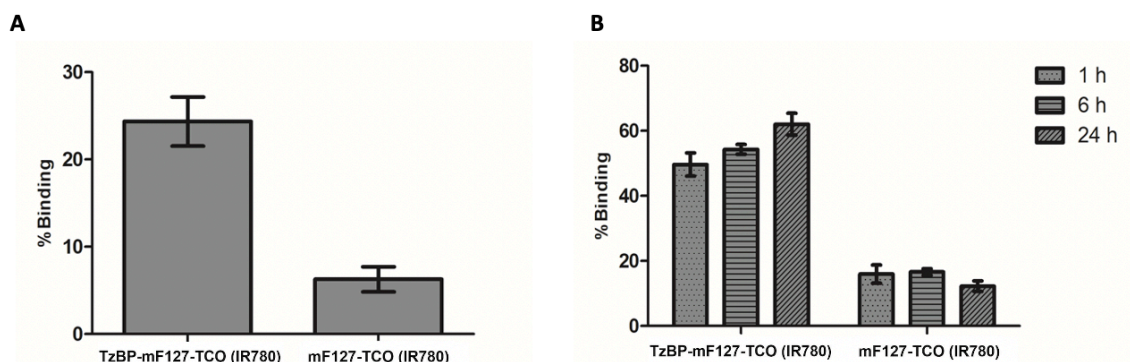


Fig 7. A) Percent binding of TzBP-mF127-TCO(IR780) and mF127-TCO(IR780) alone to hydroxyapatite (HA). % binding was calculated by using a no salt control. Significant difference was seen in binding to HA with TzBP-mF127-TCO(IR780) vs. mF127-TCO(IR780) micelles suggesting specific binding occurs due to the presence of the tetrazine modified BP. $p = 0.05$ ($n=3$). B) Percent binding of TzBP-mF127-TCO(IR780) and mF127-TCO(IR780) pre-targeted to HA after 1, 6, and 24 h. The percent binding was calculated by using a no salt control. $p = 0.05$ ($n=3$).

In addition to functionalizing the surface of micelles with a targeting vector, selective delivery can also be achieved using a pre-targeting strategy. Here, a targeting vector containing either a tetrazine or TCO group is administered first and allowed to localize at the target site. This is followed by administration of the counterpart which selectively couples to its IEDDA reaction partner *in vivo*. [25,48,49]. This approach was evaluated with the HA binding assay where HA salt was combined with TzBP or saline prior to the addition of mF127-TCO(IR780). mF127-TCO(IR780) was incubated with TzBP-treated HA and saline-treated HA for 1, 6, and 24 h. No-salt controls were also prepared. The additional time points were to assess whether increased binding of mF127-TCO(IR780) to TzBP occurs over time. The samples were worked up and the absorbance of supernatants measured as described above. A three-fold increase in binding to TzBP-

treated HA ($50 \pm 4 \%$) was observed for mF127-TCO(IR780) compared to the saline-treated HA ($16 \pm 3 \%$) at 1 h which increased to a five-fold increase at 24 h ($62 \pm 3 \%$ binding compared to $12 \pm 2 \%$) (Fig 7B). Additionally, the pre-targeting strategy showed 50 % binding at 1 h in comparison to the 25 % seen in the active targeting strategy. Furthermore, the percent binding increased over time (54 and 62 % binding at 6 and 24 h, respectively) suggesting that additional micelles were able to bind to the HA when allowed a longer incubation time. This data implies the TCO groups remain accessible for tetrazine ligation and mF127-TCO(IR780) may be suitable for use with pre-targeting as an alternative way to selectively target micelles.

4.6. *In vivo* Studies

4.6.1. Biodistribution of mF127-TCO labelled with [^{99m}Tc]TcTzPy

To determine the biodistribution of the core micelles, mF127-TCO, a method was developed to radiolabel the TCO groups with a ^{99m}Tc labelled tetrazine (Fig 8) .[33] The precursor, a tridentate chelate derivative of a tetrazine, was treated with [$^{99m}\text{Tc}(\text{CO})_3(\text{OH})_3$] $^+$ and the mixture heated in a microwave reactor at 60 °C for 20 min to yield [^{99m}Tc]TcTzPy. Following HPLC purification, [^{99m}Tc]TcTzPy was incubated with mF127-TCO for 30 min at room temperature producing [^{99m}Tc]TcTzPy-mF127-TCO, which was purified using centrifugal filtration where the product was isolated in 88 % radiochemical yield (RCY).

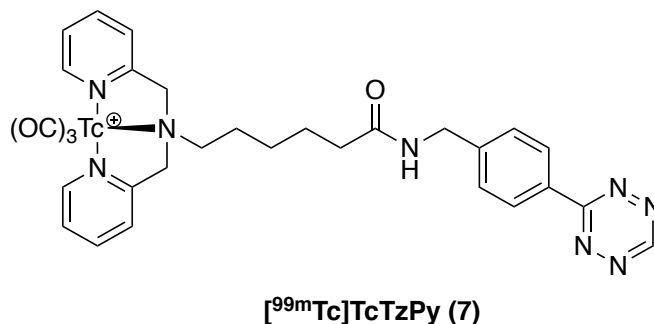


Fig 8. Compound [^{99m}Tc]TcTzPy was prepared according to a literature method [33] and used to radiolabel mF127-TCO(IR780) for biodistribution studies.

The [^{99m}Tc]TcTzPy-mF127-TCO conjugate was subsequently administered intravenously to female Balb/C mice where at 1, 6, and 24 hours post injection, animals were sacrificed, and organ/tissues were excised, rinsed in PBS, and blotted dry and the % ID/g of select tissues and fluids was determined (Fig 9). At the 1 h time point post injection, high concentration of micelles was seen in the blood, liver, and small intestines specifically, 9.42 ± 0.27 , 15.74 ± 0.13 , and 24.83 ± 1.33 % ID/g, respectively. Splenic uptake at 1 h was 1.13 ± 0.07 % ID/g and increased to 2.01 ± 0.15 % ID/g by the 24 h time point. At the 6 h time point post-injection, [^{99m}Tc]TcTzPy-mF127-TCO remained in circulation as evident by a blood concentration of 4.94 ± 0.55 % ID/g. At 24 h post injection, minimal uptake was observed in all organs as the micelles were by then largely cleared via the renal and hepatobiliary systems. Spherical nanoparticles which are 20-150 nm in size are prone to localization in the spleen and liver which explains the uptake seen in the spleen over 24 h (~ 2 % ID/g).[6] This is similar to results reported by Arranja *et al.* for indium-111 labelled Pluronic F127 micelles which showed ~ 3 % ID/g in the spleen at 24 h.[34] This data serves as the control for comparing to the BP tagged F127-TCO micelles .

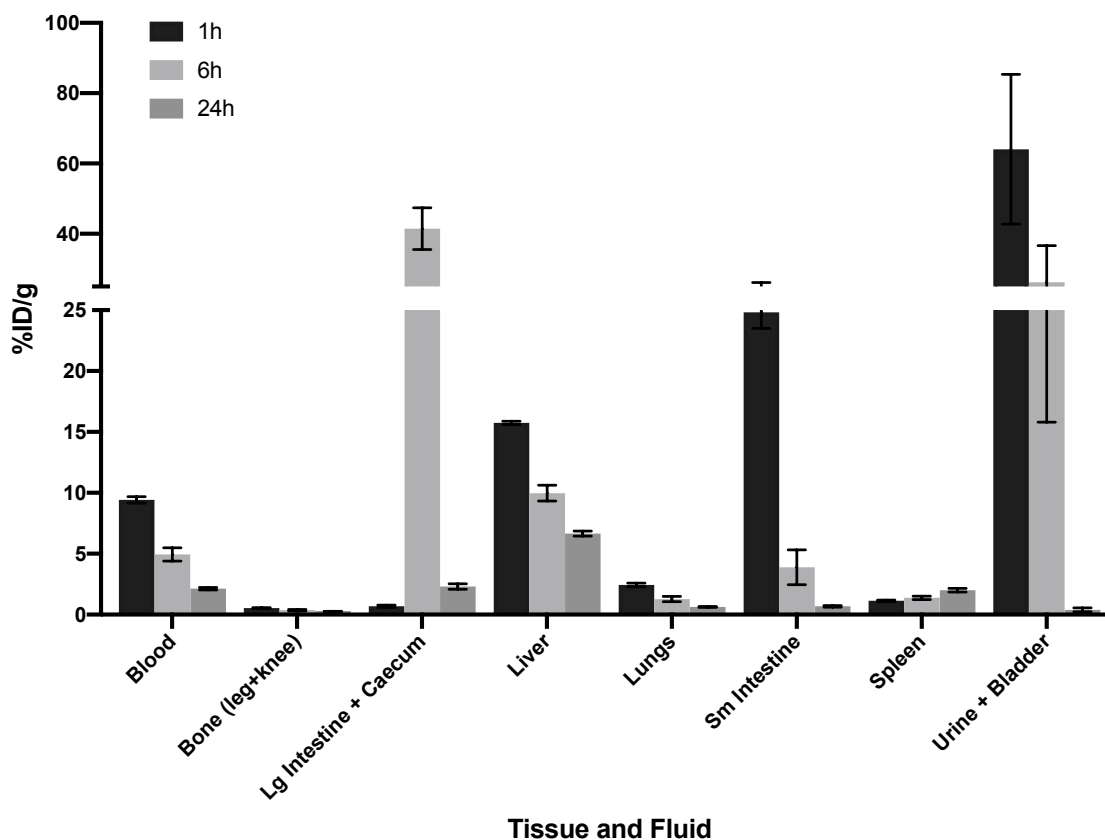


Fig 9. Biodistribution results for [^{99m}Tc]TcTzPy-mF127-TCO. Data shown was obtained from selected tissues and fluids taken from mice at 1, 6, and 24 h post injection of [^{99m}Tc]TcTzPy-mF127-TCO. Activity was normalized to tissue or fluid weight, as the mean percent injected dose per gram of tissue or fluid (% ID/g) \pm SEM. Full biodistribution results can be found in the supporting information (Fig S6).

4.6.2. Biodistribution of mF127-TCO(IR780) labelled with [^{99m}Tc]TcTzBP

The ability to modify and target the mF127-TCO was assessed by labelling them with [^{99m}Tc]TcTzBP; a ^{99m}Tc -labelled BP derivative that targets HA. The presence of ^{99m}Tc on the micelle conjugate (^{99m}Tc]TcTzBP-mF127-TCO(IR780)) made it possible to assess the biodistribution quantitatively. Additionally, having IR780 encapsulated within the micelles enables the use of photoacoustic (PA) imaging to visualize the extent of localization of material encapsulated in the micellar core to bone and key organs. The

biodistribution studies were performed in healthy female Balb/C mice ($n=3$) who were administered $[^{99m}\text{Tc}]\text{TcTzBP-mF127-TCO(IR780)}$ intravenously via tail-vein injection and sacrificed at 1, 4, and 24 h post injection. Biodistribution data, plotted as % ID/g, is displayed in Fig 10A.

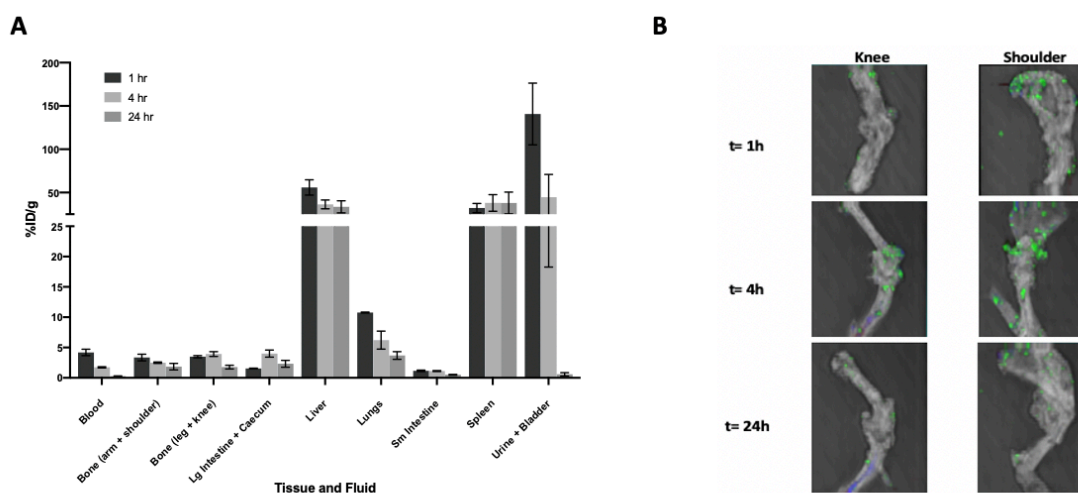


Fig 10. A) Biodistribution results for $[^{99m}\text{Tc}]\text{TcTzBP-mF127-TCO(IR780)}$ in healthy Balb/C mice. Data shown was obtained from selected tissues and fluids taken from mice at 1, 4, and 24 h post injection of $[^{99m}\text{Tc}]\text{TcTzBP-mF127-TCO(IR780)}$. Activity was normalized to tissue or fluid weight, as mean percent injected dose per gram of tissue or fluid (% ID/g) \pm SEM. Full biodistribution results can be found in the supporting information (Fig S7). B) B-Mode ultrasound images with superimposed photoacoustic images of knee and shoulder joints obtained *ex vivo* at $t= 1, 4,$ and 24 h post injection of $[^{99m}\text{Tc}]\text{TcTzBP-mF127-TCO(IR780)}$. Green is signal corresponding to IR780.

At 1 h post injection, the blood concentration of $[^{99m}\text{Tc}]\text{TcTzBP-mF127-TCO(IR780)}$ was 4.19 ± 0.52 % ID/g, which is a 2-fold decrease compared to $[^{99m}\text{Tc}]\text{TcTzPy-mF127-TCO}$ and 3-fold increase compared to $[^{99m}\text{Tc}]\text{TcTzBP}$ alone (Fig 9, 10 and S9). The decreased blood concentration compared to the nontargeted micelles, suggests that the presence of BPs on the micellar surface affected their blood residence time. Furthermore, the increased blood concentration compared to $[^{99m}\text{Tc}]\text{TcTzBP}$ alone is

expected as micelles have longer circulation times, which is consistent with [^{99m}Tc]TcTzBP being covalently bound to mF127-TCO(IR780).[50] The presence of the BP targeting group resulted in an increase in bone uptake at 1 h which was observed in the knee with [^{99m}Tc]TcTzBP-mF127-TCO(IR780) showing 3.49 ± 0.18 % ID/g, compared to [^{99m}Tc]TcTzPy-mF127-TCO which was 0.53 ± 0.04 % ID/g (Fig 10). At 24 h, uptake in the knee had decreased to 1.77 ± 0.31 % ID/g, compared to 0.26 ± 0.01 % ID/g for [^{99m}Tc]TcTzPy-mF127-TCO. These changes translate to a 6.6-fold increase in bone uptake at 1 h and 6.8-fold increase at 24 h as a result of the [^{99m}Tc]TcTzBP targeting vector anchored on the micellar surface through the tetrazine-TCO coupling reaction (Fig 10). Similar accumulation of [^{99m}Tc]TcTzBP-mF127-TCO(IR780) was observed in the shoulder joint with 3.35 ± 0.55 and 1.85 ± 0.54 % ID/g at 1 and 24 h post injection, respectively. Chaudhari *et al.* developed nanoparticles functionalized with zoledronate, an imidazole based BP, for bone targeting which exhibited < 0.5 , ~ 1.5 , and ~ 1 % ID/g at 1, 4, and 12 h post injection, respectively, in healthy bone.[41] Comparatively, the micelles described here showed higher shoulder and knee uptake of 2.50 ± 0.11 and 3.93 ± 0.39 % ID/g, respectively, at 4 h post injection. Furthermore, the increase in bone uptake is accompanied with a decrease in blood levels at both 1 and 24 h suggests that micelles are clearing from blood and actively accumulating at the target (Fig 11). The modified micelles, [^{99m}Tc]TcTzBP-mF127-TCO(IR780), were also detected in high concentrations in the liver (55.89 ± 8.84 % ID/g and 33.50 ± 6.97 % ID/g) and spleen (32.15 ± 5.30 % ID/g and 37.89 ± 12.6 % ID/g) at 1 and 24 h, respectively, which is again consistent with reticuloendothelial system (RES) uptake that is commonly observed for micelles.[34,51]

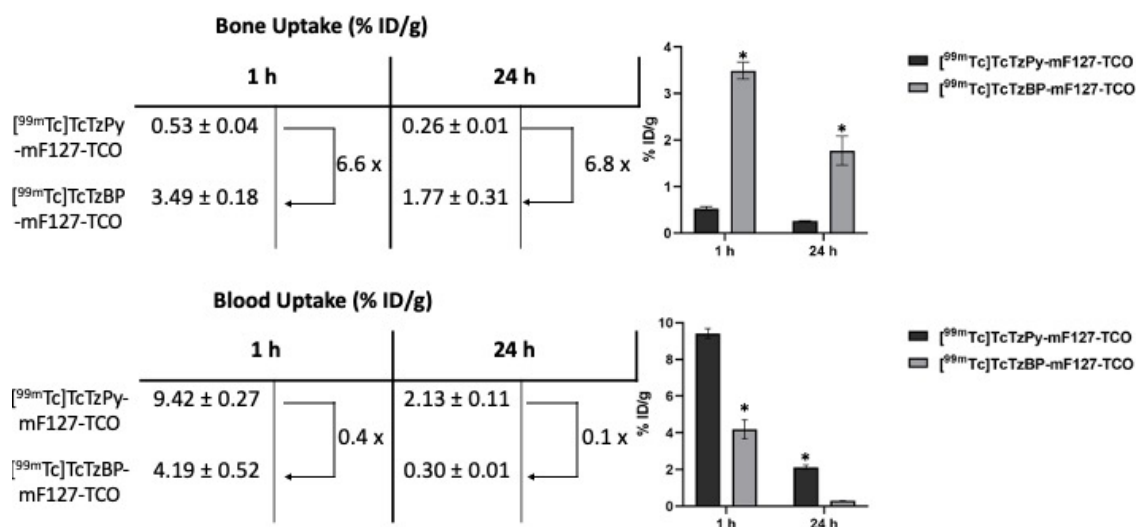


Fig 11. Comparison of [^{99m}Tc]TcTzPy-mF127-TCO and [^{99m}Tc]TcTzBP-mF127-TCO(IR780) uptake in bone (leg + knee) and blood concentrations at 1 and 24 h post injection. An increase of 6.6 and 6.8-fold increase in bone uptake was observed with [^{99m}Tc]TcTzBP-mF127-TCO(IR780) versus [^{99m}Tc]TcTzPy-mF127-TCO which does not contain a BP at 1 and 24 h, respectively (p < 0.01).

PA imaging is a cost effective and sensitive molecular imaging modality that takes advantage of the photoacoustic effect to offer a greater depth of penetration (up to 7 cm) than optical imaging (100 μm).[52,53] In addition to the biodistribution study above, *ex vivo* PA imaging of the knee and shoulder joints were conducted at t= 1, 4, and 24 h to assess the presence of the dyes, which are representative of a drug payload, at the knee and shoulder joints (Fig 10B). Both joints were thoroughly rinsed with PBS prior to imaging to remove residual blood and non-specifically bound material. Signal was evident in the shoulder and knee joints at 1 and 4 h while there was a significant decrease at 24 h which is likely associated with loss of the payload from the bone-bound micelles.

4.6.3. Biodistribution data of mF127-TCO(IR780) pre-targeted with $[^{99m}\text{Tc}]\text{TcTzBP}$

Building on the promising *in vitro* HA-binding data, the ability of mF127-TCO(IR780) to target bone *in vivo* using a pre-targeting strategy was assessed. To this end, mF127-TCO(IR780) was administered to mice 1 h after administration of $[^{99m}\text{Tc}]\text{TcTzBP}$. At 1, 4, and 24 h post injection of the micelles, mice (n=3) were sacrificed and organs excised, weighed, and radioactivity levels were counted. Additionally, *ex vivo* PA imaging of the knee and shoulder joints along with the spleen and lungs were obtained. Biodistribution data are plotted as % ID/g and PA images of the organs at t= 1, 4, and 24 h are displayed in Fig 12.

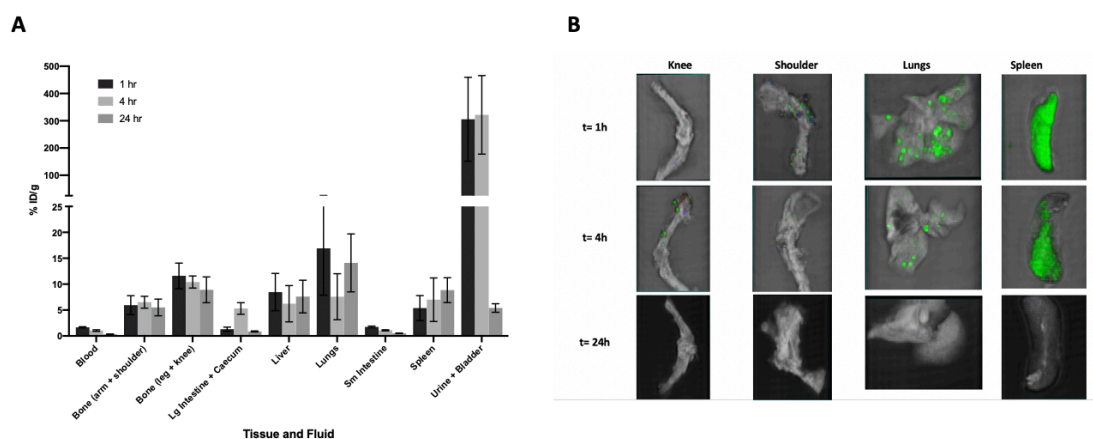


Fig 12. A) Biodistribution data obtained for pre-targeting study of mF127-TCO(IR780) with $[^{99m}\text{Tc}]\text{TcTzBP}$ in healthy Balb/c mice at 1, 4, and 24 h, reported as % ID/g. Activity was normalized to tissue or fluid weight, as mean percent injected dose per gram of tissue or fluid (% ID/g) \pm SEM. Full biodistribution results can be found in the supporting information (Fig S8). B) B-Mode ultrasound images with superimposed photoacoustic images of knee and shoulder joints, lungs and spleen obtained *ex vivo* at t= 1, 4, and 24 h post injection of mF127-TCO(IR780). The green colour is the signal corresponding to IR780.

At the 1 h time point, uptake at the shoulder and knee joints were 5.95 ± 1.82 and 11.61 ± 2.46 % ID/g, respectively. Over the 24-hour period, uptake at the shoulder remained at 5.50 ± 1.61 % ID/g while knee uptake decreased slightly to 8.91 ± 2.49 % ID/g. This distribution is similar to that of [^{99m}Tc]TcTzBP alone (Fig S9), showing that it localized successfully at the target site.

PA images of shoulder and knee were obtained *ex vivo* to determine whether the dye was similarly bound to bone. Images of the shoulder and knee joints did not exhibit any signal above background (Fig 12B). Images were then taken of other organs where uptake was evident in the spleen at 1 and 4 h, which ultimately went to background by 24 h. There was also some residual uptake in the lungs which is likely due to the presence of a small number of aggregated micelles.

The absence of signal in the shoulder and knee joints, coupled with the positive results seen with active targeting, suggests that the *in vivo* coupling reaction likely did not take place on the bone surface. There are potentially two reasons for this result. The first is a reduction in the accessibility of TCO groups on the micellar surface caused by adsorption of plasma proteins onto the micelle surface *in vivo*. [6,54,55] This would explain why *in vitro* binding to HA through pre-targeting was successful where there were no competing proteins. This is a persistent issue when preparing micelles with surface functional groups. [54,55] The second is the hydrophobic nature of the TCO groups which could cause them to move away from the hydrophilic micellar surface and towards the hydrophobic core. This would lead to an insufficient number of surface-TCO groups available to achieve the required rates needed for the *in vivo* reaction and coupling of the micelle to the tetrazine-

tagged bone. In the previous study, the comparatively more hydrophilic BP groups of [^{99m}Tc]TcTzBP are likely readily available on the surface of the micelles which resulted in successful localization of [^{99m}Tc]TcTzBP-mF127-TCO(IR780) micelles at the knee and shoulder joints. The lack of coupling *in vivo* can potentially be addressed in the future by using more hydrophilic strained alkenes.

5. Conclusions and Future Work

Pluronic F127 polymers were successfully functionalized with TCO providing a convenient handle for radiolabelling micelles and adding targeting vectors. NMR along with DLS and TEM were used to verify the synthesis of F127-TCO polymers and subsequently formed mF127-TCO as a suitable size for drug delivery. Evaluation of the TCO-derived micelles for targeted delivery using a tetrazine-derived BP (TzBP) targeting vector offered encouraging *in vitro* results, with over a 4-fold increase in binding to HA when tagged with TzBP. The mF127-TCO(IR780) also exhibited promising *in vivo* targeting when tagged with [^{99m}Tc]TcTzBP, showing a 6.6-fold increase in bone uptake when compared to a tetrazine without a targeting vector after 1 h. Additionally, encapsulating the IR780 dye within the F127-TCO micelles allowed for PA imaging to show localization of the contents within these micelles. Attempts to achieve targeting using a two-step pre-targeting strategy was unsuccessful potentially due to the reduced reactivity and/or accessibility of TCO groups.

6. References

[1] L. Wen, C. Wen, F. Zhang, K. Wang, H. Yuan, F. Hu, siRNA and chemotherapeutic

- molecules entrapped into a redox-responsive platform for targeted synergistic combination therapy of glioma, *Nanomedicine Nanotechnology, Biol. Med.* 28 (2020) 102218. doi:10.1016/j.nano.2020.102218.
- [2] T.R. Arunraj, N. Sanoj Rejinold, S. Mangalathillam, S. Saroj, R. Biswas, R. Jayakumar, Synthesis, characterization and biological activities of curcumin nanospheres, *J. Biomed. Nanotechnol.* 10 (2014) 238–250. doi:10.3233/SPE-2011-0537.
- [3] C.L. Ventola, Progress in nanomedicine: Approved and investigational nanodrugs, *Pharm. Ther.* 42 (2017) 742–755.
- [4] J. Conde, C.E. Arnold, F. Tian, N. Artzi, RNAi nanomaterials targeting immune cells as an anti-tumor therapy: The missing link in cancer treatment?, *Mater. Today.* 19 (2016) 29–43. doi:10.1016/j.mattod.2015.07.005.
- [5] S.E. McNeil, Nanoparticle therapeutics: A personal perspective, *Wiley Interdiscip. Rev. Nanomedicine Nanobiotechnology.* 1 (2009) 264–271. doi:10.1002/wnan.6.
- [6] E. Blanco, H. Shen, M. Ferrari, Principles of nanoparticle design for overcoming biological barriers to drug delivery, *Nat. Biotechnol.* 33 (2015) 941–951. doi:10.1038/nbt.3330.
- [7] G. Feng, Z. Zha, Y. Huang, J. Li, Y. Wang, W. Ke, H. Chen, L. Liu, Y. Song, Z. Ge, Sustained and Bioresponsive Two-Stage Delivery of Therapeutic miRNA via Polyplex Micelle-Loaded Injectable Hydrogels for Inhibition of Intervertebral Disc Fibrosis, *Adv. Healthc. Mater.* 7 (2018) 1–14. doi:10.1002/adhm.201800623.
- [8] K. Greish, Enhanced Permeability and Retention (EPR) Effect for Anticancer

- Nanomedicine Drug Targeting, in: *Cancer Nanotechnology*, *Methods Mol. Biol.*, 2010: pp. 25–37. doi:10.1007/978-1-60761-609-2_3.
- [9] W. Zhang, Y. Shi, Y. Chen, J. Ye, X. Sha, X. Fang, Multifunctional Pluronic P123/F127 mixed polymeric micelles loaded with paclitaxel for the treatment of multidrug resistant tumors, *Biomaterials*. 32 (2011) 2894–2906. doi:10.1016/j.biomaterials.2010.12.039.
- [10] A. Marin, H. Sun, G.A. Hussein, W.G. Pitt, D.A. Christensen, N.Y. Rapoport, Drug delivery in pluronic micelles: Effect of high-frequency ultrasound on drug release from micelles and intracellular uptake, *J. Control. Release*. 84 (2002) 39–47. doi:10.1016/S0168-3659(02)00262-6.
- [11] T. Liu, Z. Liu, J. Chen, R. Jin, Y. Bai, Y. Zhou, X. Chen, Redox-responsive supramolecular micelles for targeted imaging and drug delivery to tumor, *J. Biomed. Nanotechnol.* 14 (2018) 1107–1116. doi:10.1166/jbn.2018.2573.
- [12] M.S.H. Akash, K. Rehman, Recent progress in biomedical applications of pluronic (PF127): Pharmaceutical perspectives, *J. Control. Release*. 209 (2015) 120–138. doi:10.1016/j.jconrel.2015.04.032.
- [13] X.Q. Zhang, X. Xu, N. Bertrand, E. Pridgen, A. Swami, O.C. Farokhzad, Interactions of nanomaterials and biological systems: Implications to personalized nanomedicine, *Adv. Drug Deliv. Rev.* 64 (2012) 1363–1384. doi:10.1016/j.addr.2012.08.005.
- [14] D. Wang, S. Zhang, T. Zhang, G. Wan, B. Chen, Q. Xiong, J. Zhang, W. Zhang, Y. Wang, Pullulan-coated phospholipid and Pluronic F68 complex nanoparticles for

- carrying IR780 and paclitaxel to treat hepatocellular carcinoma by combining photothermal therapy/photodynamic therapy and chemotherapy, *Int. J. Nanomedicine*. 12 (2017) 8649–8670. doi:10.2147/IJN.S147591.
- [15] C. Pais-Silva, D. de Melo-Diogo, I.J. Correia, IR780-loaded TPGS-TOS micelles for breast cancer photodynamic therapy, *Eur. J. Pharm. Biopharm.* 113 (2017) 108–117. doi:10.1016/j.ejpb.2017.01.002.
- [16] Y. Il Chung, J.C. Kim, Y.H. Kim, G. Tae, S.Y. Lee, K. Kim, I.C. Kwon, The effect of surface functionalization of PLGA nanoparticles by heparin- or chitosan-conjugated Pluronic on tumor targeting, *J. Control. Release*. 143 (2010) 374–382. doi:10.1016/j.jconrel.2010.01.017.
- [17] X. Wei, L. Liu, X. Li, Y. Wang, X. Guo, J. Zhao, S. Zhou, Selectively targeting tumor-associated macrophages and tumor cells with polymeric micelles for enhanced cancer chemo-immunotherapy, *J. Control. Release*. 313 (2019) 42–53. doi:10.1016/j.jconrel.2019.09.021.
- [18] A. Varela-Moreira, Y. Shi, M.H.A.M. Fens, T. Lammers, W.E. Hennink, R.M. Schiffelers, Clinical application of polymeric micelles for the treatment of cancer, *Mater. Chem. Front.* (2017). doi:10.1039/C6QM00289G.
- [19] S.E. Jin, H.E. Jin, S.S. Hong, Targeted delivery system of nanobiomaterials in anticancer therapy: From cells to clinics, *Biomed Res. Int.* 2014 (2014). doi:10.1155/2014/814208.
- [20] S. Bisso, J.C. Leroux, Nanopharmaceuticals: A focus on their clinical translatability, *Int. J. Pharm.* 578 (2020). doi:10.1016/j.ijpharm.2020.119098.

- [21] H. He, L. Liu, E.E. Morin, M. Liu, A. Schwendeman, Survey of Clinical Translation of Cancer Nanomedicines - Lessons Learned from Successes and Failures, *Acc. Chem. Res.* 52 (2019) 2673–2683. doi:10.1021/acs.accounts.9b00228.
- [22] Z. Sezgin, N. Yüksel, T. Baykara, Preparation and characterization of polymeric micelles for solubilization of poorly soluble anticancer drugs, *Eur. J. Pharm. Biopharm.* 64 (2006) 261–268. doi:10.1016/j.ejpb.2006.06.003.
- [23] M. Bohorquez, C. Koch, T. Trygstad, N. Pandit, A Study of the Temperature-Dependent Micellization of Pluronic F127., *J. Colloid Interface Sci.* 216 (1999) 34–40. doi:10.1006/jcis.1999.6273.
- [24] W.J. Zhang, K. Gilstrap, L.Y. Wu, K.C.R. Bahadur, M. a Moss, Q. a Wang, X.B. Lu, X.M. He, Synthesis and Characterization of Thermally Responsive Pluronic F127-Chitosan Nanocapsules for Controlled Release and Intracellular Delivery of Small Molecules, *ACS Nano.* 4 (2010) 6747–6759. doi:Doi 10.1021/Nn101617n.
- [25] T. Reiner, B.M. Zeglis, The inverse electron demand Diels-Alder click reaction in radiochemistry., *J. Labelled Compd. Rad.* 57 (2014) 285–90. doi:10.1002/jlcr.3149.
- [26] R. Rossin, M.S. Robillard, Pre-targeted imaging using bioorthogonal chemistry in mice., *Curr. Opin. Chem. Biol.* 21 (2014) 161–9. doi:10.1016/j.cbpa.2014.07.023.
- [27] J.B. Haun, N.K. Devaraj, S.A. Hilderbrand, H. Lee, R. Weissleder, Bioorthogonal chemistry amplifies nanoparticle binding and enhances the sensitivity of cell detection, *Nat. Nanotechnol.* 5 (2010) 660–665. doi:10.1038/nnano.2010.148.
- [28] F. Emmetiere, C. Irwin, N.T. Viola-Villegas, V. Longo, S.M. Cheal, P. Zanzonico, N.V.K. Pillarsetty, W.A. Weber, J.S. Lewis, T. Reiner, ¹⁸F-labeled-bioorthogonal

- liposomes for in vivo targeting, *Bioconjug. Chem.* 24 (2013) 1784–1789. doi:10.1021/bc400322h.
- [29] A.H.A.M. Van Onzen, R. Rossin, A.P.H.J. Schenning, K. Nicolay, L.G. Milroy, M.S. Robillard, L. Brunsveld, Tetrazine - Trans-Cyclooctene Chemistry Applied to Fabricate Self-Assembled Fluorescent and Radioactive Nanoparticles for in Vivo Dual Mode Imaging, *Bioconjug. Chem.* 30 (2019) 547–551. doi:10.1021/acs.bioconjchem.9b00038.
- [30] J.A.C.M. Goos, M. Davydova, T.R. Dilling, A. Cho, M.A. Cornejo, A. Gupta, W.S. Price, S. Puttick, M.R. Whittaker, J.F. Quinn, T.P. Davis, J.S. Lewis, Design and preclinical evaluation of nanostars for the passive pre-targeting of tumor tissue, *Nucl. Med. Biol.* 84–85 (2020) 63–72. doi:10.1016/j.nucmedbio.2020.02.012.
- [31] S. Kramer, D. Svatunek, I. Alberg, B. Gräfen, S. Schmitt, L. Braun, A.H.A.M. Van Onzen, R. Rossin, K. Koynov, H. Mikula, R. Zentel, HPMA-Based Nanoparticles for Fast, Bioorthogonal iEDDA Ligation, *Biomacromolecules.* 20 (2019) 3786–3797. doi:10.1021/acs.biomac.9b00868.
- [32] Y. Wang, L. Yu, L. Han, X. Sha, X. Fang, Difunctional Pluronic copolymer micelles for paclitaxel delivery: Synergistic effect of folate-mediated targeting and Pluronic-mediated overcoming multidrug resistance in tumor cell lines, *Int. J. Pharm.* 337 (2007) 63–73. doi:10.1016/j.ijpharm.2006.12.033.
- [33] H.A. Bilton, Z. Ahmad, N. Janzen, S. Czorny, J.F. Valliant, Preparation and Evaluation of ^{99m}Tc-labeled Tridentate Chelates for Pre-targeting Using Bioorthogonal Chemistry, (2017) e55188. doi:doi:10.3791/55188.

- [34] A. Arranja, O. Ivashchenko, A.G. Denkova, K. Morawska, S. Van Vlierberghe, P. Dubruel, G. Waton, F.J. Beekman, F. Schosseler, E. Mendes, SPECT/CT Imaging of Pluronic Nanocarriers with Varying Poly(ethylene oxide) Block Length and Aggregation State, *Mol. Pharm.* 13 (2016) 1158–1165. doi:10.1021/acs.molpharmaceut.5b00958.
- [35] Y.Y. Zhang, M. Jeon, L.J. Rich, H. Hong, J. Geng, Y.Y. Zhang, S. Shi, T.E. Barnhart, P. Alexandridis, J.D. Huizinga, M. Seshadri, W. Cai, C. Kim, J.F. Lovell, Non-invasive multimodal functional imaging of the intestine with frozen micellar naphthalocyanines, *Nat. Nanotechnol.* 9 (2014) 631–638. doi:10.1038/nnano.2014.130.
- [36] R. Torres Martin De Rosales, C. Finucane, S.J. Mather, P.J. Blower, Bifunctional bisphosphonate complexes for the diagnosis and therapy of bone metastases, *Chem. Commun.* 3 (2009) 4847–4849. doi:10.1039/b908652h.
- [37] A. Postma, T.P. Davis, A.R. Donovan, G. Li, G. Moad, R. Mulder, M.S. O’Shea, A simple method for determining protic end-groups of synthetic polymers by ¹H NMR spectroscopy, *Polymer (Guildf).* 47 (2006) 1899–1911. doi:10.1016/j.polymer.2006.01.050.
- [38] S. Zalipsky, Alkyl succinimidyl carbonates undergo Lossen rearrangement in basic buffers A side reaction producing β-alanine and derivatives through Lossen rearrangement was found to accompany hydrolysis of alkyl succinimidyl carbonates in basic aqueous buffers., *Chem. Commun.* (1998) 69–70.
- [39] M.A. Gauthier, M.I. Gibson, H.A. Klok, Synthesis of functional polymers by post-

- polymerization modification, *Angew. Chemie - Int. Ed.* 48 (2009) 48–58.
doi:10.1002/anie.200801951.
- [40] Y.-M. Lam, N. Grigorieff, G. Goldbeck-Wood, Direct visualisation of micelles of Pluronic block copolymers in aqueous solution by cryo-TEM, *Phys. Chem. Chem. Phys.* 1 (1999) 3331–3334. doi:10.1039/a902369k.
- [41] K.R. Chaudhari, A. Kumar, V.K.M. Khandelwal, A.K. Mishra, J. Monkkonen, R.S.R. Murthy, Targeting efficiency and biodistribution of zoledronate conjugated docetaxel loaded pegylated pbca nanoparticles for bone metastasis, *Adv. Funct. Mater.* 22 (2012) 4101–4114. doi:10.1002/adfm.201102357.
- [42] S.W. Morton, N.J. Shah, M.A. Quadir, Z.J. Deng, Z. Poon, P.T. Hammond, Osteotropic therapy via targeted layer-by-layer nanoparticles, *Adv. Healthc. Mater.* 3 (2014) 867–875. doi:10.1002/adhm.201300465.
- [43] W.L. Ye, Y.P. Zhao, H.Q. Li, R. Na, F. Li, Q.B. Mei, M.G. Zhao, S.Y. Zhou, Doxorubicin-poly (ethylene glycol)-alendronate self-assembled micelles for targeted therapy of bone metastatic cancer, *Sci. Rep.* 5 (2015) 1–19. doi:10.1038/srep14614.
- [44] T.J. Martin, *Experimental and Clinical Pharmacology: Bisphosphonates - mechanisms of action*, *Aust. Prescr.* 23 (2000) 130–132. doi:10.18773/austprescr.2000.144.
- [45] M.T. Drake, B.L. Clarke, S. Khosla, Bisphosphonates: Mechanism of action and role in clinical practice, *Mayo Clin. Proc.* 83 (2008) 1032–1045. doi:10.4065/83.9.1032.
- [46] J.S. Lewis, A.D. Windhorst, B.M. Zeglis, eds., *Radiopharmaceutical Chemistry*,

- Springer International Publishing, Cham, 2019. doi:10.1007/978-3-319-98947-1.
- [47] K. Libson, E. Deutsch, B.L. Barnett, Structural Characterization of a ^{99}Tc -Diphosphonate Complex. Implications for the Chemistry of $^{99\text{m}}\text{Tc}$ Skeletal Imaging Agents, *J. Am. Chem. Soc.* 102 (1980) 2476–2478. doi:10.1021/ja00527a066.
- [48] B.M. Zeglis, C. Brand, D. Abdel-Atti, K.E. Carnazza, B.E. Cook, S. Carlin, T. Reiner, J.S. Lewis, Optimization of a Pre-targeted Strategy for the PET Imaging of Colorectal Carcinoma via the Modulation of Radioligand Pharmacokinetics., *Mol. Pharm.* 12 (2015) 3575–3587. doi:10.1021/acs.molpharmaceut.5b00294.
- [49] R. Rossin, T. Lappchen, S.M. van den Bosch, R. Laforest, M.S. Robillard, Diels–Alder Reaction for Tumor Pre-targeting: In Vivo Chemistry Can Boost Tumor Radiation Dose Compared with Directly Labeled Antibody, *J. Nucl. Med.* . 54 (2013) 1989–1995. doi:10.2967/jnumed.113.123745.
- [50] J.Y. Kim, W. Il Choi, Y.H. Kim, G. Tae, S.Y. Lee, K. Kim, I.C. Kwon, In-vivo tumor targeting of pluronic-based nano-carriers, *J. Control. Release.* 147 (2010) 109–117. doi:10.1016/j.jconrel.2010.06.010.
- [51] J.P. Jee, J.H. Na, S. Lee, S.H. Kim, K. Choi, Y. Yeo, I.C. Kwon, Cancer targeting strategies in nanomedicine: Design and application of chitosan nanoparticles, *Curr. Opin. Solid State Mater. Sci.* 16 (2012) 333–342. doi:10.1016/j.cossms.2013.01.002.
- [52] M. Xu, L. V Wang, Photoacoustic imaging in biomedicine Photoacoustic imaging in biomedicine, *Rev. Sci. Instrum.* 041101 (2006) 41101–41122. doi:10.1063/1.2195024.
- [53] X. Qin, F. Li, Y. Zhang, G. Ma, T. Feng, Y. Luo, P. Huang, J. Lin, In Vivo

Photoacoustic Detection and Imaging of Peroxynitrite, *Anal. Chem.* 90 (2018) 9381–9385. doi:10.1021/acs.analchem.8b01992.

- [54] A. Salvati, A.S. Pitek, M.P. Monopoli, K. Prapainop, F.B. Bombelli, D.R. Hristov, P.M. Kelly, C. Åberg, E. Mahon, K.A. Dawson, Transferrin-functionalized nanoparticles lose their targeting capabilities when a biomolecule corona adsorbs on the surface, *Nat. Nanotechnol.* 8 (2013) 137–143. doi:10.1038/nnano.2012.237.
- [55] A.E. Nel, L. Mädler, D. Velegol, T. Xia, E.M.V. Hoek, P. Somasundaran, F. Klaessig, V. Castranova, M. Thompson, Understanding biophysicochemical interactions at the nano-bio interface, *Nat. Mater.* 8 (2009) 543–557. doi:10.1038/nmat2442.

Chapter 6: Summary and Future Work

6.1. Summary

The overarching objective of this thesis was to assess the utility of pre-targeting and bioorthogonal chemistry to create targeted ^{99m}Tc and micelle based diagnostic agents. Initially, a new family of tetrazine ligands that were capable of being labelled with ^{99m}Tc were prepared. Once synthesized, the tridentate chelates were radiolabelled with $[\text{}^{99m}\text{Tc}(\text{CO})_3(\text{OH}_2)_3]^+$ and characterized prior to *in vivo* biodistribution studies with a TCO-functionalized small molecule: TCO-BP (Chapter 2). Using a pre-targeting strategy, bone uptake was evident, which is evidence of bioorthogonal chemistry taking place *in vivo*. The most hydrophobic derivative prepared showed high non-specific uptake in the hepatobiliary organs as well as the intestines while the hydrophilic derivative exhibited rapid renal clearance resulting in low target (bone) binding.

Subsequently, the ^{99m}Tc -labelled tetrazines were evaluated with an established TCO-functionalized monoclonal antibody (huA33 mAb) for pre-targeting *in vivo* SPECT imaging and biodistribution studies (Chapter 3). The aim here was to see if it would be possible to overcome the disparity between the “short” half-life of ^{99m}Tc and the long *in vivo* half-life of antibodies. Imaging studies unfortunately showed poor tumour accumulation of both the developed ^{99m}Tc -tetrazine ligands, with $\sim 1\%$ ID/g and tumour: blood ratios < 1 . We hypothesized the poor pharmacokinetics (PK), high non-specific uptake and short blood circulation time of the ligands contributed to the low tumour uptake.

In an attempt to address the limitations of the ^{99m}Tc complexes, Pluronic F127 polymeric micelles were utilized to encapsulate the hydrophobic ^{99m}Tc -tetrazine as a way to modify its PK profile (Chapter 4). The encapsulation resulted in a statistically significant increase in blood concentrations at 1 and 6 h ($p < 0.0005$) and reduction in liver uptake at 6 h ($p < 0.005$). However, the increase in blood residence time did not translate into an increase in bone uptake when evaluated with the TCO-BP targeting vector and a pre-targeting strategy. This is likely a result of the micelle payload being released while also in circulation as opposed to only at sites with high concentrations of TCO-BP resulting in insufficient concentrations of the ^{99m}Tc -tetrazine for ligation at the bone.

Recognizing the potential utility of biorthogonal chemistry and the interest in creating targeted micelles, the Pluronic F127 polymer used in chapter 4 was functionalized with TCO groups. The aim was to develop micelles capable of targeted delivery through the use of a tetrazine-derived targeting vector. The modified F127-TCO polymer was characterized by NMR and a titration with a commercially available tetrazine indicated the presence of 1.3 ± 0.2 TCO groups per polymer. The F127-TCO polymers were used to encapsulate IR780 and the prepared micelles were found to be 25 ± 10 nm in size by DLS and ~ 20 nm by TEM. Additionally, a bisphosphonate-derived tetrazine (TzBP) targeting vector was synthesized and radiolabelled with ^{99m}Tc for preparing bone targeting micelles. The targeting ability of non-radioactive TzBP-mF127-TCO(IR780) was assessed using a hydroxyapatite (HA) binding assay. Using an active targeting approach, F127-TCO micelles treated with TzBP (TzBP-mF127-TCO(IR780)) yielded a four-fold increase in binding versus the controls. For the pre-targeting approach, where HA was treated with

TzBP followed by incubation with mF127-TCO(IR780), three-fold increase in binding compared to controls was seen at 1 h and increasing to five-fold at 24 h.

Beyond the HA binding assay, *in vivo* biodistribution studies assessing bone targeting with [^{99m}Tc]TcTzBP-mF127-TCO(IR780) were conducted through both the active and pre-targeting strategies. The active targeting approach showed ~7-fold increase in bone binding when F127-TCO micelles (mF127-TCO) were tagged with [^{99m}Tc]TcTzBP compared to when tagged with [^{99m}Tc]TcTzPy. Because the micelles were loaded with IR780, PA imaging was performed and a signal corresponding to IR780 at the knee and shoulder joints was observed, further confirming localization of the ^{99m}TcTzBP-mF127-TCO(IR780) at the site. However, when investigating the pre-targeting approach, insufficient concentrations of mF127-TCO(IR780) were present in the bone to be visualized through *ex vivo* PA imaging at any of the time points.

6.2. Future Work

6.2.1. Optimizing ^{99m}Tc-tetrazine ligand

The unfavourable uptake of the ^{99m}Tc-tetrazines prepared herein when used with TCO-antibodies can be addressed by modifying the tetrazine ligand itself to improve its pharmacokinetics. The ^{99m}Tc-tetrazine ligands are comprised of three components: chelate, linker and tetrazine. Between the derivatives prepared in Chapter 2, changes to the chelate and linker were made to tune the hydrophobicity/hydrophilicity of the ligands. While more attempts to identify the ideal linker length or chelate are valid options to explore, the use of an alternative tetrazine may be of interest as well. A bis-pyridyl tetrazine has been reported which has rapid kinetics ($k_2 = 1.3 - 3.2 \times 10^4 \text{ M}^{-1}\text{s}^{-1}$ in PBS) with TCO, which is

faster than the commercially available tetrazine currently used ($k_2 = 6 \times 10^3 \text{ M}^{-1}\text{s}^{-1}$ in PBS).¹ An ^{111}In -labelled derivative of this tetrazine has been previously demonstrated rapid localization in TCO-tagged tumours and produced images with high signal to noise ratio.² The most hydrophilic $^{99\text{m}}\text{Tc}$ -tetrazine ligand which showed rapid renal clearance can be modified by substitution with the more lipophilic bis-pyridyl tetrazine to reduce the overall hydrophilicity of the ligand without interfering with the stable tridentate chelate or biocompatible PEG linker. Subsequently, pre-targeting *in vivo* studies with a TCO-antibody would be conducted to determine its biodistribution. The rapid reaction kinetics coupled with the refined lipophilicity could potentially improve the *in vivo* coupling efficiency of the $^{99\text{m}}\text{Tc}$ -tetrazine and TCO-antibody over the approach reported in Chapter 3.

6.2.2. Targeting solid tumours

Although the developed mF127-TCO exhibited preferential binding to bone with the tetrazine-bisphosphonate targeting vector, the utility of these micelles may be more suited for targeting solid tumours. Due to the EPR effect, the mF127-TCO would be expected to passively accumulate in tumour vasculature creating a higher concentration of one of the reacting partners in the IEDDA reaction. This would help promote coupling to tetrazine-derived targeting vectors while also creating a mechanism for retention of the micelle encapsulated PA dye within tumour tissue.

Initially, the previously synthesized $^{99\text{m}}\text{Tc}$ -tetrazine bisphosphonate ($[\text{}^{99\text{m}}\text{Tc}]\text{TcTzBP}$) could be used for targeting the hydroxyapatite in the tumour microenvironment of malignant cells. For this purpose, cancer cell lines MDA-MB-231 or

4T1, which are known to develop microcalcifications could be used.^{3,4} MDA-MB-231 is a highly aggressive and invasive human breast cancer cell line frequently used in bone metastasis research.³ This cell line has also proven to be mineralising which results in formation of microcalcifications within the tumour, an ideal target for our bone-targeting micelles. Alternatively, 4T1 is a murine breast cancer cell line that also produces aggressive and vascularized tumours and has extensively been used for monitoring development of microcalcifications.⁴

For *in vivo* studies, mice would be inoculated with MDA-MB-231 or 4T1 xenografts. For the active targeting strategy, mice would be administered [^{99m}Tc]TcTzBP-mF127-TCO and biodistribution studies conducted to quantify the uptake of the radiolabelled micelles within the tumours. Initial biodistribution studies at 1, 4, and 24 h would provide a good indication of the micelles ability to target microcalcifications within the tumour to be compared to our previous results of bone targeting biodistribution studies in healthy mice. Further optimization may be needed to determine the ideal time point for maximal tumour uptake. Prior to testing the pre-targeting approach, biodistribution studies with ^{99m}TcTzBP would need to be conducted in mice bearing the MDA-MB-231 or 4T1 tumours to determine the delay between the [^{99m}Tc]TcTzBP and F127-TCO micelles injection. Based on previous unpublished results from our lab, a one-hour delay provides sufficient accumulation of [^{99m}Tc]TcTzBP at bone but has yet to be determined in tumours. For pre-targeting, mice would be administered ^{99m}TcTzBP followed by a separate injection of TCO-modified micelles. Similar to the protocol in Chapter 5, the mF127-TCO(IR780)

should be used to visualize their accumulation and click within the tumour based on PA signal from IR780 to validate biodistribution data from [^{99m}Tc]TcTzBP accumulation.

6.2.3. Modifying pharmacokinetics of micelles

An alternative method for improving uptake of the micellar payload at the bone target could be through modifying the pharmacokinetic profile of the micelle carrier. As a proof of concept, an attempt to increase the blood circulation lifetime of the F127-TCO micelles was conducted by preparing a tetrazine-derived bovine serum albumin (BSA) construct for tagging the micelles.⁵ BSA is extensively used in pharmaceutical research because of its availability, biodegradability, and non-toxicity.⁶⁻⁸ Albumin-bound nanoparticle drug formulations are clinically approved (Abraxane) and also in clinical trials where the presence of the albumin on the nanoparticle surface increases blood residence time by decreasing opsonization after systemic administration.⁶ The BSA protein was derivatized according to Figure 6.1.

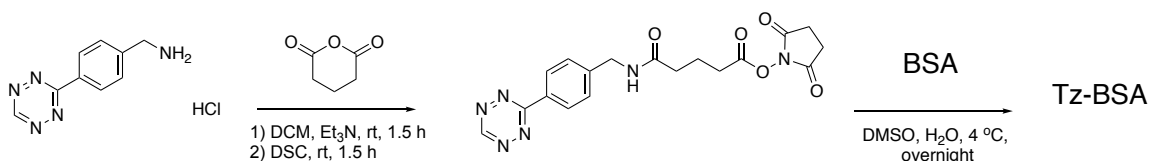


Figure 6.1. Functionalization of BSA with tetrazines.

Using MALDI-MS analysis, the degree of functionalization was determined to be 6.75 tetrazines/BSA monomer. A preliminary *in vitro* study was conducted to determine the ability of mF127-TCO to selectively bind to TzBSA over unfunctionalized BSA. The NIR dye, IR 780, was encapsulated within the micelles and the correlating absorbance signal was used to determine the degree of binding of the micelles. Although results demonstrated a statistically significant ($p= 0.003$) increase in binding of mF127-

TCO(IR780) to TzBSA over BSA alone (1.4×), further optimization is needed to verify selective binding due to the presence of tetrazine.

Following this, *in vivo* studies can be conducted to evaluate whether the addition of the TzBSA affects the blood residence time of the micelle as well as the distribution. An increase in the blood half-life of the micelles and their payload would be advantageous in avoiding first pass clearance which would otherwise reduce the bioavailability of the unshielded payload. The protein-tagged micelle platform could also branch beyond simply BSA derivatives and include a range of different protein and biomolecule surface modifiers where the products would be able to encapsulate a range of diagnostics and therapeutics.

6.2.4. Triggered release with ultrasound

In addition to shielding the payload and modifying its pharmacokinetics, polymeric micelles can be further developed for triggered release of the payload at a specific site. Factors such as micelles stability, size of the hydrophobic core, and the drug diffusion rate affect drug release from the micelles.⁹ The release can be augmented with an external stimulus such as ultrasound (US) frequency or internal trigger such as a change in pH in a tumour microenvironment.

Low US frequencies (20-100 kHz) have a greater depth of penetration but suffer from a lack of focus in comparison to higher frequencies (1 to 3 MHz) which can be focused but have a shallower penetration depth.⁹⁻¹¹ Lower frequencies are better suited for deeper situated tumours but run the risk of damaging healthy tissue from the cavitation effect, production of air bubbles. Several reports of US-triggered release from micelles showed enhanced intracellular drug uptake. Husseini *et al.* reported a 70 kHz US frequency for

triggering doxorubicin release from Pluronic P105 micelles was less efficient than 20 kHz.¹² Similar results were reported by Marin *et al.* who demonstrated 10 % drug release with 20 kHz at a lower power density compared to a higher power density at 1 MHz being needed for the same releasing efficiency.¹³ Both approaches noted drug re-encapsulation can occur upon removal of the US pulse.^{12,13}

Enhanced release of the tetrazine encapsulated micelles or the TCO-derived micelles could be investigated by application of lower frequency US waves. The protocol for appropriate US pulse duration and cycles would need to be optimized. Then *in vivo* therapy studies with compound **5** (^{99m}Tc-tetrazine ligand from chapter 4) with TCO antibodies and F127-TCO containing a chemotherapeutic such as doxorubicin targeted to MDA-MB-231 or 4T1 tumours could be conducted. Mice would be monitored for binding of the ^{99m}Tc or tumour regression due to doxorubicin release when subject to US versus the appropriate non-irradiated controls. Further studies could explore the need for micelle stabilization to develop formulations sensitive to specific US frequencies.^{12,13}

6.3. References

- (1) Rossin, R.; Robillard, M. S. Pre-targeted Imaging Using Bioorthogonal Chemistry in Mice. *Curr. Opin. Chem. Biol.* **2014**, *21*, 161–169.
- (2) Rossin, R.; Läppchen, T.; van den Bosch, S. M.; Laforest, R.; Robillard, M. S. Diels–Alder Reaction for Tumor Pre-targeting: In Vivo Chemistry Can Boost Tumor Radiation Dose Compared with Directly Labeled Antibody. *J. Nucl. Med.* **2013**, *54* (11), 1989–1995.
- (3) O’Grady, S.; Morgan, M. P. Deposition of Calcium in an in Vitro Model of Human

- Breast Tumour Calcification Reveals Functional Role for ALP Activity, Altered Expression of Osteogenic Genes and Dysregulation of the TRPM7 Ion Channel. *Sci. Rep.* **2019**, *9* (1), 1–12.
- (4) Cox, R. F.; Hernandez-Santana, A.; Ramdass, S.; McMahon, G.; Harmey, J. H.; Morgan, M. P. Microcalcifications in Breast Cancer: Novel Insights into the Molecular Mechanism and Functional Consequence of Mammary Mineralisation. *Br. J. Cancer* **2012**, *106* (3), 525–537.
- (5) Chen, H.; Wang, G.; Lang, L.; Jacobson, O.; Kiesewetter, D. O.; Liu, Y.; Ma, Y.; Zhang, X.; Wu, H.; Zhu, L.; et al. Chemical Conjugation of Evans Blue Derivative: A Strategy to Develop Long-Acting Therapeutics through Albumin Binding. *Theranostics* **2016**, *6* (2), 243–253.
- (6) Nosrati, H.; Sefidi, N.; Sharafi, A.; Danafar, H.; Kheiri Manjili, H. Bovine Serum Albumin (BSA) Coated Iron Oxide Magnetic Nanoparticles as Biocompatible Carriers for Curcumin-Anticancer Drug. *Bioorg. Chem.* **2018**, *76*, 501–509.
- (7) Yu, Z.; Yu, M.; Zhang, Z.; Hong, G.; Xiong, Q. Bovine Serum Albumin Nanoparticles as Controlled Release Carrier for Local Drug Delivery to the Inner Ear. *Nanoscale Res. Lett.* **2014**, *9* (1), 1–7.
- (8) Zhao, D.; Zhao, X.; Zu, Y.; Li, J.; Zhang, Y.; Jiang, R.; Zhang, Z. Preparation, Characterization, and in Vitro Targeted Delivery of Folate-Decorated Paclitaxel-Loaded Bovine Serum Albumin Nanoparticles. *Int. J. Nanomedicine* **2010**, *5* (1), 669–677.
- (9) Oerlemans, C.; Bult, W.; Bos, M.; Storm, G.; Nijsen, J. F. W.; Hennink, W. E.

Polymeric Micelles in Anticancer Therapy: Targeting, Imaging and Triggered Release. *Pharm. Res.* **2010**, *27* (12), 2569–2589.

- (10) Sirsi, S.; Borden, M. State-of-the-Art Materials for Ultrasound-Triggered Drug Delivery Rational Design of Ultrasound-Triggered Drug Carriers. *Adv Drug Deliv Rev* **2015**, *15*, 3–14.
- (11) Wang, J.; Pelletier, M.; Zhang, H.; Xia, H.; Zhao, Y. High-Frequency Ultrasound-Responsive Block Copolymer Micelle. *Langmuir* **2009**, *25* (22), 13201–13205.
- (12) Hussein, G. A.; Runyan, C. M.; Pitt, W. G. Investigating the Mechanism of Acoustically Activated Uptake of Drugs from Pluronic Micelles. *BMC Cancer* **2002**, *2*, 3–8.
- (13) Marin, A.; Sun, H.; Hussein, G. A.; Pitt, W. G.; Christensen, D. A.; Rapoport, N. Y. Drug Delivery in Pluronic Micelles: Effect of High-Frequency Ultrasound on Drug Release from Micelles and Intracellular Uptake. *J. Control. Release* **2002**, *84* (1–2), 39–47.

APPENDIX I

Supporting Information for Chapter 2

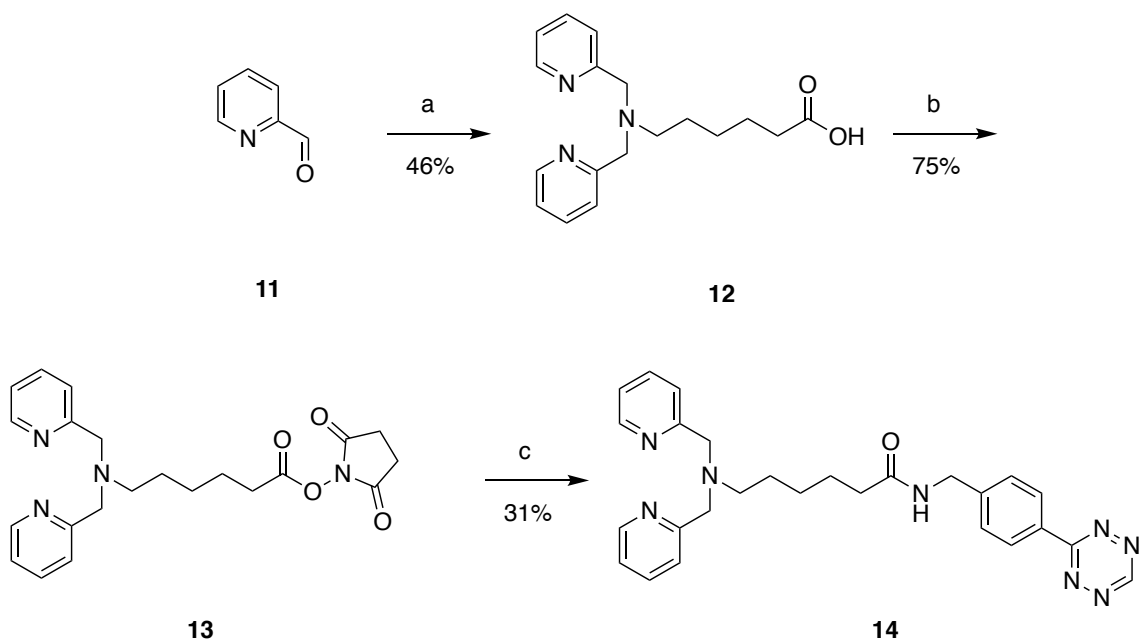


Figure S2.1. Synthesis of **1** from **13**. a) $\text{NaBH}(\text{OAc})_3$, DCE, 6-aminocaproic acid, rt, 12 h. b) NHS, EDC, ACN, rt, 12 h. c) (4-(1,2,4,5-tetrazin-3-yl) phenyl) methanamine hydrochloride, Et_3N , ACN, rt, 1 h.

6-{Bis[(2-pyridyl)methyl]amino}hexanoic acid (12) 2-pyridinecarboxaldehyde (89.7 mmol, 2.4 eq.), 6-aminocaproic acid (**11**) (38.1 mmol, 1.0 eq.) were added in anhydrous DCE (100 mL) and stirred under argon gas (Ar) for 1.5 h at room temperature. Sodium triacetoxyborohydride ($\text{NaBH}(\text{OAc})_3$) (128 mmol, 3.4 eq.) was added and left to stir overnight under Ar at room temperature. The solvent was evaporated under reduced pressure resulting in viscous orange oil. MeOH (150 mL) was added to the crude oil giving a yellow opaque solution. The solvent was removed under vacuum. Crude product

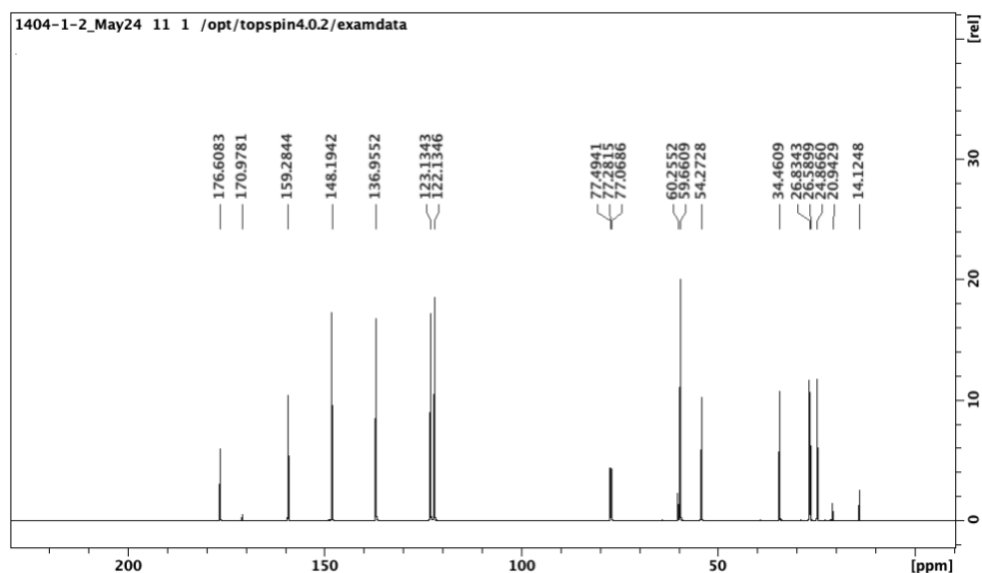


Figure S2.3. ^{13}C NMR (150 MHz, CDCl_3) of **12**.

1-(7-{Bis[(2-pyridyl)methyl]amino}-2-oxoheptyl)-2,5-pyrrolidinedione (13**).**

Compound **12** (0.325 mmol, 1.0 eq.) and NHS (0.645 mmol, 2.2 eq.) were combined in anhydrous ACN and stirred for 15 min at room temperature. EDC (0.645 mmol, 2.2 eq.) was added and the reaction was stirred overnight at room temperature under Ar. Solvent was removed using rotary evaporation under reduced pressure. The compound was purified using semi-preparative HPLC (10-35% solvent B over 2-20 min), $R_t = 10.5$ min. The solvent was dried under reduced pressure giving a colourless, transparent oil (100 mg, 75%): ^1H NMR (600 MHz, CDCl_3): δ 8.80 (d, $J = 6.0$ Hz, 2 H), 8.18 (dt, $J = 12, 6.0, 6.0$ Hz, 2 H), 7.87 (d, $J = 6.0$ Hz, 2 H), 7.66 (t, $J = 6.0$ Hz, 2 H), 4.38 (s, 4 H), 2.81 (s, 6 H) 2.54 (t, $J = 6.0$ Hz, 2 H), 1.62 (m, 4 H), 1.33 (m, 2 H). ^{13}C $\{^1\text{H}\}$ NMR (150 MHz, CDCl_3): δ 169.29, 168.40, 152.59, 144.50, 143.61, 126.48, 125.41, 56.49, 54.74, 30.47, 25.67, 25.34, 24.99, 23.90.

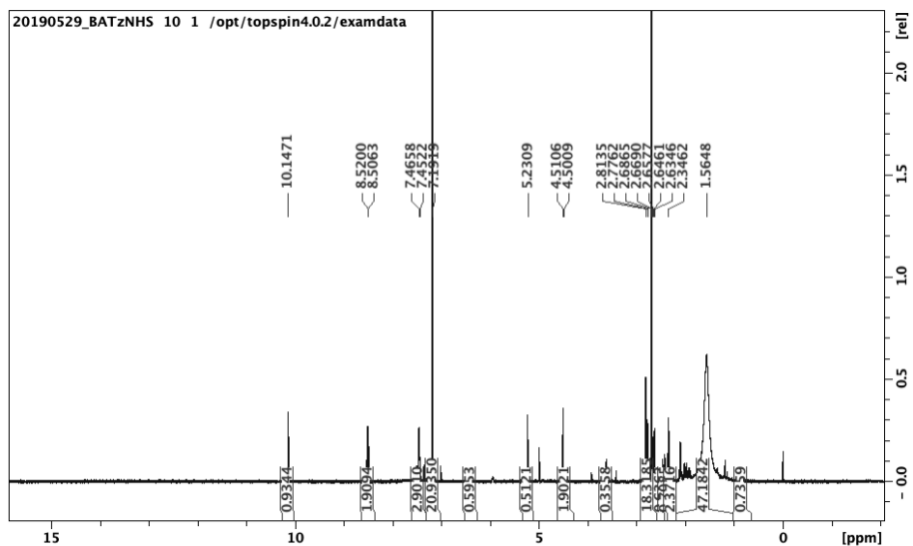


Figure S2.4. ^1H NMR (600 MHz, CDCl_3) of **13**.

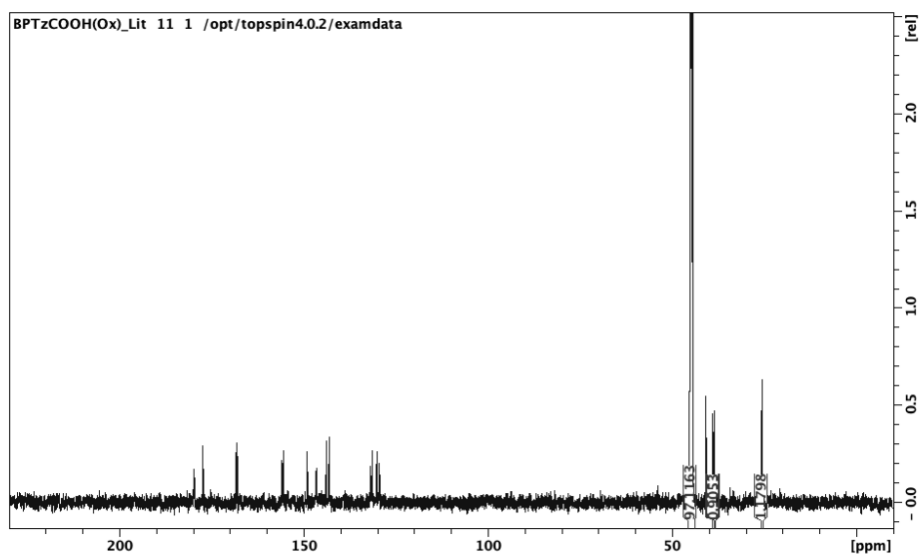


Figure S2.5. ^{13}C NMR (150 MHz, CDCl_3) of **13**.

6-{Bis[(2-pyridyl)methyl]amino}-1-({*p*-(1,2,4,5-tetrazin-3-yl)phenyl)methyl}amino)-1-hexanone (14**). Compound **13** (0.325, 1.0 eq.) and (4-(1,2,4,5-tetrazin-3-yl) phenyl) methanamine hydrochloride (0.325 mmol, 1.0 eq.) were combined in anhydrous ACN with Et_3N and stirred for 1 hour at room temperature under Ar. The compound was**

purified using semi-preparative HPLC (10-30% solvent B over 2-20 min) $R_t = 11$ min.

The solvent was removed through rotary evaporation giving a dark pink hygroscopic solid (48.8 mg, 31% yield): ^1H NMR (600 MHz, CDCl_3): δ 10.19 (s, 1 H), 8.72 (d, $J = 6.0$ Hz, 2 H), 8.51 (d, $J = 6.0$ Hz, 2 H), 8.04 (t, $J = 6.0$ Hz, 2 H), 7.76 (d, $J = 6.0$ Hz, 2 H), 7.54 (t, $J = 6.0$ Hz, 2 H), 7.49 (d, $J = 12$ Hz, 2 H), 7.14 (t, $J = 6.0$ Hz, 1 H), 4.52 (d, $J = 6.0$ Hz, 2 H), 4.42 (s, 4 H), 2.95 (t, $J = 9.0$ Hz, 2 H), 2.27 (t, $J = 6.0$ Hz, 2 H), 1.72 (m, 2 H), 1.62 (m, 2 H), 1.31 (m, 2 H). ^{13}C NMR (150 MHz, CDCl_3): δ 173.79, 166.41, 157.89, 151.76, 146.37, 144.41, 141.59, 130.60, 128.63, 126.00, 125.13, 56.69, 54.49, 43.27, 35.38, 25.74, 24.77, 24.35. HRMS (ES⁺) m/z for $\text{C}_{27}\text{H}_{30}\text{N}_8\text{O}$: calcd 483.2621, observed 483.2621 $[\text{M}-\text{H}]^+$.

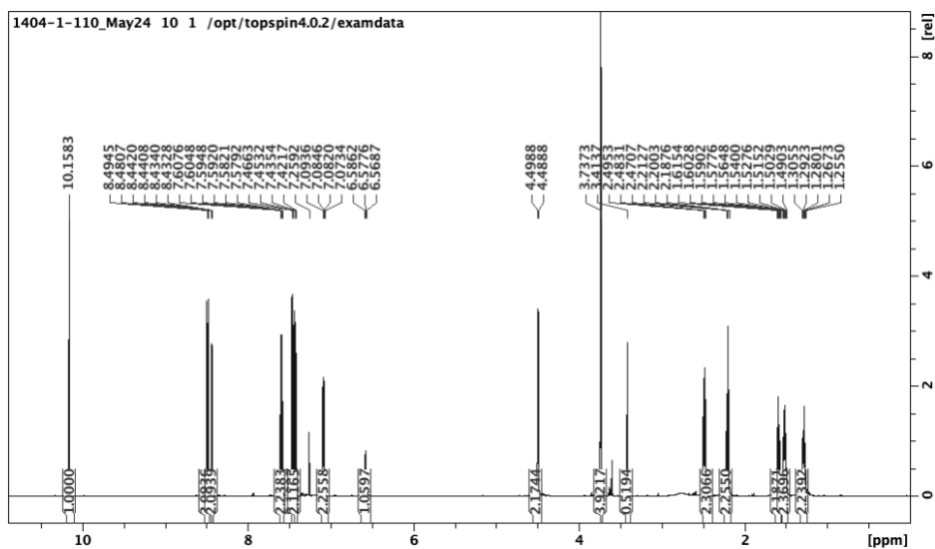


Figure S2.6. ^1H NMR (600 MHz, CDCl_3) of **14**.

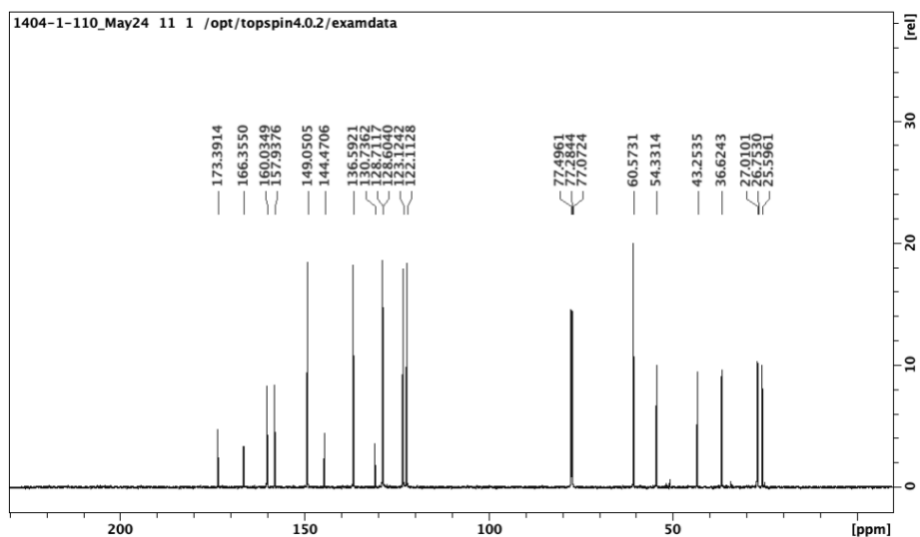


Figure S2.7. ^{13}C NMR (150 MHz, CDCl_3) of **14**.

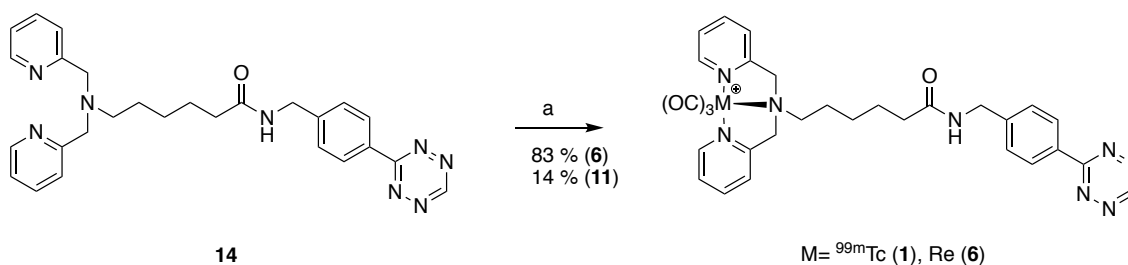


Figure S2.8. Synthesis of **1** and **6** from **14**. a) $[\text{M}(\text{CO})_3(\text{H}_2\text{O})_3]^+$, MW, 20 min, 60 °C, pH 3.5, MeOH, saline. M= $^{99\text{m}}\text{Tc}$ (**1**) and Re (**6**).

Synthesis of $[\text{}^{99\text{m}}\text{Tc}(\text{CO})_3(\text{OH}_2)_3]^+$. A sealed microwave vial containing $\text{K}_2[\text{BH}_3\text{CO}_2]$ (8-10 mg), Na_2CO_3 (15 mg), $\text{Na}_2\text{B}_4\text{O}_7 \cdot 10\text{H}_2\text{O}$ (20 mg), Na/K-tartrate (25 mg) was purged with Ar for 10 minutes. $^{99\text{m}}\text{TcO}_4^-$ in 4 mL of saline was added to the vial and the $^{99\text{m}}\text{TcO}_4^-$ was reduced to $[\text{}^{99\text{m}}\text{Tc}(\text{CO})_3(\text{OH}_2)_3]^+$ through a microwave reaction (3 minutes at 100 °C with 10 s of pre-stirring.) The pH of the solution was adjusted to 3.5 using ~400 μL of 1M HCl.

6-{Bis[(2-pyridyl)methyl]amino}-1-([p-(1,2,4,5-tetrazin-3-yl)phenyl]methyl)amino}-1-hexanone technetium-99m tricarbonyl complex (6). 250 μL of $[\text{}^{99\text{m}}\text{Tc}(\text{CO})_3(\text{OH}_2)_3]^+$ in saline (82.88 MBq) was added to **1** (2 mg) dissolved in 250 μL MeOH. The reaction was conducted in a microwave for 20 minutes at 60 $^\circ\text{C}$ (pH= 3.5.) The compound was purified using analytical HPLC (30-40% solvent B over 2-20 min) $R_t=11.2$ min (R.C.Y.: 83%.) Log P= 0.399.

6-{Bis[(2-pyridyl)methyl]amino}-1-([p-(1,2,4,5-tetrazin-3-yl)phenyl]methyl)amino}-1-hexanone rhenium tricarbonyl complex (11). Compound **1** (84 mg, 0.27 mmol) was combined with $[\text{Re}(\text{CO})_3(\text{H}_2\text{O})_3]\text{Br}$ (130 mg, 0.32 mmol) in dry ACN for 20 min at 60 $^\circ\text{C}$ in a microwave vial. The reaction was conducted in a microwave for 20 minutes at 60 $^\circ\text{C}$ (pH= 3.5.) The compound was purified using analytical HPLC (30-40% solvent B over 2-20 min) $R_t=11$ min. The solvent was evaporated yielding a pink film (24 mg, 15 %).

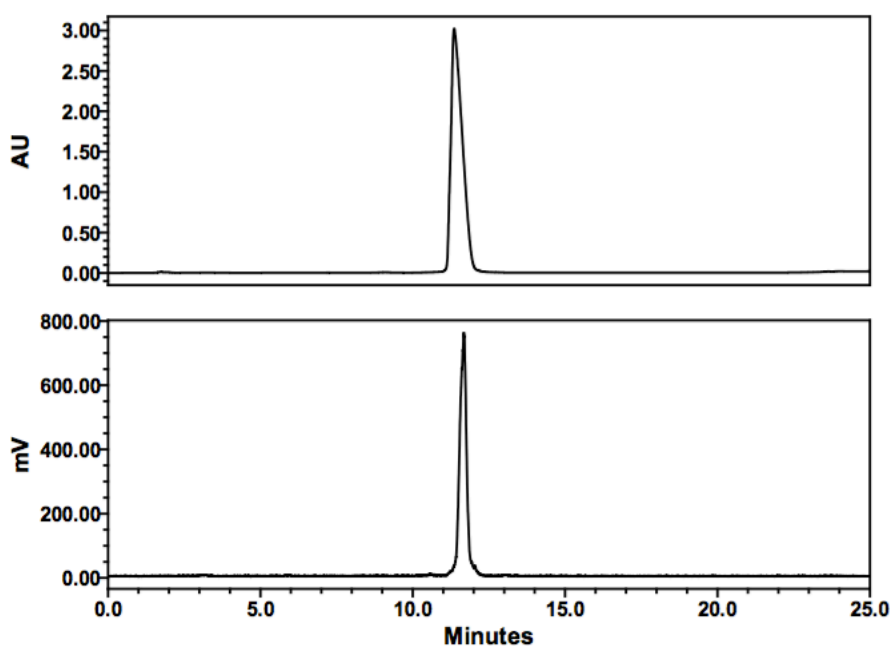


Figure S2.9. HPLC chromatograms (UV and γ) of **6** (top) co-injected with **1** (bottom).

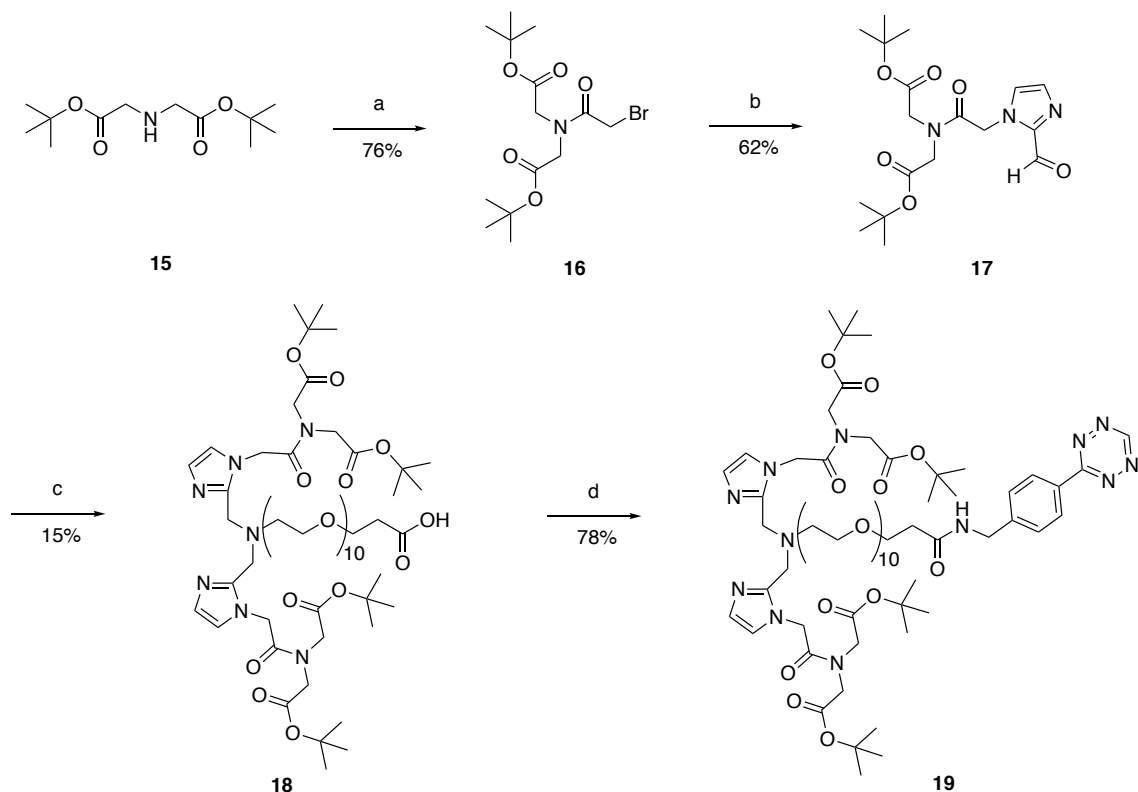


Figure S2.10. Synthesis of compound **19** from **15**. a) Bromoacetyl bromide, Et₃N, DCM, rt, 2 h. b) Imidazole 2-carboxaldehyde, potassium iodide, DIPEA, DMF, 80 °C, 12 h. c) NH₂-PEG₁₀-CH₂CH₂COOH, NaBH(OAc)₃, DCE, rt, 12 h. d) (4-(1,2,4,5-tetrazin-3-yl)phenyl) methanamine hydrochloride, PyBOP, DIPEA, DMF, rt, 12 h.

***Tert*-Butyl [(*tert*-butoxycarbonylmethyl)(2-bromoacetyl)amino]acetate (**16**).¹³**

Compound **15** (di-tert butyl iminodiacetate) (0.408 mmol, 1 eq), bromoacetyl bromide (0.533, 1.3 eq), and Et₃N (0.1 mL) were combined in DCM and stirred at room temperature for 2 hours. The reaction mixture was diluted with DCM (15 mL) and washed with water (3 x 20 mL). The organic layer was collected and dried over sodium sulphate. The solvent was evaporated under reduced pressure and the residue was purified using Biotage SP1 using 10-50% hexanes in EtOAc yielding dark yellow oil. (565 mg,

76%): ^1H NMR (600 MHz, CDCl_3): δ 4.09 (s, 2 H), 4.06 (s, 2 H), 3.86 (s, 2 H), 1.49 (s, 9 H), 1.46 (s, 9 H). ^{13}C $\{^1\text{H}\}$ NMR (150 MHz, CDCl_3): δ 167.9, 167.7, 167.3, 83.3, 82.5, 51.9, 49.4, 28.3, 28.2, 25.7. HRMS (ES $^+$) m/z for $\text{C}_{14}\text{H}_{24}\text{BrNO}_5$: calcd. 366.25, observed 388.0731 $[\text{M}-\text{Na}]^+$.

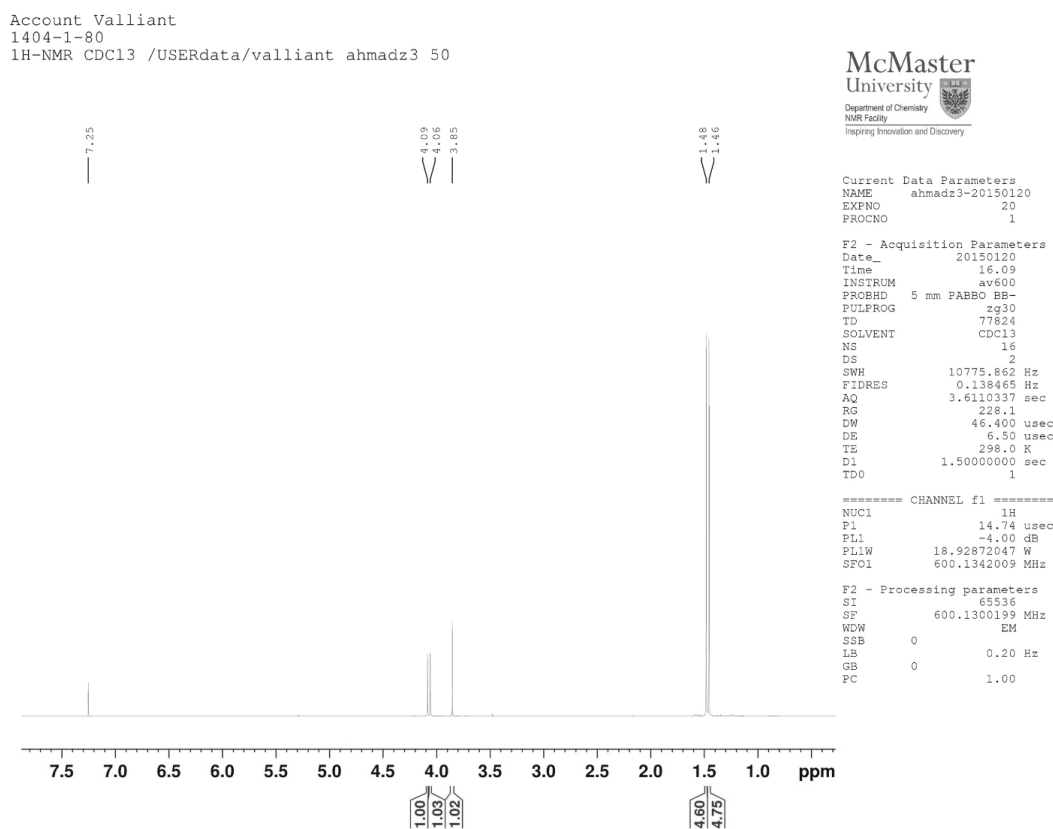


Figure S2.11. ^1H NMR (600 MHz, CDCl_3) of **16**.

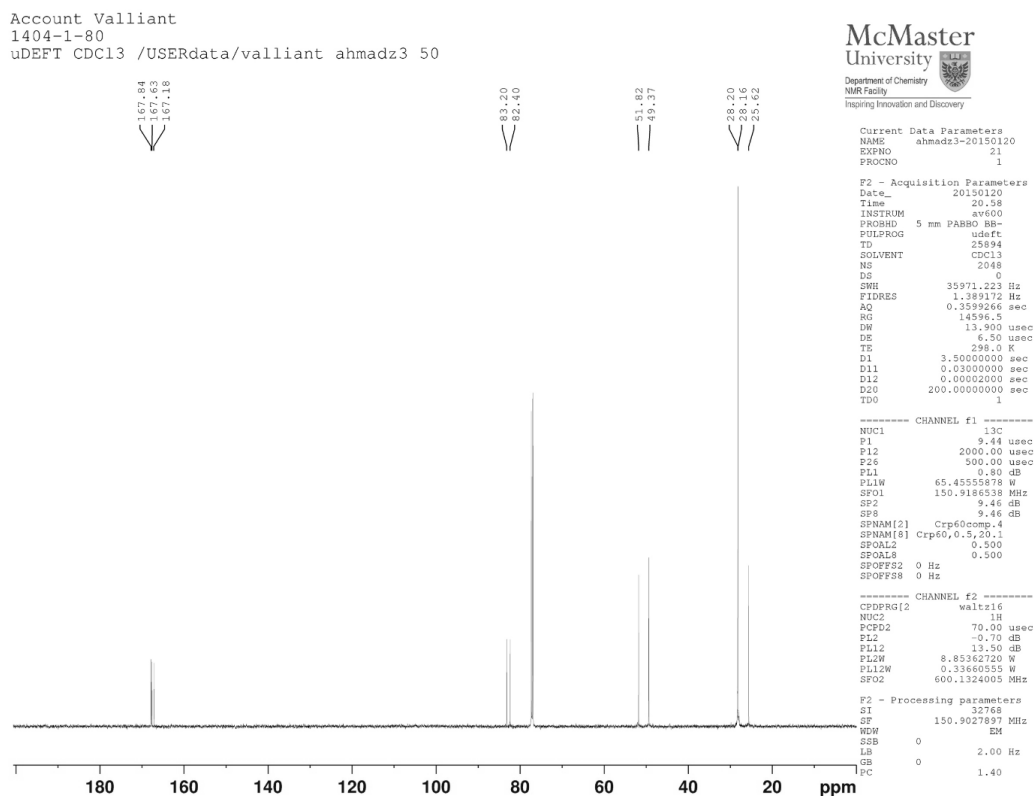


Figure S2.12. ^{13}C NMR (150 MHz, CDCl_3) of **16**.

Tert-Butyl $\{(tert\text{-butoxycarbonylmethyl})[2\text{-}(2\text{-formyl-}1H\text{-imidazol-1-yl)acetyl]amino\}$ acetate (**17**).¹³ Compound **16** (1.54 mmol, 1.0 eq), imidazole 2-carboxaldehyde (1.85 mmol, 1.2 eq), potassium iodide (KI) (4.63 mmol, 3.0 eq) and DIPEA (0.62 mL) were combined in anhydrous DMF (30 mL) and left to stir overnight under Ar at 80 °C. The solvent was evaporated under reduced pressure. The crude was diluted with DCM (50 mL) and washed with water (3 x 50 mL). The organic layer was collected, dried over Na_2SO_4 and dried under vacuum. The crude was purified with Biotage SP1 using 1-10% MeOH in DCM yielding a pale orange solid. (351 mg, 62%):

^1H NMR (600 MHz, CDCl_3): δ 9.77 (s, 1 H), 7.32 (s, 1 H), 7.26 (s, 1 H), 5.31 (s, 2 H), 4.15 (s, 2 H), 4.09 (s, 2 H), 1.52 (s, 9 H), 1.44 (s, 9 H). ^{13}C $\{^1\text{H}\}$ NMR (150 MHz, CDCl_3): δ 182.7, 167.8, 167.0, 143.4, 132.0, 128.1, 83.7, 82.6, 51.1, 49.9, 47.8, 28.3. HRMS (ES+) m/z for $\text{C}_{18}\text{H}_{23}\text{N}_3\text{O}_6$: calcd 381.43, observed 404.1800 $[\text{M}-\text{Na}]^+$.

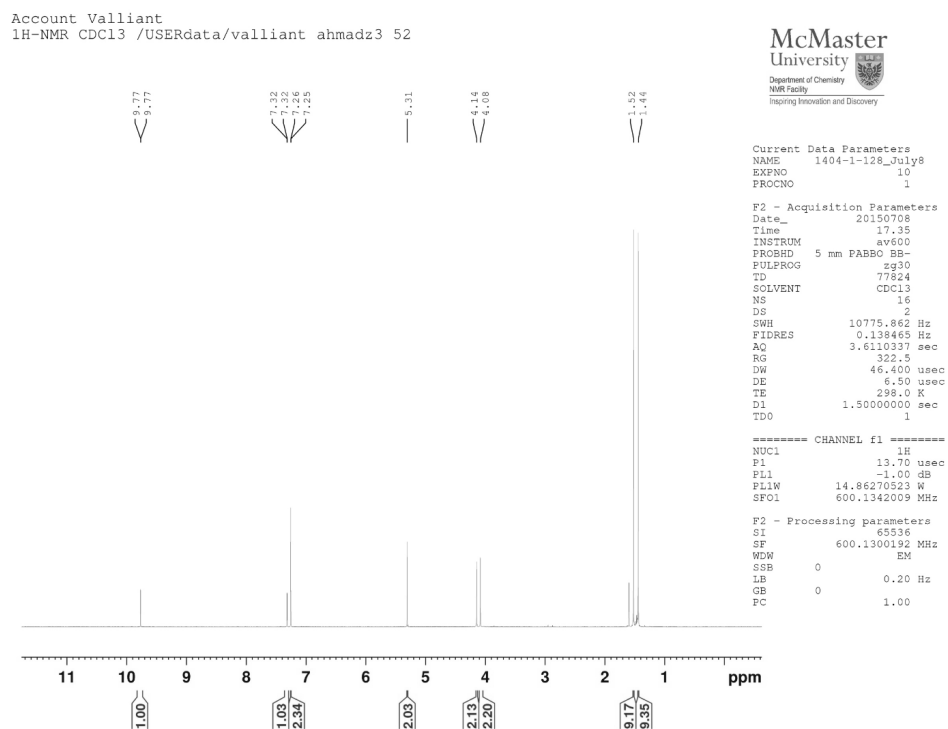


Figure S2.13. ^1H NMR (600 MHz, CDCl_3) of **17**.

oil: (102 mg, 15 %): ^1H NMR (600 MHz, CDCl_3): δ 6.96 (s, 2 H), 6.90 (s, 2 H), 5.04 (s, 4 H), 4.18 (s, 4 H), 4.00 (s, 4 H), 3.81 (s, 4 H), 3.77 (t, $J= 6.0$ Hz, 2 H), 3.64-3.54 (m, CH_n), 2.81 (t, $J= 6.0$ Hz, 2 H), 2.58 (t, $J= 6.0$ Hz, 2 H), 1.49 (s, 9 H), 1.42 (s, 9 H). ^{13}C $\{^1\text{H}\}$ NMR (150 MHz, CDCl_3): δ 174.4, 168.2, 167.9, 145.8, 125.4, 122.4, 83.2, 82.3, 70.9-67.4, 53.9, 50.41, 49.4, 47.5, 28.3, 28.3. HRMS (ES $^+$) m/z for $\text{C}_{59}\text{H}_{101}\text{N}_7\text{O}_{22}$: calcd 1260.7078, observed 1260.7108 $[\text{M}-\text{H}]^+$

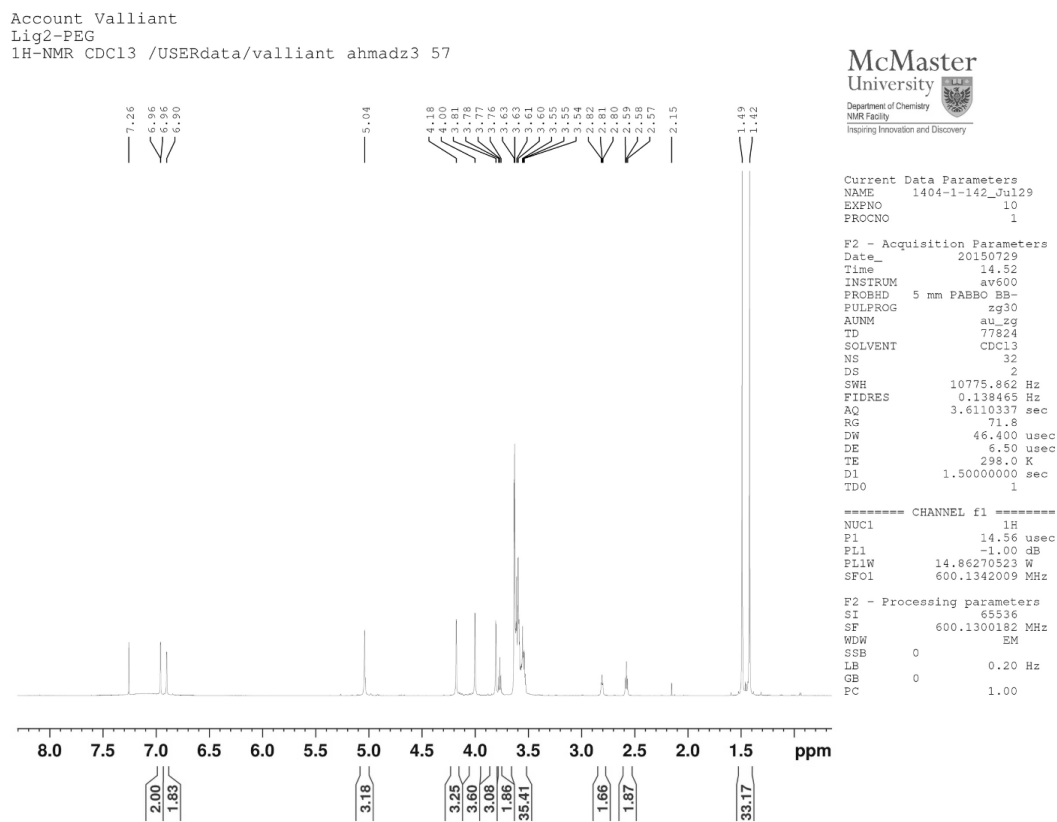


Figure S2.15. ^1H NMR (600 MHz, CDCl_3) of **18**.

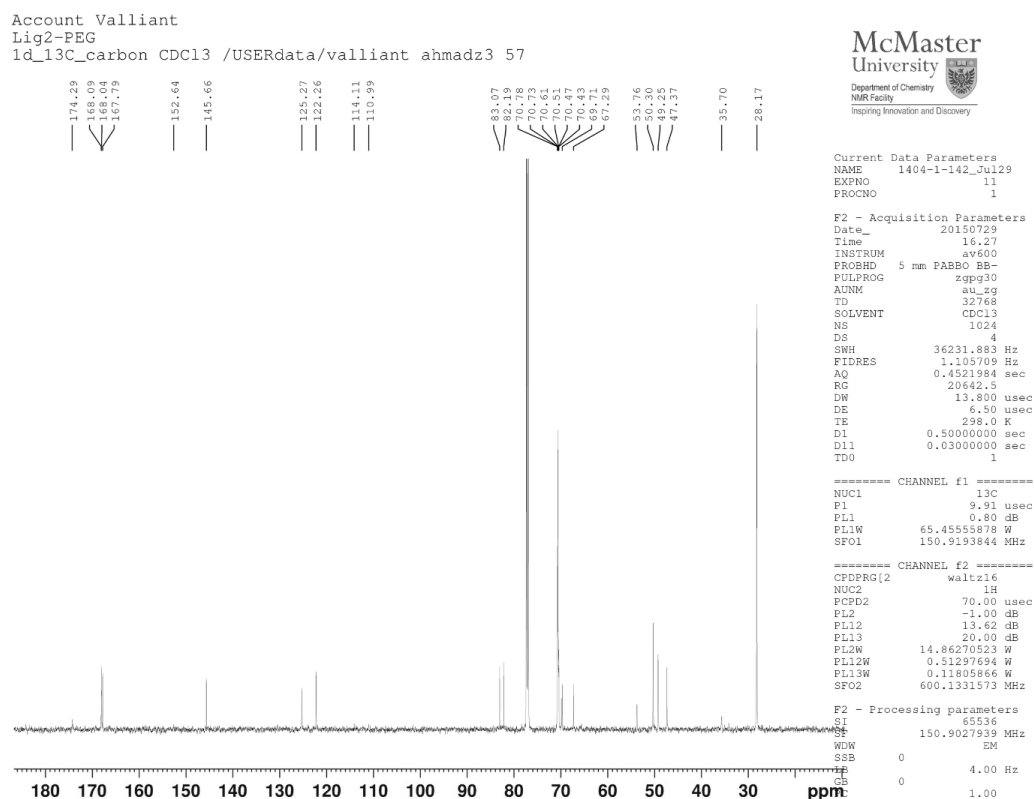


Figure S2.16. ^{13}C NMR (150 MHz, CDCl_3) of **18**.

***tert*-Butyl [(*tert*-butoxycarbonylmethyl){2-[2-((1-[2-[bis(*tert*-butoxycarbonylmethyl)amino]-2-oxoethyl)-2*H*-imidazol-2-yl)methyl]}{2-[2-(2-[2-(2-[2-(2-[2-(2-[2-(2-[3-oxo-3-({*p*-(1,2,4,5-tetrazin-3-yl)phenyl]methyl;amino)propoxy]ethoxy}ethoxy) ethoxy]ethoxy}ethoxy)ethoxy]ethoxy}ethoxy]ethyl}amino}methyl)-2*H*-imidazol-1-yl]acetyl}amino]acetate (**19**).**

Compound **18** (0.048 mmol, 1.0 eq) was combined with PyBOP (0.119 mmol, 2.5 eq) in anhydrous DMF (4 mL) and stirred for 15 minutes at room temperature. DIPEA (0.25 mL) and (4-(1,2,4,5-tetrazin-3-yl) phenyl methanamine hydrochloride (0.105 mmol, 2.2

eq.) in anhydrous DMF (3 mL) and stirred for 15 minutes at room temperature. The two solutions were combined and stirred overnight under Ar at room temperature. The solvent was evaporated under reduced pressure. The crude was purified using semi-preparative HPLC (5-39 % solvent B over 0-17 min), $R_t = 15$ min, yielding a pink solid (160 mg, 78%): ^1H NMR (600 MHz, CDCl_3): δ 10.2 (s, 1 H), 8.57 (d, 2H), 7.54 (d, 2 H), 7.01 (s, 2H), 6.89 (s, 2H), 5.10 (s, 4 H), 4.19 (s, 4 H), 4.00 (s, 4 H), 3.88 (s, 4 H), 3.79 (t, $J=6.0$ Hz, 2 H), 3.39-3.53 (m, 52 H) 2.84 (s, 2 H), 2.58 (t, $J=6.0$ Hz, 2 H), 1.50 (s, 18 H), 1.42 (s, 18 H). ^{13}C $\{^1\text{H}\}$ NMR (150 MHz, CDCl_3): δ 172.1, 168.1, 167.7, 167.4, 166.4, 165.7, 157.9, 146.1, 144.8, 130.4, 128.6, 128.4, 122.7, 82.3, 70.5-69.3, 67.4, 54.2, 50.5, 49.8, 47.7, 46.4, 43.0, 28.1. HRMS (ES+) m/z for $\text{C}_{68}\text{H}_{108}\text{N}_{12}\text{O}_{21}$: calcd 1429.7830, observed 1429.7881 $[\text{M}-\text{H}]^+$

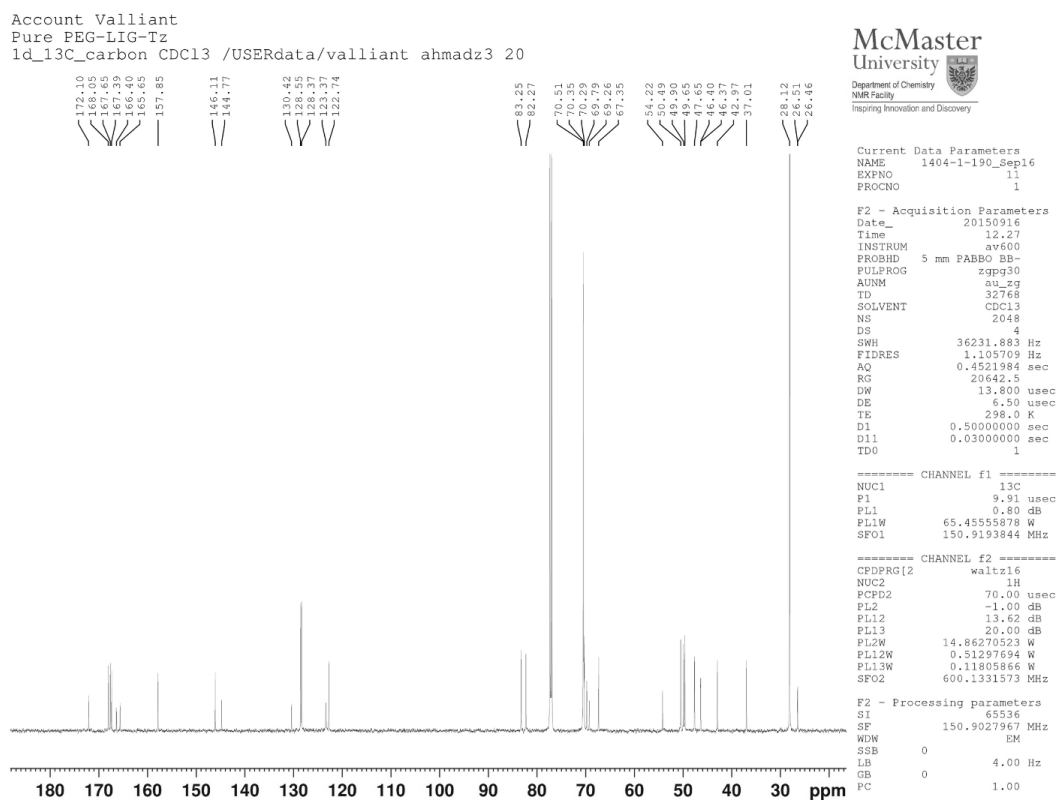


Figure S2.18. ¹³C NMR (150 MHz, CDCl₃) of **19**.

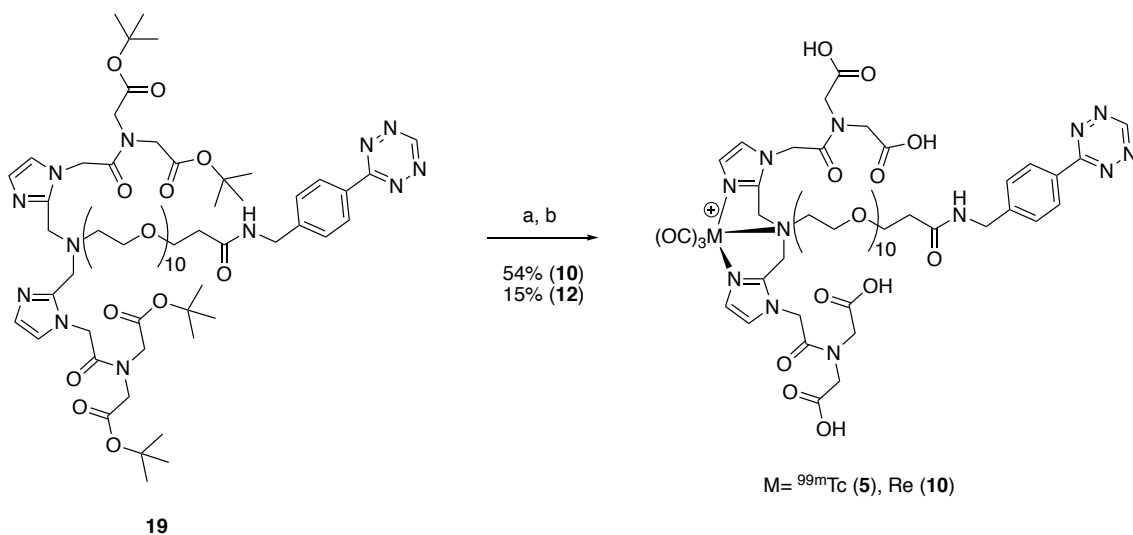


Figure S2.19. Synthesis of compounds **5** and **10** from **19**. a) $[M(\text{CO})_3(\text{H}_2\text{O})_3]^+$, MW, 20 min, 60 °C, pH 3.5, MeOH, saline M=^{99m}Tc (**5**) and Re (**10**). b) DCM, TFA, MW, 60 °C, 10 min (**5**), 11 min (**10**).

[(Carboxymethyl){2-[2-({[(1-{2-[bis(carboxymethyl)amino]-2-oxoethyl}-2*H*-imidazol-2-yl)methyl]{2-[2-(2-{2-[2-(2-{2-[2-(2-{2-[3-oxo-3-({[*p*-(1,2,4,5-tetrazin-3-yl)phenyl]methyl;amino)propoxy]ethoxy}ethoxy)ethoxy]ethoxy]ethoxy}ethoxy)ethoxy]ethyl}amino)methyl]-2*H*-imidazol-1-yl]acetyl}amino]acetic acid technetium-99m tricarbonyl complex (**5**). 250µL of [^{99m}Tc(CO)₃(OH₂)₃]⁺ in saline (731 MBq) was added to **19** dissolved in 250 µL MeOH. The reaction was conducted in a microwave for 20 minutes at 60 °C (pH= 3.5.) The compound was purified using analytical HPLC (5-39 % solvent B over 12 min, 39-100% solvent B over 12-20 min), R_t= 14.9 min (R.C.Y.: 54%).)

[(Carboxymethyl){2-[2-({[(1-{2-[bis(carboxymethyl)amino]-2-oxoethyl}-2*H*-imidazol-2-yl)methyl]{2-[2-(2-{2-[2-(2-{2-[2-(2-{2-[3-oxo-3-({[*p*-(1,2,4,5-tetrazin-3-yl)phenyl]methyl;amino)propoxy]ethoxy}ethoxy)ethoxy]ethoxy}ethoxy)ethoxy]ethoxy}ethoxy]ethyl}amino)methyl]-2*H*-imidazol-1-yl]acetyl}amino]acetic acid

y}ethoxy)ethoxy}ethyl}amino}methyl)-2*H*-imidazol-1-yl}acetyl}amino}acetic acid

rhenium tricarbonyl complex (10). Compound **19** (10 mg, 0.007 mmol) was combined with $[\text{Re}(\text{CO})_3(\text{H}_2\text{O})_3]\text{Br}$ (4.9 mg, 0.0084 mmol) in dry ACN for 20 min at 60 °C in a microwave vial. The solvent was evaporated, and the crude was dissolved in 1:1 DCM:TFA (1 mL) to be microwaved for 11 min at 60 °C. The solvent was evaporated, and the compound purified by HPLC (5-39 % solvent B over 12 min, 39-100% solvent B over 12-20 min), $R_t = 14.9$ min, yielding a pink oil (2.2 mg, 15%). HRMS (ES+) m/z for $\text{C}_{55}\text{H}_{76}\text{N}_{12}\text{O}_{24}\text{Re}$: calcd 1475.4653, observed 1475.4668 $[\text{M}-\text{H}]^+$

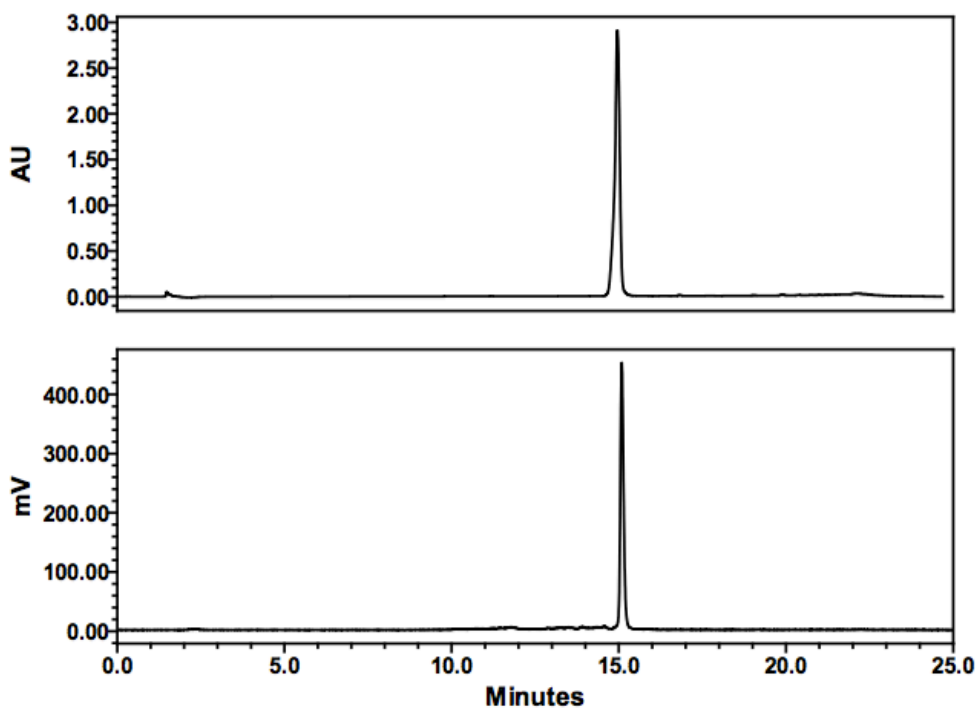


Figure S2.20. HPLC chromatograms (UV and γ) of **10** (top) co-injected with **5** (bottom).

APPENDIX II

Supporting Information for Chapter 5

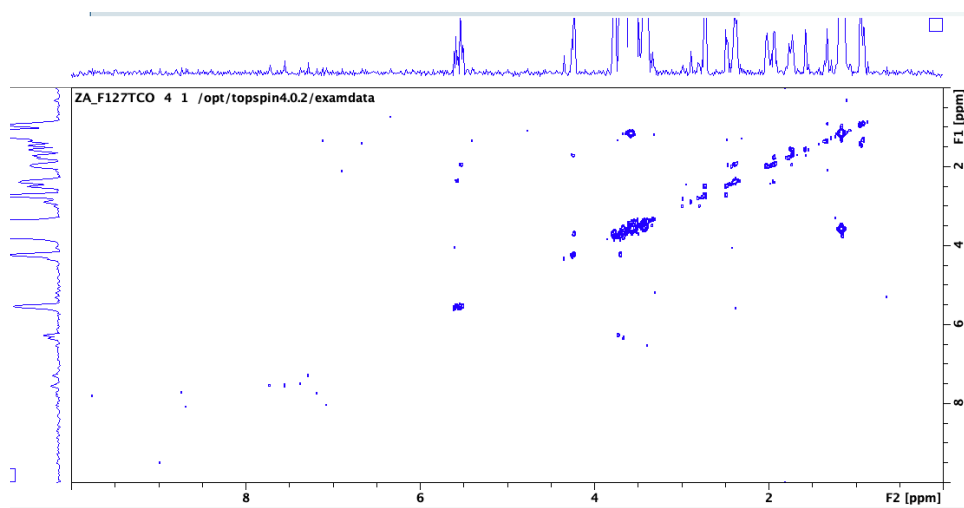


Fig S 1. COSY NMR of F127-TCO polymers (**3**).

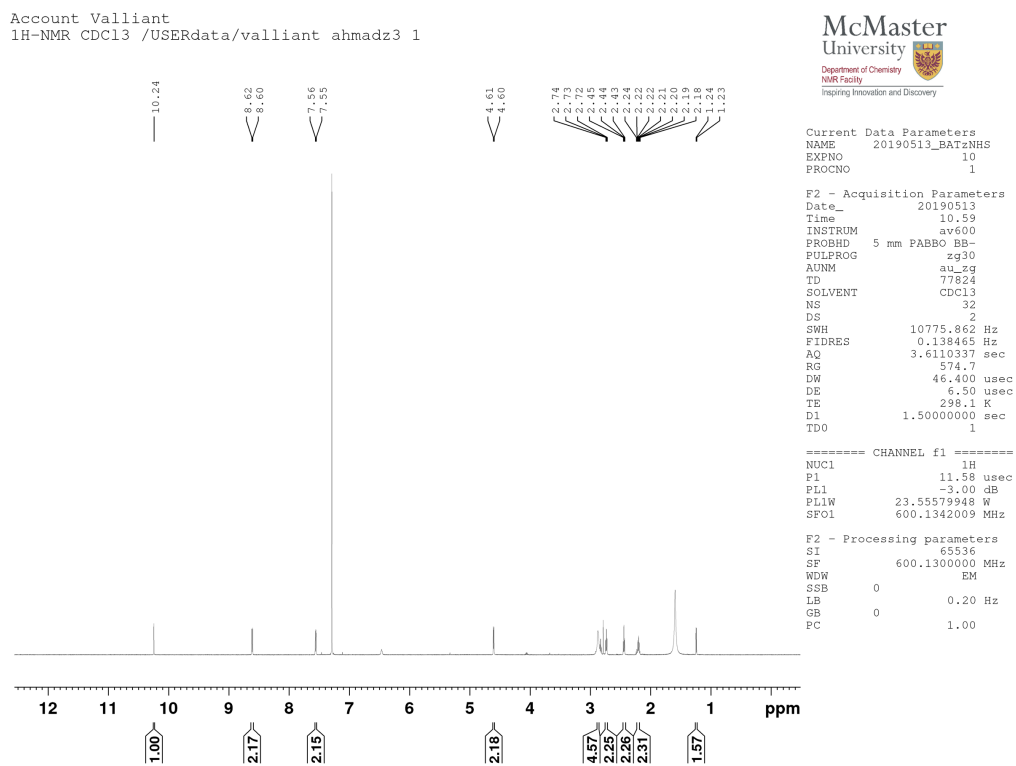


Fig S 2. ¹H NMR of TzNHS (4)

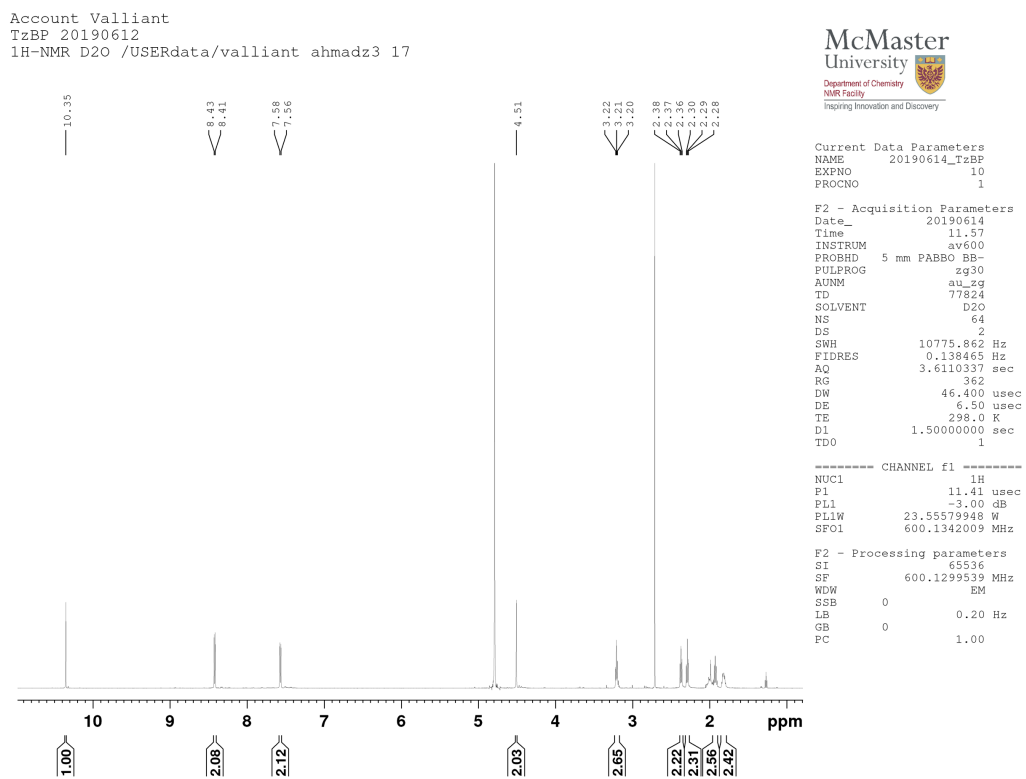


Fig S 3. ¹H NMR of TzBP (5).

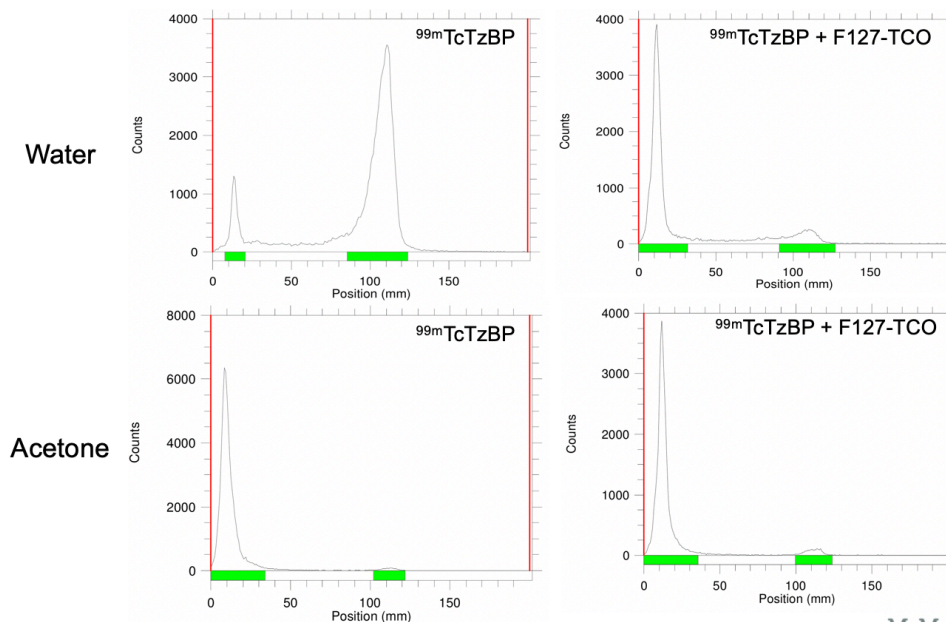


Fig S 4. iTLC of ^{99m}Tc TzBP (**6**) and $^{99m}\text{TcTzBP} + \text{F127-TCO}$ polymers run using water and acetone as eluents: 12 % $^{99m}\text{TcO}_2$ ($R_f = 0.069$), 88 % $^{99m}\text{TcTzBP} + ^{99m}\text{TcO}_4^-$ ($R_f = 0.53$), and 2 % $^{99m}\text{TcO}_4^-$ ($R_f = 0.56$), 98 % $^{99m}\text{TcTzBP} + ^{99m}\text{TcO}_2$ ($R_f = 0.054$).

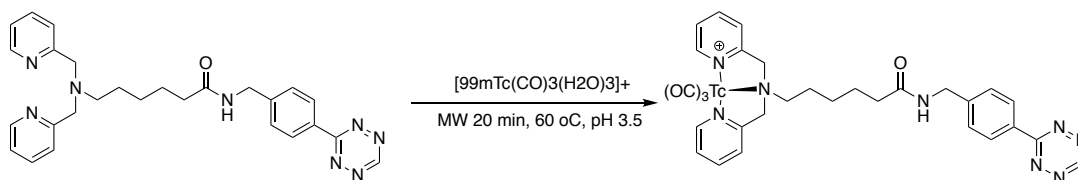


Fig S 5. Radiolabeling scheme of ^{99m}Tc TzPy (**7**).

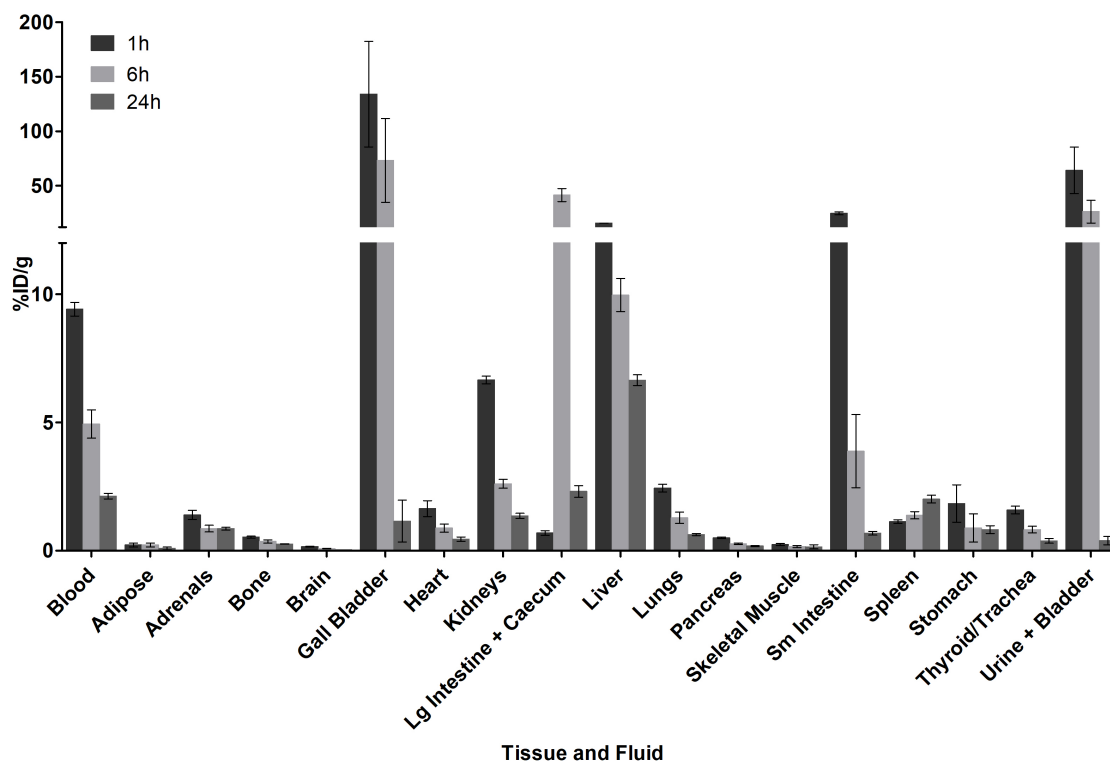


Fig S 6. Biodistribution results for $[^{99m}\text{Tc}]\text{TcTzPy-mF127-TCO}$, full tissue list. Data shown was obtained from selected tissues and fluids taken from mice at 1, 6, and 24 h post injection of $[^{99m}\text{Tc}]\text{TcTzPy-mF127-TCO}$. Activity was normalized to tissue or fluid weight, as mean percent injected dose per gram of tissue or fluid ($\% \text{ ID/g}$) \pm SEM.

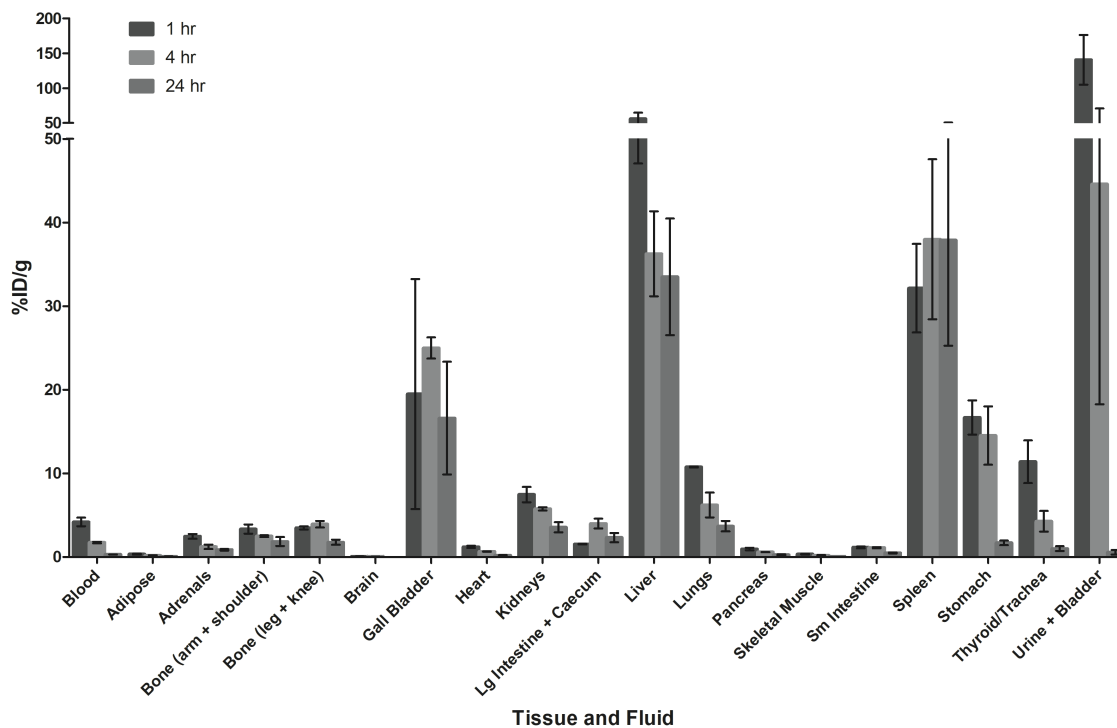


Fig S 7. Biodistribution results for $[^{99m}\text{Tc}]\text{TcTzBP-mF127-TCO}(\text{IR780})$ micelles in healthy Balb/C mice. Data shown was obtained from selected tissues and fluids taken from mice at 1, 4, and 24 h post injection of $[^{99m}\text{Tc}]\text{TcTzBP-mF127-TCO}(\text{IR780})$. Activity was normalized to tissue or fluid weight, as mean percent injected dose per gram of tissue or fluid (% ID/g) \pm SEM.

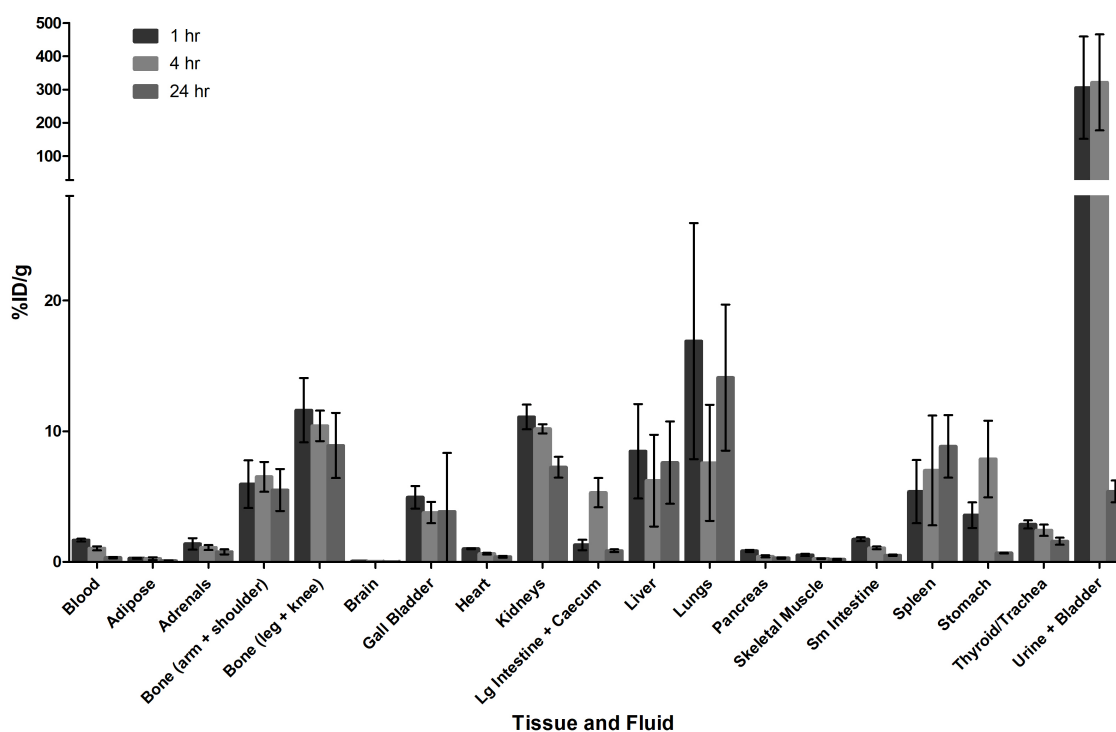


Fig S 8. Biodistribution data obtained for $[^{99m}\text{Tc}]\text{TcTzBP}$ when pre-targeting for subsequent administration of mF127-TCO(IR780) in healthy Balb/C mice at 1, 4, and 24 h, reported as % ID/g. Activity was normalized to tissue or fluid weight, as mean percent injected dose per gram of tissue or fluid (% ID/g) \pm SEM.

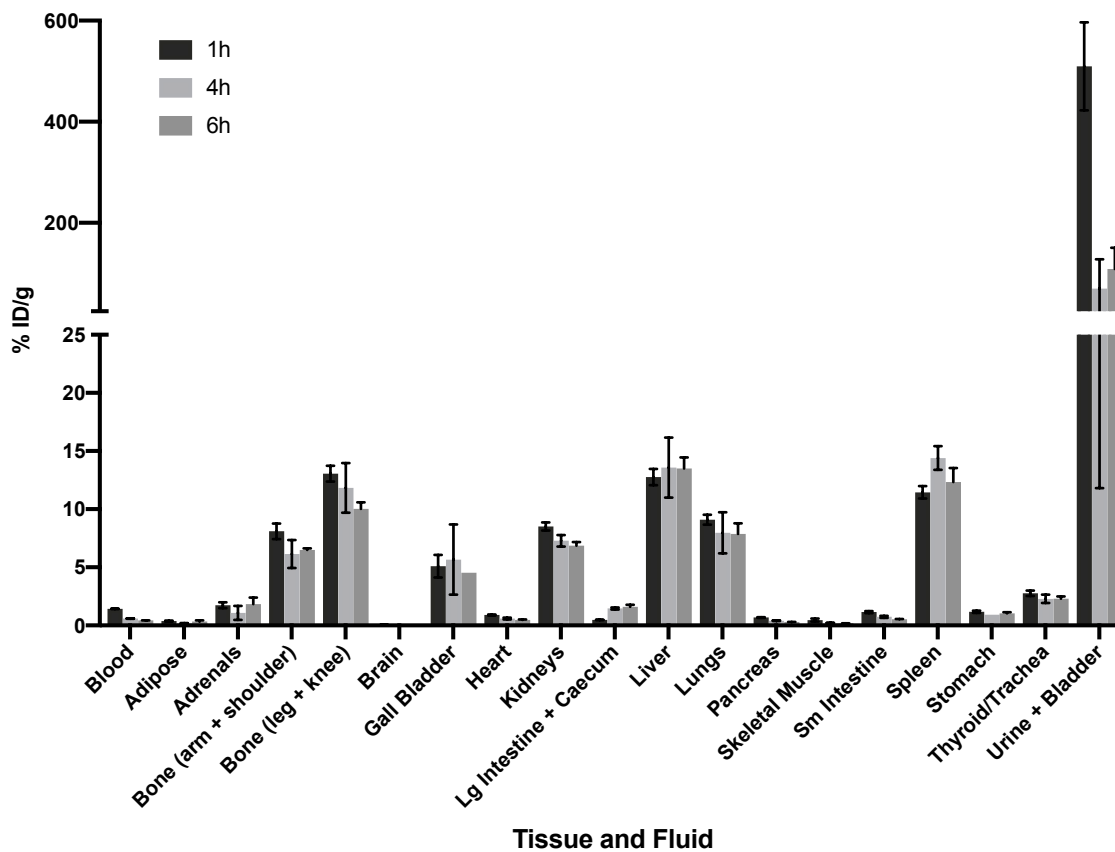


Fig S 9. Biodistribution data obtained for $[^{99m}\text{Tc}]\text{TcTzBP}$ in healthy Balb/C mice at 1, 4, and 6 h, reported as % ID/g. Activity was normalized to tissue or fluid weight, as mean percent injected dose per gram of tissue or fluid ($\% \text{ ID/g}$) \pm SEM.

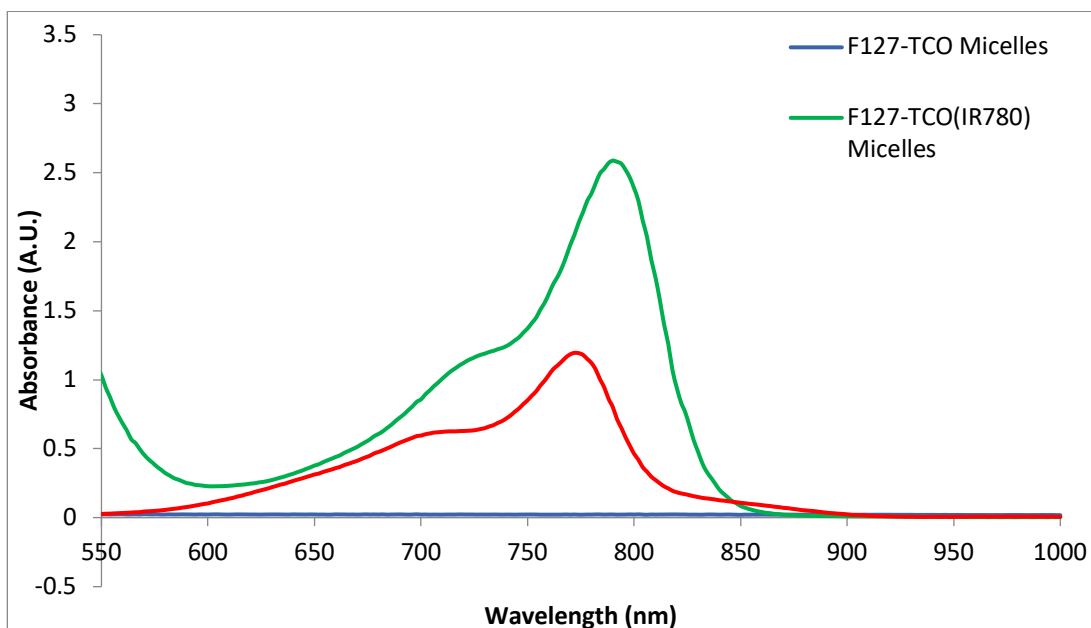


Fig S 10. Absorbance measurements of IR-780 dye (green), F17-TCO(IR780) micelles (red), and blank F127-TCO micelles (blue) scanned over 550-1000 nm. The absorbance maxima for IR780 around 780 nm remains unchanged when the dye is encapsulated within the micelles. The micelles do not exhibit any absorbance signal at that wavelength.